DISSERTATION

submitted to the

Combined Faculties of the Natural Sciences and Mathematics

of the Ruperto-Carola-University of Heidelberg, Germany

for the degree of

Doctor of Natural Sciences

Put forward by
M. Sc. Sebastian Hietzschold
Born in Oberhausen, Germany
Oral examination: 13.12.2017

Surface Functionalization of Nickel Oxide and Gallium Nitride for Hybrid Opto-Electronics

Referees: Prof. Dr. Wolfgang Kowalsky
Prof. Dr. Albrecht Winnacker

Surface Functionalization of Nickel Oxide and Gallium Nitride for Hybrid Opto-Electronics —This thesis examines the influence of surface functionalization by self-assembled monolayers (SAMs) on two different materials, (i) nickel oxide and (ii) gallium nitride.

(i) Thin solution-processed films of nickel oxide (sNiO) were modified with dipolar self-assembled monolayers of 4-cyanophenyl-phosphonic acid (CYNOPPA) to improve the energy level alignment and the chemical compatibility to the donor in F$_4$ZnPc:C$_{60}$ organic photovoltaic devices. A detailed analysis of infrared and photoelectron spectroscopy showed the chemisorption of the molecules with a nominal layer thickness of around one monolayer. The spectroscopic results gave further insight into the chemical composition of the SAM. Density functional theory calculations were employed to reveal energetically allowed binding configurations of the phosphonate anchor group. CYNOPPA successfully increased the work function of the sNiO up to 5.1-5.2 eV, leading to a well-matched Fermi level of the hole-contact layer to the ionization potential of the donor. Unexpectedly, the improved alignment did not lead to a higher power conversion efficiency. Instead, a significant reduction of the fill factor was observed, which was assigned to the formation of a transport barrier due to a low conductive interface region. However, it was shown that the barrier can be reduced by doping the oxide hole-contact layer and thereby increase its charge carrier density.

(ii) For the goal of GaN nanowire surface state passivation and control of the corresponding band bending, different GaN planes were functionalized with self-assembled monolayers. A step-by-step procedure of solvent cleaning, plasma treatment and HCl etching was developed to guarantee clean surfaces for SAM growth. X-ray photoelectron spectroscopy (XPS) measurements showed that oxygen as well as carbon contents could be reduced to a minimum with this procedure. SAM precursor with different anchoring groups were tested to find the best binding partner for the GaN surface. The SAM quality and passivation functionality was determined by Kelvin probe surface photovoltage and contact angle measurements. It was shown that amines and thiols suffer from low surface coverage on GaN(0001) under ambient conditions. Hence, an oxide template layer was grown for the attachment of phosphonic acids (PAs). Two phosphonic acids with different intrinsic dipole moments were applied to oxidized high quality GaN(0001) and GaN$(1\bar{1}00)$ surfaces grown by molecular beam epitaxy. XPS and contact angle measurements revealed dense monolayer coverage of the PA-SAMs. Despite the oxide buffer layer, the band bending of the GaN was reduced by the chemisorption and molecular backbones of the PAs. Continuous-wavelength photoluminescence (cw-PL) measurements showed an increase of the total PL intensity, which suggests that a reduction of the band bending is essential for high luminescence quantum yields.

Oberflächenfunktionalisierung von Nickeloxid und Galliumnitrid für hybride Optoeletronik —Im Rahmen dieser Arbeit wird der Einfluss von Oberflächenfunktionalisierung mit selbstorganisierenden Monolagen (SAMs) auf zwei verschiedenen Materialien untersucht: (i) Nickeloxid und (ii) Galliumnitrid.

(i) Lösungs-prozessierte Nickeloxid Dünnschichtfilme wurden mit selbstorganisierenden Monolagen modifiziert, um die Energieanpassung und chemische Kompatibilität zum Absorber in $F_4ZnPc:C_{60}$ Solarzellen zu verbessern. Eine detaillierte Analyse durch Infrarot- und Photoelektronenspektroskopie bestätigte die Chemisorption der Moleküle mit einer nominellen Schichtdicke von etwa einer Monologe. Die Ergebnisse der Spektroskopie lieferten zudem Einsicht in die chemische Zusammensetzung der SAMs. Mit Hilfe von Dichtefunktionaltheorie konnten die energetisch günstigsten Bindungskonfigurationen der Moleküle auf der Oxid-Oberfläche aufgezeigt werden. Durch die Funktionalisierung wurde die Austrittsarbeit der Nickeloxid-Filme auf 5.1-5.2 eV erhöht. Diese Werte liegen nahe am Ionisationspotential des Absorbers, sodass eine gute energetische Anpassung zwischen Lochkontakt und Donator gewährleistet sein sollte. Entgegen der Erwartung führte die verbesserte energetische Anpassung jedoch nicht zur Erhöhung der Energieeffizienz der Solarzelle. Stattdessen wurde ein starker Einbruch des Füllfaktors beobachtet, der durch eine Transportbarriere für Ladungsträger verursacht wurde. Die Transportbarriere wurde auf eine niedrig leitfähige Grenzfläche zurückgeführt und konnte durch Dotierung und Erhöhung der Ladungsträgerdichte im Nickeloxid reduziert werden.

(ii) Um die Oberflächenzustände von Galliumnitrid und die damit einhergehende Bandverbiegung zu beeinflussen, wurden verschiedene GaN Oberflächen mit SAMs funktionalisiert. Ein Protokoll aus Lösungsmittelreinigen, Sauerstoffplasma behandeln und Salzsäure ätzen wurde entwickelt, um saubere Oberflächen für die Anlagerung der SAMs zu garantieren. Messungen mit Photoelektronenspektroskopie (XPS) zeigten, dass Kohlenstoff- und Sauerstoffanteile auf der Oberfläche bis zu einem Minimum durch die Prozedur reduziert wurden. SAM Präkursoren mit verschiedenen Ankergruppen wurde getestet, um den passenden Bindungspartner für die GaN Oberfläche zu finden. Die Qualität und Funktionalität der SAMs wurde mit Photospannungs- und Kontaktwinkelmessungen beurteilt. Amine und Thiole auf GaN(0001) erreichten nur geringe Bedeckungen. Daher wurden dünne Oxidschichten zur Anbindung von Phosphonaten gewachsen. Zwei Phosphonate mit unterschiedlichen intrinsischen Dipolmomenten wurden auf hoch reine oxidierte GaN(0001) und GaN($1\bar{1}00$) Oberflächen aufgebracht. XPS und Kontaktwinkel zeigten sehr dichte Bedeckungen der PA-SAMs. Trotz der Oxid-Pufferschicht wurde die Bandverbiegung durch die Chemisorption und die Molekül-Rückgrate reduziert. Erste Photolumineszenz-Messungen mit kontinuierlicher Anregungswellenlänge zeigten eine Erhöhung der PL Intensität. Dies lässt darauf schließen, dass die Reduzierung der Bandverbiegung für hohe Lumineszenz-Quantenausbeuten essentiell ist.

Contents

Acronyms

AFM	Atomic force microscopy
BB	Band bending
BHJ	Bulk heterojunction
FHJ	Flat heterojunction
FTIR	Fourier-transform infrared spectroscopy
HOMO	Highest occupied molecular orbital
HTL	Hole transport layer
KP	Kelvin probe
LUMO	Lowest unoccupied molecular orbital
OPV	Organic photovoltaic
PA	Phosphonic acid
PCE	Power conversion efficiency
SAM	Self-assembled monolayer
SEM	Scanning electron microscopy
SPV	Surface photovoltage
TMO	Transition metal oxide
TRPL	Time-resolved photoluminescence
UHV	Ultra-high vacuum
UV	Ultraviolet
VBM	Valence band maximum
XPS	X-ray photoelectron spectroscopy

1. Introduction

Even though silicon semiconductor industry dominates the electronics market today, there are applications that cannot be properly implemented by silicon technology alone. These are for example efficient ultraviolet direct band gap LEDs or low-cost high band gap tandem photovoltaic cells on a large scale [1]. Both applications need fundamental research and can be realized by the usage of high performance inorganic and versatile organic materials. Combining their strengths and functionality to enhance quantum efficiencies of hybrid opto-electronic devices is the purpose of this work.

Organic photovoltaics

Tremendous efforts and funds were put into the research of low-cost, non-toxic and earth-abundant materials for next generations of photovoltaic cells and light-emitting devices. The most prominent representatives are organic light-emitting diodes (OLEDs), organic photovoltaic cells (OPVs) and organic field-effect transistors (OFETs). Pope *et al.* observed electroluminescence in organic anthracene crystals already in 1963 [2]. This was followed by the discovery of conductive polymers with π-conjugated electron systems by Heeger, MacDiarmid, and Shirakawa [3], who were awarded the Nobel prize in chemistry in 2000 [4]. The breakthrough of organic semiconductors can be attributed to the first organic electroluminescent diodes by Tang and Van Slyke [5,6]. Solution-processing of whole devices like OLEDs and OPVs can dramatically reduce production costs and increase the fabrication throughput on a large scale [7]. However, flexible multilayer OPVs still provide only 13.2% PCE in the lab and 7-8% in production [8,9]. Despite the need for more efficient acceptors [10], it was well said by Herbert Kroemer that „the interface is the device“, especially when oxides come into play [11]. Thin metal oxide films, like MoO_3 and NiO, became very important as charge carrier selective and energy level aligning hole-contact layers in OPVs [12]. However, their surface characteristics, especially the work function, strongly depend on the processing history and exposure to adsorbates. This fact is shown in a preliminary experiment on MoO_3 thin films. To achieve control over the work function and chemical compatibility of nickel oxide hole-contact layers, the nickel oxide surface is functionalized with self-assembled monolayers of phosphonic acids in the first part of this work.

Gallium nitride LEDs

While researchers managed to grow thin crystalline films of GaAs from the melt already before 1980 [13], the growth of GaN was more challenging due to its high melting point. After 1981, Isamu Akasaki and his student Hiroshi Amano progressively developed a deeper understanding of metal-organic vapor phase epitaxy (MOVPE) and successfully applied this technique to grow thin crystals of GaN. In the beginning the crystals were grown heteroepitaxially on sapphire substrates [14]. Due to large mismatch of the lattice constants and thermal expansion coefficients the resulting crystals exhibited high densities of dislocations. However, the implementation of aluminum nitride (AlN) buffer layers significantly increased the crystal quality [15]. Building on this knowledge, Akasaki also found a way to n-dope the material with Si, but failed to explain the thermal activation process of p-type doping with Mg [16]. At the same time Shuji Nakamura adapted the epitaxy technique at Nichia Chemical Corporation and was able to resolve Mg donor activation by thermally driving out hydrogen that was incorporated during the growth process [17]. This breakthrough led to the development of GaN pn-junctions and thereby efficient blue light-emitting diodes based on GaN with long-lasting lifetimes [18–20]. In 2014 Akasaki, Amano, and Nakamura were honored with the Nobel prize in physics for their pioneering research [21].

Since then, the GaN field has steadily progressed towards higher efficiencies and variable wavelength emission with ternary alloys and quantum well structures. A major drawback observed in planar GaN-LEDs was a shrinking external quantum efficiency with increasing current densities, often referred to as “efficiency droop” [22]. Operating LEDs at lower current densities is not desirable for high emission intensities. Another option would be to increase the active area, which would increase the cost per emitted photon due to the growth upscaling. To overcome the efficiency quenching, research groups started to grow high quality three-dimensional GaN nanowires with high aspect ratios [23,24]. However, the huge surface area associated with three-dimensional nanowires can exhibit high densities of defect states, which in turn are detrimental to the luminescence of LEDs based on GaN nanowires [25,26]. The second part of the work will focus on wet-chemical surface state passivation routes, their impact on the electronic and chemical properties of different GaN surface planes, and their influence on time-resolved photoluminescence measurements is investigated.

Outline

The thesis is structured as follows: In Chapter 2, a comprehensive theoretical background is provided. Transition metal oxides are discussed in terms of their band structure and different classifications. Within the context of organic solar cells, the interpretation of current-voltage characteristics is discussed and an introduction to donor-acceptor systems is given. Afterwards, the adsorption kinetics of self-assembled monolayers are briefly discussed, followed by a closer description of the crystal structure, surface states and photovoltage of GaN. Chapter 3 presents background information on the utilized experimental techniques and summarizes the used samples, materials and fabrication steps. The surface characteristics of transition metal oxides and the incorporation of solution-processed nickel oxide as hole-contact layers are discussed in Chapter 4. The wet-chemical passivation of gallium nitride surface states is investigated in Chapter 5. Finally, the author concludes his work and puts the results into a broader context in Chapter 6.

2. Theoretical background

The following chapter provides the theoretical background needed for a comprehensive understanding of the results and their interpretation. The first part summarizes the physical concepts of transition metal oxides. Afterwards a short introduction into current-voltage characteristics and donor-acceptor systems of organic solar cells is given. The transition from the concepts of organic photovoltaics to III-V semiconductors is made by a description of the general adsorption kinetics of self-assembled monolayers. In the second part the properties of gallium nitride, especially the crystal and surface structure are discussed, which are finally linked to surface photovoltage measurements.

2.1. Transition metal oxides

A comprehensive review on transition metal oxides (TMOs) and their energy level-alignment to organic semiconductors was provided by Greiner *et al.* [27,28], which will be briefly summarized here.

In general, TMOs are chemical compounds of oxygen atoms bound to a transition metal. Transition metals are elements with an incomplete *d*-shell and are widely used as catalysts because of their high reactivity. The terminology transition stems from the fact, that the *d*-orbital occupancy increases in the periodic table with increasing atomic number of the metal. TMOs can be semitransparent and obtain a variety of different oxidation states. The partial occupation of the *d*-orbitals can furthermore lead to unpaired electron spins and thereby to magnetic moments on the atomic scale, which renders some TMOs paramagnetic or ferromagnetic.

Figure 2.1 gives an overview of the most common transition metal oxides divided into classes of their *d*-shell filling. Band structures were calculated according to crystal field theory assuming an ionic bonding model without considering the cation coordination geometry [27]. The non-spherical ionic environment can lead to a splitting of the *d*-bands, which is *a priori* assumed here for simplicity. It results that the valence bands of the ionic crystals are mainly determined by occupied O 2p states, while the conduction bands are given by unoccupied metal *d*-states. From left to right the *d*-orbital occupancy increases till the metal bands are completely saturated.

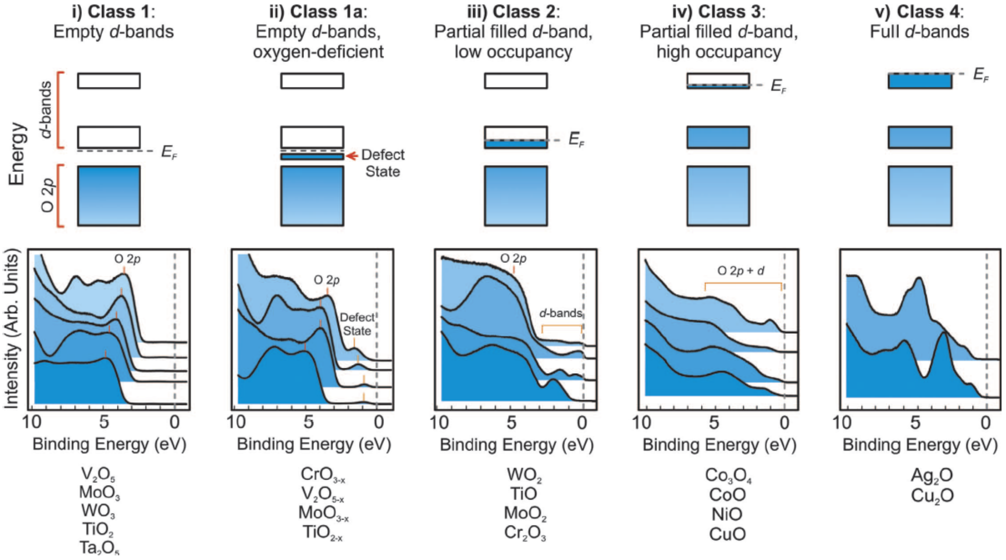

Figure 2.1.: Schematic energy band diagrams for different classes of transition metal oxides (top). The classes differ between the degree of the *d*-band occupancy. The bottom row shows the corresponding valence band photoemission spectra. Reprinted from [28].

Class 1 constitutes a group of oxides with totally empty *d*-bands, often called d^0 oxides. Among them are for example V_2O_5, MoO_3, WO_3 or TiO_2. In their stoichiometric form the forbidden energy gap between the completely filled O 2p band and the empty metal *d*-band is so large that these TMOs are insulators. However, their natural character and the fabrication environment often lead to the formation of a non-stoichiometric crystal structure. For instance, an oxygen deficient $MoO_{3\text{-x}}$ can be obtained through the growth and annealing of a MoO_3 thin film in oxygen deficient environments like vacuum [29]. The deficiency leads to a high density of occupied defect states close to the metal conduction band. Such defect states are metal cations with a different oxidation state compared to their stoichiometric oxidation state. The change of oxidation state in turn follows the charge compensation induced by the presence of deficiency. As the energy splitting between these defect states and the empty metal *d*-band is quite low, the occupied states act like shallow donors. This is the reason why these defective oxides exhibit *n*-type semiconducting properties and became interesting as semitransparent charge transport layers for hybrid solar cells over the past years [29–32].

Class 2 and 3 constitute a group of TMOs with a partially filled *d*-band. They only differ in the density of occupation. Materials like WO_2, TiO and

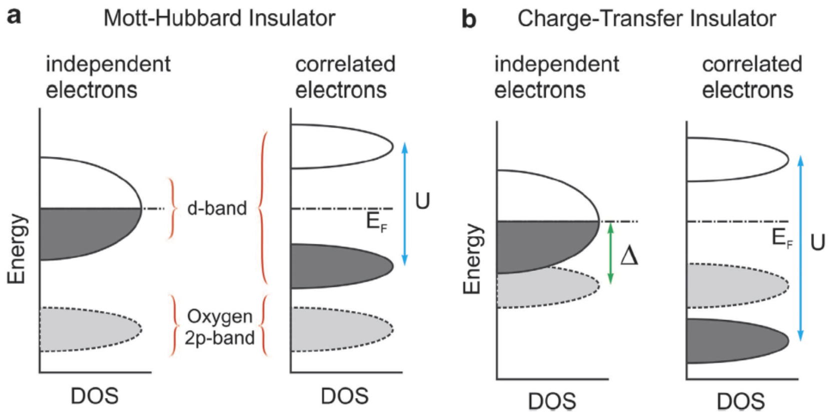

Figure 2.2.: Schematic energy band diagrams of a) a Mott-Hubbard insulator and b) a charge-transfer Insulator. The left columns of both insulator models show the independent-electron model, while the right column accounts for electron-electron correlations. Fermi levels are indicated with dashed lines. An occupied density of states (DOS) is shaded in dark grey for the *d*-band and light grey for the O 2p band, respectively. The Mott-Hubbard term is denoted as (U) and the charge-transfer term as (Δ). Reprinted from [28].

MoO_2 with a low occupancy of *d*-electrons tend to show metallic character. Class 3 oxides like CoO, NiO and CuO with a high electron occupancy are also expected to show metallic character, however, it was observed that they are rather insulating. The insulating properties were addressed to Coulomb repulsion and electron exchange interactions within models developed by Mott [33] and Hubbard [34–39]. Both models are illustrated by schematic energy band diagrams in Figure 2.2. If electrons are considered independent, the energy bands are split into a fully occupied O 2p band and a half filled *d*-band as already shown in Figure 2.1 iii) and iv). However, if the electron occupancy in narrow bands is high, electrons can not be treated independently anymore. Strong Coulomb repulsion and Pauli exclusion can force electrons to become localized onto single metallic cations [40]. This, on the other hand, introduces a forbidden energy gap between the highest occupied *d*-electron states and the lowest unoccupied *d*-bands. The energy difference is called Hubbard term or parameter (U), which depends on the repulsive interaction of the cation valence electrons. In this model the conductivity is expected to be determined by a thermally activated hopping transport of *d*-electrons from one metal site to another, which results in low charge carrier mobilities.

In the picture of a charge-transfer insulator a high degree of hybridization of metallic *d* and O 2p orbitals is assumed, such that their relative energetic

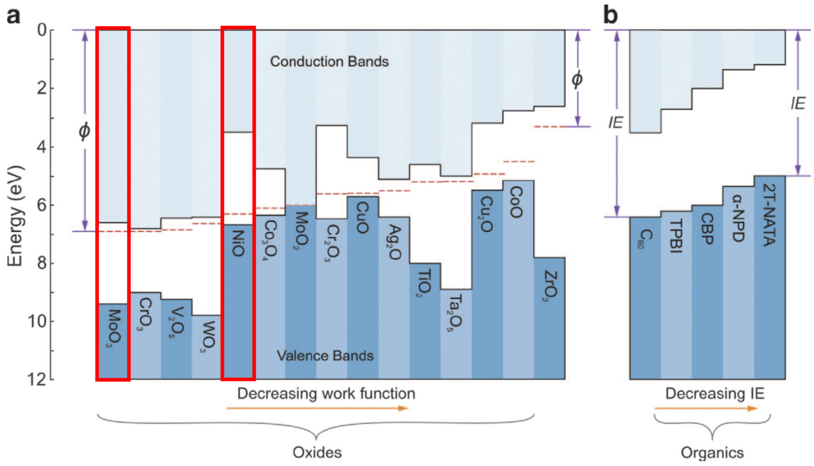

Figure 2.3.: Schematic energy level diagrams of a) several transition metal oxides and b) several organic semiconductors. Highlighted are the TMOs that were investigated in this work. All materials are aligned to a common vacuum level in this representation. Lower shaded regions depict the valence bands and the upper shaded regions the conduction bands, respectively. The dashed red lines highlight the position of the corresponding Fermi levels. Note the difference in *p*-type and *n*-type oxide semiconductors. Reprinted and adapted from [28].

positions are already difficult to differentiate in the independent-electron model [41] (see Figure 2.2 b)). Note that also in this case metallic conductivity is expected but not observed. Hence, the charge-transfer model only holds under consideration of electron-electron correlations. The major difference of a charge-transfer insulator is the mechanism by which charge is transferred. While in the Mott-Hubbard model electrons hop from *d* to *d* sites, here electrons are transferred from O 2p anions to metallic cations if the Hubbard term is larger than the required energy for charge transfer (Δ). The charge-transfer energy is mainly determined by the electronegativity between the metal cation and the oxide anion. Note that a change of the oxidation state implies also a change of the electronegativity and *vice versa*. Hence, the metal oxide behaves like an insulator or semiconductor depending on the energy splitting. Interestingly, the energy gap of a charge-transfer insulator might be tuned by the electronegativity of the involved ions. In his review Greiner stated that NiO is believed to be a charge-transfer insulator [27]. However, it was also stated that NiO is a Mott-Hubbard insulator [42]. More recently, an article proposing a mixture of both models was published by Schuler *et al.* [43], which is in agreement with the prediction by Zaanen and Sawatzky [41] from 1985.

Despite the uncertainty on the exact type of insulator, there is a mechanism for non-metallic conductivity in both systems. It was shown above that the stoichiometry is an important factor. In case of MoO_3 the incorporation of oxygen vacancies induces occupied states of metallic centers with reduced oxidation states, e.g Mo^{5+} instead of stoichiometric Mo^{6+}. These states can be seen as shallow donors close to the conduction band leading to *n*-type band transport. The mechanism for vacancy doping in NiO is the exact opposite. From the picture of the insulator models, it would either be beneficial if the high occupancy of the *d*-band is reduced or the electronegativity for charge transfer increased. Both could be achieved by excess oxygen, that forms unoccupied O 2p states close to the valence band acting as shallow acceptors. This would lead to higher oxidation states of the metallic Ni, e.g. from Ni^{2+} to Ni^{3+}, and to *p*-type conductivity. Another idea would be to fill the highly occupied but partially filled metal *d*-band similar to the *p*-type semiconductors with full *d*-bands (d^{10}) in Class 4. An example of such a Class 4 material is cuprous oxide (Cu_2O), which became a prototypical conducting oxide for photovoltaic applications [44,45]. Note that the charge transport mechanism for both type of insulators would still imply rather low carrier mobilities.

Figure 2.3 shows an overview of the most commonly used transition metal oxides in connection with organic semiconductors. TMOs are sorted by increasing work function and aligned to a common vacuum level. The main TMOs MoO_3 and NiO investigated in this work are highlighted in red. Typical organic acceptor molecules are shown in decreasing order of the ionization energy. The difference in *n* and *p*-type character between MoO_3 and NiO can clearly be seen and should be kept in mind within the scope of the results presented in Chapter 4.

2.2. Organic solar cells

In this section a brief introduction to current-voltage characteristics of solar cells is given. The characteristics will be discussed within the scope of a photovoltaic cell based on an inorganic *pn*-junction. The diode model also applies to OPV cells, however, their working principle requires a more differentiated description. Therefore, a detailed discussion on organic solar cells based on donor-acceptor systems is provided in the section thereafter.

2.2.1. Current-voltage characteristics

The typical current-voltage characteristics of solar cells follow a diode behavior (see Figure 2.4). Under illumination the curve can be obtained either by

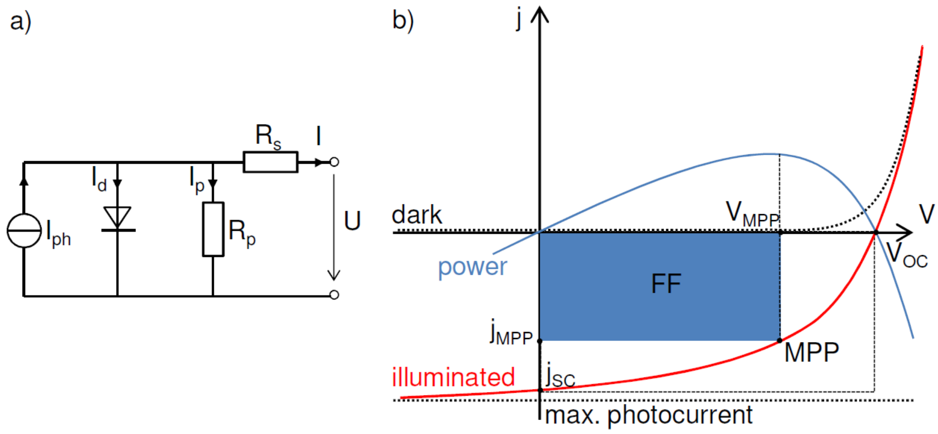

Figure 2.4.: Schematic illustration of solar cell characteristics. a) Equivalent circuit of the single diode model accounting for series and parallel resistances. b) Typical JV-characteristics of a solar cell. MPP is the maximum power point. The fill factor is highlighted as a blue area. Reprinted from [47].

measuring the voltage drop across a variable resistor or by sinking the output current with a variable voltage source. Most semiconductor parameter analyzer today work according to the latter principle. If the diode is driven by an external power source without illumination, the current flow through the diode can be described according to Shockley [46] by the ideal diode equation

$$I = I_0(\mathrm{e}^{\frac{qV}{k_bT}} - 1), \tag{2.1}$$

in which I_0 refers to the reverse leakage current and V to the applied bias. If the solar cell is short-circuited and no external bias applied ($V = 0$), drift and diffusion currents in the device equal and no net current is measured. At forward bias the built-in field, which is a barrier for diffusion, gets lowered and the chemical potential of the n-region is raised over the one of the p-region. This forces a diffusion current from n to p, which increases exponentially with the input voltage. At reverse bias the chemical potentials are shifted in the opposite direction, such that the enhanced electric field between p and n drives a net drift current. As the minority carrier density in the p-region is quite low, the drift current is low as well. This current is often referred to as leakage current in reverse direction of the diode and can be seen below the x-axis of the current-voltage characteristic. Generally, current densities denoted as j are preferred over total currents I, as the normalization to the geometry allows better comparability between different devices.

Under illumination, photogenerated electron-hole pairs are separated in the presence of the built-in field. This leads to a photocurrent of electrons from p to n, which is denoted as I_{ph}. If the contact resistance is low, the total current in Equation 2.2 becomes

$$I = I_0(\mathrm{e}^{\frac{qV}{k_bT}} - 1) - I_{\mathrm{ph}}. \tag{2.2}$$

A negative sign reflects that the photocurrent points in the oppposite direction to the diffusion current in dark. Therefore, the whole current voltage curve is shifted to negative values under illumination. At zero bias the short-circuit current (J_{sc}) can be extracted. J_{sc} predominantly depends on the illumination intensity. In forward bias direction the chemical potentials of both sides become separated, such that electrons residing in the n-region exhibit a higher potential energy than electrons in the p-region. The combination of the higher potential energy, often referred as photovoltage, and the photocurrent enables the solar cell to power external loads. The maximum voltage at open-circuit (V_{oc}) can be extracted by compensating the built-in field completely with an external bias. While at J_{sc} no potential energy can be gained from the system, there is no extractable current at V_{oc}. For these reasons it is only possible to obtain energy from a solar cell between J_{sc} and V_{oc} in the fourth-quadrant of the JV curve. The ideal operation point is the maximum power point (P_{MPP}), where the product of potential energy and photocurrent is highest. The efficiency of the cell (η) is the ratio of P_{MPP} and the solar power input

$$\eta = \frac{P_{\mathrm{MPP}}}{P_{\mathrm{in}}} = \frac{V_{\mathrm{MPP}} \cdot I_{\mathrm{MPP}}}{P_{\mathrm{in}}} = FF \cdot \frac{V_{\mathrm{oc}} \cdot J_{\mathrm{sc}}}{P_{\mathrm{in}}} = \mathrm{PCE} \tag{2.3}$$

in which FF is the fill factor, highlighted as a blue area in Figure 2.4 b).

Of course, in reality solar cells deviate from ideality and the fill factor is limited by parasitic resistances. Such resistive effects are commonly added as a series (R_{s}) and shunt resistance (R_{sh}) in the equivalent circuit model (see Figure 2.4 a)). The series resistance accounts for the conductivity across the device, while the shunt is often referred to as current leakage paths. To obtain high fill factors, the series resistance should be low and the shunt resistance high.

2.2.2. Donor-acceptor systems

Organic solar cells are photovoltaic devices based on small molecules or polymers to convert light to electricity. Figure 2.5 shows the fundamental energy conversion chain in a bilayer, or flat-heterojunction, donor-acceptor system (D/A). If the heterojunction is illuminated through the transparent anode with photons larger in energy than the optical band gap, localized electron-hole pairs are generated due to transition of an electron from a π-HOMO to the π^*-LUMO orbital on molecules in the donor bulk. The efficiency of photon absorption is denoted as η_{PA} and depends on the absorption coefficient $\alpha(\lambda)$ and the thickness of the donor layer. To enhance η_{PA} the donor should exhibit a high absorption in the spectral range of sunlight. Note that the metallic cathode is leading to reflection of transmitted photons and interference in the donor might also play an important role. Excited electron-hole pairs exhibit typical binding energies (E_B) of $\geq 0.2\,\mathrm{eV}$ in organic semiconductors [48–50] and are able to diffuse on a length scale of 5 nm to 30 nm in most organic photovoltaic materials [51,52]. The seperation of these large exciton binding energies would require electric fields larger than $10^6\,\mathrm{V\,cm^{-1}}$ [53,54].

If the exciton is able to reach the acceptor interface without recombining either radiatively or non-radiatively, it can be dissociated into free charge carrriers due to the difference of the chemical potentials between donor and acceptor ($\approx \Delta$LUMO). The diffusion efficiency η_{ED} depends on the ratio of the diffusion length L_D, which is determined by the diffusion constant D and the excitonic lifetime τ according to $L_D = \sqrt{D\tau}$, and the thickness d of the donor layer. This leads to a trade-off between layer thickness for high absorptivity $\alpha(\mathrm{cm^{-1}})$ and L_D in planar heterojunctions. Therefore, alternative heterjunction morphologies were developed, which guarantee high η_{PA} and high η_{ED} at the same time. The most common approach is the bulk-heterojunction architecture, where the donor-acceptor system is mixed and exhibits a high ratio of nearby interfaces [47]. As shown in Figure 2.5 iii) the ideal structure would be a comb-like morphology in which the donor/acceptor interface is distanced at L_D and the thickness of the donor optimized to $1/\alpha$. However, this structure is still a technical challenge and has not been successfully realized so far. Nevertheless, even with BHJ donor-acceptor systems, where the interfacial recombination probability is increased, photocurrents can significantly be improved [55,56].

At the donor-acceptor interface the dissociation of the exciton might be described by a direct charge transfer rate η_{CT}, which is driven by the difference of chemical potentials or an electric field and can occur on the timescale of 50-100 fs [58,59]. However, numerous groups reported on the formation of a charge transfer (CT) state at the donor-acceptor interface [60]. In the presence of such an intermediate state, electrons are not directly free after the transfer from LUMO of the donor to the LUMO of the acceptor. The electron still experiences the attractive Coulomb force of the defect electron residing on a

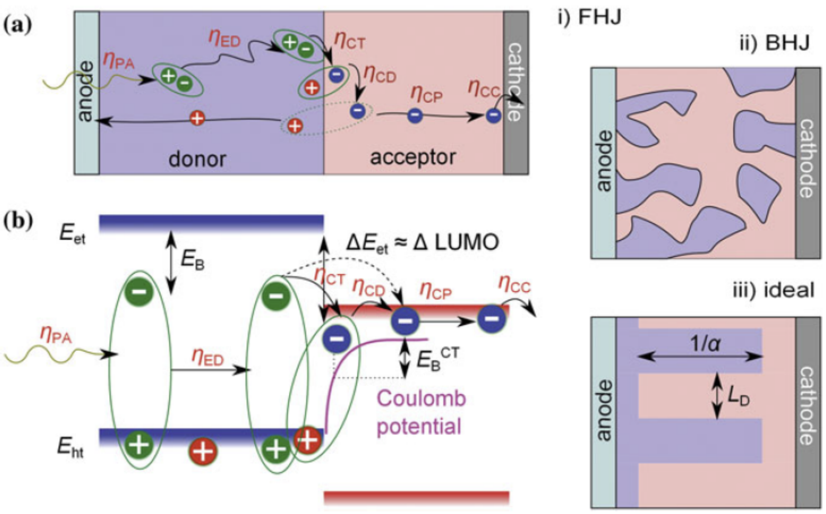

Figure 2.5.: Schematic illustration of the fundamental mechanisms in organic solar cells. a) Energy conversion chain in a simple donor-acceptor i) flat-heterojunction involving several quantum efficiencies η_i. ii) Bulk-heterojunction and iii) the ideal comb-like structure are depicted on the right. b) Illustration of the photoexcitation followed by diffusion and free charge carrier generation. The energy difference $\Delta E_{et} \approx \Delta$LUMO is seen as the driving force to overcome the exciton binding energy. At the interface between donor and acceptor the Coulomb potential of the charge transfer (CT) state is shown. Reprinted from [57].

neighboring donor molecule. Such an excited interface state bears the risk to relax into a ground state and thereby missing its dissociation. The relaxation of the CT state is often called *geminate*, as the electron-hole pair was excited on the same molecule. A detailed discussion of *geminate* recombination has been reported e.g. by Credington *et al.* [61,62]. The reactivation of a CT state ($\tau \approx$ 1-100 ns [63]) into free charge carriers would require additional energy and can be described as a temperature- and field-dependent process. It remains unclear if this reactivation occurs or electrons are more likely transferred into hot CT states, where the excess energy leads to a direct exciton dissociation [64]. Nevertheless, the CT state can be an additional loss channel in the energy conversion chain of the donor-acceptor system and the driving force for charge separation *via* the difference in chemical potentials should be large to obtain high η_{CT}.

Once free charge carriers are generated, the transport efficiencies η_{CP} and thereby charge carrier mobilites of the donor and acceptor materials become an important factor. While often electron mobilities in small molecules like C_{60} are comparably high ($\mu_{C_{60}} \approx 2 \frac{\mathrm{cm}^2}{\mathrm{V\,s}}$) [65], the hole mobility of F_4ZnPc as a donor might be quite low ($\mu_{\mathrm{F_4ZnPc}} \approx 10^{-5} \frac{\mathrm{cm}^2}{\mathrm{V\,s}}$) [66]. For free charge carriers *non-geminate* recombination can become a significant loss channel, which means recombination of carriers that were excited on different molecules. It is often not well defined, whether *non-geminate* is only specified to bimolecular recombination in the bulk or if it also accounts for non-radiative recombination channels at trap states and the electrodes. While charge separation was shown to be mainly a consequence of chemical potentials at the D/A interface, the current flow of free charge carriers can be described by electrical and chemical potential gradients. Note that the latter is consistent with the model for an inorganic *pn*-junction (see Section 2.2.1).

A very clear picture on current flow in OPV was provided by Gregg and Hanna [54], which will briefly be discussed in the following. In thermal equilibrium the current density of electrons through the device is given by a superposition of drift and diffusion currents, which follow

$$J_n(x) = n(x)\mu_n \nabla U(x) + k_b T \mu_n \nabla n(x), \tag{2.4}$$

wherein $n(x)$ is the concentration of mobile electrons, μ_n the electron mobility, k_b the Boltzmann constant and T the temperature. In a non-equilibrium situation, which means under the perturbation of illumination or external bias the current density is often described by the quasi-Fermi levels in the system.

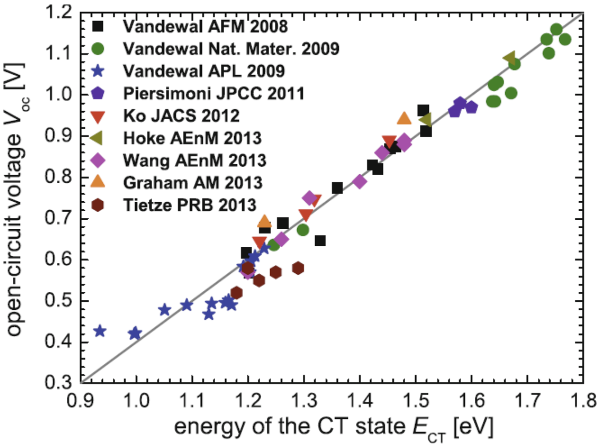

Figure 2.6: Correlation of the open-circuit voltage V_{oc} to the energy of the CT state E_{CT}. Reprinted from [67].

For electrons this is defined as

$$E_{Fn} = E_{cb}(x) + k_b T \ln[n(x)/N_c], \tag{2.5}$$

with E_{cb} being the potential energy of the conduction band edge, which means $U(x) + \text{const.}$ bias, and N_c the density of electronic states at the bottom of the conduction band. Combining both equations provides the electron current as

$$J_n(x) = n(x)\mu_n \nabla E_{Fn}. \tag{2.6}$$

As already mentioned above, it is very important to differentiate that in OPV the predominant force for charge separation is the difference in chemical potentials at the donor-acceptor interface. While in inorganic *pn*-junctions charge separation mainly occurs by the built-in electrical field, here, the carrier concentration gradient $\nabla n(x)$ is essential. That is why groups have reported on photovoltaic operation in OPV independent of the built-in field and independent of the electrode work functions [5]. In this case the V_{oc} is predominantly determined by the differences in quasi-Fermi levels for electrons and holes

$$qV_{oc}(I) = (E_{Fn} - E_{Fp})_{\max}, \tag{2.7}$$

which in turn depends on the light intensity I and thereby photogenerated charge carriers. In the simplest approximation the maximum obtainable V_{oc} depends on the effective band gap ($E_g^{\mathrm{eff}} \approx E_{\mathrm{CT}}$), approximately the difference between the HOMO of the donor and the LUMO of the acceptor minus the Coulomb attraction of the CT state. Under consideration of the CT state and energy loss by relaxation of the CT state and *non-geminate* recombination of free charge carriers the V_{oc} follows as

$$V_{oc} \approx \frac{E_g^{\mathrm{eff}}}{e} - \Delta, \tag{2.8}$$

wherein Δ is the loss term [68] and often found illumination and temperature dependent between 0.4-0.6 eV [69,70]. The relation has been found in several independent experiments and is shown in Figure 2.6 for different energies of CT states. It can be concluded that loss channels are still affecting the maximum achievable PCE in OPV devices and that performances are still far from the Shockley-Queisser limit [71].

2.3. Self-assembled monolayers

Self-assembled monolayers (SAMs) were defined as monomolecular layers that form spontaneously on a substrate surface upon exposure to solution or gas phase of an amphiphilic surfactant [72–74]. The term surfactant therein describes surface active molecules, which consist of a ligand group acting as an anchor, a backbone and a functional head group as shown in Figure 2.7. SAMs can be fabricated as Langmuir-Blodgett films [75], from gas phase [76], or from immersion techniques [77]. As long as the bonding is guaranteed by a proper anchoring group, all other constituents can be substituted for the specific modification purpose. This gives SAMs a high degree of chemical variability, which in turn opens a broad spectrum of functionalization possibilites. A comprehensive list of possible ligands can be found for example in [76] and [78]. For noble metal surfaces, thiols ($R-SH$) are the most frequent and most studied SAM precursor. Thiols establish a strong thiolate bond with metal atoms and show close packing densities on gold [79]. Therefore, these systems can be used as model systems for the comparison with other ligands and substrates [80]. For metal oxides several molecular anchors have been proposed over the last years, e.g. silanes ($R-SiX_3$), carboxylates ($R-COOH$) and phosphonic acids ($R-P(O)(OH)_2$). In this work phosphonic acids were of major interest, because they are known to form highly dense monolayers on hydroxylated oxide surfaces via a strong covalent phosphonate bonding [81–86].

Many spectroscopic studies have shown that surfactants do not necessarily stick vertically to the surface [87], but rather exhibit a tilt angle with respect to the surface normal of the substrate. Depending on the degrees of freedom that are determined by the bonding configuration and depending on the rigidity of the backbone, the molecules might also show a rotational angle. Both angles

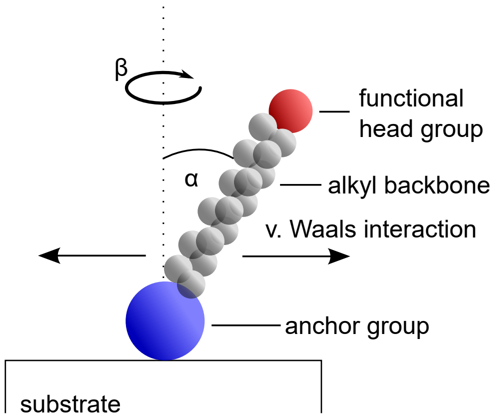

Figure 2.7: Schematic illustration of a typical surfactant used as SAM precursor. The tilt angle to the surface normal is denoted as α and the degree of rotational angle by β (azimuth angle).

can further be influenced by van der Waals interactions between the backbones of neighboring molecules.

Adsorption kinetics are mainly a thermodynamically driven process [88]. Figure 2.9 shows the typical potential that a molecule experiences in the near-surface region of a substrate. A molecule that approaches the surface by diffusion from an infinite distance r may collide inelastically at the surface and lose kinetic energy. If the amount of energy loss is high the molecule can be captured by attractive forces from dipole-dipole interactions with surface atoms, which decay with $1/r^6$ that is reflected in the Lennard-Jones-Potential. This adsorption stage is often referred as physisorption and drawn as a lying-down phase, in which no net orientation is given (see Figure 2.8). Enthalpies for physisorption of n-alkanethiols are often in the range of $-(50\text{-}100\frac{\mathrm{kJ}}{\mathrm{mol}})$ [89]. If the adsorbate carries enough energy or energy is supplied to the system the molecule can overcome the activation enthalpy for chemisorption. The chemisorption potential can be described by the Morse-Potential, which depends on the internuclear separation of the adsorbed and surface atoms. Molecules that are chemisorbed often relax from higher vibronic states into the ground state. The relaxation is driven by thermal exchange and diffusion across the substrate surface.

As already implied by the terminology, the chemisorption goes along with a change of the chemical structure, while the physisorption does not. In case of thiols for example, the sulfur atom assumes a semi-covalent bonding with an Au-atom [74], while the proton is homolytically dissociated [90]. A negatively charged thiolate ($\mathrm{Au\text{-}S^-}$) remains. The molar enthalpy for chemisorption of n-alkanethiols is about $-126\frac{\mathrm{kJ}}{\mathrm{mol}}$ [91]. If an adsorbate is in a higher energy state near the surface, it can still turn back into a physisorption state or also desorb completely. In thermodynamic equilibrium absorption and desorption

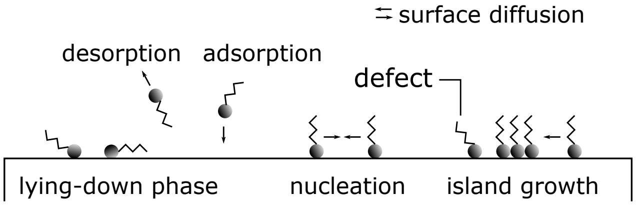

Figure 2.8.: Schematic illustration of the different stages of SAM formation including adsorption, desorption, nucleation and island growth. SAMs can also exhibit defective sites, which might lead to incomplete coverage.

dynamics are balanced.

The microscopic picture can be described macroscopically by a thermodynamic potential ΔG in dependence of the state variables pressure p, temperature T, and by the amount of surfactant substance n. The relation is defined by the Gibbs fundamental equation

$$\Delta G = \Delta H - T\Delta S. \tag{2.9}$$

ΔG refers to the free enthalpy of the closed system and is a driving force for the adsorption process. A negative free enthalpy always points towards the potential minimum and thereby to the lowest energy state. Self-assembled monolayers exhibit the advantage that they react exergonic ($\Delta G < 0$), which means that they assemble spontaneously without external energy supply. It follows that the chemisorption is an exothermic reaction ($\Delta H < 0$) and thereby theoretically irreversible under steady increase of the entropy ($\Delta S > 0$). If as many as possible vacant adsorption sites become occupied by surfactants, a minimum of the total energy can be achieved.

Such a thermodynamic equilibrium also implies a chemical equilibrium, which assumes a constant ratio between adsorption (k_+) and desorption rates (k_-) [92]. In that case the equilibrium or binding constant (K) follows the law of mass action and is linked to the Gibbs free energy ΔG^0 according to

$$K = \frac{k_+}{k_-} = \exp - \frac{\Delta G^0}{RT}, \tag{2.10}$$

wherein $R = 8.314\,\mathrm{J\,mol^{-1}\,K^{-1}}$ is the gas constant and T the temperature given in K. K is only constant if the enthalpy of the adsorption is independent of coverage. The Gibbs free energy at standard conditions ($T_0 = 298\,\mathrm{K}$) is material specific and can be consulted in literature. The steady-state surface

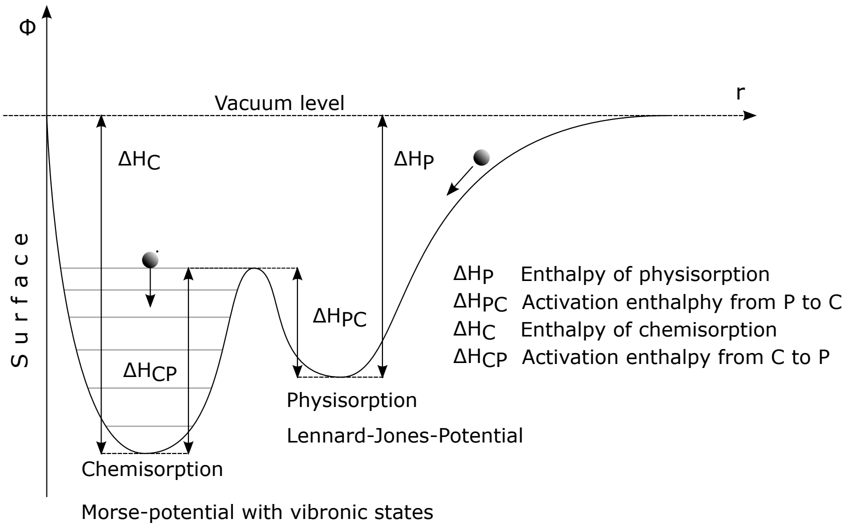

Figure 2.9.: Schematic illustration of surfactant adsorption. Superposition of the Lennard-Jones-Potential and Morse-Potential seen for a molecule approaching the surface from an infinite distance r. ΔH denote the adsorption enthalphies and P and C physisorption and chemisorption, respectively.

coverage Θ follows K by a Langmuir-isotherm [92,93]

$$\Theta = \frac{KC}{1+KC}, \tag{2.11}$$

in which C refers to the molar concentration of the solution. Note that this euqation can easily be transformed into other state variables like pressure by the ideal gas law.

Figure 2.10 a) shows typical Langmuir adsorption isotherms in dependence of C for different constant temperatures. The degree of coverage increases already quickly for low concentrations and then starts to saturate more slowly for higher concentrations. If the temperature is lowered the concentration required to achieve a specific surface coverage is lowered. However, low temperatures can also induce kinetic restrictions. It is therefore not sufficient to just increase the molar concentration of the SAM precursor to achieve high coverage rapidly. For single crystalline surfaces Langmuir isotherms describe adsorption coverage well, but they often fail for porous or polycrystalline surfaces, where Brunauer-Emmett-Teller (BET) isotherms show better agreements.

As the rate of sites becoming occupied is proportional to the amount of vacant sites, the time-dependent evolution of the coverage is often described with the Avrami kinetic model $\frac{d\Theta}{dt} = k(1-\Theta)$, wheras the integration leads

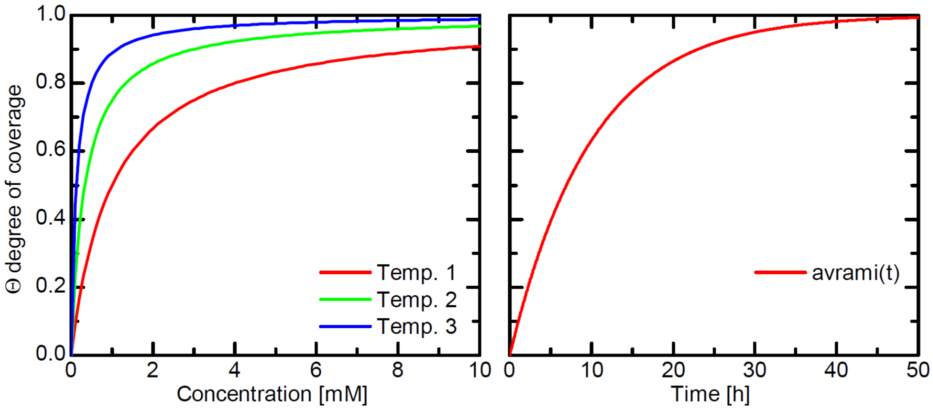

Figure 2.10.: Langmuir isotherms showing the degree of coverage Θ in dependence of the molar concentration of the SAM precursor. Isotherms were plotted for three different temperatures, where the third (blue) curve corresponds to the lowest temperature. b) The time-dependent evolution of the coverage can be described by the Avrami kinetic model [88]. Reprinted from [94].

to $\Theta = 1 - \exp(-kt)$ with k being the rate constant. Figure 2.10 b) shows the degree of coverage over time within this model. It can be seen that full coverage takes several hours and immersion times should be chosen long in order to achieve high quality monolayers. While the physisorption or lying down phase is pretty fast, the self-assembly to highly ordered dense films is a slow process as the attraction of molecules through van der Waals interactions of the backbones is comparably weak [95]. However, it was recently shown by Alt *et al.* that SAM function does not necessarily follow monolayer quality and that even immersion times of 5 s can lead to significant improvements of the threshold voltage in organic-field effect transistors (OFETs) [79].

As previously discussed the chemisorption leads to a chemical change at the substrate surface. In case of thiols a negatively charged thiolate (Au-S$^-$) remains. Furthermore, through the spatial overlap of the wavefunctions of surface and adsorbate atoms, the electron density spilling out of the surface can be condensed, which is often referred as the *pillow effect* [96]. Both effects can give rise to a permanent bonding dipole Δ_{BD}. For most applications SAM precursor are synthesized with a permanent dipole moment μ_0, which is the vector sum of all polar dipole moments of the molecular compounds [97]. According to the Helmholtz equation for an array of n permanent dipole moments per unit area, the change of the vacuum level (ΔE_{vac}) or work function can be described by

$$\Delta E_{\mathrm{vac}} = \frac{e\mu_{\perp}}{\epsilon_0 A} = \frac{e\mu_0 \cos(\alpha)}{\epsilon_{\mathrm{eff}}\epsilon_0 A}. \tag{2.12}$$

The vacuum level is only affected by the surface orthogonal projection $\mu_{\perp}$ of the permanent dipole moment μ_0. α describes the tilt angle, which was introduced in Figure 2.7, e the elementary charge, ϵ_0 the electric field constant, and A the area that is occupied by the adsorbate. Addittionally, ϵ_{eff} considers a change in the polarization at the surface upon formation of a monolayer with permanent dipoles. Thus the overall change in work function can be written as follows:

$$\Delta\Phi = \Delta_{BD} + \Delta E_{\mathrm{vac}}. \tag{2.13}$$

In conclusion, it has to be mentioned that the term self-assembled monolayer is widely used for any kind of monolayer of molecules and sometimes without differentiation. This was also critized by Peter J. Hotchkiss, a pioneering student at Georgia-Tech for the attachement of phosphonic acids to metal oxides [98]. The self-reactivity of SAM formation always depends on the cleanliness of the substrate. Contaminations can delay the assembly as they have to be replaced first. Sometimes SAMs also do not result in strongly covalent systems and the term SAM is then misleading. This work will proof the chemisorption of phosphonic acids and thereby justify the terminology.

2.4. III-V nitride semiconductors

For many years now research groups progressed the development of wide-band gap semicoductors based on silicon, II-IV and III-V compounds. The most prominent representatives for each class are silicon carbide (SiC), zinc selenide (ZnSe) and gallium nitride (GaN). SiC and GaN have shown exceptional thermal and chemical stability, which renders them promising materials for high-temperature applications. Their large band gap energies enables short-wavenlength opto-electronics like blue and UV light-emitting diodes (LEDs). ZnSe became interesting as a material for blue to green laser diodes [99], however, short laser lifetimes were observed [20] and contact resistances to ZnSe need to be lowered for efficient device operation [100,101].

Table 2.1 compares the physical properties of GaN in relation to aluminum nitride (AlN), 6H-SiC, sapphire, gallium arsenide (GaAs) and silicon. 6H-SiC is one of the numerous polytypes of SiC with an unfavorable indirect band gap of 2.9 eV. This is why GaN with its direct band gap of 3.4 eV has shown superior luminescence efficiencies over 6H-SiC. All presented compounds show high thermal conductivities and low thermal expansion coefficients. Despite AlN they also posses high electron mobilities.

One of the challenges for the growth of high purity GaN is the choice of the ideal substrate, which requires matching of lattice constants and thermal expansion coefficients. As high pressures and temperatures are required, the growth of GaN crystals from the melt is very inefficient. The progress of metal organic vapor phase epitaxy and molecular beam epitaxy allowed to circumvent this problem. During the first GaN growth studies sapphire was favored as a substrate for heteroepitaxy, because of its hexagonal symmetry and wide availability [102]. However, it can clearly be seen that the lattice constants differ significantly, which induces strain after growth and high densities of dislocations. Therefore, researchers introduced different buffer layers to optimize the lattice match of GaN to the growth substrate. AlN exhibits quite similar lattice constants and GaN crystals grown on AlN seed layers showed reduced background carrier concentrations, dislocation densities and an increase in band-to-band photoluminescence while suppressing emission from states within the band gap. Background carrier concentrations are a consequence of the incorporation of Si and O into the crystal lattice. Such foreign atoms can act as shallow donor states close to the conduction band and thereby n-dope the semiconductor. Cheaper commercial GaN templates are often provided on sapphire with AlN buffer layers today (see Section 5.2.1). However, background carrier concentrations and dislocation densities can still be optimized by the more expensive homoepitaxially growth on GaN template substrates.

2.4.1. Crystal structures

A crystal solid can be described as a fixed arrangement of atoms in a configuration of minimal free energy. As the principle of minimum energy holds also for neighboring atoms, a crystal solid growth as a repetitive pattern in three dimensions.

The most frequently observed GaN crystal structures are shown in Figure 2.11. From left to right are presented the zincblende, the wurtzite and the rock-salt structure. Zincblende and rock-salt have a cubic basal plane, while the wurtzite structure has a hexagonal one. Therefore, the growth of GaN zincblende requires cubic substrates and the growth of GaN wurtzite requires hexagonal substrates. Under normal conditions GaN is only thermodynamically stable in the wurtzite configuration. However, some groups were also

Table 2.1.: Overview on the most relevant GaN material properties in relation to other semiconductor compounds. Values are given for room temperature (300 K). The table was adapted from [102].

Material	Lattice paramters [Å]	Band gap [eV]	Electron mobility [cm^2 / V s]	Thermal conductivity [W / cm · K]	Thermal expansion coefficients [$10^{-6}\,\mathrm{K}^{-1}$]
GaN	$a = 3.189$	3.4	900	1.3	5.5
	$c = 5.185$				3.17
AlN	$a = 3.112$	6.2	1 [103]	2.0	4.2
	$c = 4.982$				5.3
6H-SiC	$a = 3.08$	2.9	600	4.9	4.2
	$c = 15.12$				4.68
Sapphire	$a = 4.758$	8.7 [104]	4000 [105]	0.5	7.5
	$c = 12.99$				8.5
GaAs	$a = 5.6533$	1.4	8500	0.5	6
Si	$a = 5.4301$	1.1	1400	1.5	3.59

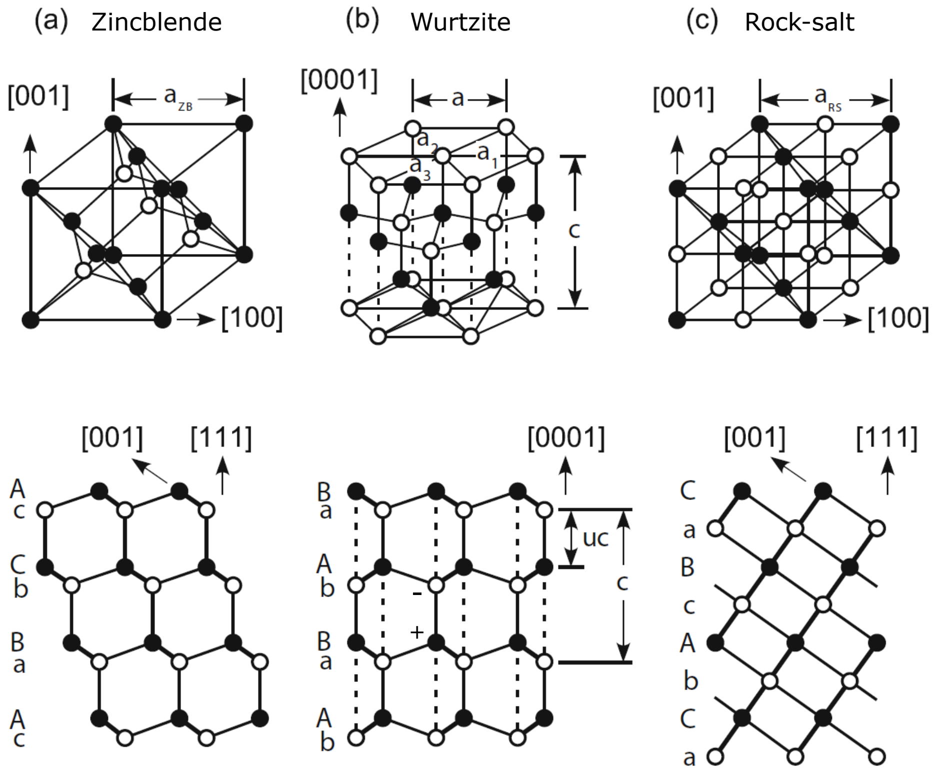

Figure 2.11.: Illustration of the common GaN atomic crystal structures. From left to right are shown the a) zincblende, b) wurtzite, and c) rock-salt structure. The upper row shows the crystal structure in three dimensions. The lower row shows the corresponding two-dimensional lattice in real space. Closed circles represent Ga cations and open circles N anions. Note that the uppermost Ga-layer is not shown in the upper wurtzite representation. Lattice constants are given as a_i and c. The ionic bonding length between cation and anion along [0001] is denoted as uc. Electrostatic forces with an extended bonding length are depicted as dashed lines. The stacking order is labeled for different atom positions in the [0001]-plane with simple letters, case-sensitive to cation and anion, respectively. Reprinted and adapted from [106].

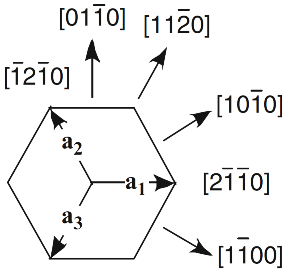

Figure 2.12: Schematic illustration of the fundmental lattice vectors in the hexagonal [0001] plane. $[1\bar{1}00]$ is referred to as m-plane and $[11\bar{2}0]$ to the a-plane wurtzite GaN. Reprinted and adapted from [106].

able to grow and transform GaN into the meta-stable zincblende structure [107,108]. The experiments were driven by the hope for better GaN doping capabilities in a cubic rather than a hexagonal crystal. At very high pressures ($\geq 30\,\mathrm{GPa}$) GaN can even undergo a phase-transition from the wurtzite to the rock-salt crystal structure [109]. The wurtzite structure is often referred to as α-GaN and the zincblende as β-GaN phase. Because of the stability and meaning for this work, only the wurtzite α-GaN structure will be discussed further.

In the hexagonal wurtzite structure the GaN typically grows along the c-axis described by the Miller-Bravais indices [0001]. The coordination geometry is tetrahedral, wherein the Ga cation is bound to four N anions. Ga shares its three valence electrons ($4s^2 4p^1$) with the nitrogen ($2p^3$) to complete the L-shell of the nitrogen atom and form a strong ionic bond. Lattice constants are typically $a = 3.189\,\text{Å}$ and $c = 5.185\,\text{Å}$ [102] (compare Table 2.1). The ionic bonding length along the c-axis is denoted as uc and typically around $2\,\text{Å}$ [106,110]. From the two-dimensional perspective a stacking sequence of bAaBbAaB can be seen. Lower cases correspond to two different positions of anions and capitals to two different positions of cations in the [0001] orientation. Note that the uppermost Ga-layer is not shown in the three-dimensional wurtzite representation. Electrostatic forces between atoms in different layers, which additionally strengthen the wurtzite GaN crystal, are shown as dashed lines.

One of the major issues that has been found with GaN crystals grown along the c-axis is the high spontaneous and piezoelectric polarizability predicted by Bernardini *et al.* [111]. Spontaneous polarization can lead to strong electric fields ($3\frac{\mathrm{MV}}{\mathrm{cm}}$) along the growth axis [112]. Such high fields can induce high sheet carrier densities at GaN quantum well hetero-interfaces and force a spatial separation of electron and hole wavefunctions, which in turn decreases the recombination efficiency of excitons in such structures [113]. This effect became also known as the Quantum Confined Stark Effect (QCSE) [114]. It can have a

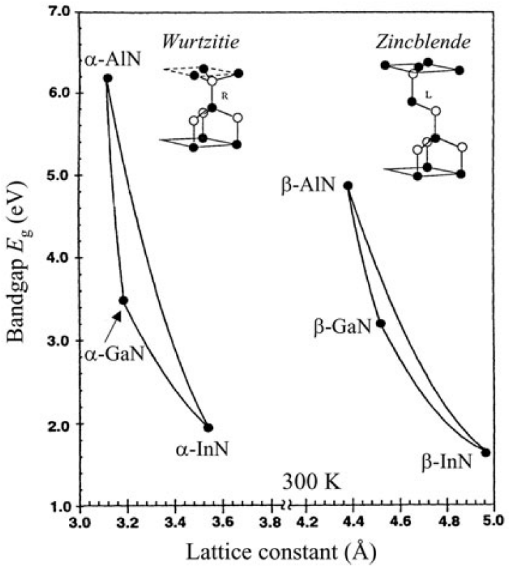

Figure 2.13: Correlation between band gap energy and lattice constants for wurtzite and zincblende GaN in alloys with AlN and InN. Unit cells for the wurtzite and zincblende structure are shown as insets. Reprinted from [118].

significant impact on light-emitting devices based on *polar* III-V semiconductor crystals. For this reason groups started to put effort into the growth of GaN along other hexagonal crystal axes. The most important are the *non-polar* orientations m-plane $[1\bar{1}00]$ and the a-plane $[11\bar{2}0]$ (see Figure 2.12) [115,116], which show much lower polarization constants [117]. The author emphasizes that the term polarity is commonly used in literature for the termination of the GaN face, which is either Ga-polar or N-polar depending on the last atomic surface layer (see Section 2.4.2). Throughout the course of this work polarity will also be used for the face termination and the investigation of c-plane and m-plane will imply *polar* and *non-polar* substrates, respectively.

Despite the drawback of polarization effects, the lattice constants of the most common III-V nitride semiconductors GaN, AlN and InN enabled band gap engineering for opto-electronics through the growth of ternary alloys and heterostructures. Figure 2.13 shows the relation between the band gap energy of the α- and β-GaN crystal structure and their lattice constants. The formation of alloys with AlN and InN with different ratios of the three materials can open a wide continuous range of achievable emission wavelengths.

2.4.2. Surface states and bands

It is well-known that the surface properties of semiconductors may strongly differ from the bulk due to the abrupt ending of the lattice periodicity. Nevertheless, the principle of minimum energy also applies to the surface, which

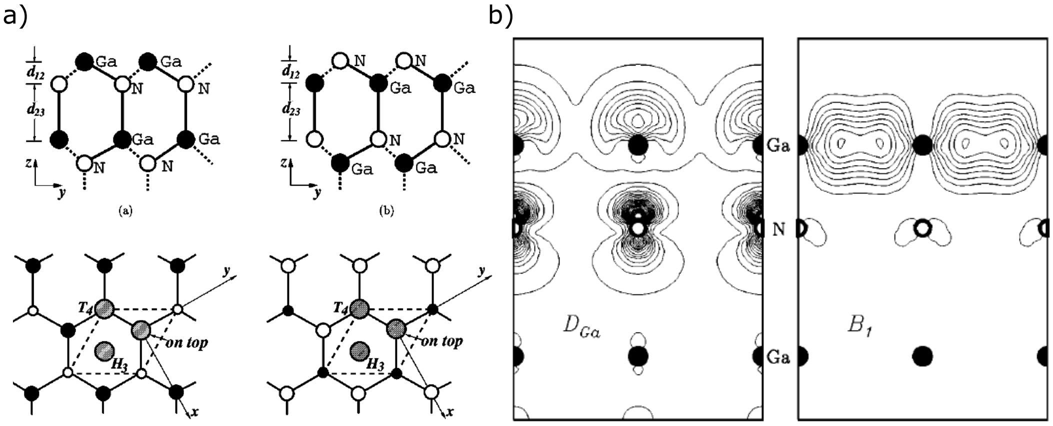

Figure 2.14.: Illustration of the surface structure of GaN. a) Two-dimensional side-view of an ideal GaN(0001) (left) and an ideal GaN(000$\bar{1}$) (right) surface. b) Charge density contours of Ga dangling bonds (D_{Ga}) on the left and Ga bridge bonds (B_1) on the right for Ga on top adatoms. Solid lines represent an increased charge density relative to the ideal GaN(0001) surface. The view is presented in the x-z-plane of a). Reprinted and adapted from [110].

means that the surface itself pursues its most stable configuration. This might imply defect formation, surface reconstruction or adsorption and incorporation of foreign atoms like contaminants from the environment.

Numerous groups have reported on the surface structure and reconstruction of GaN surfaces over the past decade. A detailed description of the favorable (1×1) reconstruction was provided by Wang *et al.* [110]. Figure 2.14 a) shows a side-view of the ideal GaN(0001) surface in which the surface is terminated by a topmost layer of Ga atoms. This equals the schematic representation of the hexagonal crystal structure presented in Figure 2.11. In the opposite direction of the c-axis the crystal is terminated by nitrogen. For this reason the GaN(0001) surface is commonly called Ga-polar and the GaN(000$\bar{1}$) surface N-polar. Below the ideal structures a top-view of possible (1×1) reconstruction unit cells for both polarities are shown [110]. Note that this is only one possibility and that many other reconstructions were investigated [119,120]. The most likely adsorption sites for Ga and N adatoms are denoted as T_4, H_3, and on-top. On-top refers to an adsorption site directly above a Ga atom of the last GaN(0001) substrate layer. T_4 is a site above a nitrogen atom of the second surface layer and H_3 adatoms reside in hollow sites above the surface. The same applies to the N-polar surface, but on-top and T_4 correspond to N and Ga substrate surface atoms, respectively. Figure 2.14 b) shows the density functional theory calculated contour plots of the charge densities with on top Ga adatoms on the reconstructed GaN(0001) surface. The left graph shows the reconstruction with adatoms resulting in Ga dangling bonds and the right graph shows Ga adatoms that form metallic bridge bonds. While the increased charge densities in case of Ga dangling bonds extends into the next lower surface layer the increased charge density of Ga bridges is spatially localized to the last surface adatom layer.

Why surface states of GaN are so important to investigate was shown through extensive theoretical calculations by van de Walle and Segev [121,122]. The resulting surface band structures of GaN-(2×2) surfaces are shown in Figure 2.15 a) and b). Gray lines represent the projected bulk band structures, which confirm the direct band gap of GaN at the Γ-point of the Brillouin zone. Surface bands are highlighted as solid red lines. For adatoms residing on T_4-sites on the GaN(0001)-(2×2) surface two surface states are predicted. One is found 2.8 eV above the valence band maximum and just below the conduction band minimum. The other one is observed 1.7 eV above the VBM. These states are also found for the (2×2)-H_3 reconstructed GaN($000\bar{1}$) surface, but closer to the VBM. On both surfaces the upper states are empty and the lower surface bands occupied.

The density of states plots reveal the nature of these surface bands. On reconstructed *c*-plane GaN surfaces a high density of unoccupied Ga dangling bonds (Ga db) and a high density of occupied Ga-3Ga bridges are seen. This is in agreement with the charge density calculations on GaN(0001)-(1×1) by Wang *et al.* [110] (see Figure 2.14). High densities of dangling bonds are also predicted for the *non-polar* *m*-plane GaN. However, it is expected that the *m*-plane exhibits also a high amount of N dangling bonds, which are found close to the VBM. In both cases, such high state densities in the band gap can lead to Fermi level pinning. In other words, the Fermi level gets locked to a certain position within the band gap, which can lead to high barrier heights at device interfaces and thus be detrimental for the device performance. As a further consequence such defect states can act as non-radiative Shockley-Read-Hall recombination centers like bulk defects.

Even though the computations by van de Walle and Segev are quite comprehensive for nearly ideal GaN surfaces, there is one important aspect that is not covered, which is the formation of oxides and suboxides on the real GaN surface. The most stable thermal oxide that was found on GaN is Ga_2O_3, which can be grown at very high temperatures [123] (750-800 °C) but also at room temperature with high oxygen exposures [124]. Similar to the bulk GaN phases, Ga_2O_3 can also exhibit different polytypes, for example β-Ga_2O_3 [125]. Optical properties can for example be found in [126]. The thermal oxide of GaN was applied as a gate dielectric in several MOSFET applications showing

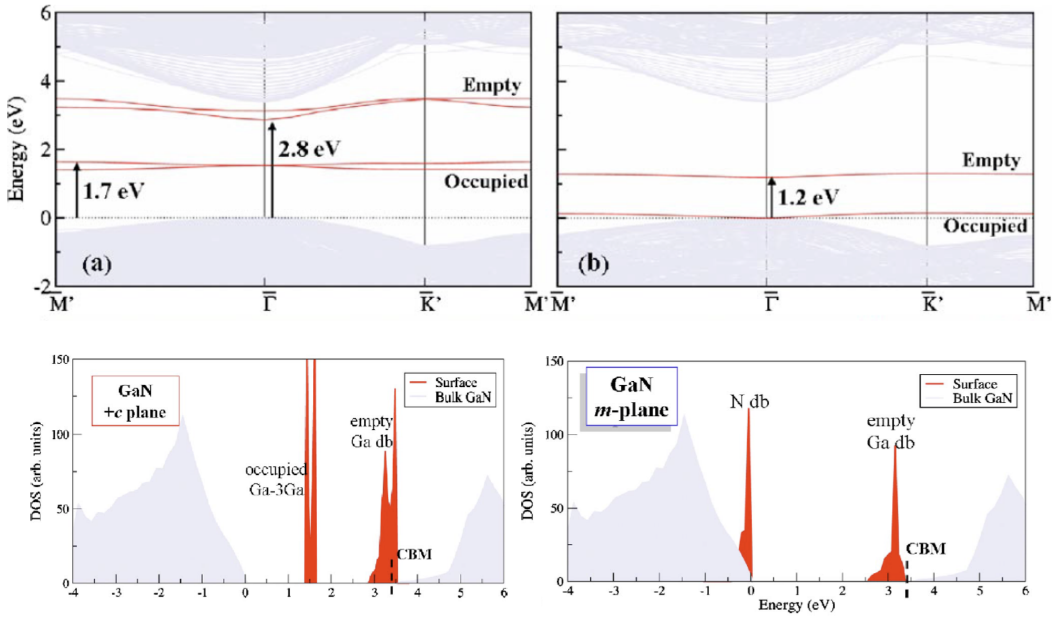

Figure 2.15.: Top: Electronic band structures of the a) (2×2)-Ga(0001)-T_4 and b) (2×2)-GaN(000$\bar{1}$)-H_3 reconstructed surfaces. Gray lines correspond to the projected bulk band structure. Zero energy is set to the bulk VBM. Surface states are drawn as red lines. Energy differences between the bulk band structure and surface states are depicted by arrows. Bottom: Density of states for the reconstructed (2×2) Ga(0001)-T_4 (left) and for the stable *non-polar* GaN(1$\bar{1}$00) (right) surface. Reprinted and adapted from [122].

low interface state densities. Nakano *et al.* reported on interface state densities of $5.5 \cdot 10^{10}\,\mathrm{eV}^{-1}\,\mathrm{cm}^{-2}$. Furthermore, no presence of discrete interface traps was observed and thereby an unpinned Fermi level was proposed [127]. However, oxides on semiconductor surfaces can lead to high densities of negative charges [128,129], which is discussed further in the next section. The study of gallium nitride oxides is still an ongoing process and more light has to be shed on this topic [130].

2.4.3. Surface photovoltage

The presence of surface states can have a significant impact on the electrostatic potential at semiconductor surfaces. If one assumes a Gaussian distribution of midgap surface states, surface bands will be occupied by electrons to a certain energy, which is known as the charge-neutrality level (CNL) [128]. The charge-neutrality level defines the energy below which occupied states are charge-neutral and positively charged when empty. Above the CNL occupied surface states lead to a negative surface charge and are neutral when empty. Thus, the occupancy of surface states around the CNL renders the surface either neutral, positively or negatively charged. In case of an intrinsic semiconductor the CNL equals the Fermi level. However, if the Fermi level of an *n*-doped semiconductor lies above the charge-neutrality level surface states become occupied by negative charges.

It was shown in the previous section that for GaN(0001) there can be a high density of unoccupied surface states due to Ga dangling bonds close to the conduction band. Furthermore, it was described that GaN shows high background carrier concentrations, which *n*-dope the GaN. Both observations shift the Fermi level very close to the CBM, both, in the bulk and at the surface. The fact that the surface states are unoccupied and slightly lower in energy makes them favorable to become occupied by electrons from donor states (e.g. Si) close to the surface. In other words, Ga dangling bonds in turn act like acceptor states.

If the Fermi level of the occupation rises above the charge-neutrality level the surface becomes negatively charged, which compensates the charge of ionized donors in the surface region. The more the surface states become occupied the more it becomes unfavorable for further electrons to move towards the surface. Thus, the near-surface region becomes depleted by majority electrons, which is often referred to as a depletion region. The depletion is correlated with an electric field between the negatively charged surface and the positively charged ionized dopants. The gradient of the electric field E between both

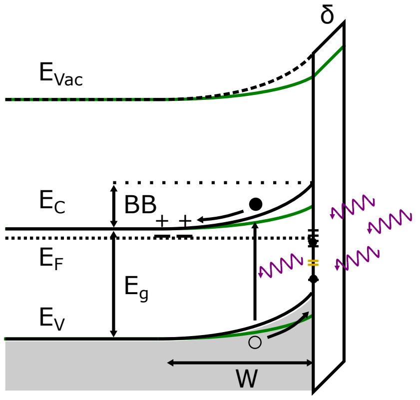

Figure 2.16: Schematic illustration of the surface photovoltage effect. Above band gap (UV) photons excite electron-hole pairs in the space-charge region, which then dissociate. Minority carriers recombine with trapped electrons at the surface and thereby reduce (green) the band bending (BB). Short black lines indicate the presence of surface states by Ga dangbling bonds and bridges. Short yellow lines indicate oxide acceptor states. Near-surface ionized donor states carry positive charge.

sides can be described by the one-dimensional electrostatic Poisson equation

$$\frac{dE}{dx} = \frac{\rho}{\epsilon}, \tag{2.14}$$

wherein ρ is the charge density and ϵ the permittivity. Assuming that there are no free carriers within the depletion region and that the doping concentration is constant, the solution of the Poisson equation results in a width of the depletion region that is determined by the ratio of surface charge density (n_s) and ionized dopants (N_D) according to:

$$W = \frac{n_s}{N_D} = \sqrt{\frac{2\Phi\epsilon_0\epsilon_r}{q^2 N_D}}, \tag{2.15}$$

in which Φ describes the barrier height for electrons to move towards the surface. Note that the same barrier height applies for electrons in surface states in order to move back into the bulk. The barrier height is often used in the context of charge transfer at semiconductor interfaces. Here, the barrier height will be referred as band bending (BB).

To probe the height of the band bending, surface photovoltage (SPV) measurements became widely established. An extensive review on surface photovoltage phenomena was provided for example by Leeor Kronik [131]. Figure 2.16 shows a schematic illustration of the surface photovoltage effect considering occupied donor states by Ga-3Ga bridges close to the valence band and partially filled Ga-dangling bonds to which the Fermi level was pinned. If the semiconductor surface is illuminated with photons larger than the band gap, electron-hole pairs will be excited in the depletion region and dissociated by the electric field. Majority electrons will thereby be forced back into the bulk and minority carriers towards the surface where they recombine with trapped surface carriers. The recombination leads to a lowering of the band bending as indicated by green lines. Of course, the illumination leads to a non-equilibrium situation and a splitting of the quasi-Fermi levels. For simplicity the Fermi level is nonetheless drawn as a straight line. In case of band-to-band illumination the recombination statistics via surface trap states can mainly be described by Shockley-Read-Hall recombination. However, there is also the possibility to directly photoionize trap states with sub-band gap photons, such that electrons overcome the potential barrier and drift back into the bulk where they can undergo mainly radiative, Auger and non-radiative trap state assisted recombination.

If it is assumed that a high intensity of photons can lead to a complete suppression of the band bending, the technique allows to directly access its absolute value. However, in real experiments even high intensities do not lead to a complete flattening of the bands depending on the recombination efficiency and crystal quality. As already indicated in the previous section many semiconductor surfaces, including the one of GaN, tend to form thin oxides (~ 1 monolayer) [128,132,133]. The oxide formation can also go along with the formation of acceptor like states that can further be occupied by electrons (depicted as yellow lines) [134–136]. Radiative recombination from GaN oxide states has been reported by Shalish *et al.* in terms of a yellow luminescence [137–139]. The deep lying oxide trap states were found 2.2 eV below the conduction band. Furthermore, it is known that oxides and hydroxides form not only surface states but also a permanent surface dipole δ indicated by the solid region here. Such surface dipoles may change upon chemical changes at the surface. This differentiated consideration will be of importance for the later analysis of the SPV measurements on wet-chemical functionalized GaN surfaces in Chapter 5.

3. Experimental background

Most of the experiments and fabrication steps presented in this work were performed inside a clean room and at the clustertool, which is an interconnected system of vacuum chambers and characterization techniques (see Figure 3.1). Organic solar cells were mainly fabricated in the organic and metal evaporation chambers. Solution-processed films of nickel oxide were spin-coated in the clustertool glovebox and subsequently annealead in air. Complementary studies of the fundamental properties of nickel oxide and gallium nitride were performed in the IR spectroscopy, the photoelectron spectroscopy and the ultra-high vacuum scanning probe microscope (UHV-SPM). All scanning electron microscope images and a first back-illuminated surface photovoltage experiment on GaN were carried out in the Auriga scanning probe system shown on the right. The wet-etching of GaN was performed in an acid fume hood and the functionalization of the surfaces in a separately installed glovebox. Kelvin probe measurements were performed outside the vacuum environment and in ambient atmosphere. Solar cell characterization was done in ambient outside the clean room. GaN samples were provided and anlyzed with time-resolved photoluminescence at the Paul-Drude-Institut in Berlin.

3.1. Analytical methods

In the following sections the main analytical methods and setups are introduced. The author likes to thank Sabina Hillebrandt and Valentina Rohnacher for the infrared measurements and evaluation, which also applies to Florian Ullrich for the variety of photoelectron spectroscopy measurements.

3.1.1. Atomic force microscopy

The atomic force microscope (AFM) was developed by G. Binnig, C. Quate and C. Gerber in 1986 [141], shortly after the invention of the first working scanning tunneling microscope by G. Binnig and H. Rohrer in early 1980 [142]. The working principle of the AFM is based on the line-by-line scanning of a very sharp tip across the surface topography of a sample. The tip is typically attached to a cantilever as shown in Figure 3.2 a). While the tip interacts with

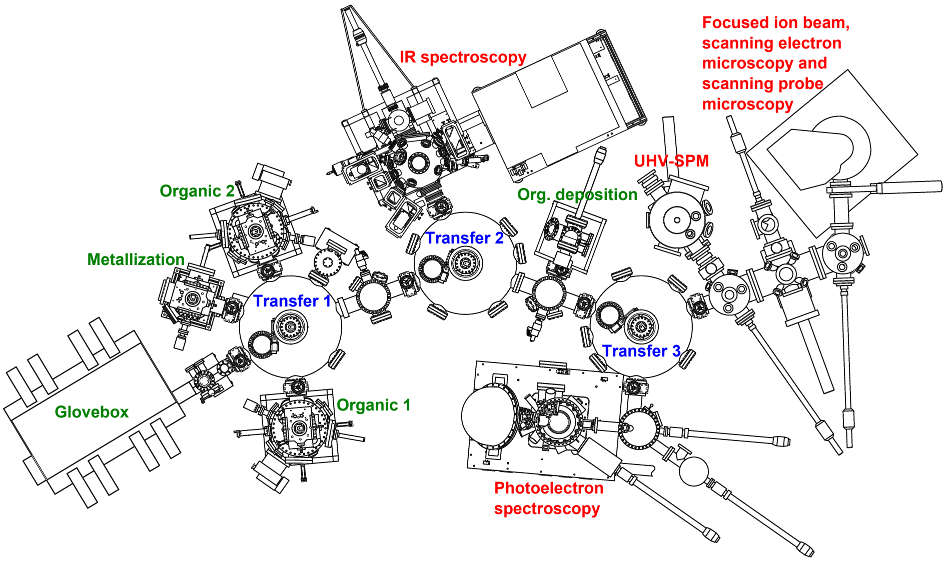

Figure 3.1.: Schematic illustration of the clustertool. Main components are the interconnected evaporation chambers, the IR and XPS spectroscopy as well as the scanning probe systems. Reprinted from [140].

long and short range forces at the surface, the cantilever becomes deflected. The deflection can be tracked with the reflection of a laser beam focused onto the backside of the cantilever, which is then detected by a four-quadrant photodiode. The deviation of the laser spot on the photodiode is used as input for a feedback loop, which maintains a constant deflection of the cantilever by varying the tip-sample distance through the height-adjustment of a piezo driven xyz-stage. This is the most basic AFM operation principle to obtain a map of the surface topography and often called *contact* or DC mode.

Figure 3.2 b) shows a typical force-distance curve that is recorded during the approach of the cantilever to the surface. When the tip is in proximity to the surface it encounters attractive forces, mainly caused by van der Waals interactions. As soon as the tip gets in direct contact with the surface, it will enter a repulsive force regime. This force regime is commonly used for measurements in DC mode. However, the direct contact may damage or contaminate the tip [143]. Operating in the negative force regime or *non-contact* range often results in an unstable feedback, as this regime is narrow and the tip-sample distance can change abruptly depending on scan speed, surface composition and cantilever material.

To avoid permanent direct tip-sample contact and to enable scanning in *non-contact* mode with a larger force range, the *tapping* or alternating current

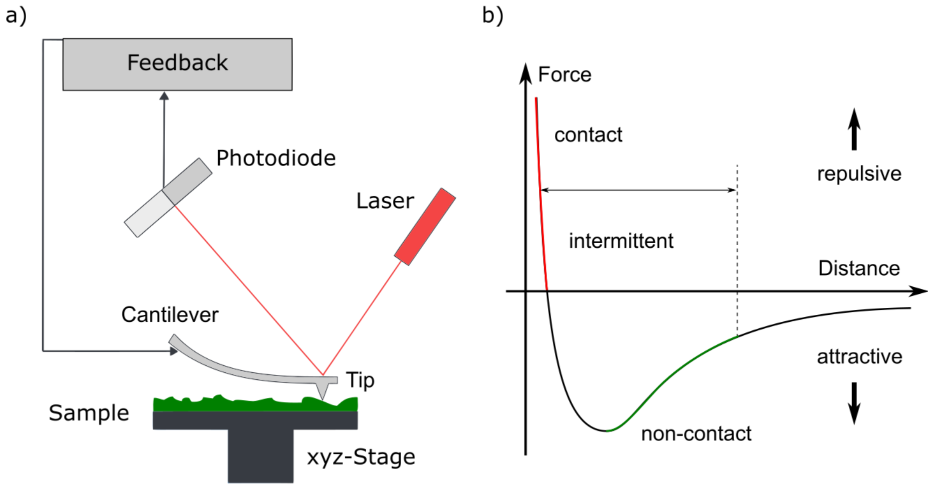

Figure 3.2.: Schematic illustration of the AFM working principle. a) Basic components of an AFM with feedback loop for maintaing the tip-sample distance. b) Force-distance curve seen for a tip approaching the sample surface from right to left on the distance axis.

(AC) mode was introduced and became the most common principle today. In *tapping mode* the cantilever is continuously oscillated close to its resonance frequency ω_0. The oscillation leads to a periodic deflection of the cantilever, which is detected in the same way as in DC mode. When the tip starts to interact with surface atoms, the oscillation frequency and phase changes and the amplitude becomes dampened. The interaction force is approximately proportional to the tip-sample spacing. For large distances, the vibration amplitude has a Lorentzian form of

$$A(\omega) = \frac{A_0(\omega_0/\omega)}{\sqrt{1 + Q^2(\omega/\omega_0 - \omega_0/\omega)^2}}, \tag{3.1}$$

where A_0 is the resonance amplitude and ω_0 the resonance frequency. $Q = \frac{\omega_0}{\Delta\omega}$ is the quality factor and a measure of the steepness of the Lorentzian curve. The dampening of the cantilever oscillation can be described in a first approximation by Hookes law ($F \propto -kx$), where k is the spring constant of the cantilever and x the displacement of the spring. This leads to a shift of the resonance frequency according to $\omega_0' = c\sqrt{k - F'}$, where F' is the derivative of the force acting on the spring and c the mass of the spring [144]. If the interaction force is small compared to the spring constant $F' \ll k$, the change in amplitude

ΔA can be described by

$$\Delta A = (2A_0Q/3\sqrt{3}k)F'. \tag{3.2}$$

The change in amplitude ΔA is often used as the error signal of the feedback loop to maintain a fixed tip-sample distance. This operation is also called *amplitude-modulated* AFM. If stiff cantilevers with high frequencies are used ($> 100\,\mathrm{kHz}$) the tip-sample interaction can predominantly be kept in the attractive force regime without entering the repulsive regime. As the tip might contact the surface for a very short time in every oscillation, the mode is also denoted as *intermittent* contact mode. Furthermore, Equation 3.2 shows that small oscillation amplitudes, which means small energies in the oscillating system, and high Q-factor cantilevers can increase the sensitivity and thereby improve the signal-to-noise ratio.

AFM measurements shown in Chapter 4 and 5 were performed with a customized DME UHV-AFM and Arrow NCPt cantilevers from Nanoworld. These 160 µm long, 45 µm wide and 4.6 µm thick cantilevers are made of silicon coated with PtIr at the tip as well as the reflective side. They have a spring constant of $k = 42\,\mathrm{N\,/\,m}$ and a resonance frequency of $\approx 285\,\mathrm{kHz}$. The tip has a height of $10 - 15\,\mathrm{\mu m}$ and a radius of $< 10\,\mathrm{nm}$.

3.1.2. Kelvin probe

In 1861 the Kelvin probe (KP) method was discovered by Lord Kelvin, who observed a charge exchange between copper and zinc plates with an electroscope when they were brought into electrical contact [145]. The contact electricity is a consequence of the different Fermi edges between the materials driving electrons from the lower to the higher work function material until both Fermi levels reach thermal equilibrium (see Figure 3.3). The charge transfer gives rise to an electric field and thereby to a potential difference. This difference is reflected in a shift of the vacuum levels, which is often called contact potential difference V_{cpd} (CPD). Thus, the Kelvin probe method emerged as a non-destructive standard technique to measure the work function of metals and semiconductors.

Modern Kelvin probe setups are built with a Kelvin oscillator, presumably a gold tip or grid, which forms a capacitance with the measured sample. When the oscillator is driven close to its resonance frequency ($\approx 100\,\mathrm{Hz}$), the

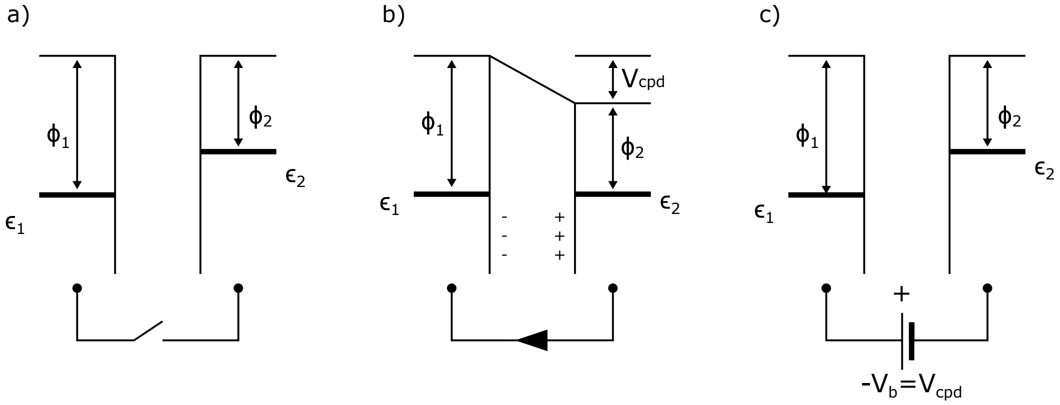

Figure 3.3.: Illustration of the Kelvin probe principle. a) When two materials with different work functions ϕ_i are brought into contact, b) a current will establish until the Fermi levels ϵ_i are in thermal equilibrium. c) The built contact potential can be extracted by applying a reverse backing voltage $-V_b$. Adapted from [146].

time-dependent capacitance between probe and sample can be described by

$$C(t) = \frac{\epsilon_0 \epsilon_r A}{d(t)}, \tag{3.3}$$

where $d(t)$ is the current distance, A the area of the probe, and ϵ_0 and ϵ_r the electric field constant and the relative permittivity, respectively. The current distance $d(t)$ depends on the mean distance d_0 and the amplitude d_1 of the sinusoidal excitation oscillation, such that

$$d(t) = d_0 + d_1 \sin \omega t. \tag{3.4}$$

The influenced surface charge is then given by $Q = C \cdot (V_{\text{cpd}} + V_b)$ and the induced current in the circuit follows $I_{\text{ind}}(t) = \frac{dQ}{dt}$. This leads to a peak-to-peak output-voltage V_{ptp} of

$$V_{\text{ptp}} = (V_{\text{cpd}} + V_b) R_{I/V} \frac{d_1}{d_0} C_0 \omega \sin(\omega t + \phi), \tag{3.5}$$

where C_0 is the mean capacity at mean distance d_0 and $R_{I/V}$ the resistance of the operational amplifier. V_{cpd} can be obtained by nullyfing the output voltage V_{ptp} through an equal but opposite backing voltage V_b. This method was first introduced by Zisman *et al.* in 1932 [147]. In a real experiment V_b is not randomly swept until the correct bias is found, but V_{ptp} is measured for a predefined range of V_b and the zero of V_{ptp} extrapolated.

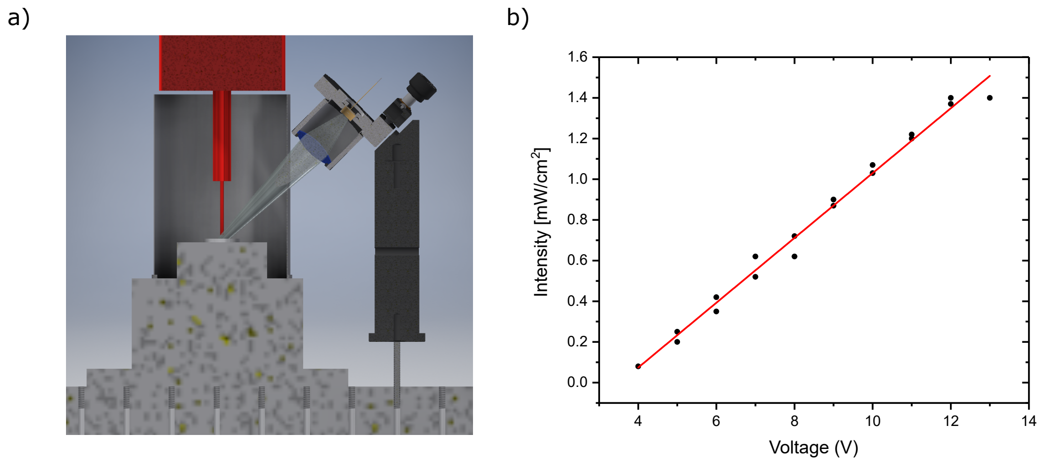

Figure 3.4.: Illustration of the ambient Kelvin probe setup for surface photovoltage measurements. a) 3D rendered model of the Kelvin oscillator shielded with a Faraday cage in front of the illumination LED. b) Intensity of the UV-LED in dependence of the applied bias. Intensity scales linearly over a range of 10 V. The model was created by Stefan Brackmann.

As V_{cpd} depends on the reference electrode and is thereby a relative quantity, the absolute work function of the tip needs to be calibrated against a reference sample with known absolute work function. Often highly ordered pyrolytic graphite (HOPG) is used for this purpose [148]. Through the difference of the reference work function and the measured CPD, the work function of the tip

$$\Phi_{\mathrm{tip}} = \Phi_{\mathrm{ref}} - \mathrm{CPD}_{\mathrm{tip-ref}}, \tag{3.6}$$

and sample

$$\Phi_{\mathrm{sample}} = \Phi_{\mathrm{tip}} + \mathrm{CPD}_{\mathrm{tip-sample}}, \tag{3.7}$$

can be calculated. Note that the sign inverts, when the bias polarity is switched between sample and tip.

Surface photovoltage

Ambient work function measurements were performed by Stefan Brackmann with a KP Technology single-point Kelvin probe. The gold tip with 2 mm diameter was driven at a frequency of 74.9 Hz with an amplitude of around 50 µm. In order to extend the system for surface photovoltage measurements the setup was equipped with a UV-light source and an LED driver (see

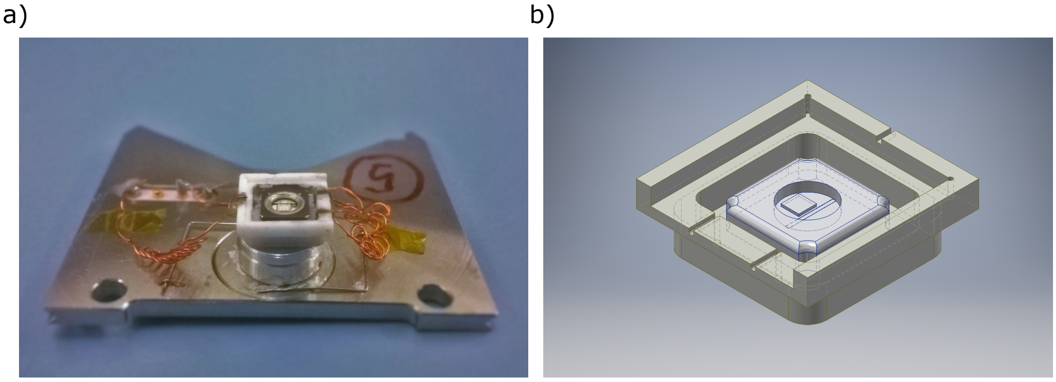

Figure 3.5.: Illustration of the sample holder for Kelvin probe surface photovoltage measurements in vacuum. a) Picture of AFM sample holder. A high-power UV-LED was incorporated into a custom-built ceramic holder for back-side illumination. The LED was contacted with the sample holder pins over thin capton-isolated cupper wires. b) 3D rendered model of the custom-built sample holder with the UV-LED positioned at the bottom. Slits were shaped into the ceramic to allow fixing of the wires.

Figure 3.4a)). For band-to-band illumination of GaN a 355 nm XSL-355-5E LED was purchased from Roithner Lasertechnik GmbH. The LED is specified for a power of 4.2 mW with a spectral half width between 1 and 20 nm [149]. A silica lens in front of the LED was used to focus the beam onto the sample surface. Light intensities at the sample position were calibrated with a 365 nm UV-optometer. As shown in Figure 3.4 b), the intensity scales linearly with the bias voltage and a maximum of $1.4\,\mathrm{mW}\,/\,\mathrm{cm}^2$ could be achieved.

A high-vacuum surface photovoltage measurement was performed with the KP-AFM in the Zeiss Auriga Cross-Beam System. The same cantilevers as described in Section 3.1.1 were chosen to measure the work function during the back-side illumination of a GaN sample. For the illumination a ceramic sample holder incorporating a high-power UV-LED was built (see Figure 3.5). The sample was positioned face-up on top of the LED, so that the light is coupled in through the substrate. The surface mount LED employed was a RLCU-440-365 from Roithner Lasertechnik GmbH [150]. It is specified with output powers between $40 - 90\,\mathrm{mW}$ at 4 V and 350 mA current, exhibits a viewing angle of 120° and a spectral half width of about 9 nm. Connecting cables were coiled to release strain from the sample socket, which is important for proper AFM measurements.

3.1.3. Scanning electron microscopy

The scanning electron microscope (SEM) was introduced to extend the resolution limit of optical microscopes, which is determined by the wavelength of the used photons. This limit can be lowered by the de Broglie wavelength of accelerated electrons

$$\lambda_e = \frac{h}{\sqrt{2m_e eV}}, \tag{3.8}$$

where h denotes the Planck constant, m_e the mass of an electron, and V the acceleration voltage. In typical SEM operation field-emitted electrons are accelerated through a Wehnelt cylinder between 1 keV and 30 keV yielding a theoretical resolution below 0.5 Å. The accelerated beam is focused by a configuration of electrostatic and magnetic lenses to a spot size of $\sim$ 1 nm. The focal spot is scanned line-by-line across the surface leading to high-energy back scattered electrons, isotropic emission of low-energy secondary electrons and X-rays. The cross-section for back-scattering of primary electrons depends on the atomic number of the materials in the investigated film. Films with different atomic composition can thereby give a clear material contrast, which is not the case for optical microscopes. High-energy back-scattered electrons stem from deeper surface layers in the vicinity of the beam and can be detected with the in-lens detector, which is placed inside the electron column. The distribution of kinetic energies of low-energy secondary electrons depends on the emission depth. Therefore, with a different take-off angle of a second Everhart-Thornley type detector, a higher topography contrast can be achieved. All images presented in this work were taken with the in-lens detector at a base pressure of $< 1 \times 10^{-5}$ mbar. The setup is specified for an experimental resolution of 1.2 nm.

3.1.4. Photoelectron spectroscopy

Photoelectron spectroscopy allows to measure the distribution of binding energies of electrons in a sample. The technique is based on the external photoelectric effect in which an electron is excited from an atomic shell by incoming photons. If the energy is large enough the electron travels to the surface and is ejected into vacuum. On the way to the surface the electron can undergo inelastic scattering processes and lose energy. Thus, the spectrum of emitted electrons is a superposition of primary electrons at distinct energy peaks and a secondary electron continuum down to zero kinetic energy. The kinetic energy distribution of electrons leaving the sample can be measured

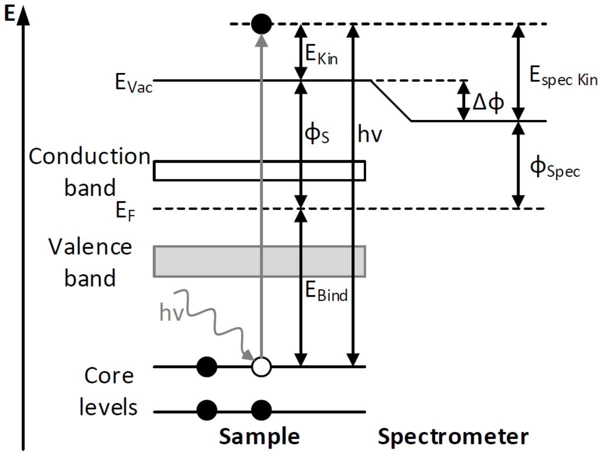

Figure 3.6: Illustration of the fundamental principle of photoelectron spectroscopy. Electrons are excited by the photon energy $h\nu$ and leave the sample with kinetic energy E_{kin}. Reprinted from [94].

with a hemispherical energy analyzer and written as

$$E_{\text{kin}} = h\nu - E_{\text{bin}} - \Phi_{\text{s}}, \tag{3.9}$$

where E_{kin} is the kinetic energy of the emitted electrons, $h\nu$ the incoming photon energy, E_{bin} the binding energy of the electrons in the sample and Φ_{s} the work function of the sample.

Figure 3.6 shows an illustration of the fundamental principle of the photoelectric effect for an electron released from a core level in the sample. As the analyzer itself is in electrical contact with the sample holder, a contact potential between sample and analyzer is established. Depending on the relative position of the work functions of sample and analyzer, electrons can either get further accelerated or decelerated. Thereby, the kinetic energy spectrum is shifted by the work function difference of sample and analyzer. As the actual work function of the analyzer is difficult to determine, the Fermi edge of a metal reference sample is measured to calibrate the kinetic energy scale.

Photoelectron spectroscopy can be performed with different photon energies, predominantly X-rays (XPS) or ultra-violet light (UPS). For UPS the spectral lines of He I (21.2 eV) and He II (40.6 eV) discharge lamps are commonly used yielding a higher cross-section with electrons from the valence band. However, the materials investigated in this work showed a strong interaction with UV-irradiation. Therefore, measurements were done with XPS using a PHI Versa Probe II equipped with a monochromatized Al-Kα anode as X-ray source ($h\nu$ = 1486.6 eV). Survey spectra were recorded with 187.5 eV, core level spectra with 11.75 eV, valence bands with 23.5 eV and the secondary electron cut-off with 5.85 eV pass energy. The kinetic energy scale was referenced to the

Fermi edge of an *in-situ* cleaned Ag foil. The base pressure of the measuring chamber during all experiments was kept at 10^{-9} mbar. A take-off angle of 90° was standard. Core level fits were done utilizing Voigt profiles after subtraction of a Shirley background [151]. All XPS measurements and data evaluations were performed by Florian Ullrich (TU Darmstadt).

3.1.5. Fourier-transform infrared spectroscopy

The Fourier-transform infrared spectroscopy (FTIR) is a technique to measure the absorption of infrared light of a sample. Through the absorption of electromagnetic radiation in the infrared, permanent or induced dipoles between two atoms in a molecule can couple to the incoming light and thereby be excited to a vibration. The strength of these molecular vibrations depends on the polarizability of the corresponding atoms and can be described by the combination of the dielectric function of solids and the atomar polarizability according to the Clausius-Mossotti-Relation [152].

To measure the intensity of the absorption, the sample is exposed to IR-radiation of a broadband light source in a Michelson interferometer as shown in Figure 3.7. The focused light beam of the light source is divided into two separate beams by a beam splitter. While one beam is reflected at a stationary mirror, the other one is reflected by a movable mirror. The position of this mirror leads to an optical path difference Δx. Both waves recombine at the beam splitter and are focused onto the sample of interest. The interaction of the lightwaves with an optical path difference leads to constructive and destructive interference for varying wavenumbers. By varying the optical path difference, an intensity distribution $I(\Delta x)$ can be accumulated. The interferogram of a sample needs to be Fourier transformed in order to find the intensity distribution of absorption modes depending on the excitation frequency $I(\tilde{\nu})$. More information on the theoretical background can be found in [153,154].

IR-transmission spectra were measured with a Bruker Vertex 80v FTIR spectrometer. The mercury cadmium telluride (MCT) detector was cooled with liquid nitrogen to obtain a high signal-to-noise ratio. A silicon carbide source was heated for the emission of IR-radiation. Presented spectra are averages over 200 scans with a resolution of 4 $\mathrm{cm^{-1}}$. The mid-infrared range is covered from 650 $\mathrm{cm^{-1}}$ −6000 $\mathrm{cm^{-1}}$. All measurements were performed with p-polarized light. The sample compartment was purged with nitrogen at normal pressure, because under vacuum hydrocarbons from chamber walls adsorbed on the metal oxide surface and water was removed from the bulk film.

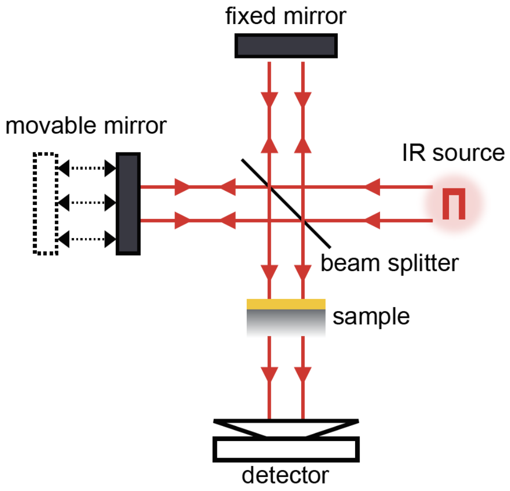

Figure 3.7: Illustration of a typical Michelson interferometer adapted for the use in FTIR experiments. The source light beam is divided by a beam splitter. Split beams are reflected at a stationary and a moving mirror with an optical path difference with which they interfere again at the beam splitter before passing the sample and hitting the detector. Reprinted from [153].

Relative transimission spectra were obtained after dividing the transmitted intensity by the intensity of a reference measurement

$$I_{\text{rel}}(\tilde{\nu}) = \frac{I_s(\tilde{\nu})}{I_{\text{ref}}(\tilde{\nu})}, \tag{3.10}$$

where $I_s(\tilde{\nu})$ is the absorption spectrum of the sample and $I_{\text{ref}}(\tilde{\nu})$ the intensity of the reference sample. This provides information on the dielectric properties of the last deposited layer. For the temperature-dependent experiment on as-deposited sNiO films in Section 4.3.2, the spectra were divided by the signal of the clean and also heated Si substrate. The CYNOPPA treated sNiO films were measured relative to the exact same as-deposited sNiO samples. All IR measurements and data evaluations were performed by Sabina Hillebrandt and Valentina Rohnacher (Universität Heidelberg).

3.1.6. Time-resolved photoluminescence

Time-resolved photoluminescence (TRPL) measures the transient light emission of a material after pulsed optical excitation. In a semiconductor the absorption of light can lead to the excitation of an electron from the valence to the conduction band. If the energy of the absorbed photon is larger than the optical band gap, unbound charge carriers are generated. Coulomb-bound excitons with lower energy can form, if the energy of the incoming photons is slightly lower than the band gap. Excitons in GaN have a binding energy of around 26 meV [155] and thus can be stable even at room temperature [156]. Electrons in such higher energy states tend to return to the valence band after

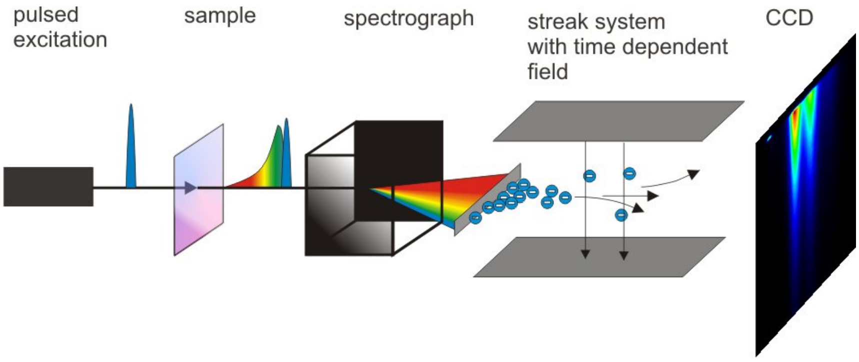

Figure 3.8.: Illustration of a typical TRPL setup with streak camera. The pulsed excitation passes the sample and is analyzed in a spectrograph. The spectrum is converted into charge carriers emitted from a photocathode. Afterwards, carriers are spatially sorted by a time-dependent field before they hit a phosphorescent screen. Events are recorded with a charge-coupled device (CCD). Reprinted from MPIP Mainz, Frederic Laquai group [157].

a certain time. The relaxation can occur either by radiative or non-radiative recombination with characteristic time constants, which are often influenced by defect and donor states. Hence, with TRPL the lifetime of such excited states can be probed and information on charge carrier dynamics gained.

Figure 3.8 illustrates a typical TRPL setup, which is similar to the one used for the measurements in Section 5.3.4 and Section 5.4.2. From left to right, the pulsed laser excitation is focused onto the sample of interest and the transient photoluminescence analyzed in a spectrograph. If the lifetime of the excited states is in the range of 1 ns to ms, the spectrally resolved decay of the photoluminescence can directly be detected with a gate intensified charge-coupled device (gated ICCD). However, if the lifetimes of the excited states become smaller than ns and thereby faster than the lower limit of most ICCD exposure times, a streak system is required. The streak system allows to spatially separate electrons emitted from the photocathode in the spectrograph. The separation occurs through the deflection of the electrons in a time-dependent field, which is synchronized with the duration of the laser pulse. Delayed electrons will thereby hit the phosphorous detection screen at different spatial positions, which is then recorded by a CCD camera. Hence, a map of the PL intensity over time and wavelength is obtained. Taking a profile along the intensity over time at a specific wavelength gives then a typical TRPL lifetime spectrum.

For the experiments on GaN, a Verdi pumped COHERENT MIRA 900 Ti:sapphire laser was used with a central wavelength of 850 nm and a pulse duration of 200 fs at 76 MHz repetition rate. Pulses are then shifted to 1300 nm in an optical parametric oscillator and reduced to 325 nm with two stages of second harmonic generation (SHG). The laser beam is focused onto the sample with an x-y-z movable LMU-10-X-NUV objective. Its numerical aperture of 0.25 results in a spot size of around 3 µm ×11 µm. The transient photoluminescence is collected with the same objective and fed into a Horbia Jobin Yvon Spex 1681 spectrometer, which exhibits a photon energy resolution of a few meV. The spectrally dispersed light is detected with a Hamamatsu C5680 streak camera with a temporal resolution of several ten ps. Neutral density filters can be incorporated into the optical beam path to reduce the fluence. A maximum fluence of 20 µJ cm^{-2} can be achieved. The cw-PL equivalent power is about 4 mW at 325 nm. Note that for measuring the total PL intensity it is sufficient to use a continuous wavelength HeCd laser (cw-PL) as excitation source. Samples can be cooled with liquid helium in the cryostat in a range of $10 - 300$ K. For more information on the measurement setup the interested reader may refer to [158]. All TR-PL measurements were performed and evaluated by Dr. Chiara Sinito (Paul-Drude-Institut, Berlin).

3.1.7. Solar cell characterization

Organic solar cells discussed in Chapter 4 were characterized by Jakob Bombsch with an LOT LS0816-H solar simulator. The solar source is a 1000 W xenon arc lamp with a spectral irradiance comparable to the standard terrestrial spectrum of AM 1.5G. The emission intensity of 100 mW cm^{-2} was calibrated with a certified silicon solar cell (RR106O, Radboud University, Nijmegen). Current-voltage characteristics were measured under illumination and dark condition in a 2-wire configuration with a Keithley 2601B source meter. As temperature variations can influence the correct determination of device parameters, all cells were evaluated in a comparable warm state after several measurement runs under illumination.

3.1.8. Goniometry

Goniometry is a technique to measure the surface energy of samples by measuring the contact angle to water and solvents of varying polarity. The contact angle is extracted at the three-phase interface of the liquid droplet on a substrate surface according to the illustration given in Figure 3.9. An optical camera system detects the drop shape. The contact angle Θ can be fitted by the Young-Laplace equation, correlating the surface tension σ_s of the solid, the surface tension of the liquid σ_l and the surface tension between the liquid

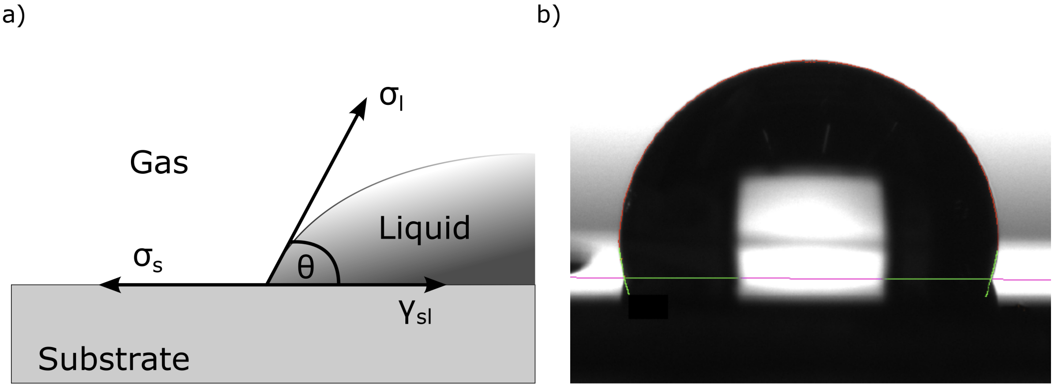

Figure 3.9.: Illustration of the contact angle measurement at the three-phase interface of a liquid droplet on a substrate surface. a) σ_s denotes the surface tension of the solid, σ_l the surface tension of the liquid, γ_{sl} the surface tension between liquid and substrate. b) Optical camera image of a water droplet on a hydrophobic solid substrate. The contour of the droplet is fitted and the baseline set to the droplet interface to the substrate.

and the solid γ_{sl}:

$$cos\Theta = \frac{\sigma_s - \gamma_{sl}}{\sigma_l}. \tag{3.11}$$

Drop shapes and contact angles were analyzed and measured with a Krüss DSA 100 goniometer. Water droplets with a volume of 1 µl were dispensed onto the substrates and the contact angle was extracted according to the Young-Laplace fit.

3.2. Preparation methods

The following sections describe the preparation methods. First, a list of the used materials and GaN samples is given. Afterwards, the fabrications steps are explained in more detail.

3.2.1. Materials and samples

The list of materials is structured according to the logical order of the result Chapters 4 and 5. Materials incorporated into organic solar cells are briefly described. Exact molecular structures can be found in the appendix. An overview on the GaN samples supplied by the PDI is given, followed by an overview on the variety of SAM precursor tested on the GaN surface.

Molybdenum oxide - MoO_3

Molybdenum oxide is a high work function transition metal oxide and widely used as a hole-contact layer [29]. Its *n*-type conductivity stems from oxygen vacancies, which form during the growth under vacuum conditions. Here, MoO_3 thin films were processed by thermal evaporation of Molybdenum(VI) oxide in vacuum at a base pressure of $\leq 10^{-7}$ mbar. The average evaporation rate was between 5-10$\frac{\text{Å}}{\text{min}}$. Molybdenum(VI) oxide powder was purchased from Sigma-Aldrich at 99.97% trace metal basis.

Solution-processed nickel oxide - sNiO

NiO is a promising material for hole injection and extraction, as it is one of the few *p*-type transition metal oxides. It has a large band gap, high work function and good electron blocking capabilities due to its low electron affinity. Solution-processed nickel oxide films were fabricated from an acetic acid nickel(II) salt according to Manders *et al.* [159]. Nickel(II) acetate tetrahydrate was purchased from Sigma-Aldrich at 99.998% trace metal basis. The fabrication procedure is described in more detail in section Section 3.2.2.

4-cyanophenyl-phosphonic acid - CYNOPPA

4-cyanophenyl-phosphonic acid ($C_7H_6NO_3P$) was used as a precursor for self-assembled monolayers, as it has a strong permanent dipole moment 3.59 D [160], a well conjugated π-system and the cyano-group can improve the surface energy and thereby wettability for printing applications. CYNOPPA was purchased from Manchester Organics (CAS: 16672-78-9) with a purity of 96%. The material was further purified through recrystallization by Maximilian Ackermann (OCI) to a degree that nothing more than the molecular components were observed in the nuclear magnetic resonance (NMR) spectrum. A detailed description of the application of the molecule is given in Section 3.2.5.

4'(dimethylamine)-[1,1'biphenyl]-4-phosphonic acid - DiDi2PA

4'(dimethylamine)-[1,1'biphenyl]-4-phosphonic acid is a novel PA-SAM precursor and was synthesized by Simon Benneckendorf (OCI). The name was abbreviated DiDi2PA to indicate the presence of 2 benzene rings attached to the PA group. A free-standing molecular dipole moment of -9.4 D was calculated. The full publication of the synthesis was still pending at the time of writing this work.

Fluorinated Zinc Phtalocyanine - F_4ZnPc

Phtalocyanines, especially ZnPc [5], have been intensively used and modified for the application as a donor material in organic photovoltaics. Its chemical structure allows for a variety of chemical substitutions, including the central metal atom or the ligands. It was shown that the substitution does not significantly affect the optical band gap and the absorption properties [161,162]. Gradual fluorination of F_nZnPc became a major topic in literature and showed to significantly lower the HOMO and LUMO levels of ZnPc leading to higher effective band gaps in OPV cells and thereby larger V_{oc} [68,163]. HOMO and LUMO of F_4ZnPc are commonly measured at -5.3 eV and -3.9 eV. F_4ZnPc was supplied by BASF SE after purification by vacuum sublimation.

Buckminster fullerene - C_{60}

Buckminster fullerenes and their derivatives became the most prominent acceptor materials over the last years. C_{60} shows a strong electron accepting character and high electron mobilities [65,164]. Common HOMO and LUMO levels are -6.2 eV and -4.0 eV, respectively. The fullerene was purchased from American Die Society ($>$ 99,9%) and was not further purified.

1,3,5-tris(2-N-phenylbenzimidazolyl)-benzene - TPBi

TPBi was introduced as a cathode buffer layer for organic photovoltaic cells to prevent exciton quenching at the top metal electrode [165,166]. Furthermore, it was observed that the underlying C_{60} layer is smoothened by the deposition of TPBi giving a better growth template for the top electrode and preventing the metal from diffusing into the active layer [140]. 5 nm to 8 nm thin TPBi buffer layers can improve the V_{oc} of CuPc cells without a significant increase in series resistance due its high electron mobility [167] . TPBi was purchased from Sensient Technologies.

Gallium nitride - GaN

In order to study the feasibility of functionalizing GaN nanowire facets, a series of GaN template substrates were provided by Dr. Thomas Auzelle (PDI). In the beginning the focus was solely put on the *c*-plane GaN(0001) surface. Table 3.1 shows an overview on the supplied GaN(0001) samples, whereas carrier concentrations and dislocation densities are compared. It can be seen that the dislocation density for the homoepitaxially grown bulk GaN samples is at least two orders of magnitude lower than for the heteroepitaxially on sapphire grown *c*-plane GaN(0001) commercial KymaTech template. Due to the high cost of free-standing samples, only a single commercial KymaTech bulk sample was available in the beginning. *p*-type GaN was also investigated by means of Kelvin probe, but is not further discussed in the scope of this work. The high quality *c*-plane and *m*-plane samples with very low dislocation densities and background carrier concentrations were grown by molecular beam epitaxy (MBE) and were supplied in a later stage of the project.

Table 3.1.: Overview on the GaN samples studied in this work.

Sample	Orientation	Face	Type	Carrier concentration [cm^{-3}]	Dislocation density [cm^{-2}]	Substrate	Thickness [µm]
Kyma template [168]	(0001)	Ga	n	$> 5 \cdot 10^{17}$	$< 1 \cdot 10^{9}$	sapphire	5
Kyma bulk [169]	(0001)	Ga	n	$> 5 \cdot 10^{17}$	$< 1 \cdot 10^{7}$	free-standing	250
	(000$\bar{1}$)	N					
11OK1101-2	(0001)	Ga	p (Mg)	unknown	unknown	sapphire	500
PDI *c*-plane	(0001)	Ga	n	$< 5 \cdot 10^{16}$	$< 5 \cdot 10^{5}$	free-standing	0.9
PDI *m*-plane	(1$\bar{1}$00)	Ga/N	n	$< 5 \cdot 10^{16}$	$< 8 \cdot 10^{7}$	free-standing	1.1

SAM precursor for GaN

A series of different SAM precursor was evaluated to find a proper binding partner for the *c*-plane GaN(0001) and later also for the *m*-plane GaN(1$\bar{1}$00) surface. Table 3.2 shows an overview of the precursor materials sorted by their anchoring group. The proposed binding partner is added in a separate column. While amines came in liquid phase, thiols were supplied in solid phase. Both were diluted into toluene with the required volume or mass to yield 0.5-1 mM SAM solutions. Toluene solutions were stirred overnight at 50 ℃ with a magnetic stirring bar. GaN samples were immersed into the toluene SAM solutions for 24 h at 30 ℃ after the cleaning protocol described in Section 3.2.4. Afterwards, samples were removed from solution, thoroughly rinsed with pure toluene, blown dry with N_2 and characterized. Note that the precondition for metal binding partners are a metal terminated and oxide free surface. Therefore, the last O_2-plasma step in the cleaning protocol was not applied before application of amines and thiols. A detailed description of the

GaN functionalization with phosphonic acids from ethanol solutions is given in Section 3.2.5. Molecular structures for all presented SAM precursor are attached to the appendix.

Table 3.2.: Overview on the SAM precursor tested on the GaN surface.

Molecule	Binding partner	Solvent	CAS number
Amines			
Aniline	Metal	Toluene	62-53-3
Ethylenediamine	Metal	Toluene	107-15-3
Hexylamine	Metal	Toluene	111-26-2
Diethylenetriamine	Metal	Toluene	111-40-0
Thiols			
Perfluorodecanethiol (PFDT)	Metal	Toluene/Ethanol	34143-74-3
1-Octadecanethiol (ODT)	Metal	Toluene	2885-00-9
Phopshonic acids			
Tridecafluorooctyl-phosphonic acid (FHOPA)	Oxide	Ethanol	252237-40-4
Octyl-phosphonic acid (OPA)	Oxide	Ethanol	4724-48-5

3.2.2. Processing nickel oxide from solution

Nickel oxide films were fabricated by solving the nickel(II) acetate tetrahydrate in anhydrous ethanol, spin-coating the solution and annealing the precursor in ambient air at high temperatures. If not stated otherwise, 0.2 M solutions were preparted by dissolving 200 mg of nickel acetate in 4 ml ethanol and adding 50 µl of monoethanolamine (MEA) as stabilizer. Monoethanolamine was purchased from Sigma-Aldrich ($> 99\%$) and stored inside N_2 atmosphere. The molar ratio of nickel ions and the MEA was kept 1:1 according to the recipe proposed by Manders *et al* [159]. The nickel precursor solution was stirred at 50 ℃ in N_2 atmosphere overnight and was not aged, which is sometimes recommended in literature. Substrates for spectroscopic purposes were sonicated for 10 min in acetone/isopropyl alcohol prior use. Note that for transmission IR-spectroscopy the Si substrates need to be carefully cleaned from both sides, such that no precursor material resides on the back of the samples. Solutions were spin-coated at 2000 rpm, 2000 rpm s^{-1} for 60 s inside the clustertool glovebox and subsequently annealed for 45 min in air at 275 ℃, 325 ℃ or 400 ℃ depending on the application. During the annealing step samples were covered with a

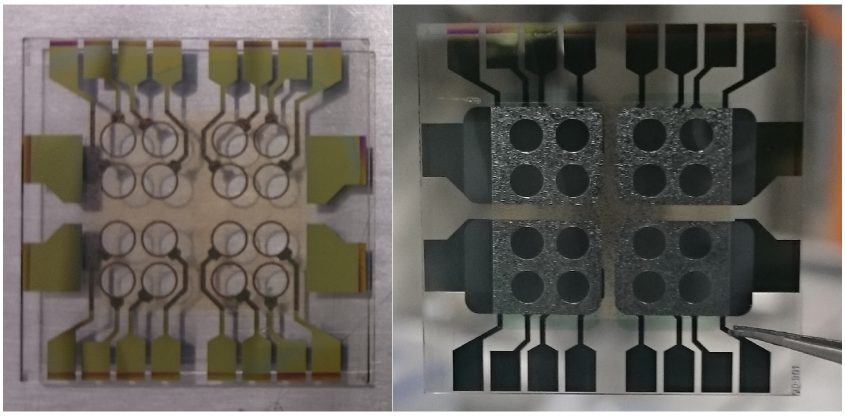

Figure 3.10.: Picture of the 16-port BASF substrate layout used for the organic solar cells. On the left the substrate is shown prior and on the right after the deposition of the device stack. The 4 mm^2 active area is given by the cross-section of the stack and the overlapping top-electrodes.

petri dish to maintain a stable temperature and atmosphere in the vicinity of the substrate surface. With these parameter set film thicknesses between 20 nm to 25 nm were obtained.

3.2.3. Fabrication of organic solar cells

Organic solar cells were fabricated by Jakob Bombsch onto $25 \times 25\,\mathrm{mm}^2$ pre-structured ITO coated glass substrates supplied by BASF SE. As shown in Figure 3.10 the substrate provides 16 active fields with an area of 4 mm^2, which are separated by a thin insulating layer. Prior use the ITO substrates were solely rinsed with isopropyl alcohol for a minute and dried with nitrogen afterwards.[1] sNiO hole-contact layers were solution-processed onto the clean substrates as described in Section 3.2.2. F_4ZnPc, C_{60}, TPBi and the silver top contact were deposited via vacuum sublimation at a base pressure of $\leq 2 \cdot 10^{-7}$ mbar. Evaporation rates for organic materials were kept at $10 \pm 1\frac{\text{Å}}{\text{min}}$. The silver top electrode was deposited at a rate of $100 \pm 10\frac{\text{Å}}{\text{min}}$. Bilayer solar cells were grown with 30 nm F_4ZnPc and 30 nm C_{60} thickness, respectively. Bulk heterojunctions were fabricated with a thickness of 50 nm by 1:1 co-evaporation and an additional 10 nm closed layer of C_{60} on top. TPBi was evaporated to a thickness of 8 nm and the silver cathode to 100 nm. Note that substrates were rotated at around 50rpm during the film growth. Prior the characterization the solar cells were encapsulated with a $17.5 \times 17.5\,\mathrm{mm}^2$ glass

---

[1] After personal communication with Paul Heimel (BASF)

slide attached to the cell with a transparent adhesive (Delo Katiobond). The epoxy resin was cured for 30 min under UV-light at an intensity of 5 mW / cm^2.

Two main solar cell architectures were investigated:

- ITO/sNiO/F_4ZnPc/C_{60}/TPBi/Ag - Flat heterojunction (FHJ)
- ITO/sNiO/F_4ZnPc:C_{60}/C_{60}/TPBi/Ag - Bulk heterojunction (BHJ)

3.2.4. Wet-chemical cleaning of gallium nitride

A cleaning protocol was developed throughout the course of this work to achieve an as cleaned as possible gallium nitride surface independent of the plane and polarity. The protocol is a sequence of wet-chemical treatments and O_2-plasma. The step-by-step recipe is given as follows:

- Gallium nitride sample of interest was cleaned in an ultrasonic bath in acetone and isopropyl alcohol for 15 min with activated heating.
- A 5 min O_2-plasma was applied to the sample. The plasma oven was evacuated to 0.3 mbar and ran at a power of 900 W. Before the actual application, the oven was run idle at least once to avoid cross-contamination with residuals of prior use. The plasma treatment was seen as an additional cleaning step to remove residual hydrocarbons.
- To remove the oxide grown by the O_2-plasma, the sample was immersed into 32% HCl for 10 min in a Teflon sample holder. The acid was purchased from Carl Roth and exhibited a pH value of ≤ 3.
- Directly after the etching step, the sample was dipped into boiling ethyl acetate. The dipping time should be kept short and the sample should be removed and blown dry with N_2 immediately. Ethyl acetate was chosen because of its high vapor pressure at room temperature and to avoid exposure of the GaN surface to solvents with oxygen or H_2O after the HCl cleaning step. However, ethyl acetate is not capable of removing residual Cl completely. Note that the choice of solvent might also influence the work function.
- Subsequently, the sample was transferred into a glovebox and annealed at 400 °C for 3 h. It was shown that this step is crucial to remove residual Cl from the surface. However, a certain amount of carbon contamination was observed afterwards. It remained unclear, whether this depended on the annealing environment or is an inevitable consequence of the annealing step itself.

- Finally, the carbon signal was successfully removed by a 5 min O_2-plasma treatment.

Of course, the last step led again to the growth of an oxide. But it was intentionally introduced as a growth template for the successful functionalization with phosphonic acids, which will be described in more detail in the Section 3.2.5 and Section 5.4.1.

3.2.5. Functionalization with phosphonic acids

Nickel oxide as well as gallium nitride were successfully functionalized with self-assembled monolayers of phosphonic acids (PAs). The functionalization followed a strict protocol independent of the substrate type and was adapted from recipes suggested in [160,170]:

- Preparation of the PA solution in ethanol with the desired concentration. Even low concentrations of around 1 mM led to satisfying coverage. The solutions were predominantly prepared in a large ethanol volume of 100 ml, which was the standard shipment quantity for anhydrous ethanol from VWR. Note that the ethanol was only opened inside the glovebox. The PA-SAM precursor was measured out in air and transferred into the N_2 atmosphere with a smaller flask. Afterwards, the material was transferred from the small to the larger volume by ethanol rinsing. The 100 ml SAM solutions were stored inside the glovebox and reused when needed. The solution quality did not suffer by storage.

- Prior use, the PA solutions stirred at 30 °C for at least 4 h with a magnetic stirring bar on a hot plate. On the one hand this ensured a homogeneously dissolved solution, on the other the temperature was used to compensate the glovebox temperature, which was slightly below room temperature.

- Samples were immersed into PA solution. Depending on the sample size, substrates were either placed face-up into small flasks or into petri dishes. It is important that the containers are sealed properly, such that the solution does not evaporate during the immersion step. Note that in case of very small samples, the solution should be added to the flasks first. For small substrates a volume of 2-3 ml was chosen. For the solar cells the solution volume was increased to 6 ml because of the large surface area in the petri dishes.

- Samples were taken from the PA solution after 10-15 h and blown dry with N_2. At these time scales the infrared spectroscopy did not see any further enhancement of the SAM quality.
- After drying, samples were annealed on a hotplate at 140 °C for 3 h to activate the phosphonate binding. Again, samples were covered with a petri dish during the annealing step. Note that the maximum temperature might depend on the stability of the PA precursor molecule.
- To remove any non-covalently bound PA molecules and avoid multilayer formation samples were transferred out of the glovebox after a short cooling down and sonicated in ethanol (VWR, 99.5%) for 20 min in an ultrasonic bath with activated heating.
- As a last step of the protocol, the samples were transferred back to the N_2 glovebox and again annealed at 140 °C for 10 min.

4. Transition metal oxides as carrier-selective contacts

Transition metal oxides (TMOs), such as MoO_3, ZnO, TiO_2 and NiO, are promising candidates as a new generation of carrier selective charge transport layers for hybrid photovoltaic cells [28,171,172]. Thin TMO films can be processed with a variety of techniques, e.g. thermal and e-beam evaporation [173], pulsed-laser deposition [174], and radio-frequency magnetron sputtering [175]. More recently, also low temperature methods have emerged to enable film growth on temperature sensitive substrates [32,176,177].

In the following chapter the physical properties of two transition metal oxides will be investigated in the light of hole-contact functionality. Firstly, vacuum-evaporated molybdenum oxide (MoO_3) and secondly, solution-processed nickel oxide (sNiO). Thin-films of sNiO are incorporated into F_4ZnPc:C_{60} bulk- and flat-heterojunction solar cells to answer the question of how the sNiO film annealing temperature and surface post-treatments affect the device performance parameters. To achieve control on the wettability and chemical compatibility of the sNiO towards the F_4ZnPc, self-assembled monolayers of phosphonic acids are grown on the sNiO surface. This is further meant to optimize the energetic alignment between hole-contact layer and highest occupied molecular orbital (HOMO) of the donor and minimize the energetic offset for efficient and balanced carrier harvesting. A brief introduction on the importance of hole-contact layers for multilayer devices is provided to the beginning. The author emphasizes that hole-contact layer and hole-transport layer (HTL) are used with the same meaning throughout this chapter.

The chapter would not be complete without the scientific contributions of Jakob Bombsch, Florian Friedrich, Valentina Rohnacher, Florian Ullrich and Sabina Hillebrandt.

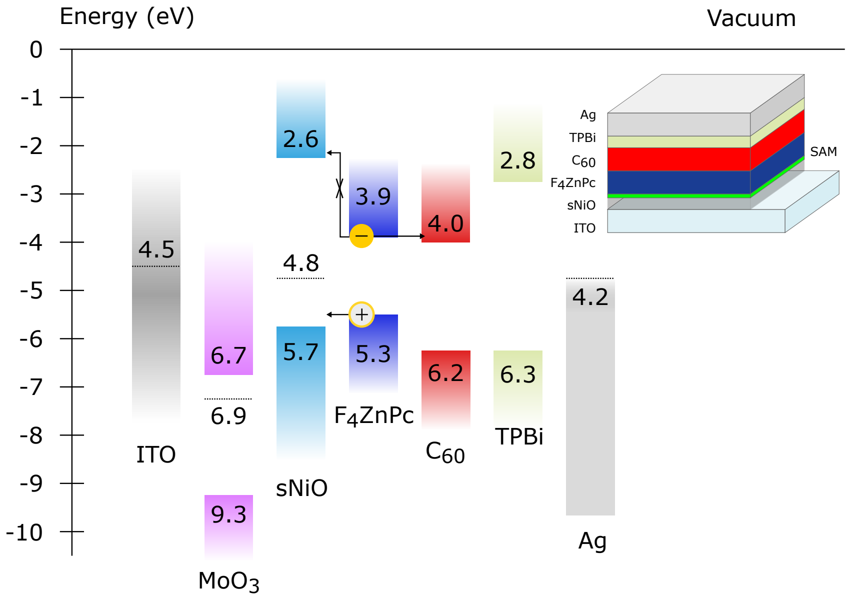

Figure 4.1.: Schematic illustration of the separate energy levels of the transition metal oxides (MoO_3, sNiO), metal contacts and organic materials in the F_4ZnPc:C_{60} solar cell device stack. The electron blocking capability of the sNiO hole-contact layer is indicated with a crossed arrow. Energy level alignment of the sNiO to the donor is dictated by the Fermi level of the interlayer. A schematic illustration of the FHJ device stack is shown as an inset.

4.1. Introduction into hole-contact layers

Hole-contact layers in organic photovoltaic devices ensure that photogenerated charge carriers are extracted only at the correct electrodes. This implies a natural thermodynamic selectivity of the energy levels of the interlayer as shown in Figure 4.1. To further guarantee high extraction rates of holes, the contact needs to be ohmic, which desires a contact layer with a Fermi level close to the HOMO of the donor. Irwin *et al.* summarized the following four crucial opto-electronic requirements for beneficial hole-contact functionality: (1) A wide bandgap ($E_{\text{gap}} > 3\,\text{eV}$) for high transparency in the visible spectrum to allow photons reach the absorber. (2) A low electron affinity to effectively block electrons and minimize surface recombination of charge carriers at the interface to the hole transport layer (HTL). (3) A high work function to properly align with the ionization potential of the donor to form an ohmic contact. (4) A good stability against moisture and contamination to ensure long device lifetimes [178]. Balanced rates of hole and electron extraction have shown to deliver the highest OPV performances [179].

Most TMOs exhibit a high transparency in the visible light regime, have energy levels that lead to carrier selectivity in layered devices and posses large conductivities to facilitate charge transport. Especially molybdenum oxide (MoO_3) and nickel oxide (NiO) became serious alternative hole extraction layers to the widely-established Poly(3,4-ethylenedioxythiophene):poly(styrenesulfonate), well known as PEDOT:PSS. The properties of poylmers in general and PEDOT:PSS in particular often depend on the manufacturer. Its acidic nature can even corrode the ITO anode [180,181]. Furthermore, morphological inhomogeneities and electron leakage through PEDOT:PSS as hole contact layer have been observed [182,183]. Sun *et al.* showed that non-stoichiometric thermally evaporated MoO_x interlayers exhibit a superior long-term air stability over devices using PEDOT:PSS [184]. A similar observation was reported by Irwin *et al.* for pulsed laser deposited NiO [178]. Such benefits made these transition metal oxides interesting for a more fundamental analysis provided in the following sections.

4.2. Vapor-phase grown molybdenum oxide

Molybdenum oxide is commonly evaporated from MoO_3 powder under vacuum conditions and tends to agglomerate into Mo_3O_9 clusters (see Figure 4.2) [29]. Its electronic properties have been extensively studied, but revised over the past years. Before 2010 it was believed that the electron affinity (EA) and ionization energy (IE) of MoO_3 thin films are as low as 2.3 and 5.3 eV, respectively [185–187]. It was shown later, that the conduction and valence band lie much deeper, around 6.7 eV and 9.7 eV [188]. Furthermore, the work function (Φ,WF) of MoO_3 thin films was determined very close to the conduction band ($\Phi_{MoO_3} = 6.86\,\text{eV}$) by UPS measurements, which rendered MoO_3 an extremely high work function n-type oxide semiconductor. With such a high work function, MoO_3 is an almost ideal hole-contact layer to a variety of organic donors with a deep lying HOMO. Additionally, the high work function can lead to doping at the interface with adjacent organics and thereby, increase the conductivity at the interface [31,188–194].

Despite the benefits that have been achieved through MoO_3, it was observed early that the properties of molybdenum oxide thin films sensibly depend on the deposition parameters, e.g. the substrate temperature [195] and the processing environment. Thin films of MoO_3 evaporated in vacuum often show an under-stoichiometric character as a result of oxygen deficiency [196,197] (see also Section 2.1). The degree of deficiency is of importance for the conductivity of the material [198]. When exposed to ambient air, MoO_3

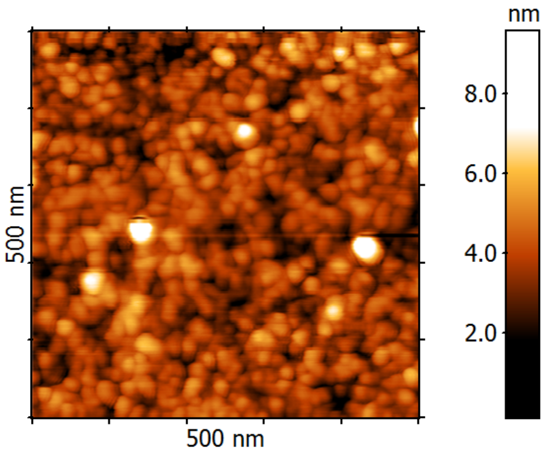

Figure 4.2: AFM topography of a 25 nm thick MoO_3 film on silicon measured *in-situ* in ultra-high vacuum shortly after evaporation. The root mean square roughness was calculated to $R_{\mathrm{rms}} = 0.94\,\mathrm{nm}$.

can loose its advantageous properties due to its hygroscopic nature [199]. However, Meyer *et al.* stated that the hole-injection efficiency into α-NPD is not affected by contamination or exposure to air [200]. Later, this hypothesis was corrected by an investigation of Zhong *et al.* showing that the hole injection barrier through MoO_3 can increase for organic donor materials with an ionization potential higher than 6 eV [201]. Furthermore, a substantial reduction of the work function upon air and oxygen exposure was observed by Irfan and coworkers [202,203]. While first successful passivation [204] and recovery [205,206] approaches either by heating or oxygen plasma treatment were presented, it has never been clearly understood whether adsorption of oxygen at the surface or diffusion of oxygen into bulk vacancies of the MoO_3 is the reason for the observed changes in the work function. As the high work function of the TMO is one of the four requirements for good hole-contact functionality, a substantial reduction would significantly influence the charge extraction rate. In order to investigate the stability of the MoO_3 work function, a long-time work function measurement was performed in the next section.

4.2.1. Evolution of the work function of molybdenum oxide in vacuum

The work function stability of MoO_3 thin films was measured with a scanning Kelvin probe in ultra-high vacuum. Scanning Kelvin probe is an extension of the atomic force microscopy with the Kelvin probe technique [207]. Both measurement principles are described in Section 3.1.1 and in Section 3.1.2, respectively. Thin films of MoO_3 were grown by thermal evaporation on polished silicon substrates in the IR chamber by Dr. Sebastian Beck. After

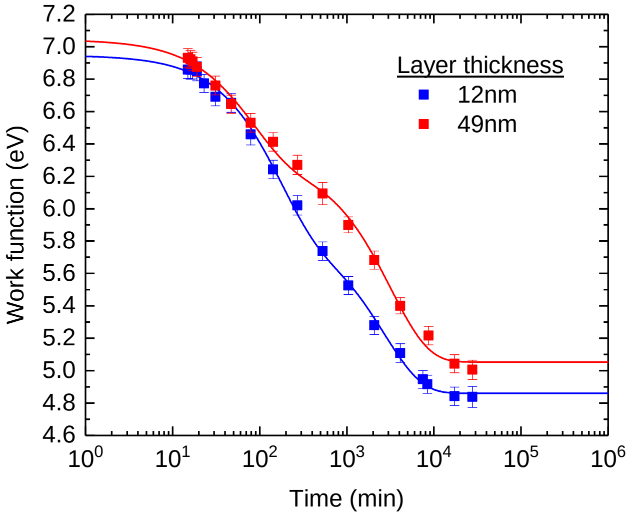

Figure 4.3: Time dependent work function of a MoO_3 thin film on silicon for two different layer thicknesses. Absolute values were obtained after calibrating the tip work function with respect to an HOPG reference sample ($\Phi_{\mathrm{HOPG}} = 4.66\,\mathrm{eV}$). Solid lines correspond to bi-exponential decay fits.

evaporation, the samples were transferred as fast as possible *in-situ* into the UHV-AFM (see clustertool in Figure 3.1). The time between the end of evaporation and cantilever approach was around 20 min. The base pressure was $1 \cdot 10^{-8}$ mbar during transfer and measurement. All data points were recorded with an automated script routine, in which the contact potential difference (CPD) between the Pt-Ir coated Si AFM-probe and the sample was measured at a distinct sample position. The distance between the tip and sample was kept constant. After every measurement point, the probe was retracted in order to avoid static charging and minimize the influence of the alternating electric field as well as the tip wear due to mechanic vibrations. Absolute work function values were obtained after calibrating the tip work function with respect to an HOPG reference sample ($\Phi_{\mathrm{HOPG}} = 4.66\,\mathrm{eV}$) [148].

Figure 4.3 shows the evolution of the work function of two MoO_3 thin films with different layer thicknesses. Within minutes after deposition the work function starts to decrease monotonously from a maximum around $6.9-7.0\,\mathrm{eV}$ down to 5.0 eV after a week in vacuum at the above mentioned base pressure. The measurement procedure of retracting and approaching the tip with a radius smaller than 10 nm can lead to slightly different measuring positions on the sample, which might be the reason for the distortion in the WF decay. Both data sets can be fitted by second-order exponential decay functions:

$$y = y_0 + A_1 \exp\frac{-x}{t_1} + A_2 \exp\frac{-x}{t_2} \tag{4.1}$$

The second-order indicates the influence of two different contaminants with two time constants t_i, presumably caused by the adsorption of molecular oxygen and residual water. The impact of hydrocarbons in the UHV environment is neglected here. For the 12 nm film values of $y_0 = 4.86\,\text{eV}$, $t_1 = 160\,\text{min}$, and $t_2 = 2677\,\text{min}$ were extracted from the fits. For the 49 nm film the values were $y_0 = 5.05\,\text{eV}$, $t_1 = 81\,\text{min}$, and $t_2 = 3190\,\text{min}$. Lifetime values were rounded to the nearest integer. It can be seen that the second adsorption process is extremely slow compared to the initial one for both MoO_3 film thicknesses. Even though the values here suggest that the first process is faster for thicker layers, a clear tendency could not be confirmed in further experiments. Hence, it can be concluded that the work function stability of vacuum evaporated MoO_3 thin films is only given for a couple of minutes, even at a base pressure of $1 \cdot 10^{-8}\,\text{mbar}$.

4.2.2. Differentiation between oxygen and water adsorbtion under controlled gas exposure

In order to differentiate between the predominant contaminants oxygen and water, the same experiment was conducted under controlled gas exposure. For this, the UHV chamber was equipped with a precision leak valve connected to a gas inlet system with a turbo pump for purifying the feed line. This allowed to provide dry oxygen at a very specific base pressure. The chamber pressure sensor was simultaneously read out during the CPD measurement to calculate the gas exposure in Langmuir L according to:

$$Exposure\,[\text{Langmuir}] = 1.33 \cdot 10^{-6} \cdot Pressure\,[\text{Torr}] \cdot Time\,[\text{s}]. \tag{4.2}$$

This is equivalent to exposing the substrate to a base pressure of $1 \cdot 10^{-6}\,\text{mbar}$ for 1 second.

Figure 4.4 depicts the exposure-dependent work function for two different MoO_3 samples. For the dry oxygen exposed sample, a first measurement point was taken before opening the precision leak valve. After that, the valve was opened and the base pressure raised to $p = 2 \cdot 10^{-6}\,\text{mbar}$. It can be seen that for exposures below $10^4\,\text{L}$ the work function decreases more slowly for the dry oxygen exposed sample than for the sample kept under residual vacuum. Above $10^4\,\text{L}$ the work function starts to saturate, but at different work functions for the two different background gases. The saturation values differ by as much as 1.75 eV.

Due to the similarity of the initial WF decrease, the fast component t_1, determined in Section 4.2.2, is addressed to the adsorption of molecular oxygen. However, it seems the flushing with oxygen does not lead to a faster decrease

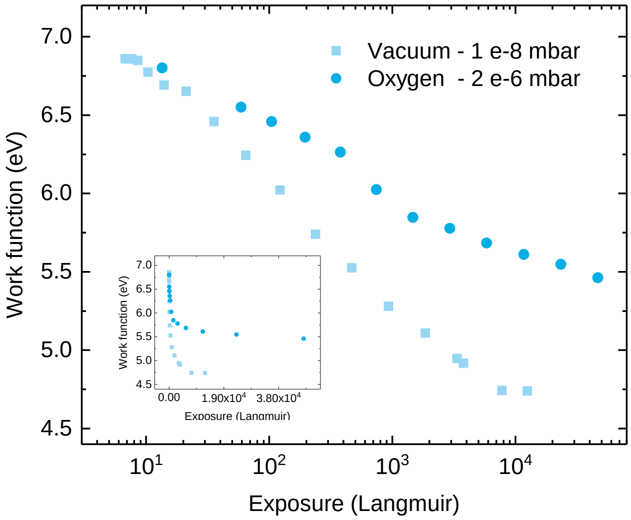

Figure 4.4: Exposure dependent work function of a 25 nm thick MoO_3 thin film on silicon for different gas composition and base pressure.

of the work function. The second-order and slower component t_2 might then be attributed to adsorption of water molecules forming a surface dipole layer, which leads to an even stronger work function decrease. At this point it is still not clear, if the work function is only affected by a surface mechanism or also by processes correlated to the bulk.

4.2.3. Correlation between work function and conductivity

To answer whether the initial decrease of the work function is solely caused by oxygen adsorption at the surface or also diffusion of oxygen into bulk vacancies, a correlated work function over conductivity measurement was performed. For this experiment $5 \times 5\,\mathrm{mm}^2$ clean glass samples were pre-structured with gold terminals as shown in Figure 4.5 a) and evaporated with 25 nm thick MoO_3 films. The channel length was 210 µm and the CPD was measured at a constant bias of +5 V between the gold finger electrodes as indicated by the position of the illustrated cantilever.

Figure 4.5 b) shows the current measured for three different samples with the same MoO_3 film thickness. Two of them were exposed to dry oxygen at a base pressure of $1 \cdot 10^{-6}$ mbar, whereas the third was kept in vacuum at a base pressure of $5 \cdot 10^{-9}$ mbar. The second sample that was exposed to oxygen was a repetition measurement on a different substrate to confirm the observations. For all samples the conductivity is below $1 \cdot 10^{-11}$ A in the beginning. Over time the current increases linearly to a few nA, more rapidly for the oxygen exposed samples (see graph inset). The semi-logarithmic plot shows that the

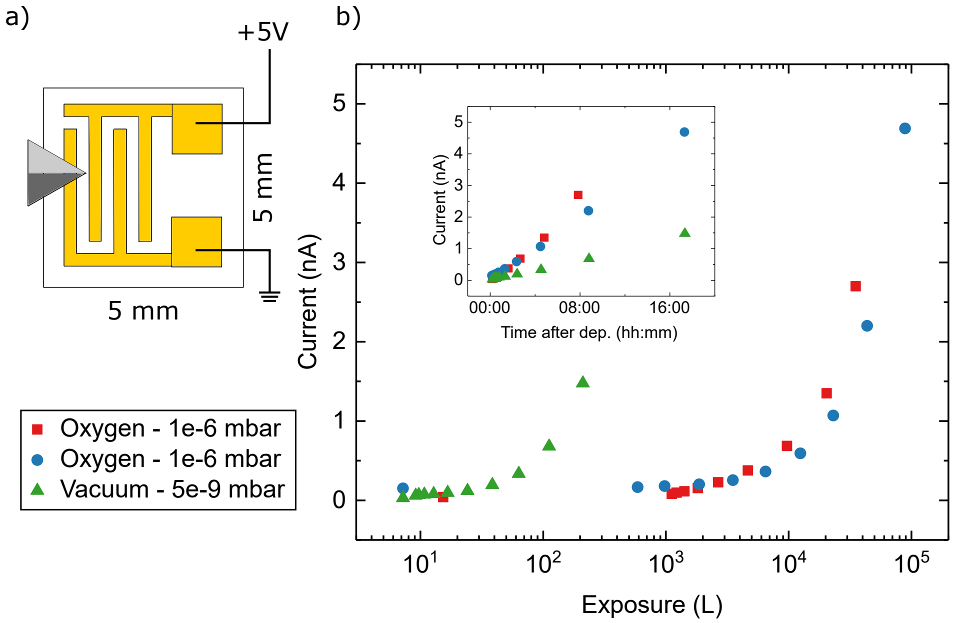

Figure 4.5.: Exposure dependent conductivity of 25 nm thick MoO_3 thin films. a) Schematic illustration of the $5 \times 5\,mm^2$ glass substrates with structured gold finger electrodes used for the current measurement. b) Semi-logarithmic plot of the current measurement for different base pressure and background gas. The red data points correspond to a repetition measurement on a different sample. The inset shows the current evolution over time in linear scale after deposition.

current increase correlates more with time and with the gas composition than with the base pressure. This corroborates that oxygen is the main component in the initial decrease of the work function and that the higher the oxygen partial pressure is the faster the current increases.

Most probably an oxidative adsorption takes place, in which an electron is transferred from the adsorbing oxygen to the surface of the MoO_3, leading to a reduction of its Mo^{6+} oxidation state, a change in surface stoichiometry and thereby, a higher n-type conductivity. The increase in conductivity is then confined as a conductive surface channel rather than a bulk conductivity increase. This contradicts the observations by Cheung *et al.* [208] proposing that air exposure leads to compensation of oxygen deficiency in the bulk and an increase in conductivity. Therefore, care should be taken, when MoO_3 thin films are exposed to ambient conditions, to conserve its exceptional high work function.

4.3. Solution-processed nickel oxide

While the high work function of MoO_3 is clearly advantageous for energy level alignment to organic donor materials with deep lying IEs, its very high electron affinity (IE ≈ 6.9 eV, see Figure 4.1) can reduce the electron blocking capability of MoO_3 hole-contact layers [12]. An approach to overcome this drawback was proposed by Schulz *et al.* using a NiO_x/MoO_3 bi-layer [209]. Nickel(II) oxide (NiO) grows in a rock-salt structure with octahedral coordination of Ni^{2+} and O^{2-} sites. It is a promising material for hole injection and extraction, as it is one of the few p-type TMOs with a large band gap, high work function and a low electron affinity (EA) [210].

Early works on NiO used pulsed laser deposition (PLD) in vacuum to precisely control the oxygen partial pressure during film growth. Irwin *et al.* were the first to incorporate PLD grown NiO as a hole contact layer into conventional P3HT:PCBM bulk-heterojunction solar cells [178]. The first use of a nickel ink to form a NiO thin film was reported by Steirer *et al.* [211]. Later on, Manders *et al.* proposed a nickel acetate precusor route to form efficient NiO hole contact layers that even outperformed reference cells with PEDOT:PSS [159,212]. However, literature still lacks information on a detailed correlation between the NiO fundamental material properties and the device characteristics. Therefore, solution-processed NiO (sNiO) thin films from the nickel acetate precursor route were investigated in more detail and its physical properties correlated to the device performance in small molecule F_4ZnPc:C_{60} solar cells. The next sections deduce the sNiO topography, chemical composition and electronic properties sequentially by AFM, IR- and XP spectroscopy.

4.3.1. Revealing the surface topography with atomic force microscopy

To get a clear picture of the surface structure of the sNiO, the precursor was spin coated and thermally annealed at 325 °C on $1.5 \times 1.5\,\mathrm{cm}^2$ ITO substrates. Afterwards the samples were carefully cleaved into $5 \times 5\,\mathrm{mm}^2$ pieces to fit the required dimension of the AFM.

Figure 4.6 shows 6 different topography images recorded with a Pt-Ir silicon cantilever in amplitude-modulated tapping mode ($k = 42\,\mathrm{N\,m^{-1}}$, $f_0 = 285\,\mathrm{kHz}$). If the cantilever is driven close to its resonance frequency (offset $10-20\%$) with maximum oscillation amplitude (DirectAC ×1, software gain factor, Figure 4.6 a-c)) the sNiO micro-structure can hardly be revealed. However, when the physical amplitude is manually reduced by a factor of ×2 or ×4 and the

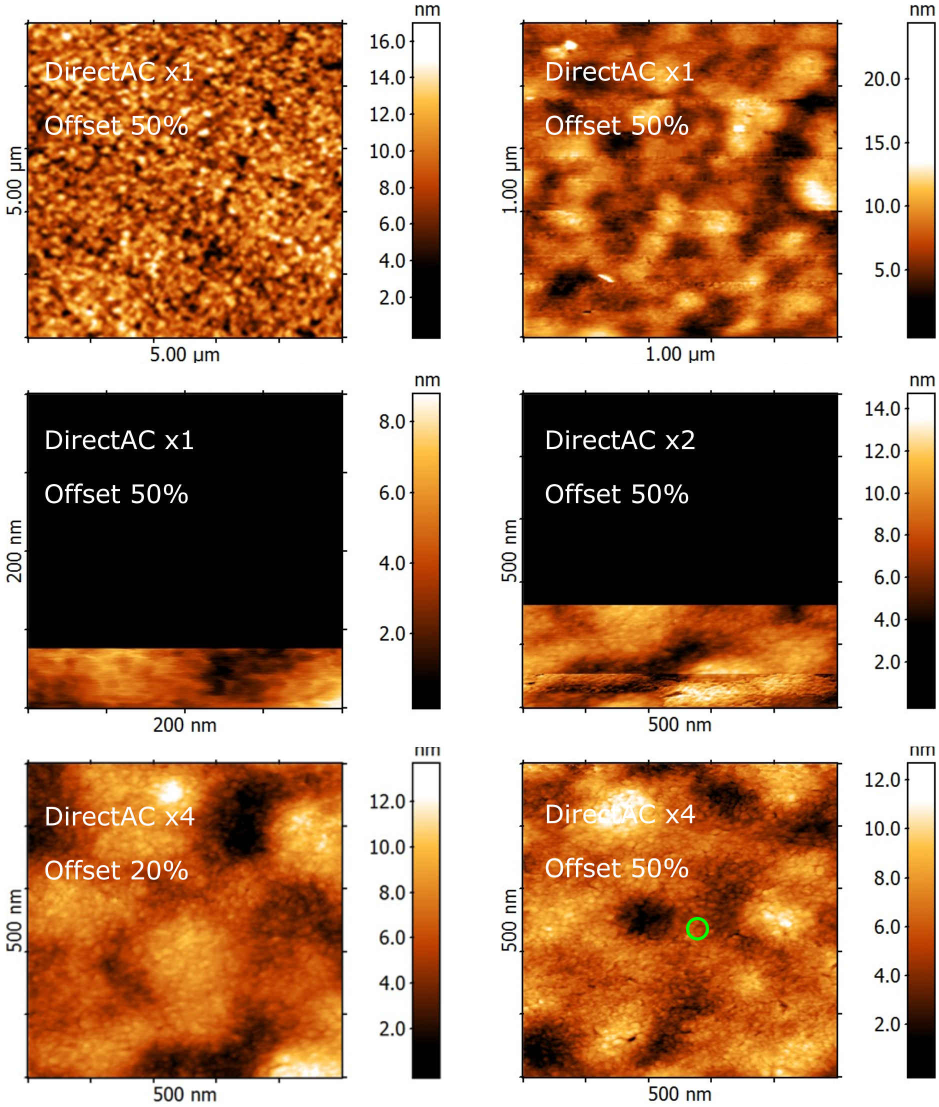

Figure 4.6.: Series of AFM images of 20 nm sNiO on ITO measured in ultra-high vacuum. In order to reveal the very small grain structure of the NiO films the physical oscillation amplitude has been reduced by the given DirectAC factors. The highest resolution could be achieved at DirectAC x4 and a frequency offset of 50%. All images were measured at a damping setpoint of 60% and include 512 × 512 scan lines per axis. A typical grain was highlighted with a red circle.

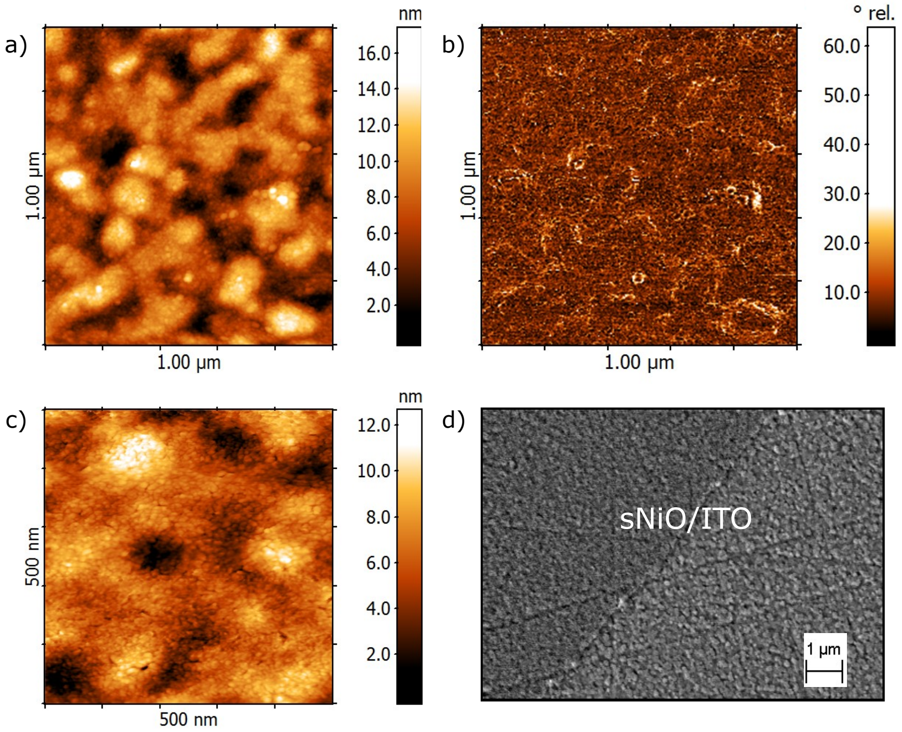

Figure 4.7.: High-resolution AFM and SEM images of sNiO on ITO. a) 1 µm ×1 µm, b) corresponding phase image c) 500 nm ×500 nm, and d) SEM image of a scratch through sNiO on ITO (scale bar 1 µm.)

digital output signal amplified by the same factor, more details of the sNiO topography appear. Selecting too small amplitudes, e.g. ×8, results in an unstable scanning operation. Here, an optimal DirectAC gain of ×4 was found. Additionally, a higher offset from the resonance frequency increases the force with which the tip interacts with the surface, thereby, also increasing the sensitivity and resolution. A frequency offset of 50% and a DirectAC gain of ×4 gave the best results (see Figure 4.6 f)).

With these parameters a grainy micro-structure of the sNiO was found, with average grain sizes smaller than 10 nm and a root mean square roughness of $R_{\mathrm{rms}} = 1.9\,\mathrm{nm}$. This value is slightly higher compared to the value found on the thermally evaporated $R_{\mathrm{MoO_3}} = 0.94\,\mathrm{nm}$. The grains can also be clearly recognized in the phase image (see Figure 4.7 b)). Dark and bright regions correspond to the underlying ITO substructure. Smaller cracks (dark marks) appear in the film due to aging after a few days in vacuum. A similar picture is given by the SEM image in Figure 4.7 d). The view shows a tweezer induced scratch through the sNiO layer. The dark grey region displays a compact sNiO layer (thickness ~ 25 nm) adapting the grainy ITO substructure (light grey).

4.3.2. Adressing the chemical structure with IR- and XP spectroscopy

The physical properties of single crystalline NiO were intensively investigated before 2000, especially by Hüfner *et al.* [213–219]. However, there are only a few detailed studies on the chemical properties of solution-processed NiO [159,220]. In this section parts of a detailed temperature-dependent infrared- and photoelectron spectroscopy are presented. Three different film annealing temperatures were investigated, 275 °C, 325 °C and 400 °C. All films were processed on thoroughly cleaned 1 cm ×1 cm Si substrates.

Figure 4.8 shows the relative transmission spectra in the mid-infrared range (MIR) of sNiO films annealed at the aforementioned temperatures. Broad absorption modes appear in the range between 3200 and 3700 cm^{-1}, and further

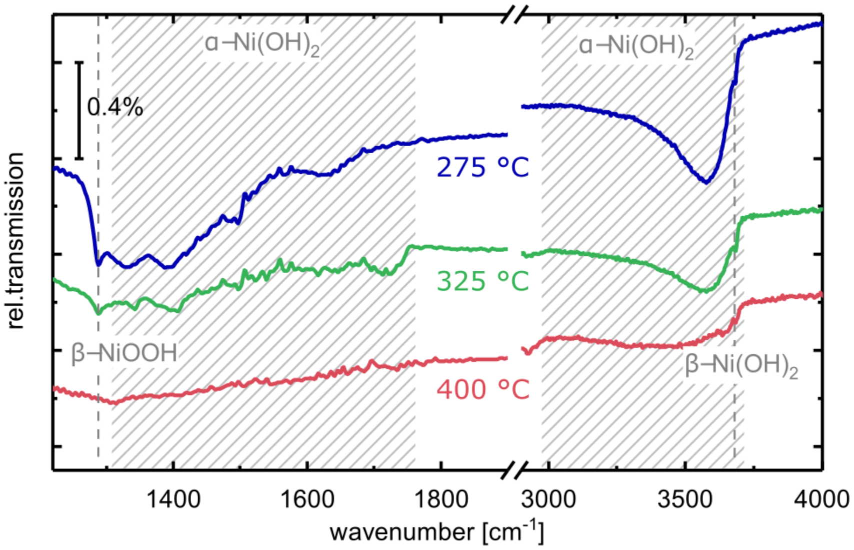

Figure 4.8.: MIR relative transmission spectra of solution-processed NiO films on double-side polished Si substrates for three different film annealing temperatures: 275 °C (blue), 325 °C (green) and 400 °C (red). The two shaded regions indicate vibrational modes of the α-Ni(OH)$_2$ phase. A dashed line at 3685 cm^{-1} highlights a characteristic absorption mode of β-Ni(OH)$_2$. At 1286 cm^{-1} another band arises from the presence of β-NiOOH.

distinct modes between 1300 and 1750 cm^{-1}. These modes can be assigned to the α-Ni(OH)$_2$ phase [221], which consists of stacked β-Ni(OH)$_2$ layers intercalated by water molecules. β-Ni(OH)$_2$ is the most common hydroxide phase of bivalent nickel (Ni^{2+}) [222]. At 275 °C and 325 °C the α-Ni(OH)$_2$ mode is more intense than at 400 °C. As the sNiO film thickness does not vary significantly from sample to sample, the decreasing intensity of these vibrational modes are not a measure of thickness, but rather a measure of the α-Ni(OH)$_2$ amount in the film. The distinct β-Ni(OH)$_2$ mode at 3685 cm^{-1} is superposed by the broader absorption of α-Ni(OH)$_2$, which makes it difficult to deduce a clear temperature dependency. Another mode can be seen at 1286 cm^{-1}, which is addressed to β-NiOOH, an oxidation product of β-Ni(OH)$_2$ [223]. This mode is more pronounced for lower annealing temperatures, especially 275 °C and 325 °C. Furthermore, it was stated that the β-NiOOH phase might be more conductive than other forms of hydroxide [220,221,224]. In general, hydroxide phases can be interpreted as a measure of precursor conversion [225]. From this it can be concluded that the higher the temperature during the annealing process, the more the precursor gets converted and the less water (α-Ni(OH)$_2$) remains in the film.

Figure 4.9 shows the Ni 2p$_{3/2}$ and O 1s core level spectra of the sNiO films measured with X-ray photoelectron spectroscopy. The films were processed

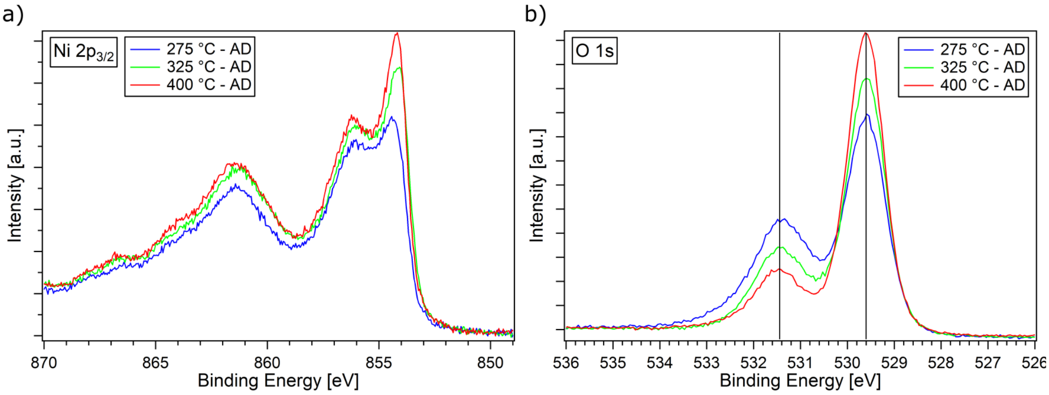

Figure 4.9.: X-ray photoelectron Ni 2p$_{3/2}$ and O 1s core level spectra of the as-deposited (AD) sNiO films annealed at 275 °C (blue), 325 °C (green), and 400 °C (red). a) The main feature (854.1 eV) in the Ni 2p spectrum can be attributed to the bivalent Ni^{2+} and the shoulder peak (856 eV) to a superposition of hydroxide components. At higher binding energies several shake-up satellites appear. b) The main peak (529.6 eV) in the O 1s spectrum displays the corresponding O^{2-} and the shoulder peak around 531 eV the hydroxide components.

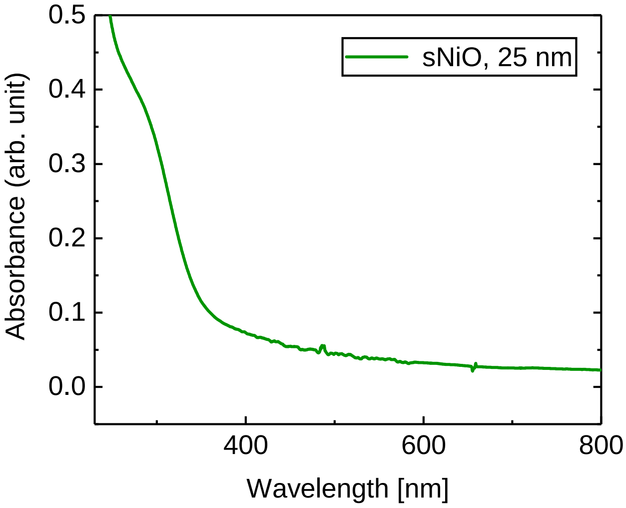

Figure 4.10: UV-vis absorption spectrum of an as-deposited sNiO film on ITO annealed at 325 °C. The wavelength was scanned from 200 nm to 800 nm. A bare ITO substrate was chosen as reference spectrum.

with the same parameters as the samples for FTIR. The Ni $2p_{3/2}$ spectrum exhibits a dominant component at a binding energy of 854.1 eV, which is commonly attributed to the bivalent Ni^{2+} in the octahedral NiO bonding configuration [214,226–228]. A similar peak is found in the O 1s spectrum at 529.6 eV belonging to O^{2-}. The shoulder peaks around 856 eV in the Ni $2p_{3/2}$ and around 531 eV in the O 1s spectrum are more complex to address. It is commonly interpreted as a superposition of NiO components that have a different binding energy due to a varying bonding configurations on the surface [220,229–232]. Furthermore, different forms of nickel hydroxides lie within this range. These hydroxides can be: Ni bulk hydroxide $Ni(OH)_2$, surface hydroxide (-OH) and oxy-hydroxide (NiOOH) [233,234]. At higher binding energies several shake-up satellites from multi-electron excitations appear [206]. The overall spectral features of the sNiO are in good agreement with previous results [159].

A clear temperature dependency can be observed. Towards higher annealing temperatures the main features increase, while the shoulders decrease. The XPS observations, thereby, confirm the conclusion drawn from the FTIR analysis. The higher the temperature during the annealing process is, the more the precursor gets converted and the less hydroxide remains in the film. The XPS results further show that the film exhibits a higher amount of stoichiometric NiO for higher annealing temperatures and that the surface is probably completely hydroxylated.

4.3.3. Electronic and optical properties

In the previous section the chemical composition of the sNiO as a function of the film annealing temperature was investigated. The question arises, how the chemical composition affects the electronic properties of the sNiO. To answer this question the work function, the total resistance and the UV-vis absorption of sNiO thin films were examined.

Figure 4.10 shows the absorbance of a 25 nm sNiO film deposited on ITO. The absorbance of a bare ITO substrate was subtracted as a reference. From the absorption onset a bandgap of 3.1 eV was estimated. The transmission of visible light is above 90%, which is one of the desired requirements for a good hole contact layer.

Figure 4.11 shows the work functions (WFs) of the sNiO films averaged for several samples over the film annealing temperature. Two techniques were used: (1) WFs measured with Kelvin probe (KP) (circles) were obtained with a macroscopic Kelvin oscillator (see Section 3.1.2) in ambient atmosphere (humidity ≈ 44%). (2) The XPS data, extracted from the secondary electron cut-off, were measured in ultra-high vacuum at a base pressure of $1 \cdot 10^{-9}$ mbar. A WF of $\Phi_{\mathrm{KP}} = (4.78 \pm 0.06)$ eV and $\Phi_{\mathrm{XPS}} = (4.81 \pm 0.19)$ eV was found at 325 ℃. Both values obtained from different measurement techniques agree within their error range. At 400 ℃ the work function is significantly lower, $\Phi_{\mathrm{KP}} = (4.38 \pm 0.04)$ eV and $\Phi_{\mathrm{XPS}} = (4.4 \pm 0.05)$ eV, but both in good agreement. The WFs values for 275 ℃ show a slight deviation. There is often an inhomogeneity of the temperature on hotplates, which makes it difficult to control the exact temperature during film formation. Furthermore, the adsorbtion of water and hydrocarbons in ambient atmosphere can lead to shielding of the true work function. Therefore, the XPS work functions obtained in vacuum can be seen as more accurate. However, the given trend allows to state that the higher the annealing temperature is, and the higher the content of stoichiometric NiO in the film becomes, the smaller the work function will be.

Figure 4.12 shows the total resistance of the sNiO in dependence of the temperature measured in a two-terminal configuration on a glass substrate. Gold electrodes were evaporated onto the sNiO films through a shadow mask (channel length ≈ 70 µm). The work function of the gold should align well to the work function of the sNiO, especially at lower temperatures. Data points were obtained again for 275 ℃, 325 ℃ and 400 ℃ film annealing temperatures.

It can be seen that the total resistance for 325 ℃ and 400 ℃ is extremely high ($R > 100\,\mathrm{M\Omega}$). These values were even above the compliance limit of the four-point probe measurement setup, which has also been recently claimed in literature [235]. The decrease in the total resistance by about one order

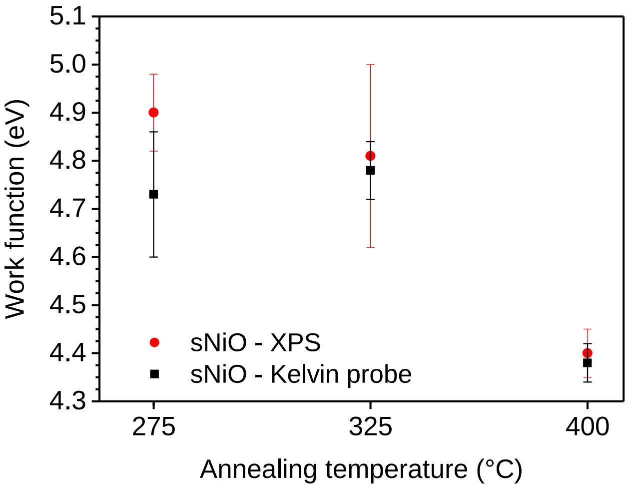

Figure 4.11: Work functions of the sNiO films annealed at 275 °C, 325 °C and 400 °C. Data were obtained by ambient Kelvin probe (square) and by XPS (circle). The work functions measured by with XPS were extracted from the secondary electron cut-off. While the Kelvin probe measurements were performed in ambient air, the XPS was operated at a base pressure of $1 \cdot 10^{-9}$ mbar.

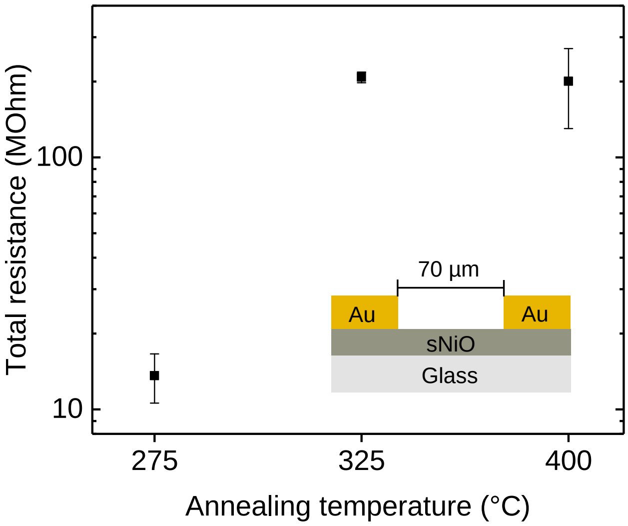

Figure 4.12: Total resistance of sNiO films on glass substrates annealed at 275 °C, 325 °C and 400 °C. Data were obtained by two-terminal I-V measurements. The channel length between the two gold electrodes was 70 µm and the bias 5 V.

of magnitude for 275 °C and thereby, lower film annealing temperatures in general, might be correlated to the higher hydroxide and, especially β-NiOOH content. This suggests that hydroxides might contribute to the conductivity in sNiO thin films, and not stoichiometric NiO.

4.3.4. Functionalization with self-assembled monolayers of phosphonic acids

From the view of interface engineering, it is very desirable to achieve full control over the electronic and chemical properties of the sNiO surface and transition metal oxides in general. A common approach to increase the work function of oxides are UV-ozone or oxygen plasma treatments [84,236]. However, their adjustment range is limited. Dipolar self-assembled monolayers (SAMs) are more versatile, as with SAMs not only the work function but also the surface energy can be tuned by tailoring the molecular backbone and its functional group [237]. SAMs have been successfully grown not only on metals [79,238] but, more recently, also on metal oxides [80,170].

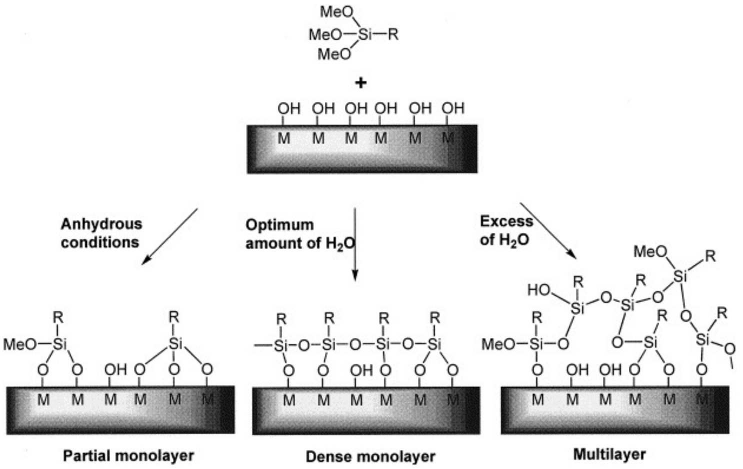

Figure 4.13.: Reaction scheme for the formation of silanes on hydroxylated surfaces. Reprinted from [239]

The IR and XPS chemical analysis revealed that the sNiO consists of a mixture of stoichiometric NiO and different hydroxide species, and that the surface is completely hydroxylated (see Section 4.3.2). Several molecular binding partners have been proposed for hydroxylated oxide surfaces over the last years [78]. Among them are, silanes, amines, catechols, carboxylates, alkynes and alkenes, and phosphonic acids [78]. Silanes are often used to

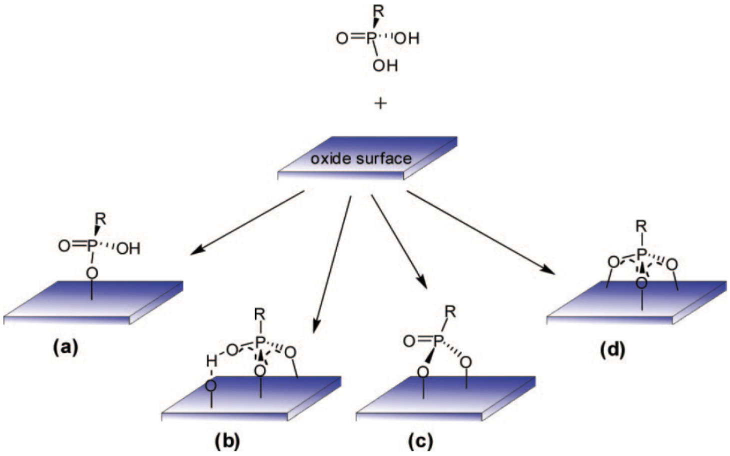

Figure 4.14.: Schematic illustration of possible binding configurations of phophonic acids on hydroxylated surfaces. These are a) monodentate, b) and c) bidentate and d) tridentate binding configuration. Reprinted from [241].

passivate trap states of SiO_2 surfaces in OFETs [240]. However, they can polycondensate by formation of oligomers in solution or on the surface. Excess water is a critical parameter in the silane formation process (see Figure 4.13) and often silane coatings result in multi- instead of monolayers [239].

Throughout the progress of the present work, also alkenes in form of styrenes, thiols and carboxylates were tested to form a SAM on sNiO. However, the best results were found for phosphonic acids (PAs) as a SAM precursor. Phosphonic acids are known to chemisorb and form highly dense monolayers on hydroxylated oxide surfaces via a strong covalent phosphonate bonding [81–86]. The phosphonate anchor can lead to different binding configurations depending on the number of PA oxygen atoms involved in the coupling process [84,237,241]. Figure 4.14 shows the typical PA binding modes observed on metal oxides. In a) only one oxygen atom interacts with the metal oxide surface leading to a monodentate configuration. b) and c) are a mixture of electrostatic and bidentate binding modes, while d) represents the tridentate binding mode in which every PA oxygen is interacting with the hydroxylated surface. Note, that the tridentate mode is the most oriented configuration with respect to the surface normal. On ITO predominantly a mixture of c) and d) was found [242].

While there are reports on SAM formation with PAs on nickel foil [243], pulsed laser deposited Ni:CoO [244], and e-beam evaporated NiO [245], the author is aware of only one short and not fully comprehensive report of SAM growth on solution-processed NiO [246]. As a SAM precursor of main interest, the commercially available 4-cyanophenyl-phosphonic acid (CYNOPPA) was chosen, as it has a strong permanent dipole moment to increase the work function [160]. Its π-conjugated backbone should facilitate efficient charge transport [247] and its cyano group (C≡N) should improve the surface energy (wettability) of the sNiO for printing applications. The molecular structure can be found in Figure A.1.

Density functional theory calculations: NiO(111)/CYNOPPA

To predict and confirm possible binding configurations of CYNOPPA on sNiO, density functional theory calculations on a completely hydroxylated NiO(111) surface were performed by Shuangying Ma and Wenlan Liu from the Institute of Theoretical Chemistry, University of Stuttgart. Figure 4.15 shows side and top views of the NiO unit cell used and the CYNOPPA molecule. The major reaction mechanism between the phosphonic acid and the hydroxylated surface is a dehydration process, in which water leaves the surface after deprotonation of the PA anchor group and dehydroxylation of surface hydroxide groups ($-$OH). Comparing the theoretical adsorption energies shows that adsorption modes with more than one water molecule involved in the dehydration process are energetically unfavorable. This is underlined by molecular dynamics simulations, which demonstrate that only mono- and bidentate binding modes are stable within ethanol. A purely-hydrogen bonded mode will not be stable during the SAM annealing step, which is introduced to activate the phosphonate binding. The most probable adsorption mode is the monodentate configuration between the dehydrated CYNOPPA and the NiO(111) surface. The tridentate bonding is energetically not accessible.

Infrared spectroscopy on sNiO/CYNOPPA

Experimentally, the growth mechanism of CYNOPPA on the sNiO surface was investigated by a complementary set of infrared and photoelectron spectroscopy measurements. CYNOPPA was applied to the surface of the sNiO as suggested by Koh *et al.* [160]. sNiO films of $\sim 25\,\mathrm{nm}$ thickness were spin coated and subsequently annealed in ambient air at 325 °C and 400 °C, respectively.

Figure 4.16 shows the MIR relative transmission spectra of CYNOPPA functionalized sNiO films, which were previously annealed at the two given temperatures. The spectra show the relative changes of the vibrational modes between the exact same substrate before and after the treatment. Measurements were performed under normal angle of incidence (AOI = 10°). Several absorption bands arise in the spectra on both sNiO layers. Modes marked with

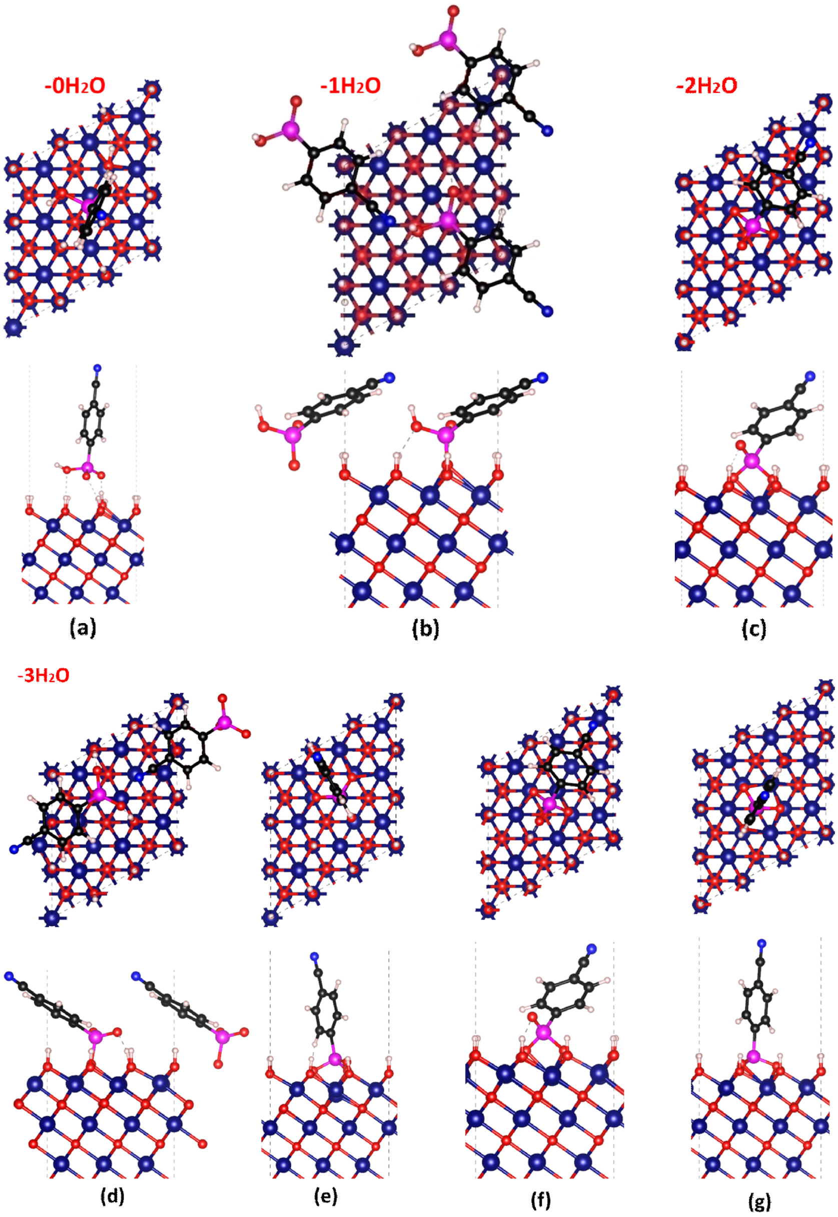

Figure 4.15.: Simulated adsorption configurations of CYNOPPA on a fully hydroxylated NiO(111) surface, where (a) is the case without a dehydration reaction (adsorption energy of $E_a = -1.109\,\mathrm{eV}$). (b) is the case with dehydration of a single water molecule ($E_b = -0.949\,\mathrm{eV}$), (c) with dehydration involving two water molecules ($E_c = -0.097\,\mathrm{eV}$), and (d)-(g) a reaction with dehydration involving three water molecules ($E_d = +1.021\,\mathrm{eV}; E_e = +0.673\,\mathrm{eV}; E_f = +0.809\,\mathrm{eV}; E_g = +0.570\,\mathrm{eV}$). (g) is referred to the tridentate binding configuration.

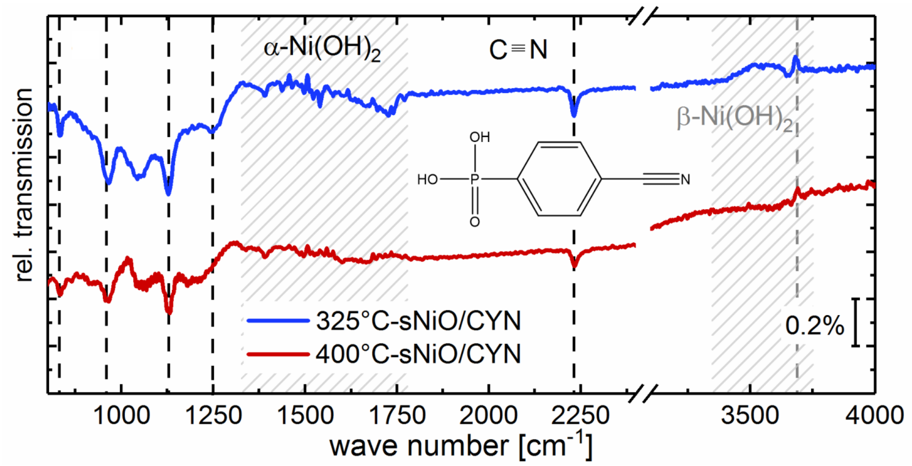

Figure 4.16.: MIR relative transmission spectra of the CYNOPPA functionalized sNiO thin films, which were previously annealed at 325 °C (blue) and 400 °C (red). Characteristic vibrational modes of CYNOPPA are depicted with dashed black lines. At 833 cm^{-1}, 966 cm^{-1}, and 1250 cm^{-1} absorption bands of the phosphonate and at 1130 cm^{-1} the stretching vibration of the phenyl ring can be observed. The absorption mode of the cyano stretching vibration is located at 2231 cm^{-1}. The reduction of β-Ni(OH)$_2$ by the CYNOPPA treatment is highlighted with a light grey dashed line. Characteristic modes of α-Ni(OH)$_2$ are marked with grey stripes.

black dashed lines were assigned to vibrational modes of the molecule with the help of density functional theory calculations. The stretching vibration of the phenyl ring can be addressed to the vibrational mode at 1130 cm^{-1}. Another characteristic mode can be observed at 2231 cm^{-1}, which is attributed to the stretching vibration of the (C≡N) group. The weaker vibrational modes at 833 cm^{-1}, 966 cm^{-1}, and 1250 cm^{-1} belong to absorption bands of the phosphonate. The existence of all these characteristic peaks is a clear evidence that CYNOPPA is adsorbed on the surface.

Positive absorption bands are observed between 1280 cm^{-1}-1700 cm^{-1} and 3500 cm^{-1} $-$3700 cm^{-1}. These features are assigned to changes of hydroxides of the sNiO layer, as discussed in Section 4.3.2 [221,248]. With this, the pronounced peak at 3670 cm^{-1} can be addressed to a reduction of β-Ni(OH)$_2$ and the broader mode around 3500 cm^{-1} to a change in α-Ni(OH)$_2$. The weak vibrational mode of the phosphonate, in particular the broadened P=O mode, and the reduction of Ni(OH)$_2$ indicate a chemisorption of CYNOPPA on the sNiO. Furthermore, the overall intensity of the characteristic modes of the molecule, ($< 0.4\%$), is in good agreement with the thickness of a monolayer.

If there is no change in orientation between both samples, the (C≡N) stretching vibration can be related to the amount of molecules. It was proven in a separate experiment that the peak heights do not vary under different AOI. Hence, a smaller amount of CYNOPPA is present on sNiO with higher film annealing temperatures and less Ni(OH)$_2$ [225,249]. Both observations lead to the conclusion that the PA binds predominantly to the Ni(OH)$_2$ on the sNiO surface.

X-ray photoelectron spectroscopy on sNiO/CYNOPPA

To determine the stoichiometry of the chemisorbed molecules and the layer thickness of CYNOPPA on sNiO, X-ray photoelectron spectroscopy measurements were performed. In Figure 4.17 a) shows the Ni 2p$_{3/2}$ core level spectra for sNiO films annealed at 325 °C and 400 °C after CYNOPPA modification. The spectra were normalized to the intensity of the main peak to allow a clear comparison of the spectral shape. As shown in Section 4.3.2, the overall spectral features of the sNiO are in good agreement with previous observations. Small but significant changes of the peak shapes after CYNOPPA functionalization can be seen. The changes are weaker for sNiO annealed at 400 °C. This finding agrees with the IR measurements revealing a smaller amount of CYNOPPA at higher annealing temperatures. To validate that the peak changes are not only caused by the exposure to ethanol, the sNiO substrates were immersed into anhydrous ethanol without PA, but same process parameters, and characterized

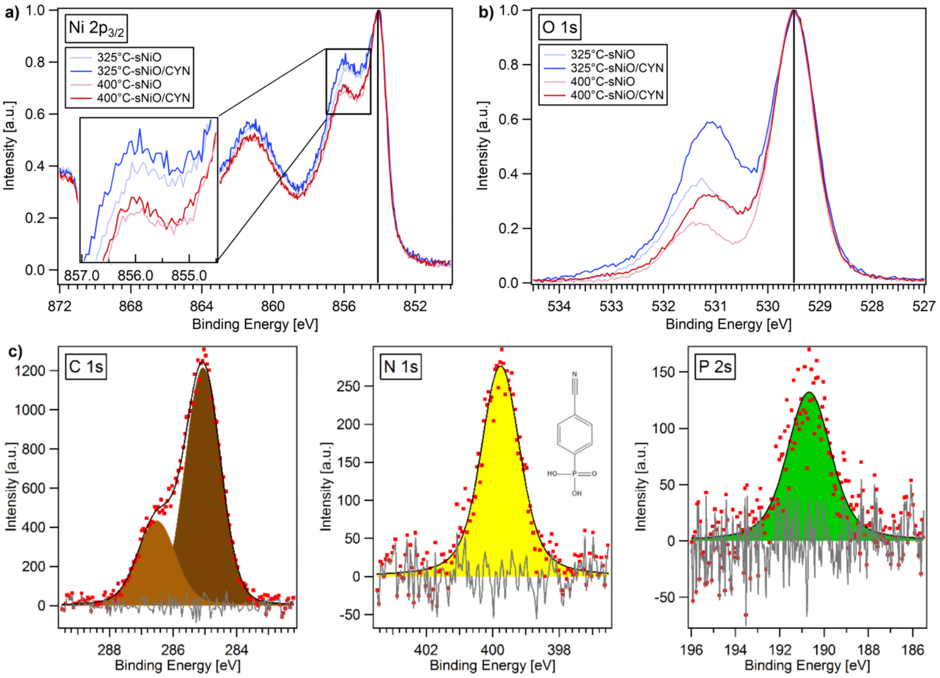

Figure 4.17.: Background corrected and normalized a) Ni $2p_{3/2}$ and b) O 1s core level spectra for 325 °C (blue) and 400 °C (red) annealed sNiO films with and without CYNOPPA treatment. Spectra were shifted in binding energy to the maximum of the 325 °C sample. In both spectra, the intensity of the peak shoulder is altered after PA adsorption, highlighted in the zoomed inset of a). c) The spectral components P 2s, C 1s and N 1s are fitted with Voigt functions, exemplary for a substrate annealed at 325 °C. The C 1s signal exhibits two different species, and N 1s and P 2s only one.

afterwards. No variation in the peak shapes were observed, which evidences that the peak changes are indeed due to chemisorption of CYNOPPA on sNiO. Similar variations of the peak shape can be observed in the according O 1s core levels in Figure 4.17 b). However, an unambiguous interpretation of substrate changes from the O 1s spectra is not possible, as the signals of the different PA oxygen atoms overlap with the side-peak of the sNiO spectra.

Figure 4.17 c) shows the C 1s, N 1s, and P 2s detail core level spectra, exemplarily for a 325 °C sample. The P 2s and N 1s core level have distinct features at a binding energy of 191 eV and 400 eV, respectively. This indicates that none of the two species underwent any chemical reaction or decomposition. The C 1s spectrum is split into two signals: a major component at 285 eV corresponding to aromatic carbon with hydrogen termination [170] and a minor component at 286.6 eV from contributions of the C≡N group [250]. Furthermore, there is also a contribution of the carbon connected to the phosphonic anchor [251]. Through the integration of the spectral areas by Voigt fits and division by the respective atomic sensitivity factors, a carbon ratio of 1:2.6 can be found, which agrees well with the ratio of molecular carbon atoms of 1:2.5. An overall molecular stoichiometry of 8.4 carbon to 1 nitrogen to 1.2 phopshor was calculated. As a reference the intensity of the N 1s core level was chosen. This finding adopts the molecular structure of CYNOPPA (7:1:1) well. According to the Lambert-Beer law, $d = -\lambda \ln \frac{I_d}{I_0}$, the nominal layer thickness of CYNOPPA can be determined by measuring the intensity of the background-corrected Ni $2p_{3/2}$ spectrum before (I_0) and after (I_d) PA treatment. The inelastic mean free path λ (1.84 nm) of electrons contributing to the Ni $2p_{3/2}$ signal was calculated according to the equation of Tanuma, Powell and Penn [252]. This yields nominal layer thicknesses for CYNOPPA of around 0.75 nm (325 °C) and 0.50 nm (400 °C), respectively. These qualitative values are close to the molecular length of a single CYNOPPA molecule (0.81 nm). Their variation might result from the lower coverage of molecules at 400 °C.

As already explained at the beginning of this chapter (see Chapter 4.1), the work function and energy levels at the sNiO surface will play an important role for the functionality as hole-contact layer. Therefore, WFs and the valance band maxima were measured as a function of the sNiO film annealing temperature and the surface treatment. Table 4.1 shows the work functions measured with XPS by the secondary electron cut-off edge and the valence band maxima by the valence band onset relative to the Fermi level (E_F). The values for the as-deposited sNiO were taken from Figure 4.11 and already discussed in Section 4.3.3. CYNOPPA, denoted as sNiO/CYN successfully increases the WF of the sNiO (325 °C) from (4.81 ± 0.19) eV to (5.21 ± 0.12) eV. While it can be confirmed that an oxygen plasma (OP) treatment leads to a strong increase in WF [220,253], it does not matter in terms of absolute WF values, if an OP step is applied prior the CYNOPPA functionalization. However, it appears that the final WF value is almost independent of the initial WF. DFT calculations further strengthen the hypothesis that the change in WF is not mainly attributed to the net dipole moment of the CYNOPPA molecule, but rather to a charge transfer between the surface hydroxides and the phopshonate group. It might also be that E_F becomes pinned to surface states that arise in the band gap of the sNiO due to the chemical bonding.

The large VBM of 0.86 eV, which means the distance between the Fermi level E_F and the valence band onset, of the as-deposited sNiO films show that the material is only weakly *p*-type. Such a low doping level could explain the very high total resistances measured in Section 4.3.3. The oxygen plasma treatment leads to a decrease of the VBM, which might go along with an increased charge carrier density at the sNiO surface through the oxidation process and conversion of β-$Ni(OH)_2$ into β-NiOOH as discussed in Section 4.3.2.

Conclusion on sNiO/CYNOPPA

In conclusion, the combination of IR, DFT and XPS results allows to state that the chemisorbed CYNOPPA layer is a SAM, with a chemical bonding of the phosphonate, mostly to the $Ni(OH)_2$. Furthermore, a superposition of mono- and bidentate binding configurations was found and the net-orientation of the SAM molecules to the surface normal is influenced by the energetically favorable binding modes. Also the grainy microstructure of the sNiO surface might play an important role here. Nevertheless, the CYNOPPA SAM successfully increases the sNiO work function to 5.1-5.2 eV and tunes the water contact angle from $(21 \pm 2)^\circ$ to $(42 \pm 3)^\circ$ (see Figure 4.18), which is consistent with a

Table 4.1.: Work functions (WF) and valence band maxima (VBM) measured after the functionalization of the sNiO surface with CYNOPPA, denoted as sNiO/CYN. For comparison, values were also obtained for two temperatures 325 °C and 400 °C, as well as for an oxygen plasma (OP) treated sNiO surface and an OP pre-treated CYN functionalized sNiO surface. WFs were obtained from the secondary electron cut-off edge and the VBM from the valence band onset relative to the Fermi level position.

	T [°C]	WF [eV]	VBM [eV]
sNiO	325	4.81 ± 0.19	0.86
	400	4.40 ± 0.05	0.97
sNiO/CYN	325	5.21 ± 0.12	0.94
	400	5.09 ± 0.18	1.00
sNiO/OP	325	5.55 ± 0.08	0.68
	400	5.63 ± 0.13	0.75
sNiO/OP/CYN	325	5.20 ± 0.11	0.92
	400	5.18 ± 0.11	0.88

previously reported value for CYNOPPA on ITO [160].

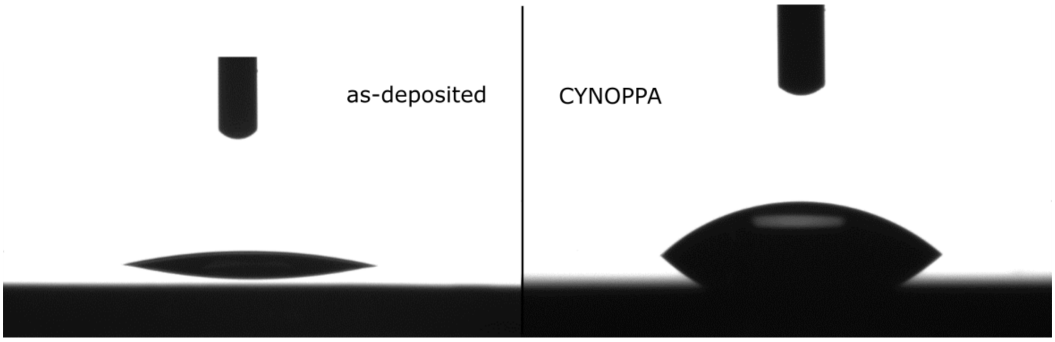

Figure 4.18.: Water contact angle measurements with a droplet dispensed on (left) as-deposited and (right) CYNOPPA modified sNiO films annealed at 325 °C. The contact angle was tuned from $(21 \pm 2)^\circ$ to $(42 \pm 3)^\circ$ due to the CYNOPPA SAM formation.

4.4. Incorporation of sNiO into small molecule F_4ZnPc:C_{60} solar cells

In this section the solution-processed nickel oxide is investigated as a hole contact layer in both, flat- (FHJ) and bulk-heterojunction (BHJ) small molecule F_4ZnPc:C_{60} organic solar cells. The influence of the previously studied chemical composition and electronic properties on the device performance are discussed. Every subsection will show J-V characteristics of one representative device of many as a function of the parameter of interest in a four quadrant figure. The left column of the figure will show the J-V curves obtained under illumination and the right the data obtained in the dark. Additionally, each subsection will contain a table summarizing the average device performance parameters of the completely characterized solar cell batch.

4.4.1. Importance of charge selectivity: ITO versus ITO/sNiO

To demonstrate the importance of a charge selective contact layer for the functionality of an organic solar cell, bulk-heterojunction (BHJ) F_4ZnPc:C_{60} devices with and without sNiO were fabricated on $2.54 \times 2.54\,\text{cm}^2$ pre-structured ITO glass substrates. The sNiO was prepared at a film annealing temperature of 325 °C.

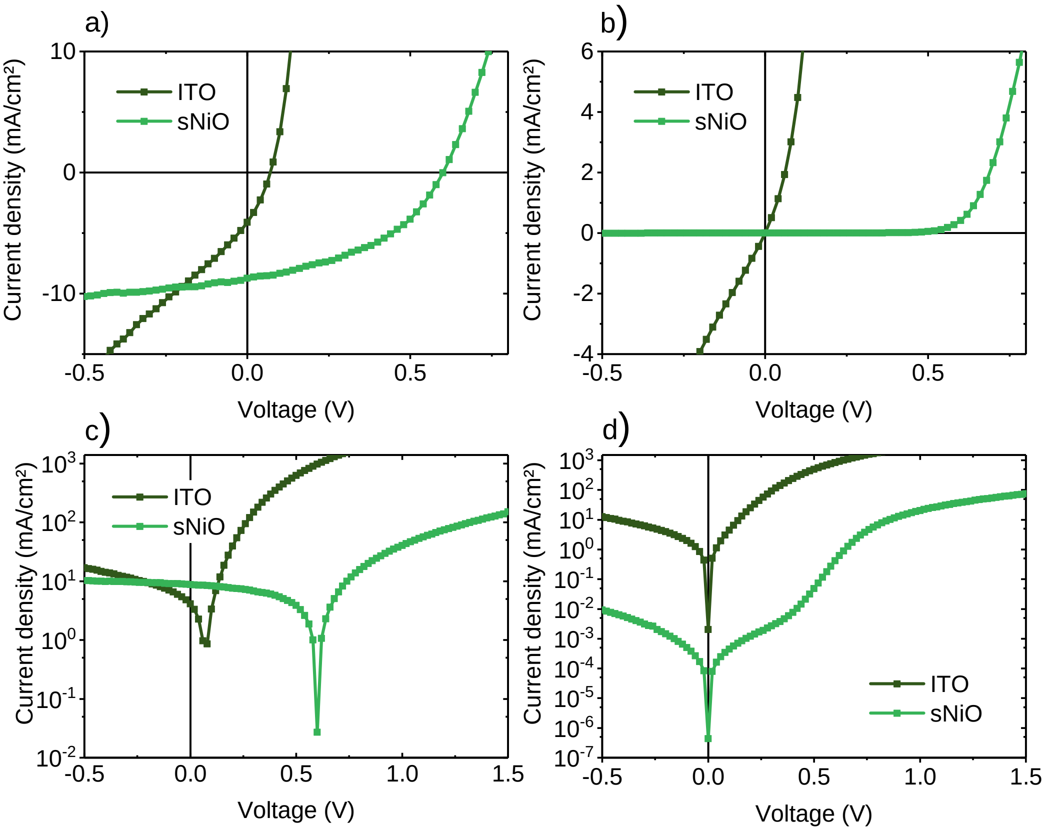

Figure 4.19.: J-V characteristics of F_4ZnPc:C_{60} BHJ solar cells with and without a 20 nm thin sNiO film as hole contact layer. The left column shows the cell under illumination, the right the corresponding dark currents. Both were plotted in linear a) and b), as well as in semi-logarithmic scale c) and d).

Table 4.2.: Averaged device performance parameters of $F_4ZnPc:C_{60}$ BHJ solar cells with and without 20 nm sNiO as hole contact layer (16 cells). Work functions (Φ) of the respective anode materials have been added, as the increase in work function by the sNiO also improved V_{oc}.

BHJ	Φ [eV]	J_{sc} [$mA\,cm^{-2}$]	V_{oc} [V]	R_s [$\Omega\,cm^{-2}$]	FF [%]	PCE [%]
ITO	4.64 eV	4.0 ± 0.6	0.07 ± 0.03	10 ± 2	31 ± 8	0.10 ± 0.07
ITO/sNiO	4.81 eV	8.5 ± 0.3	0.59 ± 0.01	16 ± 7	45.8 ± 3.4	2.29 ± 0.19

Figure 4.19 shows the corresponding J-V characteristics in linear and semi-logarithmic scale. The according averaged device performance parameter are given in Table 4.2. Short circuit current (J_{sc}) and open-circuit voltage (V_{oc}) are significantly increased due to the incorporation of the 20 nm sNiO interlayer. As a consequence the fill factor (FF) rises and the overall power conversion efficiency (PCE) improves from 0.1% to 2.3%. The slightly increased series resistance (R_s) might be due to the higher sheet resistance of the as-deposited sNiO film (see Section 4.3.3) compared to the ITO ($< 90\,\Omega\,sq^{-1}$). The shunt resistance (R_{sh}), best seen in the logarithmic plot of the dark J-V, is notably higher with the sNiO hole contact layer. Furthermore, the current in the reverse bias regime ($V < 0\,V$) clearly starts to saturate. Both observations evidence a strong reduction of photogenerated charge carrier leakage and exciton recombination towards the ITO. In other words, sNiO efficiently hinders electrons from passing to the anode, underlining the importance of a charge selective hole contact layer for high V_{oc} and balanced current flow [159].

4.4.2. Influence of the film annealing temperature

As it was shown in Section 4.3.2 and Section 4.3.3, the conversion of the nickel acetate precursor to an oxidized sNiO film is a temperature driven process and the physical properties strongly depend on the film annealing temperature [254]. The question arises how the chemical composition and electronic properties of the as-deposited sNiO hole contact layer influence the organic solar cell device performance. Manders *et al.* reported that at temperatures below 275 ℃ the precursor is not fully converted, such that the resulting films are not conductive enough for proper hole transport [159]. However, there are works claiming the opposite [204].

Film annealing temperatures of 200 ℃, 275 ℃, 325 ℃, and 350 ℃ were

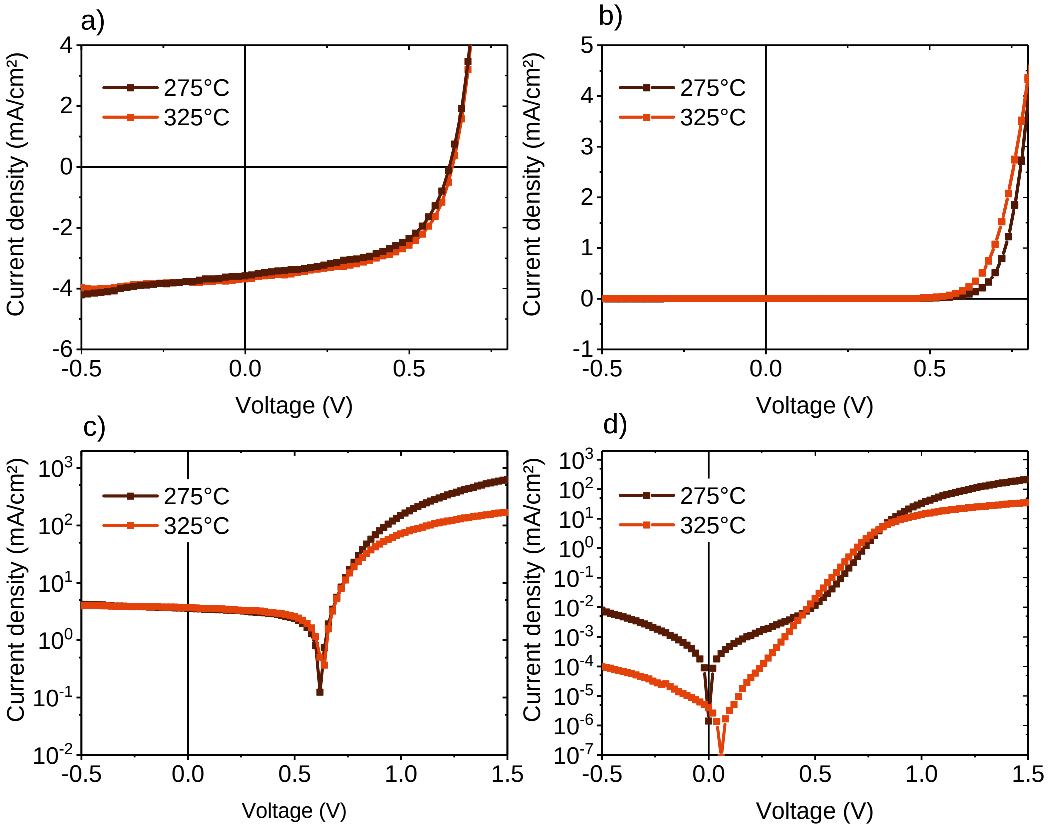

Figure 4.20.: J-V characteristics of F_4ZnPc:C_{60} FHJ solar cells with sNiO hole contact layers after different sNiO film annealing temperatures (275 °C and 325 °C). The left column shows the cell under illumination, the right the according dark currents. Both were plotted in linear a) and b), as well as in semi-logarithmic scale c) and d).

investigated throughout this work. Note, that higher temperatures would reduce the ITO conductivity and thereby, the overall device performance. Several experiments showed that devices with 200 °C sNiO are not working properly and that 350 °C sNiO provided no improvement over 325 °C.

Therefore, a closer look was taken at 275 °C and 325 °C sNiO film annealing temperature. The corresponding J-V characteristics are plotted in Figure 4.20 and Table 4.3. The 325 °C cells exhibit a 7% higher PCE compared to the 275 °C one. This can mainly be attributed to the small improvements in J_{sc} and FF. It has to be mentioned that the shunt resistance (R_{sh}) can either be extracted from J-V data obtained under illumination or from the dark curves and that these values can differ significantly due to contribution of the photocurrent in first case [220]. Here, R_{sh} differs between $(11.3 \pm 5.7) \cdot 10^4\,\Omega\,\mathrm{cm}^{-2}$ for 275 °C and $(34.5 \pm 15.8) \cdot 10^6\,\Omega\,\mathrm{cm}^{-2}$ for 325 °C. Thus, the major contribution to the small increase in J_{sc} and FF can be addressed to the difference of two orders of magnitude in the shunt. Even though, the series resistance values R_{s} are very comparable within the errors. Figure 4.20 shows that there are distinct devices, in which the sNiO 275 °C exhibits a lower series resistance and a higher current at high forward bias. This might be correlated to the lower total resistance of the lower temperature sNiO film with a larger amount of the more conductive NiOOH phase (see Section 4.3.3 and Section 4.3.2) [221].

4.4.3. Surface treatment with oxygen plasma

Oxygen plasma (OP or O_2-plasma) is often used as a cleaning process in industry. It has the ability to remove residual carbon from substrate surfaces and improve their wettability to polar solvents by increasing the surface energy through hydroxylation [255]. Furthermore, it can change the work function of metal oxides by adding a surface dipole and improve hole injection and extraction in opto-electronic devices [211,236,256]. The beneficial impact of O_2-plasma on pulsed laser deposited NiO hole contact layers was first investigated by Berry *et al.* in 2010 [257]. To study the influence of O_2-plasma on solution-processed NiO in this work, the as-deposited sNiO films were exposed to OP for 1 min at 900 W in a plasma oven. As it is known that the plasma effect can be time-dependent in ambient air [83], the substrates were immediately transferred into vacuum for evaporation of the solar cell stack.

A comparison between BHJ cells incorporating untreated and O_2-plasma treated sNiO hole contact layers are shown in Figure 4.21 and Table 4.4. As a consequence of the treatment the PCE improves by 18%, from $(2.29 \pm 0.19)\%$ to $(2.71 \pm 0.12)\%$. All device performance parameters are slightly increased

Table 4.3.: Averaged device performance parameters of $F_4ZnPc:C_{60}$ FHJ solar cells with sNiO hole contact layers (10 cells). sNiO films were annealed at 275 °C and 325 °C, respectively. Work functions (Φ) have been taken from Section 4.3.3 and are very similar for both temperatures.

FHJ	Φ [eV]	J_{sc} [mA cm^{-2}]	V_{oc} [V]	R_{s} [Ω cm^{-2}]	FF [%]	PCE [%]
sNiO 275 °C	4.90	3.60 ± 0.07	0.63 ± 0.01	21 ± 6	54.2 ± 1.9	1.22 ± 0.05
sNiO 325 °C	4.81	3.73 ± 0.05	0.63 ± 0.01	20 ± 2	55.8 ± 1.0	1.31 ± 0.02

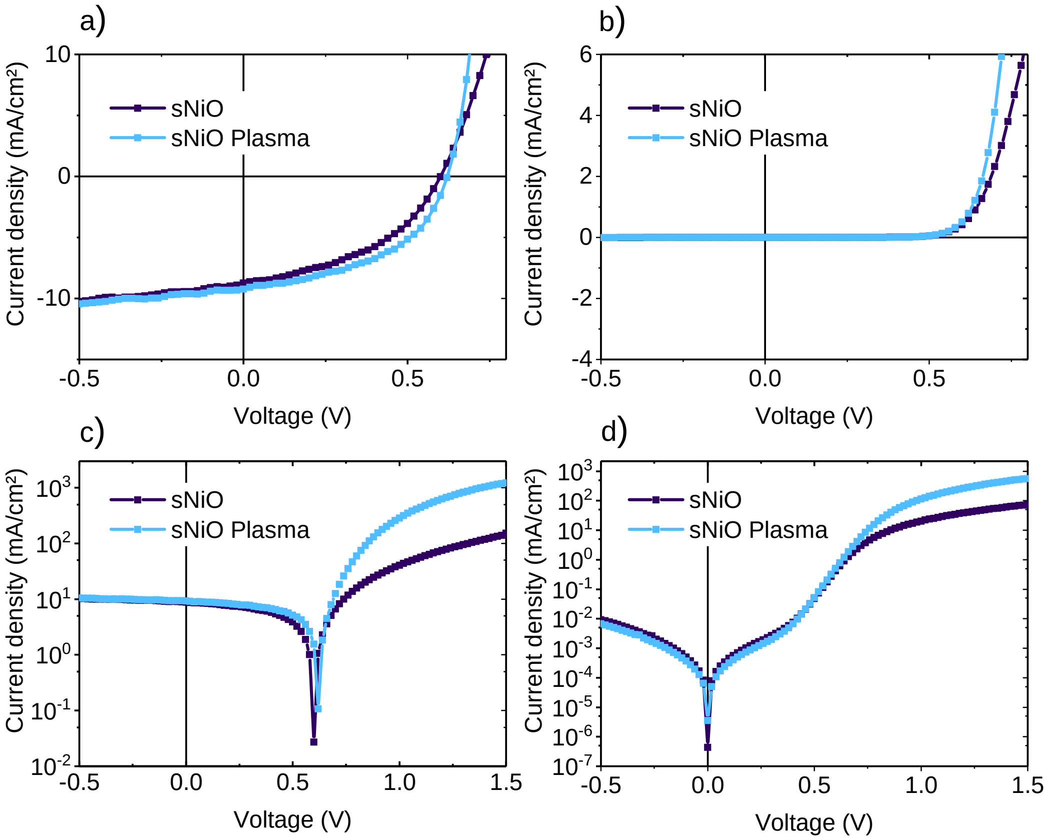

Figure 4.21.: J-V characteristics of F_4ZnPc:C_{60} FHJ solar cells with sNiO hole contact layers with and without O_2-plasma treatment. The left column shows the cell under illumination, the right the according dark currents. Both were plotted in linear a) and b), as well as in semi-logarithmic scale c) and d).

Table 4.4.: Averaged device performance parameters of $F_4ZnPc:C_{60}$ BHJ solar cells with sNiO hole contact layers (13 cells). sNiO films were either used untreated or O_2-plasma treated for 1 min. The treatment leads to a strong increase of the work function (Φ).

BHJ	Φ [eV]	J_{sc} [mA cm^{-2}]	V_{oc} [V]	R_s [Ω cm^{-2}]	FF [%]	PCE [%]
sNiO	4.81	8.5 ± 0.3	0.59 ± 0.01	16 ±7	45.8 ± 3.4	2.29 ± 0.19
sNiO/OP	5.55	8.8 ± 0.4	0.62 ± 0.01	12 ± 1	49.1 ± 0.8	2.71 ± 0.12

after the treatment. The open-circuit voltage is shifted towards (0.62 ± 0.01) V, the previously observed V_{oc} in Section 4.4.1 and Section 4.4.2, which might be attributed to an increase of the sNiO work function through the OP treatment.

Ratcliff *et al.* [220] reported on the importance of oxyhydroxy groups (NiOOH) for efficient charge transfer in P3HT:PC_{61}BM polymer BHJ solar cells with O_2-plasma treated NiO. The improvement of the device parameters was attributed to the addition of a surface dipole through the NiOOH further enhancing the electron blocking capability of the NiO. If this hypothesis holds without exception then FHJ cells should show less improvement after O_2-plasma, as fewer electrons should reach the sNiO/donor interface after exciton dissociation due to the architecture of the active layer. Table 4.5 sums up the performance parameters for equivalently built and post-treated $F_4ZnPc:C_{60}$ FHJ cells. As no significant difference in the shunt resistance (R_{sh}) was found for both architectures (see Figure 4.21 d)) and their comparison shows a clear trend towards a lowered series resistance (R_s), it can be stated that the improvement of the FF and, thereby, PCE, is directly correlated to R_s and not to less exciton or electron recombination at the hole contact layer. The improvement is mainly due to an increased conductivity and density

Table 4.5.: Averaged device performance parameters of $F_4ZnPc:C_{60}$ FHJ solar cells with sNiO hole contact layers (12 cells). Work functions are adapted from Table 4.4.

FHJ	Φ [eV]	J_{sc} [mA cm^{-2}]	V_{oc} [V]	R_s [Ω cm^{-2}]	FF [%]	PCE [%]
sNiO	4.81	4.1 ± 0.1	0.64 ± 0.01	37 ± 2	52.9 ± 0.8	1.37 ± 0.06
sNiO/OP	5.55	4.1 ± 0.1	0.64 ± 0.01	15 ± 2	60.8 ± 0.9	1.59 ± 0.09

of free charge carriers at the sNiO surface after the O_2-plasma treatment, which is supported by simulations of Wheeler and Berry *et al.* [253,257]. The increased conductivity and charge carrier density might be a consequence of the aforementioned β-NiOOH phase, whose amount correlates with the sNiO film annealing temperature (see Section 4.3.2) and is further increased through the oxidation process of the O_2-plasma. These findings go along with the decrease in the total resistance (see Section 4.3.3) and the series resistance reported here, and in in Section 4.4.2.

4.4.4. Increasing the work function with CYNOPPA

The idea to achieve full control over the physical properties of the sNiO surface and increase the sNiO work function not only by O_2-plasma (see Section 4.4.3) or by the NiO_x/MoO_3 bi-layer approach introduced by Schulz *et al.* [209], led to the concept of functionalizating the sNiO with dipolar CYNOPPA SAMs (see Section 4.3.4). In this section the CYNOPPA functionalized sNiO films, denoted as sNiO/CYN, are implemented as hole contact layers into $F_4ZnPc:C_{60}$ FHJ solar cells.

Figure 4.22 and Table 4.6 show the corresponding J-V characteristics and averaged device performance parameters, respectively. Work functions (Φ) were taken from Table 4.1. While Φ is increased similarly but slightly weaker compared to the O_2-plasma treament (compare Section 4.4.3), the WF increase due to CYNOPPA does not improve any of the device performance parameters. Instead a second photodiode behavior can be seen in the operating voltage regime of the J-V curve. Often, this behavior is called s-kink or s-shape and the author will stick to this terminology in the following. To ensure that such an effect is not only due to aging of the substrate over the two days of SAM procedure or solely caused by the exposure to ethanol, an additional device batch was built comparing cells with CYNOPPA treated sNiO layers to cells with sNiO layers that were immersed into anhydrous ethanol without PA, but same process parameters. This was in analogy to the ethanol XPS reference experiment in Section 4.3.2. This experiment showed that devices exposed to ethanol only were not distressed by an s-kink.

In view of the device performance parameters the integration of the sNiO/-CYN hole contact layers leads to a significant decrease of the PCE. This goes along with a significant decrease of the fill factor (FF) and increase in the series resistance (R_s). While the short-circuit (J_{sc}) current is slightly decreased, the open-circuit voltage V_{oc} is barely changed. The shunt resistance R_{sh} is even higher for devices with CYNOPPA. It is surprising that the V_{oc} remains unaffected in the context of the higher work functions observed both, for the

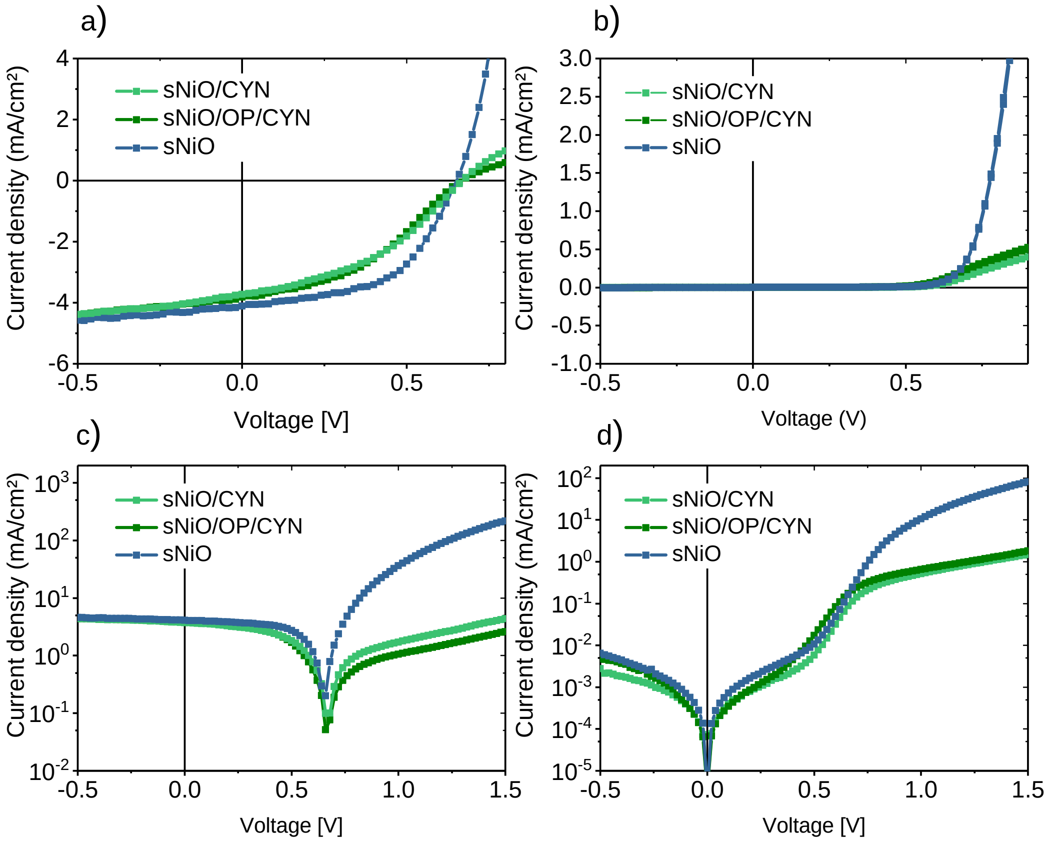

Figure 4.22.: J-V characteristics of F_4ZnPc:C_{60} FHJ solar cells with sNiO/-CYNOPPA hole contact layers. The left column shows the cell under illumination, the right the according dark currents. Both were plotted in linear a) and b), as well as in semi-logarithmic scale c) and d).

Table 4.6.: Averaged device performance parameters of F_4ZnPc:C_{60} FHJ solar cells with sNiO/CYN hole-contact layers (5-7 cells). Work functions were taken from Table 4.1.

	Φ [eV]	J_{sc} [$\mathrm{mA\,cm^{-2}}$]	V_{oc} [V]	R_{s} [$\Omega\,\mathrm{cm^{-2}}$]	FF [%]	PCE [%]
sNiO	4.81	4.1 ± 0.1	0.64 ± 0.01	37 ± 2	52.9 ± 0.8	1.37 ± 0.06
sNiO/CYN	5.21	3.7 ± 0.1	0.64 ± 0.02	118 ± 39	38.9 ± 5.1	0.95 ± 0.15
sNiO/OP/CYN	5.20	3.9 ± 0.2	0.65 ± 0.02	133 ± 56	40.3 ± 0.9	1.05 ± 0.16

O_2-plasma and for the CYNOPPA-treated sNiO surface. This means that the V_{oc} is not limited by the contacts and already dominated by the effective band gap of the donor-acceptor system [47,258]. Thus, an open-circuit voltage of 640 mV can be seen as a maximum here. It can be concluded that the sNiO/CYN modified hole-contact layer reduces the overall device efficiency as a consequence of a strong increase of the series resistance (R_{s}). This effect is completely independent of the work function.

4.4.5. Decreasing the work function with DiDi2PA

To verify that the V_{oc} is already at a maximum, but can be decreased by a non-ohmic contact with a large offset of the Fermi level to the donor, F_4ZnPc:C_{60} FHJ solar cells were built with a sNiO/SAM hole contact layer, whereas for the SAM precursor a molecule with a work function decreasing dipole moment was chosen. Despite the proof-of-concept, the molecule used here is a custom synthesized one. The synthesis was carried out by Simon Benneckendorf at the Organic-Chemical-Institute, Heidelberg. Its *IUPAC* name is 4'(dimethylamine)-[1,1'biphenyl]-4-phosphonic acid and its molecular structure can be found in Figure A.1. For convenience the name has been denoted as DiDi2PA.

Figure 4.23 shows the corresponding J-V characteristics with DiDi2PA and CYNOPPA modified sNiO in comparison to as-deposited sNiO as hole contact layer. The already observed s-kink observed for sNiO/CYN also appears with sNiO/DiDi2PA and the PCE, FF and J_{sc} are even further reduced compared to CYNOPPA. But, due to the use of DiDi2PA the V_{oc} is indeed shifted to lower values, which goes along with the decrease in the work function. Note, that this correlation is not linear with the absolute work function value. In terms of resistance, the cell with DiDi2PA exhibits a higher shunt and lower series resistance compared to CYNOPPA. Even though the device performance is drastically degraded by DiDi2PA it seems to conduct current better than CYNOPPA at high forward bias.

Together with the observations on the plasma and CYNOPPA treated sNiO in Section 4.4.3 and Section 4.4.4, one can state that the use of the dipolar SAMs do not lead to the desired or intended performance improvements in organic solar cells. The V_{oc} cannot be improved, as it is already saturating with the effective bandgap of the donor-acceptor system used here. That the dramatic increase in series resistance (R_{s}) is the major parameter causing the s-kink is hinting towards a very low conductive interface and the introduction of a transport barrier for charge carriers at the hole contact layer. The nature of this transport barrier will be investigated in the following sections.

Table 4.7.: Averaged device performance parameters of $F_4ZnPc:C_{60}$ BHJ solar cells with PA-SAM functionalized sNiO hole contact layers (5-15 cells). The table shows a comparison between two different SAM precursor, one molecule increasing the work function (CYNOPPA) and one molecule decreasing the work function (DiDi2PA).

BHJ	Φ [eV]	J_{sc} [$\mathrm{mA\,cm^{-2}}$]	V_{oc} [V]	R_{s} [$\Omega\,\mathrm{cm^{-2}}$]	FF [%]	PCE [%]
sNiO	4.81	9.3 ± 0.3	0.63 ± 0.01	9 ± 1	54.1 ± 1.2	3.17 ± 0.06
sNiO/CYN	5.21	5.0 ± 2.1	0.60 ± 0.01	214 ± 120	45.7 ± 3.4	0.83 ± 0.32
sNiO/DiDi2PA	3.68	3.8 ± 0.6	0.39 ± 0.03	99 ± 20	24.7 ± 0.5	0.36 ± 0.06

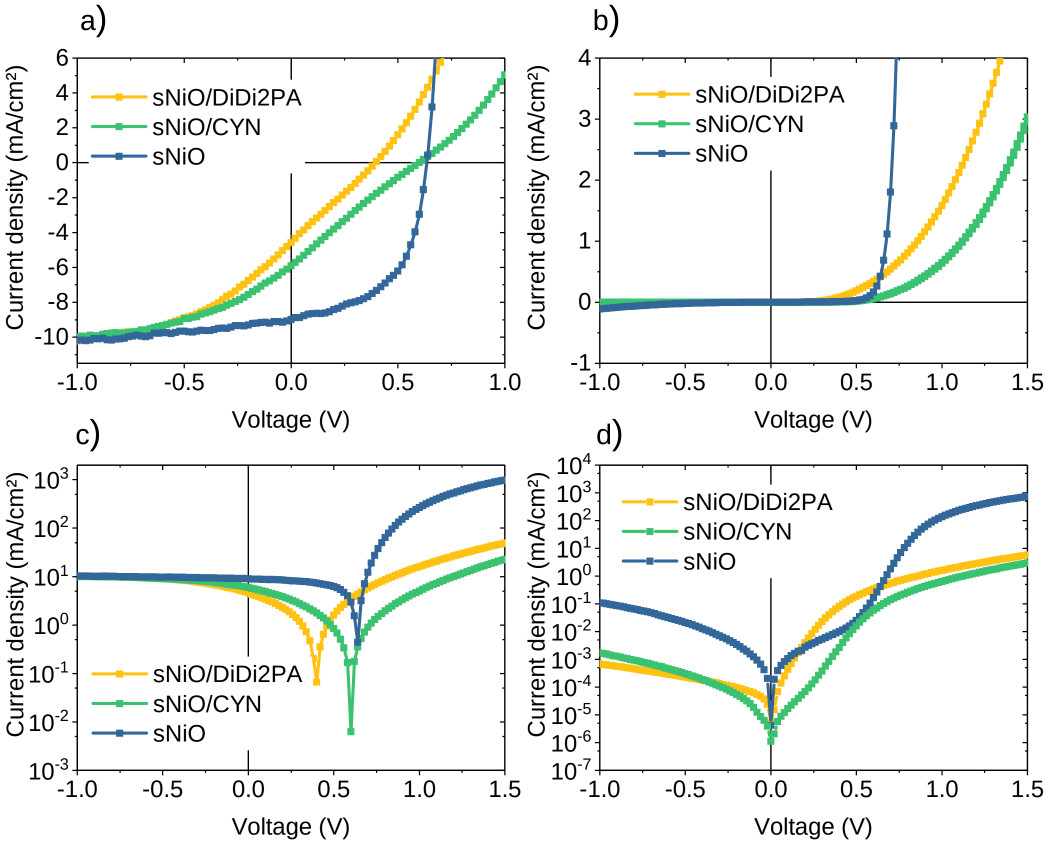

Figure 4.23.: J-V characteristics of $F_4ZnPc:C_{60}$ BHJ solar cells with PA-SAM functionalized sNiO hole contact layers. Two different SAM precursor are compared, one work function increasing (CYNOPPA) and one work function decreasing molecule (DiDi2PA). The left column shows the cell under illumination, the right the according dark currents. Both were plotted in linear a) and b), as well as in semi-logarithmic scale c) and d).

4.4.6. Determination of the barrier origin

The assumption that the device performance of organic solar cells with oxide charge extraction layers can solely be improved by matching the work function of the oxide interlayer with the energy levels of the active materials is very common [210].

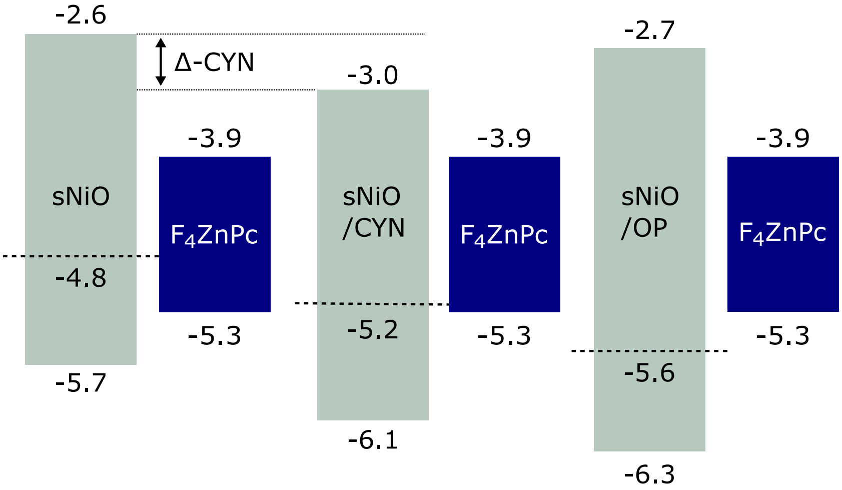

Figure 4.24.: Schematic illustration of the energy levels of the differently treated sNiO hole contact layers and the F_4ZnPc donor. From left to right are shown a) sNiO, b) sNiO/CYN, and c) sNiO/OP. Note, that the materials are aligned to a common vacuum level and the bandgaps are color filled. Electron affinities were calculated with a bandgap of 3.1 eV [259]. A widening of the NiO bandgap after OP treatment has been observed [220] reasoning a value of 3.6 eV. Fermi levels are depicted as dashed lines and the surface dipole introduced by the SAM has been denoted as Δ-CYN.

When all previous experimental results are condensed into a simple schematic illustration (see Figure 4.24), the question arises, why the O_2-plasma treated sNiO hole-contact is not leading to an s-kink but the CYNOPPA treated one is. Theoretically, the work function of the oxygen plasma treated sNiO is shifted so far that an energetic hole-extraction barrier of at least 0.3 eV is formed (compare to Figure 4.1). However, this is not reflected in the J-V curves shown in Section 4.4.3. Therefore, the origin of the transport barrier cannot only be of energetic nature in terms of energy level mismatch. Various approaches have been proposed to examine the cause for s-shaped J-V curves [57]. A few will be discussed in the following sections to probe the nature of the barrier.

4.4.6.1. Dependency on the illumination intensity

Tress *et al.* introduced a simple experimental test to distinguish between extraction and injection barriers at the electrodes of organic solar cells by varying the illumination intensity during the J-V measurement [67]. The idea behind this test is that in case of an extraction barrier charge carriers cannot leave the cell after exciton dissociation due to the low conductivity of a certain layer or due to an energetic barrier after energy level mismatch of the hole transport layer and the donor material. Both obstacles should be light dependent, as the more charge carriers are photogenerated, the more can pile-up in front of the extraction barrier. This should be reflected in a more pronounced s-kink at higher illumination intensities, which gradually disappears for lower intensities. Figure 4.25 shows this behavior in form of simulation data of normalized J-V characteristics for a) an extraction barrier and b) an injection barrier. Tress assumed an energetic barrier height of 0.3 eV for both barrier types in his simulations. Due to the dependency of the s-kink strength on the illumination intensity and through the normalization to a voltage point where the photocurrent saturates, the s-shaped J-V curves show points of intersection in case of an extraction barrier. Such intersections are not observed for an injection barrier, as this type of barrier does less depend on the amount of photogenerated carriers. There, the s-kink only disappears when the illumination intensity dependent V_{oc} becomes smaller than the built-in field. As long as V_{oc} is maintained by a sufficient amount of photogenerated carriers and larger than the built-in field, the s-kink does not change its shape (see Figure 4.25 b)).

Performing this test with the F_4ZnPc:C_{60} FHJ solar cells including an sNiO/CYN hole contact layer led to the J-V curves shown in Figure 4.25 c). The normalization was done at -0.2 V. The illumination intensity was varied between 1 to 0.001 sun by using gray filters in front of the solar source. It can clearly be seen that the shape and illumination intensity dependency mimics the character shown in a). For the as-deposited sNiO HTL a hole injection barrier of 0.5 eV and for the sNiO/OP HTL a hole extracion barrier of 0.3 eV is found, while the sNiO/CYN HTL seems to be well aligned to the ionization potential of the donor (see Figure 4.24). For these reasons it is concluded that the transport barrier is addressed to an extraction barrier, which is, however, not just a consequence of energetic level mismatch.

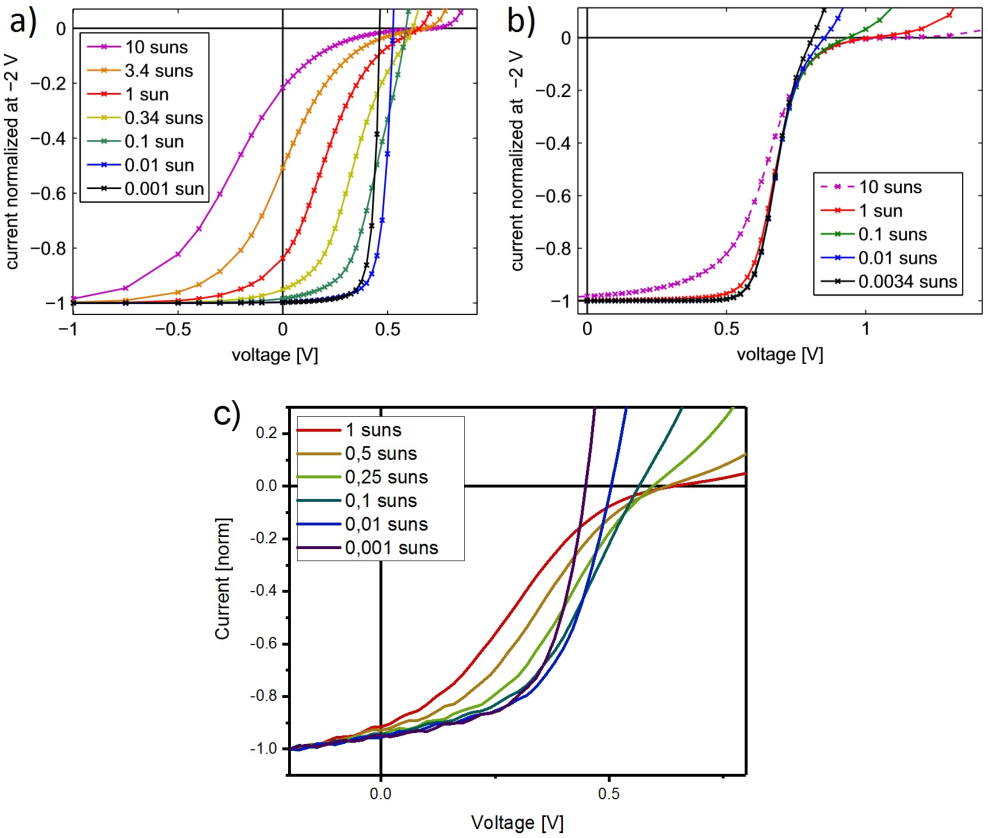

Figure 4.25.: Dependency of the s-kink on the illumination intensity. Simulation data of J-V characteristics normalized to the saturated reverse photocurrent for a) an extraction barrier and b) an injection barrier. Graph was reprinted from [258]. c) F_4ZnPc:C_{60} FHJ solar cells including an sNiO/CYN hole-contact layer. Normalization for the experimental data was done at $-0.2\,V$.

4.4.6.2. Influence of the HTL thickness

To further strengthen the hypothesis that the barrier is an extraction barrier, the s-kink can be examined for different hole transport layer thicknesses [260]. In case of an injection barrier, the strength of the s-kink should not be affected by the HTL thickness. However, in case of an extraction barrier, the electric field mainly drops over the barrier as the pile-up of charges can lead to a field-free space charge region in front of the barrier. On the one hand, the field maintaining charge generation in the active layer is lowered. On the other hand, an increased HTL thickness leads to a lower electric field in the HTL, which reduces the probability for charge carriers to cross the barrier. Hence, the s-kink gets more pronounced with increasing HTL layer thickness as shown in Figure 4.26 a).

For this experiment the sNiO HTL thickness was varied through the reduction of the precursor concentration in ethanol. Film thicknesses were then evaluated by ellipsometry measurements on reference substrates. Figure 4.26 b) shows the corresponding J-V characteristics for sNiO/CYN hole transport layers with thicknesses of 4 nm, 8 nm and 20 nm. Again, the previously seen s-kink can be observed, but the HTL layer thickness impacts the strength of the s-kink. This observation is in good agreement with the model proposed by Tress *et al.* for an extraction barrier. Therefore, the hypothesis that the s-kink observed here is a consequence of an extraction barrier is further proven.

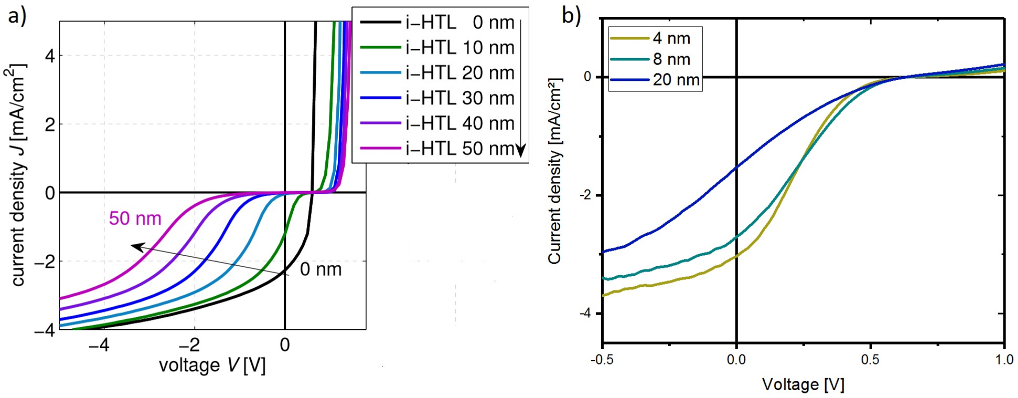

Figure 4.26.: Dependency of the s-kink on the HTL layer thickness. a) Simulated J-V characteristics for different hole transport layer thicknesses behind an extraction barrier. b) $F_4ZnPc{:}C_{60}$ FHJ solar cells including an sNiO/CYN hole contact layer, whereas the sNiO layer thickness was varied between 4 nm, 8 nm and 20 nm.

Table 4.8.: Resistances of sNiO:CuO layers with different CuAc contents.

CuAc content [wt.%]	Sheet resistance [MΩ]	Film thickness [nm]	Specific resistance [Ω m]
0	> 900	33	> 30
10	165	40	6.6
15	115	40	4.6

4.4.6.3. Increasing the charge carrier density of the HTL by doping

In Section 4.4.6.1 and Section 4.4.6.2 it was shown that the nature of the barrier introduced by the functionalized sNiO/CYN hole transport layer cannot be solely a consequence of energetic level mismatch. However, it was also proposed in Section 4.4.6.1 that the low conductivity of a certain layer in the device, and in particular of the hole-contact layer can lead to a barrier, as charges cannot efficiently be extracted anymore. Often transient photocurrent or photovoltage measurements are performed in that case [261]. As there was no opportunity to perform these kind of measurements, it was decided to increase the carrier density in the sNiO HTL by doping.

Assuming that the sNiO owes its *p*-type conductivity to excess oxygen in the crystal lattice, it should be possible to increase the conductivity by providing a higher oxygen partial pressure during the thermal decomposition of the precursor. Therefore, a test experiment was performed in which pure oxygen was supplied through the nozzle of a laboratory flask during the sNiO film annealing process. The conductivities of the resulting films were measured *via* four-point measurements. However, the sheet resistance of sNiO films and the valence band maximum was still too high and a similar oxygen enrichment as in vacuum processed pulsed laser deposited NiO could not be achieved in ambient [178].

More recently, new routes to dope the sNiO via solution-processing have been introduced in literature [235,262,263]. The routes added another precursor salt to the nickel acetate solution, typically copper acetate monohydrate (CuAc) (see Figure Table A.1). Copper acetate monohydrate was purchased from Sigma-Aldrich, and added to the nickel acetate precursor in weight percent. The conductivity of the resulting sNiO:CuO films were again measured by four-point probe measurements done on glass substrates (see Table 4.8). Film thicknesses

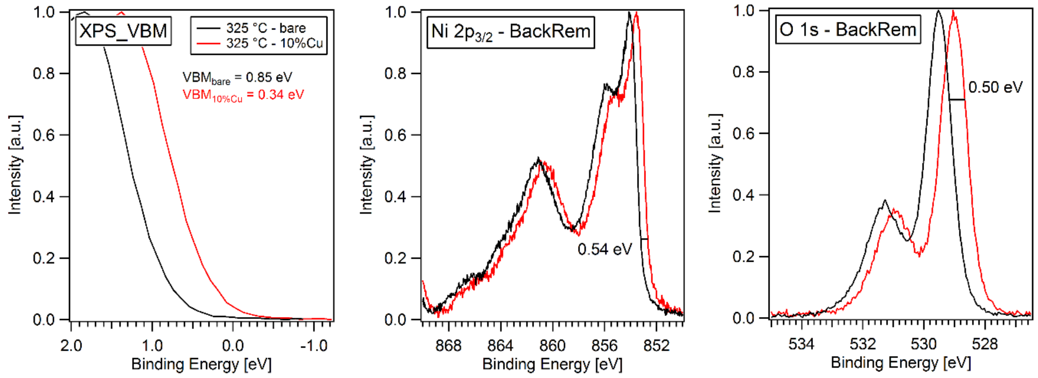

Figure 4.27.: Valence band maximum, Ni $2p_{3/2}$ and O 1s spectra of 10 wt. % doped sNiO:CuO (red) films compared to as-deposited sNiO films (black).

were obtained via ellipsometry. The specific resistance was calculated according to $\rho = R_\square \cdot d$, where ρ is the specific resistance, $R_\square$ the sheet resistance and d the film thickness. At 0% CuAc content the sheet resistance was comparably high to the values discussed in Section 4.3.3. Doping of the sNiO layers led to a significant decrease of the specific resistance from $> 30\,\Omega\,\mathrm{m}$ down to 4.6-6.6 Ω m, which is in good agreement with reports by Kim *et al.* [263].

To verify the measured resistances, a complementary XPS measurement on the sNiO:CuO doped films was performed. Figure 4.27 shows the resulting valence band maximum, Ni $2p_{3/2}$ and O 1s spectra of 10 wt. % doped sNiO:CuO films compared to as-deposited sNiO films. Both, in the VBM and the detailed spectra a shift of 0.5 eV of the onset and the core levels to lower binding energies can observed. This goes along with a shift of the Fermi level to a value of 0.34 eV above the valence band, which is much closer than for the as-deposited sNiO (compare with values in Table 4.1). Hence, the carrier density of the sNiO is successfully increased through the doping with CuO. However, this increase reminds of the common Fermi level shift induced by doping through foreign atoms in inorganic crystals. From the position of Cu with respect to Ni in the periodic table, doping of a NiO crystal with Cu should lead to an n-type doping. Doping here should not be understood as a replacement of Ni vacancies by Cu, which has been assumed in [263], but rather as a charge transfer from CuO to NiO due to the higher work function of the former (WF = 5.4 eV).

The density of holes that have been added to the film can be estimated

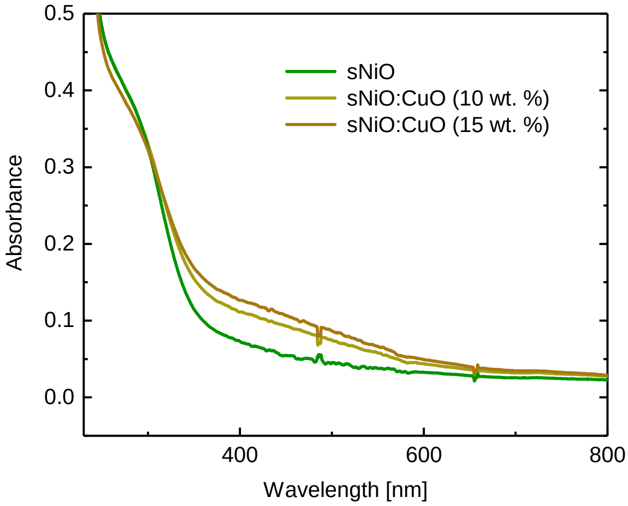

Figure 4.28: UV-vis absorption spectrum comparing an as-deposited and CuO doped sNiO films with different weight percentage. The wavelength was scanned from 200 nm to 800 nm. A bare ITO substrate was chosen as reference spectrum.

following the doping of a perfect inorganic semiconductor:

$$p = N_{\mathrm{V}} e^{-(E_{\mathrm{F}}-E_{\mathrm{V}})/k_{\mathrm{B}}T}, \tag{4.3}$$

where p is the hole density, N_{V} the effective density of states, E_{V} the valence band maximum, E_{F} the level, k_{B} the Boltzmann constant and T the temperature. Assuming the effective density of states N_{V} remains unchanged through the doping, the observed shift in $(E_{\mathrm{F}} - E_{\mathrm{V}})$ from 0.85 eV to 0.34 eV leads to an increase of hole carriers over 8 orders of magnitudes: $p_{\mathrm{doped}}/p_{\mathrm{undoped}} = 5.2 \cdot 10^8$ ($k_{\mathrm{B}}T \approx 25\,\mathrm{meV}$ at room temperature).

As the conductivity of holes σ can be calculated following

$$\sigma = pe\mu_{\mathrm{h}}, \tag{4.4}$$

where e is the charge of an electron and μ_{h} is the mobility of holes. With $\sigma = 1/\rho$, the specific resistance should decrease by 8 orders of magnitude through the CuO doping. However, this is not the case. It might be possible that the mobility in the sNiO:CuO decreases and therefore, the conductivity does not increase in the same amount as the charge carrier density. Such a decrease in mobility induced by copper doping has already been observed by Chen *et al.* [264]. Furthermore, it is questionable if N_v stays constant.

The CuO doped sNiO layers were tested in F_4ZnPc:C_{60} FHJ solar cells. The respective averaged device performance parameter were summarized in Table 4.9. Despite the slightly lower transparency of the sNiO:CuO films (see Figure 4.28), the doping leads to an improved PCE due to an increased FF.

Table 4.9.: Averaged device performance parameters of F_4ZnPc:C_{60} FHJ solar cells with sNiO:CuO hole contact layers (4-9 cells).

CuAc content	J_{sc} [$\mathrm{mA\,cm^{-2}}$]	V_{oc} [V]	R_s [$\Omega\,\mathrm{cm^{-2}}$]	FF [%]	PCE [%]
0%	3.6 ± 0.1	0.63 ± 0.01	34 ± 4	50.2 ± 1.5	1.12 ± 0.04
10%	3.8 ± 0.1	0.63 ± 0.01	26 ± 5	54.9 ± 1.1	1.33 ± 0.12
15%	3.8 ± 0.2	0.63 ± 0.02	24 ± 4	55.0 ± 0.9	1.35 ± 0.11

The increase in the fill factor is presumably a consequence of the superior conductivity of the CuO doped films leading to a significant decrease in the series resistance (R_s).

Coming back to the question whether the barrier was correlated to the conductivity of the hole contact layer, it must be stated that even though the conductivity of the as-deposited sNiO was already quite low, the sNiO worked well as a charge-selective interlayer within the organic solar cells. Furthermore, the doping with CuO led only to a small increase in the overall device performance. Neither the energy level mismatch nor the low conductivity of the sNiO hole contact layer alone can be the reason for the observed barrier.

Therefore, the 10 wt. % sNiO:CuO layers were functionalized with CYNOPPA the same way as described in Section 4.4.4 and compared to the sNiO/-CYN HTL. Figure 4.29 shows the corresponding J-V characteristics of the F_4ZnPc:C_{60} FHJ solar cells. As can be seen in all subfigures the s-kink with CYNOPPA was strongly reduced for the sNiO:CuO/CYN. The reduction of the s-kink was reflected in a recovery of the PCE and FF (see Table 4.10). This recovery has two components. On the hand, the shunt resistance was increased by two orders of magnitude with the sNiO:CuO HTL, on the other hand, the series resistance was significantly decreased. This leads to the conclusion that the combination of the sNiO and CYNOPPA-SAM forms a low conductive interface as transport barrier and that this barrier can only be overcome by a sufficent amount of charge carriers in the sNiO.

To rule out that the observed effect is only due to a lower SAM coverage on the sNiO:CuO layer, complementary IR and XPS measurements were performed on CYNOPPA-functionalized sNiO:CuO films. Figure 4.30 shows the corresponding XP core level spectra. The damping of the Ni $2p_{3/2}$ and the Cu $2p_{3/2}$ core levels after CYNOPPA chemisorption reveal an averaged nominal layer thickness of the SAM of 0.72 nm, which is in good agreement with the

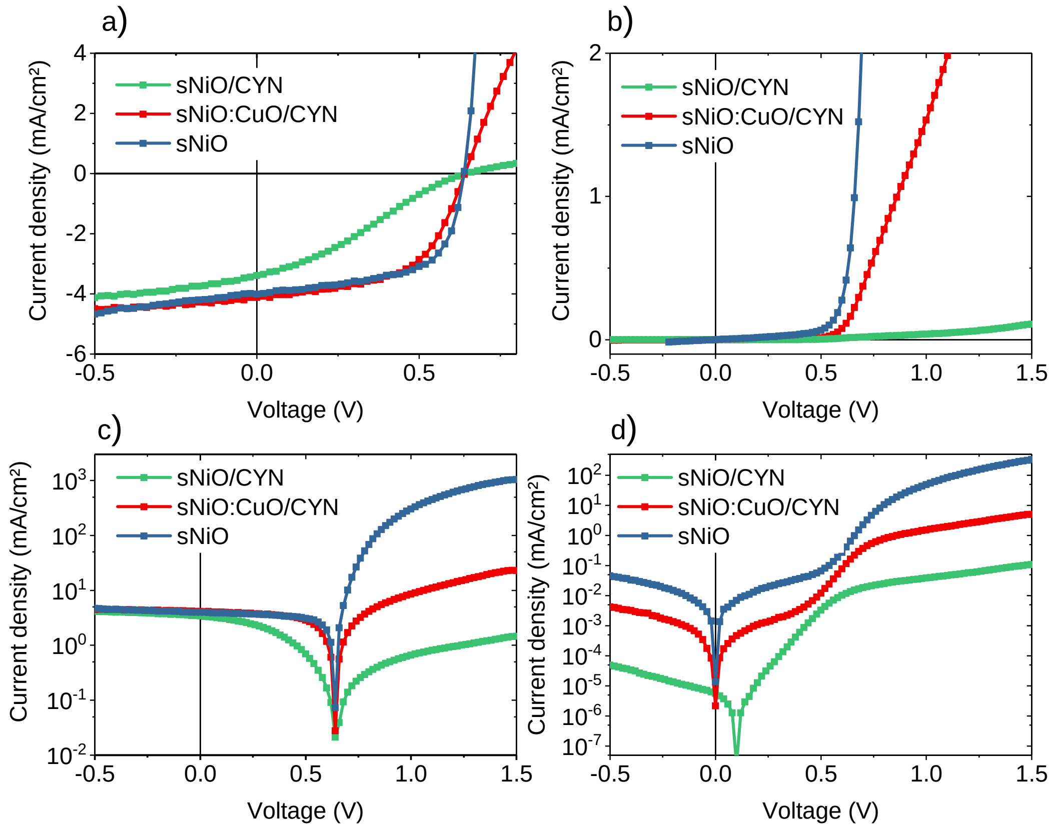

Figure 4.29.: J-V characteristics of $F_4ZnPc:C_{60}$ FHJ solar cells with sNiO/-CYNOPPA hole contact layers. The left column shows the cell under illumination, the right the according dark currents. Both were plotted in linear a) and b), as well as in semi-logarithmic scale c) and d).

nominal layer thickness of 0.75 nm found for CYNOPPA on the as-deposited sNiO (see Section 4.3.4). Furthermore, the MIR relative transmission spectra in Figure 4.31 show that there are no significant changes in the characteristic vibrational modes of CYNOPPA on the sNiO:CuO compared to the sNiO (see Figure 4.16). While the O_2-plasma treatment increased the amount of β-NiOOH, the application of the SAM reduces it. This might explain that the OP step prior the SAM deposition has no effect on the s-kink and is mostly reversed due to the SAM growth procedure (see Figure 4.22).

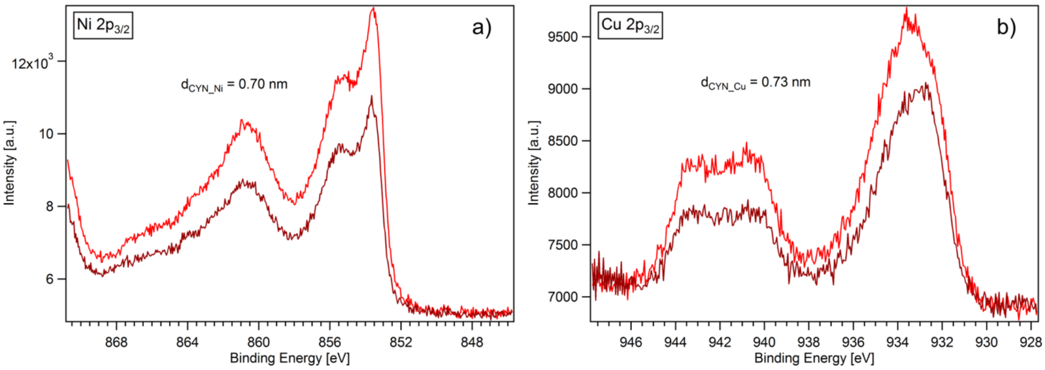

Figure 4.30.: Background corrected a) Ni $2p_{3/2}$ and b) Cu $2p_{3/2}$ core level spectra before (bright) and after (dark) the functionalization with CYNOPPA on the sNiO:CuO films. In both spectra the core levels are damped through the SAM. The damping of the Ni $2p_{3/2}$ core levels reveals a nominal layer thickness of $d_{\mathrm{CYN\_Ni}} = 0.70\,\mathrm{nm}$, and the damping of the Cu $2p_{3/2}$ core levels a value of $d_{\mathrm{CYN\_Cu}} = 0.73\,\mathrm{nm}$.

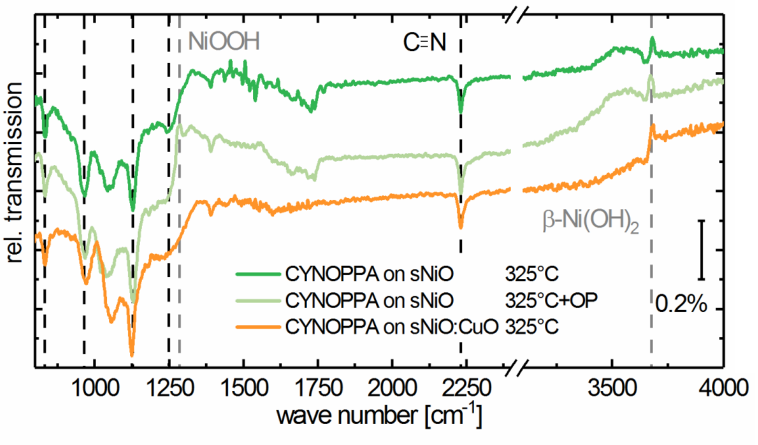

Figure 4.31.: MIR relative transmission spectra of sNiO (dark green), sNiO/OP (light green) and sNiO:CuO (orange) films functionalized with CYNOPPA. sNiO films were annealed at 325 °C. The relative changes of the plasma-induced β-NiOOH and β-Ni$(OH)_2$ peaks are marked with light grey dashed lines at 1286 cm^{-1} and 3600 cm^{-1}, respectively. Characteristic vibrational modes of CYNOPPA are highlighted with black dashed lines.

Table 4.10.: Averaged device performance parameters of F_4ZnPc:C_{60} FHJ solar cells comparing the CuO doping effect on the SAM barrier (7-13 cells).

FHJ	Φ [eV]	J_{sc} [$\mathrm{mA\,cm^{-2}}$]	V_{oc} [V]	R_{s} [$\Omega\,\mathrm{cm^{-2}}$]	FF [%]	PCE [%]
sNiO	4.81	4.1 ± 0.1	0.64 ± 0.01	37 ± 2	52.9 ± 0.8	1.37 ± 0.06
sNiO/CYN	5.21	3.7 ± 0.1	0.64 ± 0.02	118 ± 49	38.9 ± 5.1	0.95 ± 0.15
sNiO:CuO/CYN	5.05	3.9 ± 0.2	0.64 ± 0.01	63 ± 23	47.1 ± 7.8	1.25 ± 0.21

4.5. Conclusion

In this chapter, two different transition metal oxides as potential hole-contact layers were investigated. It was shown that the high work function of the widely used buffer layer MoO_3 is not stable over time and exposure to ambient gases in Section 4.2.1. Soon after evaporation of MoO_3 in vacuum, the work function started to decrease monotonously from a maximum of around $6.9 - 7.0\,\mathrm{eV}$ down to 5.0 eV. As the high work function is a desired property for good energy level alignment to donors with high ionization energies, it is important to continue with the deposition of adjacent organic donor materials quickly after the growth of the MoO_3 film. By fitting the WF decay with second-order exponential decay functions, two major components for the WF decrease were identified. To distinguish between these two, the MoO_3 films were exposed to dry oxygen in a controlled gas exposure experiment. It was shown that the WF saturation value indeed depended on the residual gas composition (see Section 4.2.2). For an increased oxygen partial pressure the work function saturated around 5.5 eV, which is 1.75 eV higher than the saturation value for the WF decay of a film that was kept in vacuum at $1 \cdot 10^{-8}$ mbar base pressure. Due to the similarity of the initial WF decrease for both gaseous environments, the fast component was addressed to the adsorption of molecular oxygen. The slower and longer lasting component was then attributed to the adsorption of residual water and the formation of a surface dipole layer. To verify if the adsorption of molecular oxygen leads also to a refilling of oxygen bulk vacancies and change in stoichiometry of the MoO_3 thin films, a correlated work function over conductivity measurement was performed in Section 4.2.3. An increase of conductivity was found agreeing with the finding by Cheung *et al.* However, the author reported that the increase of conductivity is due to the compensation of the oxygen deficiency in the MoO_3 bulk [208]. This conclusion appears questionable, as it is known that oxygen deficiency and an under-stoichiometry in MoO_x is important for its *n*-type character [197,265]. The combination of the WF decay and the increase of current measured in the two-terminal configuration hints more towards an oxidative adsorption of molecular oxygen, in which electrons are added to the surface of the MoO_3, leading to a higher charge carrier density at the surface and a more conductive surface channel. For these reasons, care has to be taken when incorporating MoO_3 as hole-contact layers, as the decrease in WF can lead to significant hole-injection barriers into organic semiconductors [202].

While the high work function of MoO_3 is clearly advantageous for energy level alignment to organic donor materials with deep lying IEs, the also very high electron affinity (IE $\approx$ 6.9 eV) can reduce the electron blocking capability of MoO_3 interlayer [12]. Therefore, NiO was investigated as a second transition metal oxide for the application as a hole-contact layer. NiO was processed from a solution-based nickel acetate precursor route as proposed by Manders *et al.* [159]. The spin-cast films were annealed in ambient air at different temperatures and fundamentally characterized. High-resolution AFM images revealed compact films with a grainy surface micro-structure with grain sizes smaller than 10 nm (Section 4.3.1). Detailed infrared- and photoelectron spectroscopy measurements in Section 4.3.2 showed that temperature is a crucial parameter for the film composition. The higher the film annealing temperature is, the more the nickel acetate precursor gets converted and the less water and $Ni(OH)_2$-phases remain. This is accompanied by a higher amount of NiO, as the signal of the bivalent Ni^{2+} in the Ni $2p_{3/2}$ core level increased with higher temperatures. While with XPS it was very difficult to distinguish between the different hydroxide phases, IR measurements allowed to observe the rise of a characteristic mode of β-NiOOH for lower temperatures, which is an oxidation product of β-$Ni(OH)_2$. Its amount was further increased by the application of O_2-plasma.

Not only the chemical composition, but also the electronic properties depended on the sNiO film annealing temperature (Section 4.3.3). Work functions were found in the range between 4.9 eV to 4.4 eV, from higher to lower temperatures. The total resistance of the as-deposited sNiO films decreased for the lower annealing temperature of 275 °C by one order of magnitude, which might be attributed to the higher residual hydroxide content, especially the β-NiOOH, which is believed to exhibit a higher conductivity over the $Ni(OH)_2$ [266]. In order to increase the work function and tune the wettability of the sNiO, dipolar self-assembled monolayers of 4-cyanophenyl phosphonic acid (CYNOPPA) were applied to the sNiO surface in Section 4.3.4. The successful chemisorption and a nominal layer thickness in the range of the molecular length of CYNOPPA was proven by XPS and IR. Furthermore, the reduc-

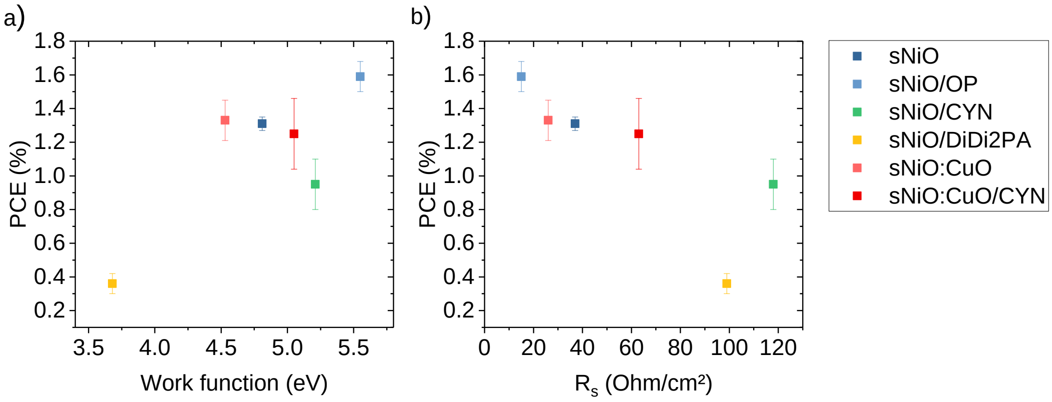

Figure 4.32.: Summary of the power conversion efficiencies (PCE) over a) the work function and b) the series resistance (R_s) found for all sNiO HTL configurations implemented into FHJ $F_4ZnPc:C_{60}$ FHJ in this work.

tion of the $Ni(OH)_2$ IR-absorption mode led to the interpretation that the CYNOPPA presumably interacts with the $Ni(OH)_2$. Density functional theory calculations gave insight into possible binding configurations of the molecule. Comparing the adsorption energies for purely hydrogen, mono-, bi- and tridentate configurations allowed only for two favorable binding modes. While the tridentate bonding is energetically unfavorable and the hydrogen bond not stable under the annealing step of the phosphonate bond formation, the mono- and bidentate configuration should be the predominant forms. Through the functionalization of the sNiO surface with the CYNOPPA SAM the contact angle to water was tuned to a value of $(42 \pm 3)°$ and the work function was increased up to $5.1 - 5.2\,\mathrm{eV}$, which is among the highest reported values for SAMs on this material.

The increased work function by a dipolar SAM was seen as an alternative route to the commonly used O_2-plasma or the NiO_x/MoO_3 bi-layer approach introduced by Schulz *et al.* [209]. Before the implementation of functionalized sNiO hole-contact layers, the sNiO was tested with different parameters in small molecule $F_4ZnPc:C_{60}$ organic solar cells. It was shown that sNiO efficiently hinders electrons from passing to the ITO anode fulfilling its function as an electron blocking layer (Section 4.4.1). Only a small variation in the series resistance was found between different distinct devices, which evidenced the reported decrease of the total sheet resistance for lower film annealing temperatures in Section 4.3.3. The application of an O_2-plasma significantly increased the work function of the sNiO up to $5.55\,\mathrm{eV}$. However, the work function increase led not to an improvement of the V_{oc}, which hinted towards an already reached saturation value of the V_{oc} dominated by the effective bandgap of the donor-acceptor system (Section 4.4.3). That this assumption holds was proven in Section 4.4.5 by the use of a novel SAM precursor, which decreased the sNiO work function, such that the V_{oc} was not maintained. Figure 4.32 summarizes the PCE values over work function and series resistance for all sNiO HTL configurations investigated in this work, without taking the temperature dependent experiment of Section 4.4.2 into account. While the O_2-plasma treatment did not induce an increase in V_{oc}, it showed, however, the lowest series resistance and highest fill factor among all sNiO HTLs. Even though the CYNOPPA SAM treated sNiO showed the second highest WF, the incorporation of the sNiO/CYN gave rise to an s-kink in the operating regime (Section 4.4.4). The s-kink was attributed to the formation of a charge transport barrier. This barrier was shown in Section 4.4.6 to be an extraction barrier and not solely a consequence of energetic mismatch at the sNiO/donor interface. It appears that the series resistance of devices with SAM-functionalized sNiO hole-contact layers is drastically increased.

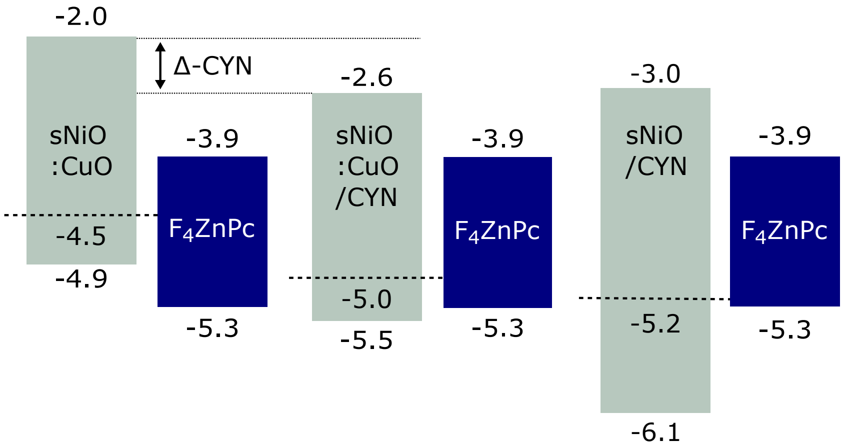

Figure 4.33.: Schematic illustration of the energy levels of the sNiO hole-contact layer after doping with CuO and functionalization with CYNOPPA with respect to the F_4ZnPc donor. Even though the Fermi level of the sNiO/CYN matches well the ionization energy of the donor, a transport barrier was observed. This barrier was overcome by doping the sNiO with CuO, where the Fermi level is even further apart from the IE of the F_4ZnPc. Note, that the materials are aligned to a common vacuum level and the band gaps are color filled. The addition of CuO leads to a slight reduction of the band gap, which was estimated around 0.2 eV by the UV-vis absorption in Figure 4.28. Fermi levels are depicted as dashed lines and the surface dipole introduced by the SAM is denoted as Δ-CYN.

As the work function and ionization energy of the F_4ZnPc are well aligned through the interface dipole of CYNOPPA (see Figure 4.33), it was concluded that the transport barrier is due to an interface region having a very low conductivity and correlated with the low intrinsic charge carrier density in sNiO. By increasing the charge carrier density in the sNiO and thereby the conductivity through doping, the s-kink could be reduced and the fill factor almost fully recovered (see Section 4.4.6.3). Hence, it is not only the work function and perfect energy level match that makes an interface functional. Especially in the case of low conductivity oxides great care must be taken to avoid such transport barriers with interface modifiers.

5. Wet-chemical passivation of gallium nitride surface states

Gallium nitride has emerged as the leading III-V semiconductor for the production of commercially available blue LEDs [267]. Over the last years, rapid progress was made in the growth of vertical GaN nanowires (NW), opening an alternative to the convential epitaxial growth of 2D-planar GaN crystals [268–270]. By formation of heterostructures and incorporation of alloys the emission wavelength of GaN nanowire LEDs has been successfully tuned [271–273].

A major drawback, however, is that GaN nanowires exhibit high densities of surface states (see Section 2.4.2), which pin the Fermi level and cause charge carrier trapping. Such traps can further act as direct non-radiative recombination centers (Shockley-Read-Hall) and induce a strong band bending towards the surface (see Section 2.4.3). The band bending goes along with a high electric field, which can lead to the spatial separation of electron and hole wavefunctions, which in turn indirectly decreases the radiative recombination efficiency (radial Stark effect) [25,26,274]. This becomes especially pronounced in high aspect ratio GaN nanowires [275,276]. Hence, a way to passivate these surface states and impact the surface electrical field is a desirable goal to improve GaN NW applications today.

This chapter will focus on surface state passivation routes, their impact on the electronic and chemical properties of the GaN surface, and their influence on time-resolved photoluminescence measurements. As a proof of principle the passivation techniques were primarily applied to planar GaN crystals with different facets and polarities. The knowledge acquired can then be transferred to nanowires in a later stage of the project, in particular for the enhancement of the Förster resonant energy transfer (FRET) at GaN/organic heterojunctions. The project has been run in collaboration with the Paul-Drude-Institut (PDI) in Berlin.

The chapter would not be complete without the scientific contributions of Stefan Brackmman and Florian Ullrich.

5.1. Introduction into GaN nanowires, planes and polarities

GaN nanowires can be grown catalyst-free by molecular beam epitaxy (MBE) on silicon with higher qualities and lower defect densities compared to GaN planar crystals grown on heteroepitaxial substrates [24,277]. GaN NWs often comprise different surface facets and polarities. Figure 5.1 shows a) the most observed crystallographic NW growth axes and b) a scanning electron image of a NW ensemble. The NWs grown at the PDI extrude along the (0001) direction, often called *c*-axis, while the sidewalls are formed by planes in the $(1\bar{1}00)$ direction, or *m*-axis. According to Fernández-Garrido *et al.*, all GaN NWs are N-polar at the top surface in the absence of structural defects of the underlying substrate [278]. However, the expression N-polar does not imply that the surface is completely terminated by N atoms as shown by Reddy and coworkers [279]. It is rather that a Ga-polar surface exhibits a higher Ga to N ratio compared to the N-polar one. Furthermore, the *m*-plane is mainly a mixture of both polarities and oxide [280]. The different polarities can significantly impact the electronic and chemical properties at the surface [281]. The Ga-polarity is believed to be chemically more resistant against etching [282], which should be kept in mind within the following context. It is very important to differentiate between these planes and polarities, when characterizing GaN samples. As the *c*-plane and *m*-plane facets are the predominant faces of GaN NWs, they will be investigated in more detail in the following sections.

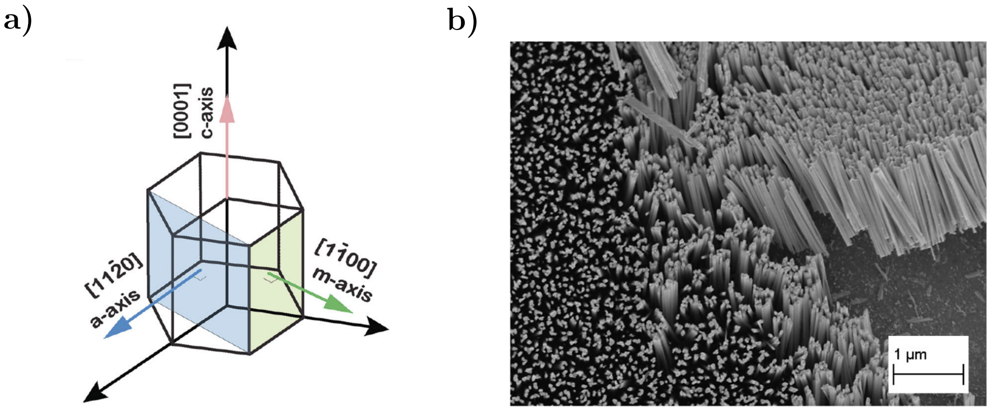

Figure 5.1.: Typical structure of GaN nanowires. a) Schematic representation of the common crystallographic growth axes of a GaN nanowire. Reprinted from [271]. b) SEM image of a GaN nanowire ensemble grown by MBE at the PDI [24]. NWs can be seen from the top on the left and due to their tilt from the side on the right.

5.2. Preparation of clean surfaces of *c*-plane GaN

For the successful passivation of GaN facets, the preparation of clean GaN surfaces is an indispensable precondition. Cleaning procedures proposed in literature can be divided into two categories: in *ex-situ* wet-chemical pretreatments and in *in-situ* cleaning procedures, either by annealing or ion bombardment [283]. Ideally, GaN surfaces are investigated after MBE growth without samples leaving the vacuum environment. However, the GaN facets are often exposed to ambient air and thereby run the risk of contamination with oxygen, water and carbon. A way to minimize the risk would be to overgrow a capping layer, which would later be removed in vacuum at high temperatures (> 700 °C), such that the original surface is recovered [284–288]. Annealing at high temperature needs to be precisely controlled as the GaN surface tends to rapidly decompose at too elevated temperatures [289–291]. Some authors reported on the use of higher temperatures and an increased surface stability when a flux of NH_3 is introduced [292–295]. After all of these procedures the atomic structure of the resulting GaN surface should be controlled with LEED to ensure comparability between experiments. If such equipment is not accessible, the use of *ex-situ* wet-chemical cleaning steps with the aim to reduce oxygen and carbon contents should be employed. The wet-chemical cleaning often begins with immersion into organic solvents followed by an aggressive etching agent as the GaN surface is stable in neutral pH environments. Typical reagents are hydrochloric acid HCl, hydrofluoric acid HF [296], sulfuric acid H_2SO_4 [297], phosphoric acid H_3PO_4, potassium hydroxide (KOH) solutions [298], or boiling aqua regia [299]. A combination of *ex-situ* wet-chemical pre-treatments and *in-situ* cleaning procedures was suggested by Mishra *et al.* [300] and more recently applied by Schultz *et al.* [301]. In this work, only the *ex-situ* wet-chemical cleaning was used. HCl was preferred as etching reagent, as it showed superior oxygen removal compared to other acids [296]. The cleaning protocol of the samples was developed in this thesis and is explained in Section 3.2.4.

5.2.1. Topography and chemical properties

The first test samples that were delivered by the PDI were commercial wurtzite *c*-plane GaN(0001) 2” wafer grown on sapphire by the company KymaTechnologies. The one-side polished GaN layer had a thickness of 5 µm and was grown by hydride vapour phase epitaxy (HVPE) on an intermediate buffer layer of

AlN. This buffer layer serves as a nucleation layer for the GaN overgrowth. More information on the sample properties can be found in Section 3.2.1.

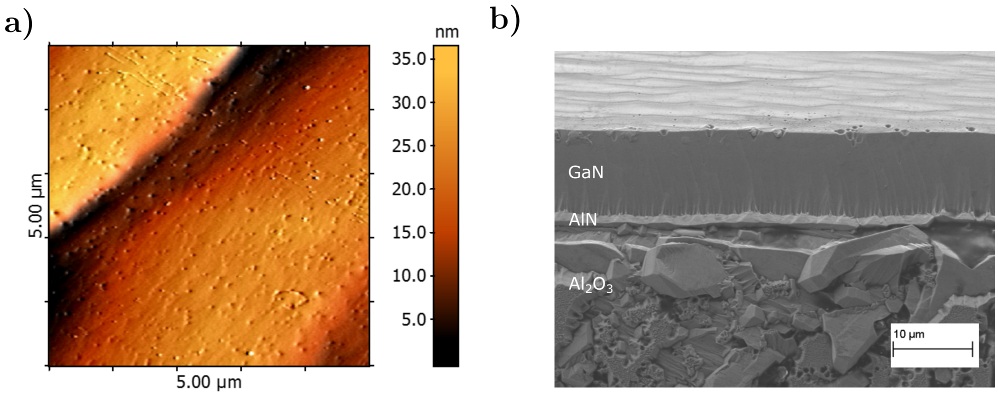

Figure 5.2.: Topography of the KymaTech GaN(0001) substrates. a) 5 µm ×5 µm UHV-AFM image of the surface topography. b) Cross-section SEM image of the same GaN sample. The intermediate AlN seed layer and the rough sapphire substrate can clearly be distinguished from the GaN layer. The sample was tilted to obtain an edge-on perspective.

In a first step the surface topography was investigated with AFM and SEM. Figure 5.2 shows the corresponding images. AFM reveals a surface topography of terraces filled with many small pits (dark spots). This surface structure can also be seen in the SEM image on the right. The sample was tilted in this view to obtain an edge-on perspective. The thin bright interfacial area between the GaN and the rough sapphire substrate corresponds to the intermediate AlN buffer layer. Many transversal lines crossing the whole GaN originate from this layer. These lines are dislocations originating from a lattice mismatch between the GaN and the substrate [302]. The pits in the AFM image could be the consequence of a high density of screw and mixed threaded dislocations, whose amount depend on the Ga/N flux ratio during the growth process [303,304].

X-ray photoelectron spectroscopy was performed to reveal the surface chemistry of the *c*-plane GaN. Figure 5.3 shows a complete XP survey spectrum of a *c*-plane GaN KymaTech sample with and without HCl cleaning procedure as suggested by Smith *et al.* [305]. The intensity of the spectrum is given in arbitrary units and ranges from binding energies between 0 eV to 1400 eV. A binding energy of 0 eV refers to the position of the Fermi level E_F. These wide-range scans with a relative low-energy resolution help to identify all elements present on the surface. From 0 to 1400 eV the following peaks can be identified: Ga 3d, Ga 3p, Ga 3s, Cl 2p, C1s, N1s, Ga LMM, O KLL, Ga $2p_{3/2}$,

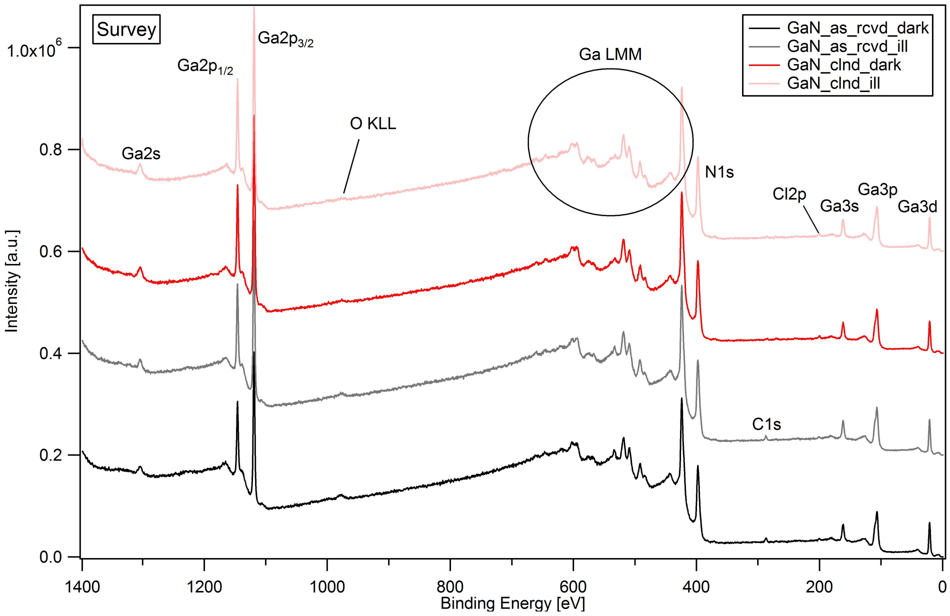

Figure 5.3.: Survey spectrum of a c-plane GaN(0001) KymaTech sample measured with XPS. Spectra were taken for samples with (cleaned) and without (as-received) HCl cleaning procedure. Both were exposed to UV-light with a wavelength of 365 nm after the first recorded survey spectrum. No significant light-induced shift was observed here.

Ga $2p_{1/2}$ and Ga 2s. The Ga LMM is a typical Auger line observed for GaN [306]. The positions of the Ga core peaks and the signal from the N 1s fit quite well to earlier XPS studies on MOCVD and MBE grown GaN by Mishra *et al.* [307] and invesitgations by Gogova *et al.* for free-standing GaN grown by HVPE [308].

In the as-received condition, a small signal of residual carbon contaminant was found around 285 eV BE, which is not surprising as no cleaning procedure was applied to the sample prior the measurement. The HCl cleaning is capable of reducing the C1s signal to a minimum. However, a trace of residual Cl can be found afterwards [309]. At first glance, no significant shift of the element peaks with illumination can be observed.

A closer look was taken at the high-energy resolved core level spectra, which are a series of scans measured around a certain binding energy of interest. Figure 5.4 shows the most characteristic GaN and adsorbate related core levels: Ga $2p_{3/2}$, N 1s, C 1s and O 1s. The Ga $2p_{3/2}$ exhibits a single component at 1119 eV BE. The N 1s core level is split into a major contribution at 399 eV, a shoulder peak at 397 eV and a tail at lower binding energies. The overall peak shapes are in good agreement with observations by Petravic *et al.* The authors also observed two peaks for MOCVD grown *c*-plane GaN on sapphire, when the surface was not previously bombarded with reactive ions [310]. The major N 1s peak was assigned to a signal from nitrogen in the bulk GaN phase, while the shoulder peak was attributed to nitrogen within an oxynitride phase [311]. However, it was also reported by others that either nitrogen dangling bonds [312] or the Ga LMM Auger line contributes to the N 1s shoulder [280]. In many publications the N 1s core level is not presented and it has to be mentioned that the position of the peaks can shift upon exposure to oxygen [280]. Therefore, the interpretation will always depend on the growth parameters, e.g. the lattice strain sensitivity [313], and surface treatments [314]. More importantly, signals of C 1s and O 1s can successfully be minimized with HCl etching. A small residual C 1s amount can always re-adsorb during sample transport through ambient atmosphere. It can be concluded that HCl etching is an efficient way to remove most but not all oxygen.

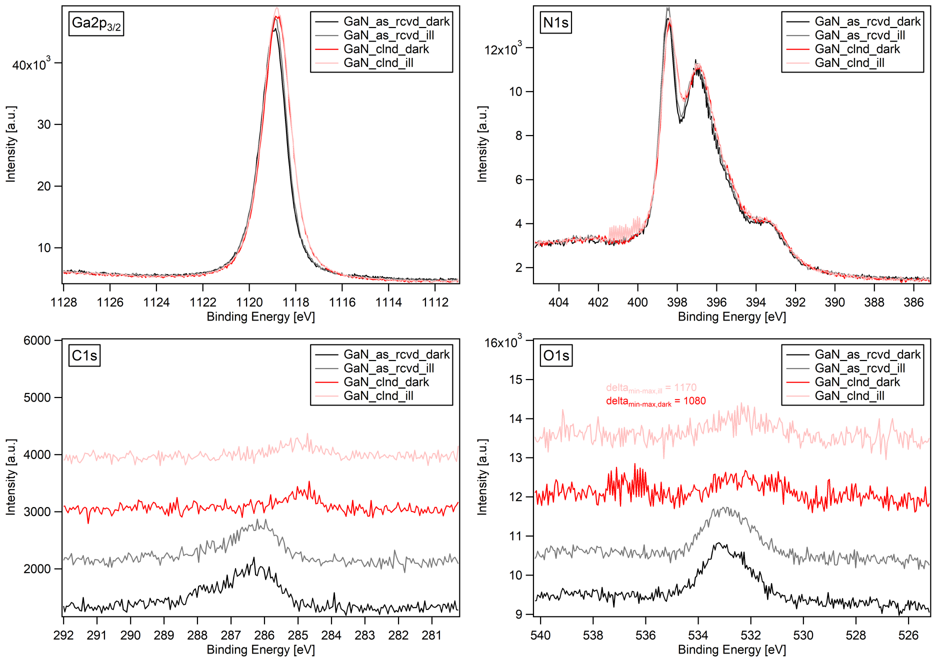

Figure 5.4.: XP detail spectra of the *c*-plane GaN(0001) core level, a) Ga $2p_{3/2}$, b) N 1s, c) C 1s, d) O 1s. The spectra were measured on the same samples as in Figure 5.3, as-received and cleaned with HCl. Both samples were measured under 365 nm illumination and in the dark. No significant shift of the core levels under illumination was observed.

5.2.2. Verification of the optical band gap

In order to evaluate the optical band gap of the *c*-plane GaN, the optical transmission was measured with UV-vis spectroscopy. Ideal direct semiconductors should predominantly absorb photons with an energy larger than the band gap. Figure 5.5 shows the optical transmittance measured over incident photon energy and wavelength of a) the *c*-plane Kyma template on sapphire (Al_2O_3) and b) the free-standing bulk GaN sample. A spectrum measured in the dark was subtracted from the signal and the total intensity was divided by the intensity of the background spectrum.

Strong oscillations are observed below the absorption onset of the KymaTech sample. These oscillations, which were also observed in separate IR measurements, are a consequence of thin film interference in the thin GaN layer ($\sim 5\,\mu m$) with high-refractive index (n=2.5) [316]. Despite the large optical band gaps of the Al_2O_3 ($> 8.8\,eV$) [317] and the AlN seed layer (6.2 eV) [318], the non-polished sapphire backside leads to strong scattering of light. For this reason the transmittance through the 100 µm thick sapphire is only 1% in the visible regime. However, the high defect density of this sample allows for optical transitions below the band gap energy and a smoothing of the absorption onset. The optical transmittance between the visible and infrared reaches 70%. In conclusion, for both samples a band gap energy of 3.4 eV

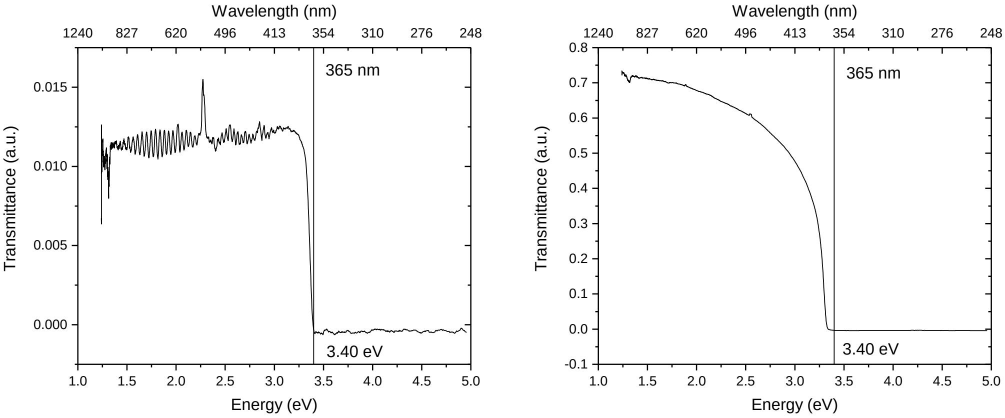

Figure 5.5.: UV-vis transmission of a) the *c*-plane Kyma GaN(0001) template on sapphire and b) the free-standing bulk GaN(0001) sample. Incident photon energies and wavelengths were used as bottom and top axis, respectively. Vertical lines were added at the absorption onset to estimate the band gap of 3.4 eV [315]. Total absorption before the band gap onset occurs for the thick free-standing GaN substrate.

was estimated, which is in good agreement with previous reports [315]. With $\lambda = hc/E_\nu$ and $\approx 1240\,\text{eV}$ this corresponds to a wavelength of 364.7 nm. Note that the free-standing GaN sample is at least 250 µm thick (see Table 3.1), which leads to the total absorption of the light before the band gap onset and makes it difficult to extract the exact value of the band gap for this substrate.

5.2.3. Determination of the valence band maximum

The previous sections discussed the chemical composition of the *c*-plane GaN(0001) surface and estimated the optical band gap from UV-vis spectroscopy. As the electronic properties of GaN nanowire surfaces are important for maximizing opto-electronic quantum efficiencies and also for improving the efficiency of redox reactions for artificial photosynthesis to split water [319], an energy band diagram of the c-plane GaN as shown in Figure 2.16 will be deduced in the following sections. The valence band maximum (VBM) was measured both, by XPS and by UPS. Many publications have reported on VBM values with UPS [294,307,320,321]. However, the interaction of UV-radiation with GaN is high and even low power densities of the incident UPS beam could *a priori* cause a shift of the VBM. For this reason, the VBM was measured with XPS instead of UPS.

Figure 5.6 shows the valence band maximum of an as-received and an HCl

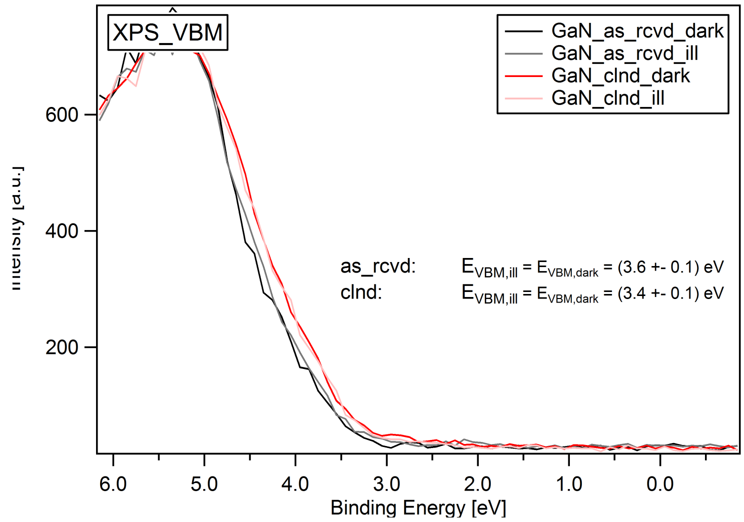

Figure 5.6.: Valence band maximum measured with XPS of an as-received and HCl cleaned c-plane KymaTech GaN(0001) sample. The VBM was also measured in dependence of the illumination with an external 365 nm light source.

cleaned c-plane KymaTech sample. The VBM is extracted from the valence band onset relative to the Fermi level ($E_\mathrm{F} = 0\,\mathrm{eV}$). For the as-received sample a VBM of $(3.6 \pm 0.1)\,\mathrm{eV}$ and for the cleaned sample a value of $(3.4 \pm 0.1)\,\mathrm{eV}$ is found. This results in a difference of 0.2 eV. As already seen for the GaN core levels in Section 5.2.1, the external 365 nm UV-light source does not impact the position of the VBM.

5.2.4. Extracting the work function

The work function and, thereby, position of the Fermi level E_F with respect to the vacuum level, can either be measured by the secondary electron cut-off (SEC) with XPS or by the contact potential difference (CPD) with Kelvin probe (see Section 3.1.2 and Section 4.3.3).

5.2.4.1. Using XPS to obtain the work function

Figure 5.7 shows the secondary electron cut-off for an as-received and HCl cleaned *c*-plane KymaTech sample. For the as-received sample, a low work function of 3.59 eV was found. Through HCl etching, the work function was significantly increased to 4.80 eV. For both samples the illumination with the external 365 nm UV-light leads to a decrease of the measured WF of around 0.30 eV and 0.19 eV, respectively. As the core levels and the VBM (compare Section 5.2.3 and Section 5.2.1) did not shift under illumination, the variation of the position of the SEC suggests a light-dependent change of the surface dipole. The work function values found here are comparable to the WF range given for the GaN(0001) surface in literature [129,307,320,321].

The light dependency of the SEC was further investigated in time-dependent experiments. Figure 5.8 shows the secondary electron cut-off before and after illumination with the external 365 nm light source of an as-received KymaTech *c*-plane sample. The turning on of the illumination leads, again, to an instantaneous decrease of the WF of around 0.3 eV. Once the exposure is turned off, the WF starts to shift back to lower binding energies and higher WFs. The process occurs on a time scale of minutes and the initial WF could not be restored within the time frame of the experiment. A simple exponential growth fit led to an estimated WF relaxation time of 200 min. Such a slow process cannot be attributed to an electronic response of the sample, which is expected on a timescale of µs-ms [322]. This result further strengthens the hypothesis that illumination induces a change of the surface potential in terms of surface dipole. Such a change might be due to photochemical adsorption or desorption of molecular oxygen and water at the surface [276], which might

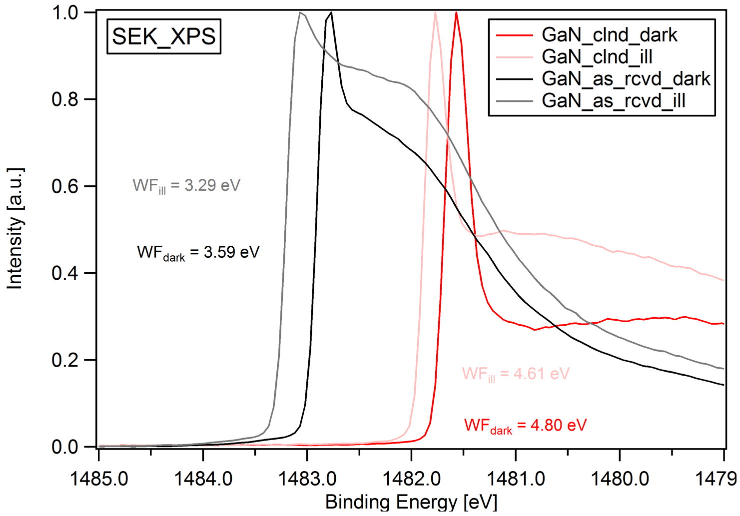

Figure 5.7.: Secondary electron cut-off measured with XPS. An as-received and HCl cleaned *c*-plane KymaTech sample were investigated with and without illumination. The respective work functions are displayed as labels to the according graphs.

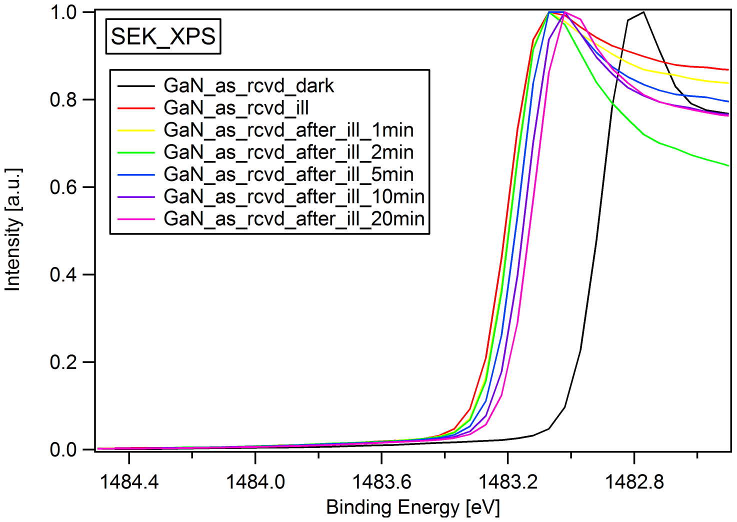

Figure 5.8.: Time-dependent response and relaxation of the secondary electron cut-off of a *c*-plane KymaTech sample under illumination with 365 nm UV-light.

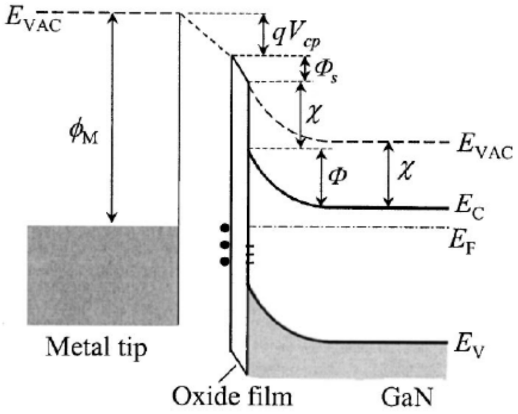

Figure 5.9: Schematic illustration showing the physical quantities that are measured with Kelvin probe on a semiconductor surface. The metal tip and the GaN are aligned via their Fermi levels E_F. Negative surface charges are drawn as filled circles. E_{Vac} is the the vacuum level, Φ_M the tip work function, qV_{CPD} the contact potential difference, Φ_S the surface dipole, χ the electron affinity, E_C conduction and E_V valence band and Φ the band bending. Reprinted from [324].

further be correlated to a comparable charge transfer as in the redox reaction of water splitting on *n*-type GaN surfaces [319,323]. It is also possible that a ligt-induced polarization of the polar GaN *c*-plane takes place.

5.2.4.2. Using Kelvin probe to obtain the work function

While the work function of metals can directly be accessed with Kelvin probe, the work function of semiconductors is more difficult to address using this technique. The contact potential difference (qV_{CPD}) between the tip of the Kelvin probe and the sample can include an additional contribution of a surface dipole (Φ_S) and band bending, which is often referred as a barrier height (Φ) and a consequence of surface trap states (see Figure 5.9 and Figure 2.16). Hence, the measurement of WF by Kelvin probe can also be influenced by the surface chemistry and illumination similarly to the secondary electron-cut off in XPS (see Section 5.2.4.1).

Figure 5.10 shows the Kelvin probe measurement of an as-received *c*-plane KymaTech sample. Prior the measurement the sample was not exposed to light for several hours. The absolute work function was obtained by calibrating the tip work function ($\Phi_{tip} = 4.75\,\text{eV}$) to an HOPG reference sample. During the first 50 data points the WF was measured in the dark. The next 50 data points the WF was measured under illumination with a 365 nm UV-LED as described in Section 3.1.2. The initial work function of 4.13 eV momentarily drops down to 3.78 eV upon the exposure to the UV-light. This initial photoresponse is denoted as surface photovoltage (SPV) and difference of 0.35 eV (SPV) between dark and illuminated was calculated, which is comparable to the light-induced shift of the SEC in Section 5.2.4.1. However, when the light

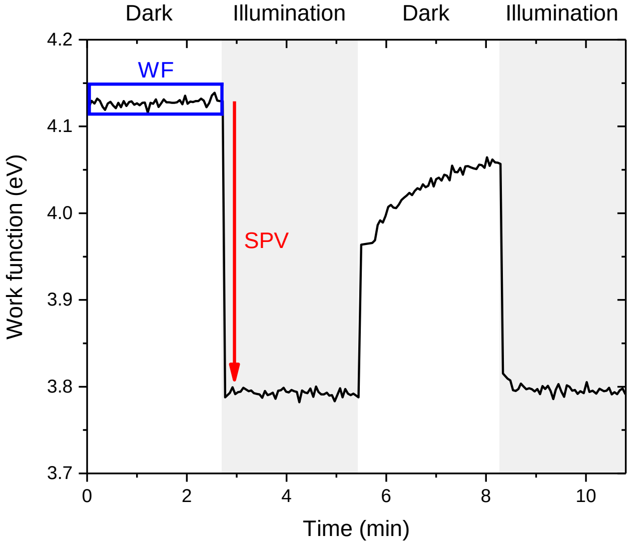

Figure 5.10: Work function under band-to-band illumination with 365 nm UV-light measured with ambient Kelvin probe on an as-received c-plane GaN(0001) sample. Illumination periods are highlighted as grey regions.

source is turned off, the WF increases immediately before rising back slowly. The fast component of this response is the major discrepancy between the Kelvin probe and the XPS measurements. Average work functions and surface photovoltages for several as-received and HCl cleaned KymaTech samples are summarized in Table 5.1. The WFs found for HCl cleaned samples are always above the as-received values. The fact that the WF values for the as-received substrates are higher compared to the results obtained by XPS might correlate with the adsorbtion of water and hydrocarbons in ambient, which can lead to shielding of the true work function. Note that the SPV observed might be superposed by a change in the surface dipole.

Table 5.1.: Averaged work functions and surface photovoltages measured for several c-plane GaN(0001) KymaTech samples. Values of as-deposited and HCl cleaned samples are compared.

GaN(0001) KymaTech	WF [eV]	SPV [eV]
As-received	4.24 ± 0.29	0.29 ± 0.10
HCl cleaned	4.45 ± 0.26	0.23 ± 0.06

5.2.5. Estimating the band bending and surface dipole

The discrepancy between the relaxation of the SEC measured with XPS (see Figure 5.8) and the WF signal measured with Kelvin probe (see Figure 5.10) can have two reasons: either the c-plane KymaTech GaN surface exhibits indeed flat-band condition and thereby, the core levels and the VBM do not shift under UV-light exposure or the surface actually has a band bending, but it cannot be resolved with the high-intensity of the XPS. In the first case, the flat-band condition would be given for the as-received as well as the HCl cleaned samples as no shifts could be observed in both cases. The existence of the band bending and its value is still an intensively and controversially discussed topic in literature [129,294,307,320,321,325–331].

As the intensity of the XPS could not be reduced and the measurement not performed in dependency of the substrate temperature as proposed by Long and Bermudez [129], the band bending was estimated by comparing the initial photoresponse of the SEC with the SPV observed with Kelvin probe. Assuming that the shift of the SEC (Δ_{SEC}) is a result of two contributions, the change of a surface dipole ($\Delta\delta$) and a change in the band bending (ΔBB), it can be written:

$$\Delta_{\mathrm{SEC}} = \Delta\delta_{\mathrm{XPS}} + \Delta\mathrm{BB}_{\mathrm{XPS}}. \tag{5.1}$$

The experimental observation of the XPS leads to the assumption that $\Delta\mathrm{BB}_{\mathrm{XPS}} = 0$, which implies that Δ_{SEC} is only a consequence of a change of the surface dipole. As mentioned in Section 5.2.4.2, the SPV measured with Kelvin probe also contains a contribution of the surface dipole and, if the intensity of the UV-light saturates the SPV, the total amount of the band bending (BB):

$$\mathrm{SPV}_{\mathrm{KP}} = \Delta\delta_{\mathrm{KP}} + \mathrm{BB}. \tag{5.2}$$

Neglecting that the measurements were performed in different environments and building the difference of Δ_{SEC} and $\mathrm{SPV}_{\mathrm{KP}}$ leads to

$$\mathrm{SPV}_{\mathrm{KP}} - \Delta_{\mathrm{SEC}} = \Delta\delta_{\mathrm{KP}} + \mathrm{BB} - \Delta\delta_{\mathrm{XPS}}. \tag{5.3}$$

If the surface dipole is changed by a similar mechanism and only influenced by the UV-light and not by a contribution of the X-rays, it can be assumed that $\Delta\delta_{\mathrm{KP}} = \Delta\delta_{\mathrm{XPS}}$. The band bending can then be extracted by

$$\mathrm{BB} = \mathrm{SPV}_{\mathrm{KP}} - \Delta_{\mathrm{SEC}}. \tag{5.4}$$

Table 5.2.: Estimated surface dipole (δ) and band bending (BB) contributions by the comparison of the initial light-induced photoresponse observed with ambient Kelvin probe and XPS.

GaN(0001) KymaTech	$\mathrm{SPV_{KP}}$ [eV]	Δ_{SEC} [eV]	δ [eV]	BB [eV]
As-received	0.29	0.30	0.30	-0.01
HCl cleaned	0.23	0.19	0.15	0.04

Despite the fact that a variety of assumptions were made, the contributions of the surface dipole and the band bending can be estimated with the values found in Section 5.2.4.1 and in Section 5.2.4.2. The resulting estimations for an as-received and an HCl cleaned *c*-plane KymaTech sample are summarized in Table 5.2. The HCl treated sample reveals a small positive band bending, which is expected for *n*-type GaN surfaces. However, the quite small absolute value of 0.04 eV is close to flat-band conditions. A first complementary UHV-KPFM back-illuminated experiment was performed at a base pressure of 1×10^{-5} mbar yielding an SPV value of 0.8 eV and thereby, a BB of 0.5 eV. This value lies within the average literature value of (0.44 ± 0.70) eV, which was averaged for different measurement techniques [129,307,320,321,325–327]. It weakens the assumption that the measurement environment can be neglected. This fact was also discussed by Foussekis *et al.* [276,322,332]. It further strengthens the hypothesis that the XPS intensity is too high to measure the band bending.

5.2.6. An approach to a complete energy band diagram

An approach to a draw a complete energy band diagram exemplary for the *c*-plane KymaTech GaN(0001) surface was developed with the values found for the optical band gap in Section 5.2.2, the valence band maximum in Section 5.2.3, the work function values in Section 5.2.4.1 and Section 5.2.4.2 and with the estimation of the surface dipole and band bending in Section 5.2.5.

Figure 5.11 shows a schematic illustration of the energy band diagram for a typical HCl cleaned c-plane KymaTech Gan(0001) sample constructed with the data summarized in Table 5.3. The conduction band minimum (E_C) was calculated by the difference of the VBM with respect to the vacuum level and the optical band gap. Note that the lower limit of the VBM was used to separate the Fermi level from E_C. This, however, clearly shows that the E_F is pinned to defect states within the band gap very close to E_C (~ 0.1 eV

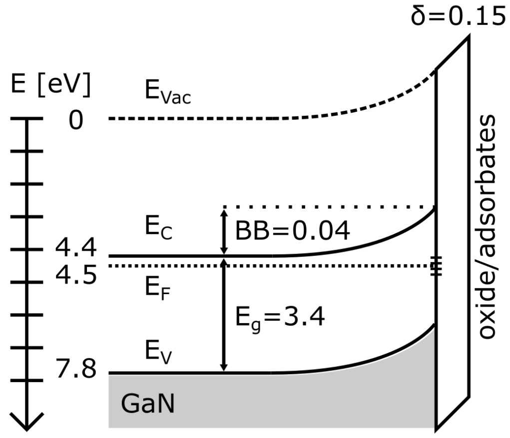

Figure 5.11: Schematic illustration of the energy band diagram deduced from XPS data and KP for an HCl cleaned *c*-plane GaN(0001) KymaTech sample. Possible surface states around the Fermi level were indicated by short lines at the interface to the surface dipole. The surface dipole may be a consequence of a thin oxygen layer and other adsorbates.

Table 5.3.: Summary of the electronic properties extracted from XPS and Kelvin probe measurements for the GaN(0001) KymaTech surface. Samples prior and after the HCl cleaning procedure are compared. Note that δ and BB are estimations by using the approach presented in Section 5.2.5.

GaN(0001) KymaTech	WF [eV]	SPV [eV]	VBM [eV]	δ [eV]	BB [eV]
As-received	4.24 ± 0.29	0.29 ± 0.10	3.6 ± 0.1	0.30	-0.01
HCl cleaned	4.45 ± 0.26	0.23 ± 0.06	3.4 ± 0.1	0.15	0.04

below). Such states have been extensively simulated by Van de Walle and Segev [121,122] (see Section 2.4.2). They attributed these surface states close to E_C to empty Ga-adatom dangling bonds at the reconstructed GaN(0001) surface. Later on, Armstrong *et al.* confirmed the existence of these defect states for *n*-type GaN nanowires using deep level optical spectroscopy [275]. A pinning of the Fermi level is a significant issue as the material becomes independent of temperature and doping level. Instead it shows rather metallic properties with low conductivities. It also hinders proper energy level alignment of other materials with GaN. Furthermore, the quantum confined Stark effect as a function of the radial GaN NW diameter has been recently observed, leading to a red shift of the emission maximum and an increase in the excitonic lifetime [25,26,329]. Different routes to passivate these detrimental surface states will be discussed in the following sections.

5.3. Functionalization of the *c*-plane

Over the past years, a number of groups have suggested surface state passivation and chemical functionalization routes for GaN and GaAs surfaces. The routes can be divided into approaches by adsorption of inorganic or organometallic molecules and purely organic molecules. Among the inorganics, the growth of SiN_x and Al_2O_3 thin layers on top of GaN and GaN/AlGaN heterostructures have shown to successfully decrease the density of surface states [333]. The adsorption of a variety of organic molecules, mostly amines, on GaN was early studied by Bermudez *et al.* [132,334–338]. However, the studies lack detailed information on the monolayer coverage and are not correlated to the photoluminescence. More recently, Schwartz *et al.* demonstrated the successful thermal and photoinduced chemisorption of 1-alkenes on the GaN surface.

In this work, several molecular binding partners were tested and investigated on the GaN(0001) surface in terms of SPV Kelvin probe measurements (see Section 5.2.4.2). In chronological order amines, thiols and phosphonic acids were studied. A complete list of the corresponding molecular structures can be found in Figure A.1.

5.3.1. Amines

As nitrogen is the natural binding partner in the crystal lattice of GaN and assuming that the surface exhibits Ga-dangling bonds after the HCl etching process, amines ($-NH_2$) might preferably interact with the GaN surface and result in strong covalent bonds. To verify the studies by Bermudez [334–336], different amines were purchased and brought into contact with the *c*-plane KymaTech GaN(0001) surface after HCl etching. Among them are, aniline ($C_6H_5NH_2$), ethylenediamine ($NH_2(CH_2)_2NH_2$), hexylamine ($CH_3(CH_2)_5NH_2$), and diethylenetriamine ($(NH_2CH_2CH_2)_2NH$). The GaN samples were immersed into a toluene solution of the neat amine for 4 hours, rinsed with toluene to remove weakly adsorbed or unbound molecules and blown dry with nitrogen afterwards.

Figure 5.12 shows the response of the work function between 365 nm band-to-band illumination periods measured by Kelvin probe. Average values are summarized in Table 5.4. The shapes of the photoresponse for all amine treated GaN samples significantly differ from the one observed on the as-received and HCl cleaned GaN (compare Section 5.2.4.2), where the SPV was instantaneous. Here, the WF decreases with an exponential decay upon illumination. Furthermore, the fast component of the WF restoration after illumination disappears for all amine treated samples. This could be due to a

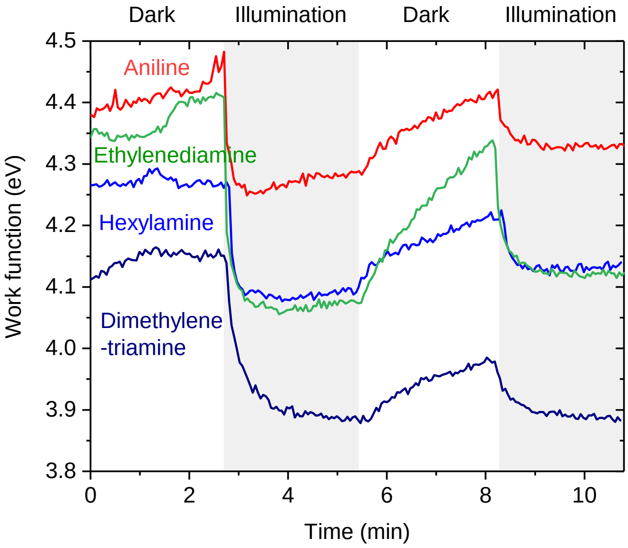

Figure 5.12: Response of the work function under band-to-band illumination of a c-plane GaN(0001) surface after adsorption of different amines. Illumination periods are highlighted as grey areas.

change in the electronic response of the sample after successful surface state passivation and thereby, a reduced band bending. However, the form of the SPV decay and the different time constants of the relaxation after illumination indicate more a photo-induced chemical change at the surface, which would be correlated to a time-dependent change of the surface dipole $\delta(t)$.

In the following the water contact angles (CA) will be discussed. Demirel *et al.* reported a water contact angle of $(65 \pm 2)°$ for a self-assembled monolayer of a diethylenetriamine derivative on Si(001) [339], which significantly differs from the value for diethylenetriamine found here. Rueckenstein *et al.* proposed a water contact angle of a polyaniline layer on glass of 77° and Sabbatani *et al.* a value of $(76 \pm 2)°$ for a dense monolayer of thiophenol on gold. Even though

Table 5.4.: Summary of the work functions, surface photovoltages and water contact angles (CA) after adsorption of amines on the KymaTech GaN(0001) surface.

Gan(0001) KymaTech	WF [eV]	SPV [eV]	CA [°]
Aniline	4.48 ± 0.09	0.22 ± 0.04	55.0 ± 5.6
Ethylenediamine	4.41 ± 0.08	0.28 ± 0.06	19.2 ± 5.8
Hexylamine	4.27 ± 0.17	0.19 ± 0.02	35.7 ± 4.1
Dimethylenetriamine	4.16 ± 0.03	0.24 ± 0.05	26.9 ± 1.3

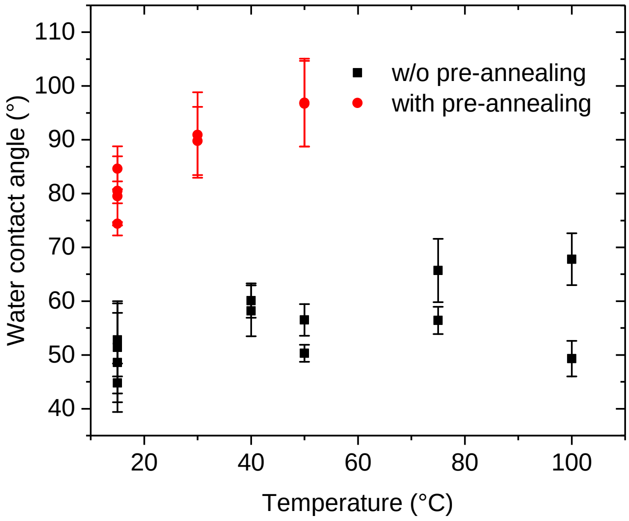

Figure 5.13: Water contact angles measured on KymaTech c-plane GaN(0001) samples after the adsorption of PFDT. The x-axis corresponds to the solution temperature during the immersion. Data points in red were obtained on substrates which were previously annealed at 370 °C.

no directly comparable values can be found in literature so far, both values are not in good agreement with the $(55 \pm 6)°$ CA for the GaN/aniline sample here. It is concluded that the KymaTech c-plane GaN(0001) surface cannot be covered by a complete monolayer of amines and that amines are not the proper choice for GaN surface functionalization under ambient conditions.

5.3.2. Thiols

Many research groups used sulfur as a passivation agent on GaN because of its good coordination chemistry with Ga [314,340–342]. Thiols are known to form strong thiolate bonds with metal atoms. However, this again presumes a highly Ga-exposed surface. As it was seen in Section 5.2.1 that the HCl cleaning procedure alone is not sufficient to remove all oxygen and turn the surface into a fully Ga-terminated one, a high temperature annealing step of the GaN sample was added prior to the thiol adsorption. The high thermal energy might be able to dissociate further hydroxyl groups and lead to their desorption [133,337]. For this reason, the samples were first HCl cleaned and then transferred into a nitrogen filled glovebox, where they were annealed at 370 °C for at least 12 hours on a hot plate. Afterwards the samples were cooled down and immersed into the thiol-toluene solution for another 12 hours, rinsed with pure toulene and dried with a stream of nitrogen.

To see whether high temperature is beneficial for the thiol coverage, a series of water contact angle measurements were performed with and without annealing step. Additionally, the temperature during the adsorption process was varied. Figure 5.13 shows the CAs for the KymaTech c-plane GaN(0001)

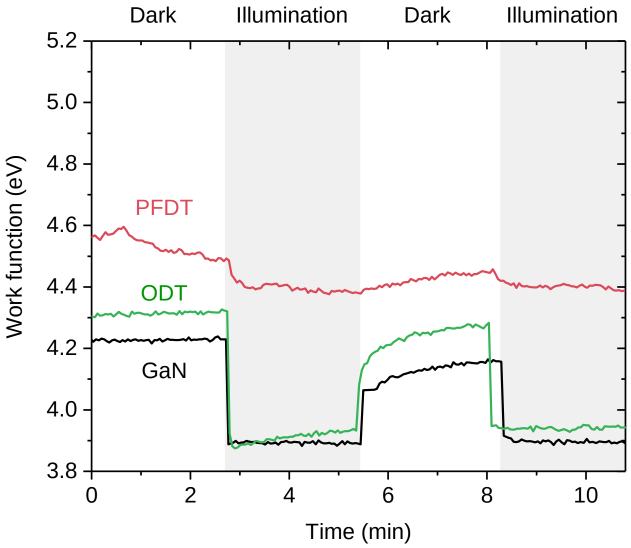

Figure 5.14: Response of the work function under band-to-band illumination of a *c*-plane GaN(0001) surface after adsorption of different thiols. Illumination periods are highlighted as grey areas.

surface after adsorption of Perfluorodecanethiol (PFDT) for different thiol solution temperatures. All measurements show a good reproducibility between multiple prepared samples. With the prior annealing step the CA values are $30° - 40°$ higher than without. Higher solution temperatures also lead to an increase of the contact angle to a maximum of $(96.0 \pm 5.9)°$. Note that the boiling temperature of toluene is 110 °C. A further increase of the solution temperature did not result in higher contact angles. Hence, a maximum PFDT coverage at 50 °C with prior annealing of the substrate was found. For a dense monolayer of PFDT on gold a maximum CA of $(115 \pm 1)°$ was reported [94]. 1-Octadecanethiol (ODT) was chosen as a second adsorption precursor. For ODT a water contact angle of $(71.5 \pm 2.1)°$ is found, which was also lower than the range of 104°-112° reported in literature [83,343]. Thus, the coverage of thiols on HCl etched GaN(0001) is not ideal here.

Figure 5.14 shows the work function between band-to-band illumination

Table 5.5.: Summary of the work functions, surface photovoltages and water contact angles (CA) after adsorption of thiols on the KymaTech GaN(0001) surface.

GaN(0001) KymaTech	WF [eV]	SPV [eV]	CA [°]
PFDT	4.47 ± 0.22	0.10 ± 0.11	96.0 ± 5.9
ODT	4.30 ± 0.08	0.38 ± 0.02	71.5 ± 2.1

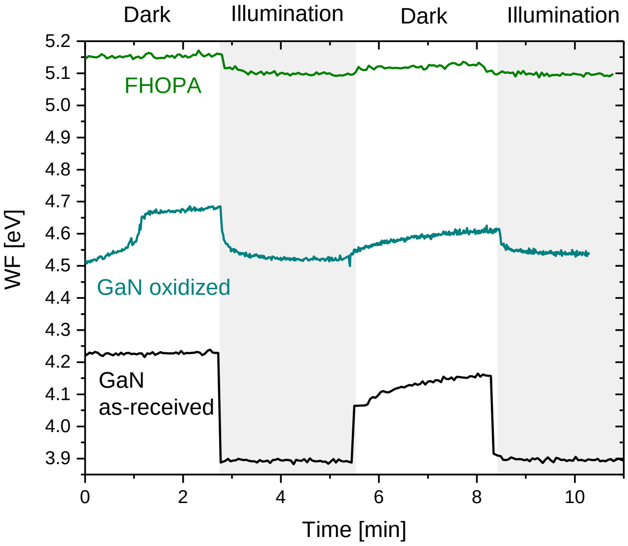

Figure 5.15: Response of the work function under band-to-band illumination of a *c*-plane GaN(0001) surface after adsorption of FHOPA. Illumination periods are highlighted as grey areas.

periods after adsorption of the thiols. Average WF and SPV values are summarized in Table 5.5. PFDT shows an average WF of (4.47 ± 0.22) eV. In comparison to the as-received and the ODT modified sample, the SPV almost completely disappears with PFDT. Furthermore, the fast WF restoration component cannot be observed anymore and the relaxation of the WF after illumination is very slow. This is not the case for the ODT sample, which does not significantly increase the work function and almost shows no difference in the SPV to the as-received GaN. This leads to the interpretation that the PFDT influences the electronic and chemical properties of the GaN surface, such that it passivates the surface and prevents a change in the surface dipole.

5.3.3. Phosphonic acids

While the thiols required a Ga-termination at the GaN surface to yield a high coverage, the simultaneous investigation of the functionalization of nickel oxide with phosphonic acids (see Section 4.3.4) led to the idea of applying PAs also on the GaN. At this point of the work, it was believed that a thin oxide layer is as detrimental to the photoluminescence as unpassivated Ga-dangling bonds [344]. Therefore, the PAs used in this section were used as a proof-of-concept. In order to adsorb the PAs, the GaN samples were not HCl etched but exposed to O_2-plasma prior to the immersion. The samples were removed from the PA-ethanol solution after 4 hours and annealed under nitrogen atmosphere at 130 °C for additional 2 hours on a hot plate to activate the phosphonate bonding.

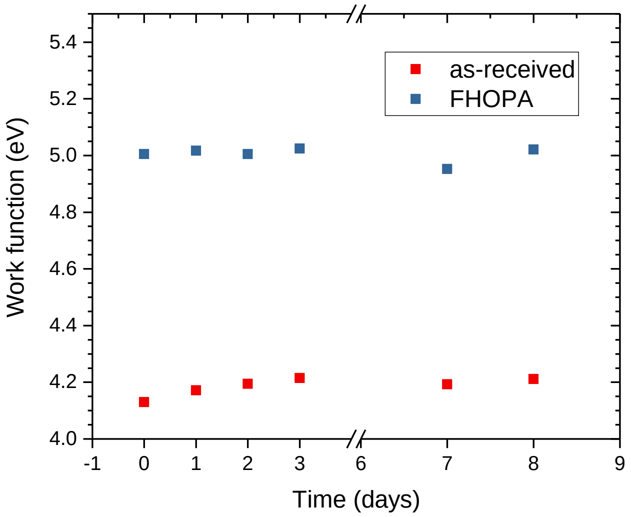

Figure 5.16: Work function stability of FHOPA on the KymaTech *c*-plane GaN(0001) compared to an as-received sample. The increased WF is stable over several days in ambient air.

Figure 5.12 shows the work function between band-to-band illumination periods measured with KP. The WFs and SPVs for different experiments are summarized in Table 5.4. From the contact angles it can be seen that the O_2-plasma leads to a strongly hydrophilic surface, while Tridecafluorooctylphosphonic acid (FHOPA) renders the surface strongly hydrophobic $(106.7 \pm 1.2)°$. This value is significantly higher compared to the value found for PFDT and is very close to the optimum of $(115 \pm 1)°$ found for dense fluorinated monolayers on gold. The work function is also increased up to (5.17 ± 0.19) eV. Both findings indicate a high coverage of FHOPA on the oxidized *c*-plane GaN(0001) KymaTech sample. The oxidization itself increases the work function only to (4.57 ± 0.05) eV.

Due to the adsorption of FHOPA not only the WF is shifted to high values, but also the SPV and the restoration after illumination disappear. This is not the case for the barely oxidized sample, where an SPV of around (0.21 ± 0.09)

Table 5.6.: Summary of the work functions, surface photovoltages and water contact angles (CA) after adsorption of FHOPA on the KymaTech GaN(0001) surface.

GaN(0001) KymaTech	WF [eV]	SPV [eV]	CA [°]
oxidized	4.57 ± 0.05	0.21 ± 0.09	< 10
FHOPA	5.17 ± 0.19	0.10 ± 0.06	106.7 ± 1.2

can be seen. However, also the fast component after illumination cannot be observed anymore for the O_2-plasma sample. Together with the findings for PFDT in Section 5.3.2, it might be argued that either the formation of an oxide layer or the adsorption of SAM precursor with high electronegative backbone, e.g. strong acceptor molecules, lead to the suppression of the fast WF recovery. Then, the fast WF recovery might be attributed to the photoinduced oxidative adsorption of molecular oxygen, which is not occuring in vacuum. Even though FHOPA and PFDT minimize the SPV and the second initiated SPV is smaller than the first, it is very difficult to extract the impact of these molecules on surface states and on the band bending with the Kelvin probe method in ambient. In terms of chemical passivation, the work function increase of FHOPA is stable over several days compared to an as-received sample (see Figure 5.16). This allows to conclude that despite the intentional growth of an oxide layer, the adsorption of FHOPA has an influence on the surface potential of the GaN and the chemical stability at the surface is increased.

5.3.4. Correlation to the photoluminescence

In order to evaluate the influence of SAM precursor with the tendency to passivate Ga surface states onto the photoluminescence, hexylamine and PFDT functionalized *c*-plane GaN(0001) samples were shipped to the PDI and investigated by TR-PL. The samples were excited with a 325 nm laser and 200 fs pulses at a spot size of 50 μm^2 (power density of 6 $W\,cm^{-2}$). Figure 5.17 shows the TR-PL measurements of the hexylamine and PFDT coated KymaTech samples compared to an oxidized and an as-received sample. The intensity is given in arbitrary units and the time in ps. The maximum intensity is the highest for the as-received sample and comparable with the PFDT sample. The intensity slightly decreases with hexylamine and even stronger for the oxidized sample. Table 5.7 compares the excitonic lifetimes that were extracted by an exponential fit of the intensity decay. It can be observed that the lifetime is barely affected by the surface treatment. Only the oxidized sample shows a slightly reduced excitonic lifetime. Even this value, however, is still within the errors of the other samples. Most probably the high defect density in the bulk of the GaN KymaTech template dominates the recombination and therefore, changes at the surface are only marginal.

In addition to the *c*-plane KymaTech sample, the bulk Kyma-Tech GaN, which exhibits a lower defect density (Table 3.1), was functionalized with PFDT and measured with TR-PL. Figure 5.18 shows the corresponding excitonic lifetimes obtained on different sample positions. Before PFDT coating the lifetime is above 310 ps. After the PFDT treatment the lifetime is reduced

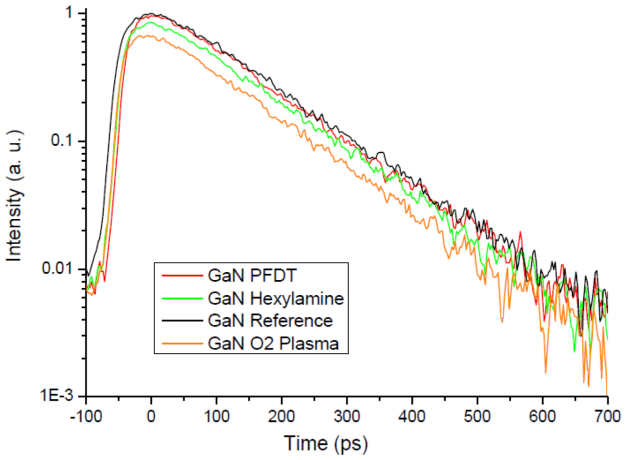

Figure 5.17: Time-resolved photoluminescence measurements of the excitonic lifetime for differently treated *c*-plane KymaTech samples.

Table 5.7.: Excitonic lifetimes for differently treated KymaTech *c*-plane GaN(0001) samples corresponding to the measurements shown in Figure 5.17.

GaN(0001) KymaTech	Lifetime τ [ps]
Reference	129 ± 10
Oxidized	120 ± 10
Hexylamine	124 ± 10
PFDT	123 ± 10

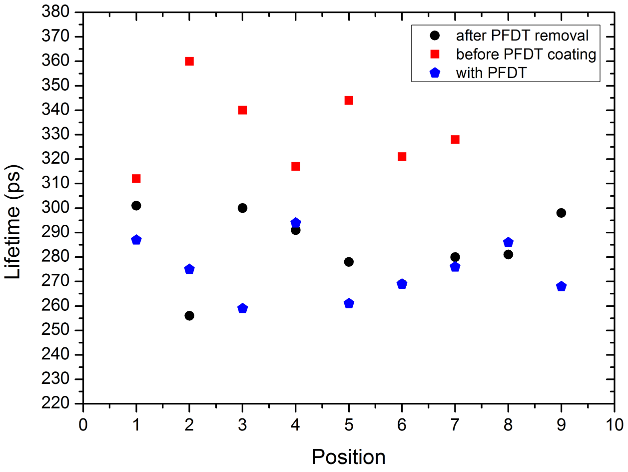

Figure 5.18: Excitonic lifetimes of the free-standing bulk GaN(0001) sample measured on different sample positions, before PFDT coating, with PFDT and after the PFDT removal.

to 270 ps. However, when the PFDT is removed from the same sample the original lifetime is not recovered. This indicates that the treatment itself leads to a slight decrease of the PL lifetime on this sample and not the PFDT modification. As the lifetimes only vary in a small ps-regime, the bulk defect density is expected to be still too high to measure surface induced changes of the lifetime.

5.4. Functionalization of the *m*-plane

With the progress of the project, new free-standing *c*-plane and *m*-plane GaN samples were grown by MBE at the PDI. These samples exhibit a very low density of dislocations compared to the previously investigated ones. Furthermore, their surface showed no roughening and surface reconstruction during the growth process leading to smooth surfaces with atomic terraces visible. Together with the knowledge gained on the c-plane KymaTech samples, the idea was established to develop a controlled wet-chemical functionalization protocol incorporating a more defined oxide layer. This protocol was applied to the higher quality *m*-plane samples and will be discussed in the following sections.

5.4.1. Oxide template layer for phosphonic acids

The protocol for an oxide template involved a strict sequence of processing steps: HCl cleaning procedure, high temperature annealing and an O_2-plasma treatment. For clarity the exact protocol is described in Section 3.2.4. Following this recipe, each step was applied to an *m*-plane sample and investigated subsequently with XPS. Figure 5.19 shows the corresponding XP survey spectra. The overall spectral features are in good agreement with the observations in Figure 5.3. Due to the different processing steps the intensities of particular core levels vary. After the HCl cleaning, a small but significant amount of residual Cl (200 eV BE) remains on the surface. These residuals can efficiently be removed by annealing the sample at 400 °C on a hot plate under nitrogen atmosphere. However, the annealing leads to the adsorption of carbon species (285 eV BE), which can finally be removed by oxygen plasma.

The plasma treatment induces to strong increase of the O 1s core level, which confirms the growth of an oxide layer (see Figure 5.20). The adsorption of FHOPA and OPA dampen the oxidized O 1s. The fact that the strength of the dampening differs between both molecules might be a consequence of a different degree of coverage. While OPA does not show any fluorine signal,

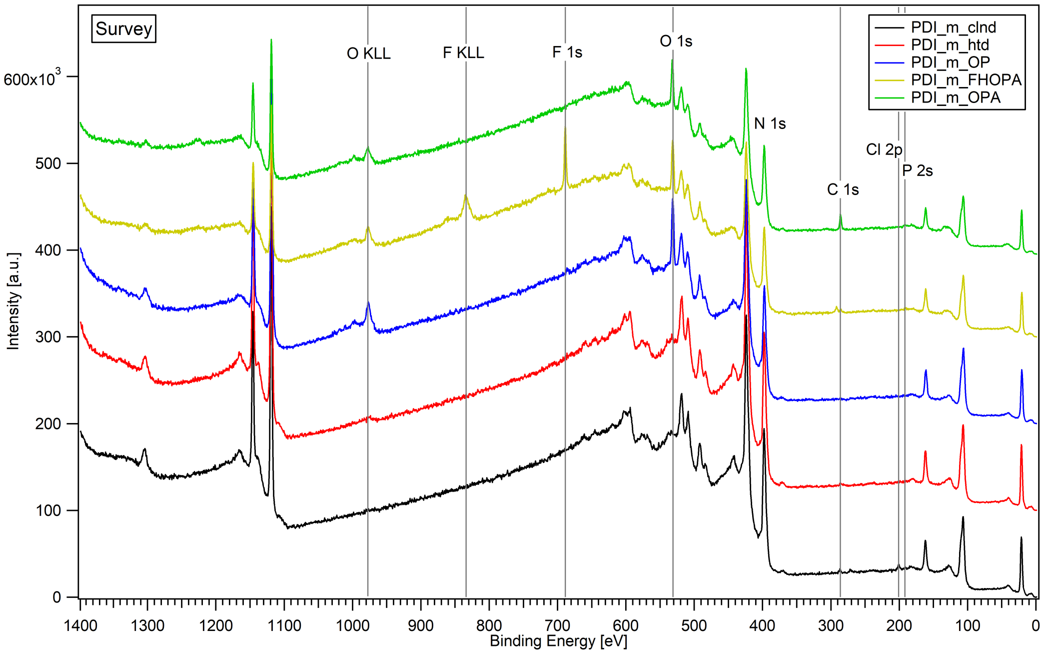

Figure 5.19.: XP survey spectra of free-standing m-plane GaN($1\bar{1}00$) samples (i) cleaned with HCl, (ii) annealed at 400 °C under nitrogen atmosphere (iii) treated with oxygen plasm, (iv) functionalized with FHOPA, and (v) with OPA.

the FHOPA sample shows two components, one at 688.5 eV and one with smaller intensity at 685 eV. These components can be assigned to the CF_2 and CF_3 of the molecular backbone of FHOPA. According to the molecular stoichiometry, the signal of the CF_3 should be much weaker, which can clearly be observed here. In addition to the damping of the O 1s core level, the peaks are shifted to higher binding energies after chemisorption of FHOPA and OPA, relative to the peak position of the oxidized Ga $2p_{3/2}$ core level. This is the first qualitative observation of a change in band bending as this shift was also seen in the VBM. The change in band bending seems to correlate with the chemical structure of the molecular backbone. The polar and electronegative FHOPA shifts the core level less than the OPA with the simple alkyl-chain. Note that both molecules lead to a bonding dipole through the phosphonate, which is believed to point in the opposite direction of the intrinsic dipole moment of the fluorinated backbone. Furthermore, FHOPA increased the work function to 5.2 eV on the KymaTech GaN(0001) (see Table 5.6) and to 5.6 eV on the GaN($1\bar{1}00$) surface, which is higher than the work function of the oxidized m-plane surface (5.2 eV). The work function for OPA on GaN($1\bar{1}00$) was around 4.0 eV.

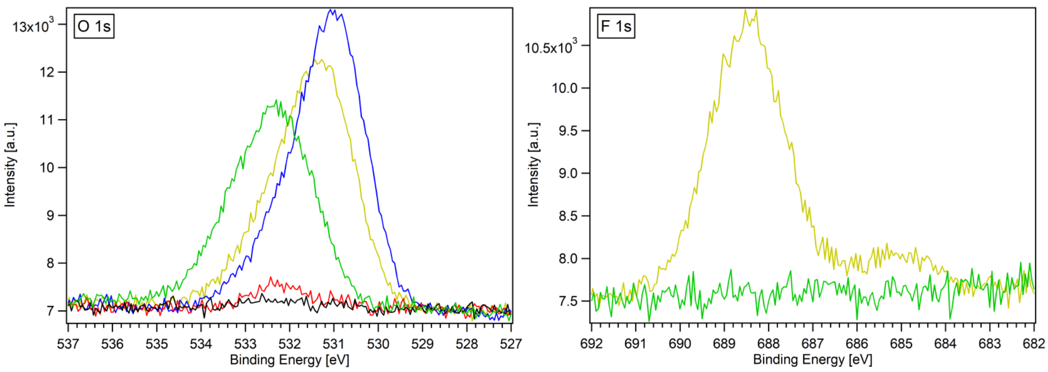

Figure 5.20.: O 1s and F 1s XP detail core level spectra for the different treatment procedures. The color list corresponds to the one given in Figure 5.19, HCl cleaned state (black), after annealing (red), after OP treatment (blue), with FHOPA (yellow) and with OPA (green). The strong increase of the O 1s indicates the growth of an oxide layer after the O_2-plasma treatment and the shift to lower binding energies a positive upward band bending. Core levels with FHOPA and OPA are shifted to higher binding energies compared to the oxidized sample, reflecting a decrease of the band bending.

It can be concluded that the oxygen plasma treatment leads a change of the surface dipole and to a positive band bending at the GaN surface. The PA-SAMs of FHOPA and OPA are capable of decreasing this BB, OPA stronger than FHOPA. Figure 5.21 depicts the proposed changes of the surface potential on *m*-plane GaN($1\bar{1}00$) for all three surface modifications. A part of the band bending reduction seems to be addressed to the chemisorption of the phosphonate and a second contribution correlated to the chemical character of the backbone. The results suggest that the backbone should be less electronegative to completely suppress BB. Furthermore, it confirms the

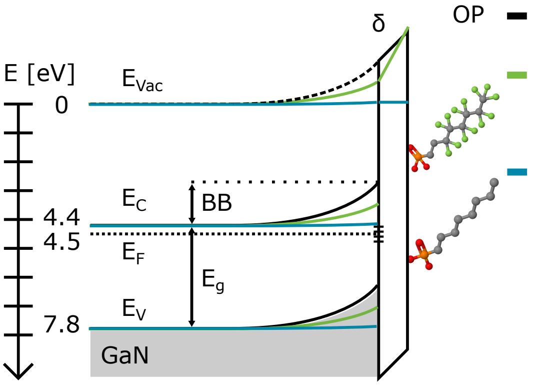

Figure 5.21: Schematic illustration of the impact of PA-SAMs on the *m*-plane GaN($1\bar{1}00$) surface. The color codes are (blue) alkyl chain (OPA), (green) fluorinated alkyl chain (FHOPA), and (black) oxygen plasma treatment (OP). For convenience the surface dipole is only drawn in the solid region indicating the adsorbate layer.

hypothesis that acceptor states are increasing the band bending of the n-type GaN surface (see Section 2.4.3). However, the attachment of an electron repelling molecule might neutralize these states.

5.4.2. Correlation to the photoluminescence

To correlate the change in band bending due to the adsorption of OPA and FHOPA with the photoluminescence, MBE grown free-standing *m*-plane and *c*-plane samples were functionalized with the PAs and shipped to the PDI for TR-PL investigation at the end of the thesis. The following section presents the first results and further measurements will follow.

Figure 5.22 shows the continuous-wave photoluminescence (cw-PL) of an oxidized reference and a FHOPA functionalized *m*-plane GaN sample. The band edge cw-PL was measured with a power of 70 µW at 300 K and 0.7 µW at 10 K. In both measurements the PL intensity is 10 times higher for the FHOPA coated samples. The TR-PL measurements were performed at 10 K and 325 nm excitation wavelength. Table 5.8 summarizes the extracted excitonic lifetimes τ_{eff} and intensities I_{PL} for the differently treated m-plane samples. A small but insignificant shortening of the lifetime from 250 ps to 190 ps with FHOPA can be observed. However, the intensity is increased by an order of magnitude. The intensity is even comparable to that of a sample with an overgrown layer of AlGaN, which is considered to act as a perfect passivation layer for MBE

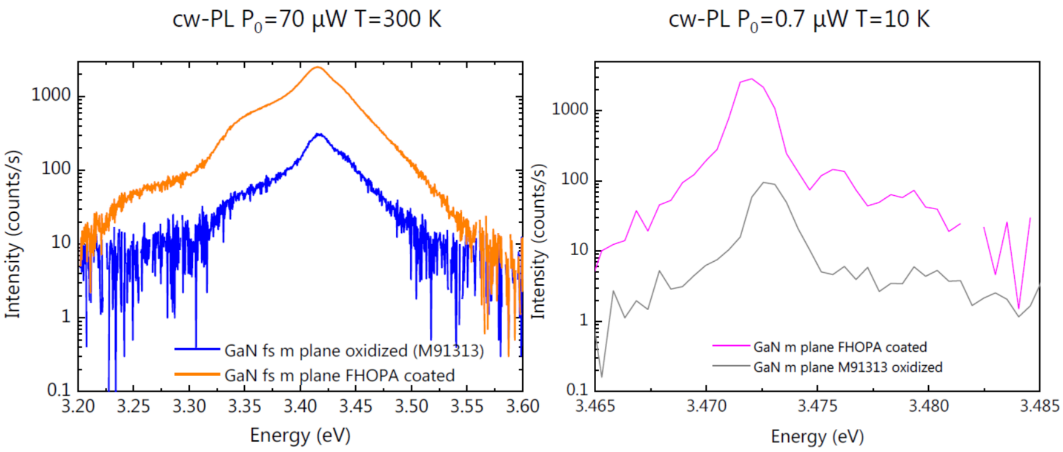

Figure 5.22.: Continuous-wave photoluminescence (cw-PL) of an oxidized (blue) and a FHOPA functionalized (orange) free-standing m-plane GaN sanple. cw-PL was performed at 300 K (left) and 10 K (right).

grown GaN due to the formation of a type I interface with GaN [345]. Recent studies for this perfect type of passivation did as well not observe an increase of the PL lifetime, which indicates that the lifetime is still dominated by non-radiative recombination in the bulk, most likely related to point defects, and not influenced by the surface. However, the total PL intensity (I_{PL}) depends on both the non-radiative decay time (τ_{nr}) and on the radiative decay time (τ_r):

$$I_{\mathrm{PL}} \propto \frac{1/\tau_r}{1/\tau_r + 1/\tau_{nr}}. \tag{5.5}$$

The radiative decay time increases in the presence of an electric field, such as band bending, which then leads to a decrease of the PL intensity and *vice versa*. Thus, the PL intensity increase might indeed be correlated with the observed difference in the band bending through FHOPA. Further investigations on OPA and the repetition of the experiment need to prove the validity of the experimental results gained in this section.

Table 5.8.: Low temperature (10 K) TR-PL excitonic lifetimes and cw-PL intensities measured on differently treated m-plane GaN samples.

Sample m-GaN	τ_{eff} [ps]	I_{PL} [cps]
as grown	240 ± 40	-
+ oxidized	-	10^2
+ AlGaN	250 ± 50	$10^3 - 10^4$
+ FHOPA	190 ± 20	9×10^3

5.5. Conclusion

In this chapter an introduction to GaN nanowires and the motivation of enhancing their photoluminescence quantum yield in a broader scope was given. GaN NWs exhibit different facets and polarities and suffer from emission quenching and a high surface to volume aspect ratio. In order to gain fundamental knowledge on the electronic and chemical properties of the different facets, planar GaN crystals were investigated as a model systems. As a precondition for the correct characterization of the surface properties, the substrates had to be cleaned in a wet chemical process to minimize the influence of contaminants. A step-by-step procedure of solvent cleaning, plasma treatment and HCl etching was developed (see Section 3.2.4) to obtain *c*-plane GaN(0001) samples with very small amounts of residual carbon and oxygen (see Section 5.2.1). In order to deduce the electronic properties of the *c*-plane GaN in the form of a complete energy diagram, the optical bandgap (Section 5.2.2), the valence band maximum (Section 5.2.3) and the work function (Section 5.2.4) were experimentally determined. While the core levels and the VBM did not shift under band-to-band illumination, the work function showed a fast decrease of 0.30 eV and 0.19 eV for an as-received and HCl-etched sample, respectively. An approach was presented to estimate the band bending, which is difficult to access with the high-intensity of the XPS setup. A discrepancy between the XPS and Kelvin probe-measured WF was observed and used to extract the band bending by the difference of the initial photoresponse, denoted as SPV in KP. A small upward band bending of 0.04 eV was found in case of the HCl cleaned sample (see Section 5.2.6). Of course, this value remains an estimation and should be handled with care. A complementary back-illuminated UHV-KPFM experiment resulted in a significantly higher SPV of 0.8 eV, which results in a band bending of 0.5 eV. Hence, it can be concluded that the measurement environment plays an important role in the determination of the surface dipole and band bending contribution to the change of the surface potential. Values given in literature often do not consider the doping level of the sample, which makes it difficult to compare different experimental results. A detailed UHV-KP control experiment is needed to shed more light onto the band bending phenomenon, which has a major influence on the opto-electronic properties of the GaN nanowires.

In order to influence the surface potential and achieve a better control over the chemical properties of the GaN surface, different functional modifiers were introduced and tested to form self-assembled monolayers on GaN. Among them were amines (Section 5.3.1), thiols (Section 5.3.2) and phosphonic acids (Section 5.3.3). While amines could not be successfully deposited as monolayers, PFDT was able to form monolayers but with low total coverage. As not all oxygen can be removed from the GaN surface by the wet-chemical etching, it will be difficult to bind a perfect monolayer of thiols onto GaN under ambient conditions. Hence, O_2-plasma was used to grow an oxygen seed layer for the coupling of phosphonic acids to the hydroxylated GaN surface (Section 5.3.3). High contact angles with water above 100° were achieved with the fluorinated PA (FHOPA), indicating the dense packing of these molecules on the oxidized surface. With FHOPA the surface was influenced electronically, as could be seen in the illumination dependent Kelvin probe measurements, and passivated chemically. The chemical passivation was reflected in the loss of the photoinduced fast and slow component of the WF restoration in ambient environment (see Figure 5.15). This hints towards that photoinduced oxidative adsorption is suppressed in ambient, which was previously not observed during the XPS measurements in vacuum.

The low quality in terms of a high defect density of dislocations in the *c*-plane GaN(0001) KymaTech template and bulk samples hindered the correlation between the surface functionalization and the photoluminescence in the first case. With the new higher quality MBE grown m-plane substrates by the PDI, a first influence of the surface modifiers on the band bending was observed (see Figure 5.20). While FHOPA did not lead to an increase of the excitonic lifetime measured with TR-PL, the intensity in cw-PL measurements was increased by one order of magnitude compared to the oxidized sample (see Figure 5.22). This might correlate with the strong upward band bending induced by the oxidization and a shift to a smaller band bending by FHOPA. However, further investigations on OPA and the repetition of the experiment need to prove the validity of the experimental results.

It can be concluded that the cleanliness of GaN surfaces under investigation is essential in order to obtain meaningful values for the surface electronic properties. The passivation by sulfur and their derivatives is only possible if the GaN surface is completely terminated by metallic Ga atoms. Hence, a compromise of a hydroxylated seed layer was found for the coupling of phosphonic acids to the GaN surface. Despite the underlying thin oxide layer, the band bending was influenced by the chemisorption and molecular backbone of the PA-modifiers. The impact on the band bending seems to correlate with the cw-PL intensity. Therefore, measuring the impact of further different molecular backbones on the total PL intensity would be of high interest to achieve controllability of the GaN surface not only chemically, but also electronically.

6. Summary and outlook

Within the scope of this work, two major topics were studied. On the one hand transition metal oxides as hole-contact layers and on the other hand the wet-chemical passivation of gallium nitride surface states. Both subjects were addressed by the fundamental characterization of the material's surface properties and its changes after functionalization with self-assembled monolayers.

In Chapter 4, the transition metal oxides MoO_3 and sNiO were investigated. Freshly vacuum evaporated MoO_3 exhibited a very high work function of around $6.9 - 7.0\,\mathrm{eV}$, which is favorable for many donor materials with high ionization potentials. However, it was shown with a time-dependent Kelvin probe microscopy experiment in ultra-high vacuum that the work function is not stable over time (see Section 4.2.1). The initial WF started to decrease within minutes after evaporation at a base pressure of $1 \cdot 10^{-8}$ mbar. After a week in vacuum a minimum value of $5.0\,\mathrm{eV}$ was determined, which is almost $2.0\,\mathrm{eV}$ below the initial value. Two major components causing the WF to decrease were identified with a controlled oxygen exposure experiment in Section 4.2.2. A fast component was addressed to the adsorption of molecular oxygen and a second slower component assigned to the formation of a surface dipole layer by the adsorption of water. To answer whether the adsorption of molecular oxygen leads also to a refilling of the bulk oxygen vacancies in MoO_3 thin films, the conductivity of such films was measured in a two-terminal configuration under vacuum and exposure to oxygen in the UHV-AFM (see Section 4.2.3). The combination of WF decay and faster increase of the current under oxygen exposure suggests that oxidative adsorption of molecular oxygen takes place, which is associated with a charge transfer to the surface of the MoO_3. It is important to be aware of the work function instability of MoO_3 and its origin during fabrication. The deposition of organic donor materials on MoO_3 should be performed as fast as possible to conserve the high work function of the material for proper energy level alignment (see Figure 4.1). The results might also be transferred to similar transition metal oxides and help to avoid the formation of energetic charge injection and extraction barriers in multilayer opto-electronic devices.

The second transition metal oxide, solution-processed NiO, showed a significantly lower initial work function compared to MoO_3 due to the fabrication under ambient conditions (see Figure 4.11). Work functions were around 4.7 eV and showed a dependency on the film annealing temperature. This correlated with the higher amount of stoichiometric NiO in the films, which was detected with infrared spectroscopy as well as photoelectron spectroscopy measurements in Section 4.3.2. In order to obtain a similarly high work function as MoO_3 thin films, the surface of the sNiO was modified with the work function increasing self-assembled monolayers of 4-cyanophenyl-phosphonic acid (CYNOPPA). The work function was successfully increased to $5.1-5.2$ eV. From an energetic point of view the CYNOPPA modified sNiO should align perfectly to F_4ZnPC donor utilized in organic photovoltaic cells here. However, the incorporation of sNiO/CYN hole-contact layers into F_4ZnPc:C_{60} bulk and flat-heterojunction solar cells led to the rise of an s-kink in the operating regime (see Figure 4.22). The s-kink was attributed to the formation of a transport barrier. Through several test experiments, including light-intensity dependent measurements (see Section 4.4.6.1) and the variation of the hole-contact layer thickness (see Section 4.4.6.2), the nature of the transport barrier was examined. It was proven that this barrier is not solely a consequence of energetic mismatch between hole-contact layer and F_4ZnPc but rather caused by a very low conducive interface region, which was reflected in a strong increase of the series resistance of devices with CYNOPPA functionalized sNiO hole-contact layers (see Figure 4.32). This allowed to conclude that the barrier is a kinetic transport barrier, which hinders holes from being extracted at sufficiently high rates. However, the barrier could be reduced by doping the sNiO hole-contact layer with CuO and thereby increasing its conductivity (see Section 4.4.6.3). The comparison to the oxygen plasma treated sNiO shows that the work function of the hole-contact layer is not the only parameter that provides interface functionality. For device optimization it might be more important to tune the intrinsic thermodynamic selectivity of metal oxide interlayers by adjusting their valence and conduction band, respectively, and increase the doping level through a change in stoichiometry of the film. Nevertheless, the results show that self-assembled monolayers of phosphonic acids can successfully be utilized to tune the surface characteristics of metal oxides, but great care must be taken when applying such surface modifiers to oxides with low intrinsic charge carrier densities in photovoltaic cells.

The knowledge obtained from the application of phosphonic acids onto metal oxides could simultaneously be transferred to the second major topic, which was the wet-chemical passivation of gallium nitride surface states in Chapter 5. Unoccupied defect states, such as dangling bonds, were discussed to act as acceptor states in the midgap of GaN and are likely to trap charge carriers (see Section 2.4.2). In first experiments on low quality heteroepitaxially grown planar GaN(0001) a step-by-step wet-chemical HCl cleaning protocol was developed to obtain a clean GaN surface for SAM growth (see Section 3.2.4). XPS measurements on the KymaTech GaN(0001) in Section 5.2.1 and on the homoepitaxially grown *m*-plane GaN($1\bar{1}00$) in Section 5.4.1 showed that oxygen as well as carbon contaminants were reduced to a minimum through this protocol. Amines and thiols were tested as binding partners and passivation agents for the GaN surface in the beginning. However, amines did not chemisorb and SAMs of thiols suffered from low coverages, probably because even after the HCl etch not all surface sites are Ga-sites. Therefore, an oxide template layer was grown on the GaN surface by an oxygen plasma treatment to enable the formation of phosphonic acid SAMs on GaN. It was shown that high coverages with Tridecafluorooctyl-phosphonic acid (FHOPA) and Octyl-phosphonic acid (OPA) were achieved on high quality *m*-plane GaN surfaces grown by molecular beam epitaxy at the PDI (see Section 5.4.1). Electronically, the oxidation of the GaN surface led to a an increase of the surface dipole and a strong upward band bending reflected in a core level shift towards lower binding energies. This confirms the hypothesis of acceptor states introduced by oxide layers discussed in Section 2.4.3. However, the band bending was successfully influenced (unpinned Fermi level) and reduced through the chemisorption of the PA-SAMs afterwards. A correlation between the magnitude of the reduction and the chemical structure of the molecular backbone was observed in Section 5.4.1, but a more quantitative analysis of the measurement results is needed. At this point one can conclude that the less electronegative the SAM backbone is the more the band bending is decreased, probably by chemical passivation of oxide acceptor states and push-back of negative surface charges into the GaN. First cw-PL measurements on GaN($1\bar{1}00$) showed that the total PL-intensity increases with FHOPA functionalization compared to the oxidized substrate (see Section 5.4.2). The excitonic lifetime stayed nearly the same, which indicates that the lifetime is still dominated by non-radiative recombination, most likely related to point defects, in the bulk of the MBE grown free-standing GaN substrates. As the quantum confined Stark effect is not expected for nanowires due to their *non-polar* side facets, the loss of quantum efficiency is mainly addressed to Shockley-Read-Hall recombination with trap states and to the spatial separation of the electron-hole wavefunctions in the presence of the electric field of the surface states (radial Stark effect [274]). The PL results with FHOPA suggest that the wet-chemical functionalization with phosphonic acids on oxidized GaN is a promising approach to achieve control on the surface's chemical and electronic properties. The findings on planar GaN substrates might be transferred to GaN nanowires, especially with *m*-plane sidewalls, and help to reduce the radial Stark effect through the influence of the PA-SAMs on the electric field at the NW surface.

In conclusion, the present work highlighted the versatility of surface functionalization of inorganic surfaces by organic molecules. The combination of high performance inorganics and functional organics enables the tunability of the chemical and electronic properties of the surface of interest, which will be of importance for optimized interfaces in hybrid opto-electronic devices in the future.

A. Appendix

Table A.1.: Overview on substances used in this work.

Substance	Molecular weight	CAS number
Nickel(II) acetate tetrahydrate (NiAc)	248.84	6018-89-9
Cupper(II) acetate monohydrate (CuAc)	199.65	6046-93-1
Molybdenum(VI) oxide	143.94	1313-27-5
Ethanolamine (MEA)	61.08	141-43-5
Fluorinated Zinc Phtalocyanine (F4ZnPc)	649.89	1120355-28-3
Buckminster fullerene (C60)	720.64	99685-96-8
1,3,5-tris(2-N-phenylbenzimidazolyl) -benzene (TPBi)	654.777	192198-85-9
SAM precursor		
Aniline	93.129	62-53-3
Ethylenediamine	60.1	107-15-3
Hexylamine	101.193	111-26-2
Diethylenetriamine	103.169	111-40-0
Perfluorodecanethiol (PFDT)	480.183	34143-74-3
1-Octadecanethiol (ODT)	286.562	2885-00-9
Tridecafluorooctyl-phosphonic acid (FHOPA)	428.086	252237-40-4
Octyl-phosphonic acid (OPA)	194.211	4724-48-5
4-cyanophenyl-phosphonic acid (CYNOPPA)	183.103	16672-78-9
4’(dimethylamine)-[1,1’biphenyl]-4 -phosphonic acid (DiDi2PA)	-	synthesized

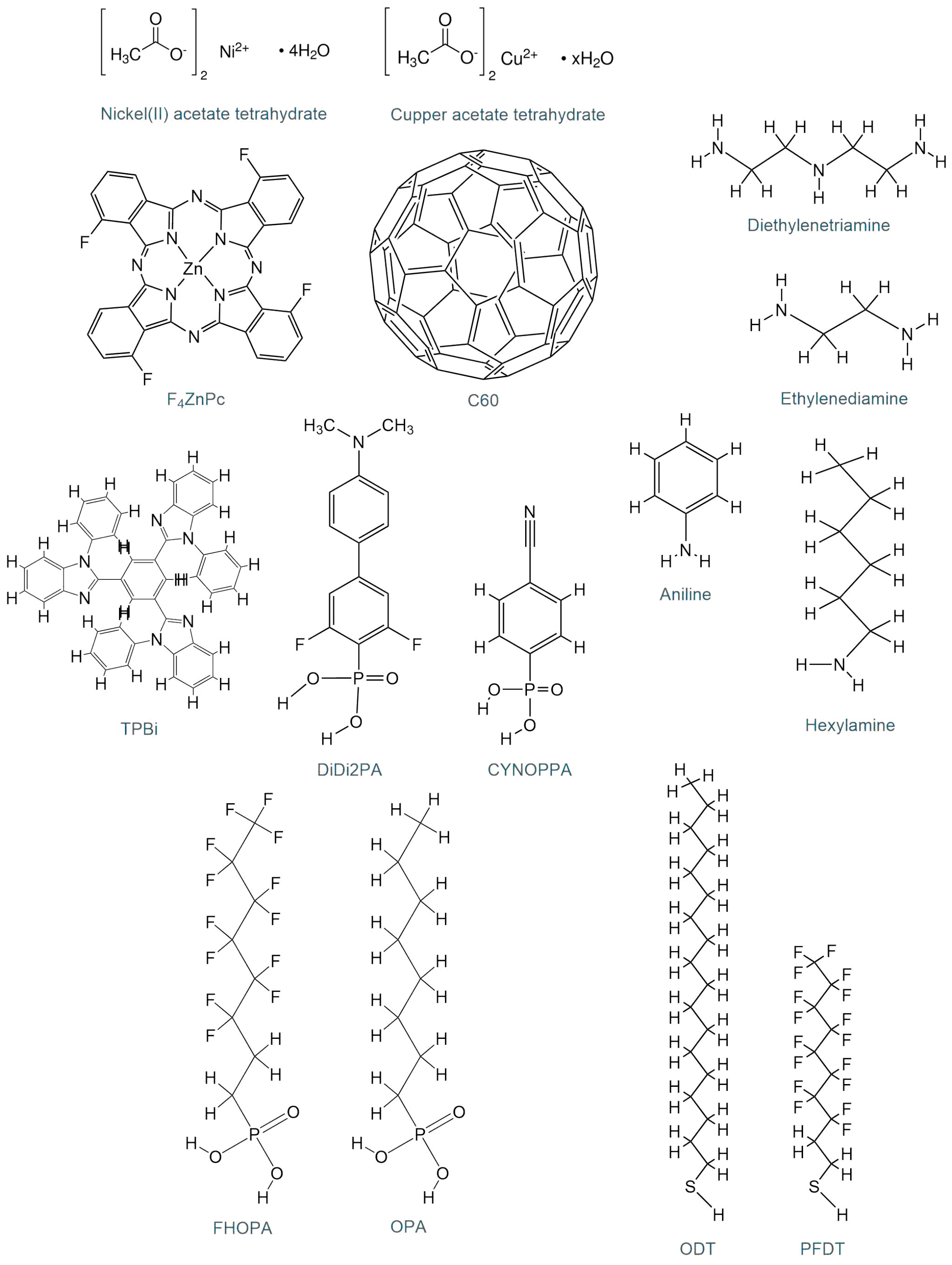

Figure A.1.: Overview on the molecular structures used in this work.

Bibliography

[1] Todorov, T. K.; Singh, S.; Bishop, D. M.; Gunawan, O.; Lee, Y. S.; Gershon, T. S.; Brew, K. W.; Antunez, P. D.; Haight, R. Ultrathin high band gap solar cells with improved efficiencies from the world's oldest photovoltaic material. *Nature Communications* **2017**, *8*, 682.

[2] Pope, M.; Kallmann, H. P.; Magnante, P. Electroluminescence in Organic Crystals. *The Journal of Chemical Physics* **1963**, *38*, 2042–2043.

[3] Chiang, C. K.; Fincher, C. R.; Park, Y. W.; Heeger, A. J.; Shirakawa, H.; Louis, E. J.; Gau, S. C.; MacDiarmid, A. G. Electrical conductivity in doped polyacetylene. *Physical Review Letters* **1977**, *39*, 1098–1101.

[4] Heeger, A. J.; Shirakawa, H.; MacDiarmid, A. G. The Nobel Prize in Chemistry 2000. `https://www.nobelprize.org/nobel_prizes/chemistry/laureates/2000/`.

[5] Tang, C. W. Two-layer organic photovoltaic cell. *Applied Physics Letters* **1986**, *48*, 183–185.

[6] Tang, C. W.; Vanslyke, S. A. Organic electroluminescent diodes. *Applied Physics Letters* **1987**, *51*, 913–915.

[7] Heckmeier, M.; Heider, U.; Maisch, R. Materialien für dünne Displays. *Physik Journal* **2015**, *14*.

[8] NREL PV efficiency chart. 2017; `https://www.nrel.gov/pv/assets/images/efficiency-chart.png`.

[9] Technical details of Heliatek films. `http://www.heliatek.com/en/heliafilm/technical-data`.

[10] Bartynski, A. N.; Gruber, M.; Das, S.; Rangan, S.; Mollinger, S.; Trinh, C.; Bradforth, S. E.; Vandewal, K.; Salleo, A.; Bartynski, R. A.; Bruetting, W.; Thompson, M. E. Symmetry-Breaking Charge Transfer in a Zinc Chlorodipyrrin Acceptor for High Open Circuit Voltage Organic Photovoltaics. *Journal of the American Chemical Society* **2015**, *137*, 5397–5405.

[11] The interface is still the device. *Nature Materials* **2012**, *11*, 91–91.

[12] Meyer, J.; Hamwi, S.; Kröger, M.; Kowalsky, W.; Riedl, T.; Kahn, A. Transition metal oxides for organic electronics: energetics, device physics and applications. *Advanced Materials* **2012**, *24*, 5408–27.

[13] Holmes, D. E.; Chen, R. T.; Elliott, K. R.; Kirkpatrick, C. G. Stoichiometry-controlled compensation in liquid encapsulated Czochralski GaAs. *Applied Physics Letters* **1982**, *40*, 46–48.

[14] Hashimoto, M.; Amano, H.; Sawaki, N.; Akasaki, I. Effects of hydrogen in an ambient on the crystal growth of GaN using Ga(CH3)3 and NH3. *Journal of Crystal Growth* **1984**, *68*, 163–168.

[15] Amano, H.; Sawaki, N.; Akasaki, I.; Toyoda, Y. Metalorganic vapor phase epitaxial growth of a high quality GaN film using an AlN buffer layer. *Applied Physics Letters* **1986**, *48*, 353–355.

[16] Amano, H.; Kito, M.; Hiramatsu, K.; Akasaki, I. P-Type Conduction in Mg-Doped GaN Treated with Low-Energy Electron Beam Irradiation (LEEBI). *Japanese Journal of Applied Physics* **1989**, *28*, L2112–L2114.

[17] Nakamura, S.; Mukai, T.; Senoh, M.; Iwasa, N. Thermal Annealing Effects on P-Type Mg-Doped GaN Films. *Japanese Journal of Applied Physics* **1992**, *31*, L139–L142.

[18] Nakamura, S.; Mukai, T.; Senoh, M. High-Power GaN P-N Junction Blue-Light-Emitting Diodes. *Japanese Journal of Applied Physics* **1991**, *30*, L1998–L2001.

[19] Nakamura, S.; Senoh, M.; Mukai, T. P-GaN/N-InGaN/N-GaN Double-Heterostructure Blue-Light-Emitting Diodes. *Japanese Journal of Applied Physics* **1993**, *32*, L8–L11.

[20] Nakamura, S.; Pearton, S.; Fasol, G. The Blue Laser Diode. The Complete Story. *Sprinver Verlag* **2000**, *2*.

[21] Akasaki, I.; Amano, H.; Nakamura, S. The Nobel Prize in Physics 2014. `https://www.nobelprize.org/nobel_prizes/physics/laureates/2014/`.

[22] Kim, M.-H.; Schubert, M. F.; Dai, Q.; Kim, J. K.; Schubert, E. F.; Piprek, J.; Park, Y. Origin of efficiency droop in GaN-based light-emitting diodes. *Applied Physics Letters* **2007**, *91*, 183507.

[23] Qian, F.; Li, Y.; Gradečak, S.; Wang, D.; Barrelet, C. J.; Lieber, C. M. Gallium nitride-based nanowire radial heterostructures for nanophotonics. *Nano Letters* **2004**, *4*, 1975–1979.

[24] Fernández-Garrido, S.; Kaganer, V. M.; Sabelfeld, K. K.; Gotschke, T.; Grandal, J.; Calleja, E.; Geelhaar, L.; Brandt, O. Self-regulated radius of spontaneously formed GaN nanowires in molecular beam epitaxy. *Nano Letters* **2013**, *13*, 3274–3280.

[25] Zhao, C.; Ng, T. K.; Prabaswara, A.; Conroy, M.; Jahangir, S.; Frost, T.; O'Connell, J.; Holmes, J. D.; Parbrook, P. J.; Bhattacharya, P.; Ooi, B. S. An enhanced surface passivation effect in InGaN/GaN disk-in-nanowire light emitting diodes for mitigating Shockley–Read–Hall recombination. *Nanoscale* **2015**, *7*, 16658–16665.

[26] Khan, J. I.; Adhikari, A.; Sun, J.; Priante, D.; Bose, R.; Shaheen, B. S.; Ng, T. K.; Zhao, C.; Bakr, O. M.; Ooi, B. S.; Mohammed, O. F. Enhanced Optoelectronic Performance of a Passivated Nanowire-Based Device: Key Information from Real-Space Imaging Using 4D Electron Microscopy. *Small* **2016**, *12*, 2313–2320.

[27] Greiner, M. T.; Helander, M. G.; Tang, W.-M.; Wang, Z.-B.; Qiu, J.; Lu, Z.-H. Universal energy-level alignment of molecules on metal oxides. *Nature Materials* **2012**, *11*, 76–81.

[28] Greiner, M. T.; Lu, Z.-H. Thin-film metal oxides in organic semiconductor devices: their electronic structures, work functions and interfaces. *NPG Asia Materials* **2013**, *5*, e55.

[29] Kröger, M.; Hamwi, S.; Meyer, J.; Riedl, T.; Kowalsky, W.; Kahn, A. Role of the deep-lying electronic states of MoO3 in the enhancement of hole-injection in organic thin films. *Applied Physics Letters* **2009**, *95*, 123301.

[30] Zilberberg, K.; Trost, S.; Schmidt, H.; Riedl, T. Solution processed vanadium pentoxide as charge extraction layer for organic solar cells. *Advanced Energy Materials* **2011**, *1*, 377–381.

[31] Hamwi, S.; Meyer, J.; Winkler, T.; Riedl, T.; Kowalsky, W. p-type doping efficiency of MoO3 in organic hole transport materials. *Applied Physics Letters* **2009**, *94*, 253307.

[32] Meyer, J.; Khalandovsky, R.; Görrn, P.; Kahn, A. MoO3 films spin-coated from a nanoparticle suspension for efficient hole-injection in organic electronics. *Advanced Materials* **2011**, *23*, 70–73.

[33] Mott, N. F. The Transitions to the Metallic State. *Philosophical Magazine* **1961**, *6*, 287 – 309.

[34] Hubbard, J. Electron Correlations in Narrow Energy Bands. *Proceedings of the Royal Society A: Mathematical, Physical and Engineering Sciences* **1963**, *276*, 238–257.

[35] Hubbard, J. Electron Correlations in Narrow Energy Bands. II. The Degenerate Band Case. *Proceedings of the Royal Society A: Mathematical, Physical and Engineering Sciences* **1964**, *277*, 237–259.

[36] Hubbard, J. Electron Correlations in Narrow Energy Bands. III. An Improved Solution. *Proceedings of the Royal Society A: Mathematical, Physical and Engineering Sciences* **1964**, *281*, 401–419.

[37] Hubbard, J. Electron Correlations in Narrow Energy Bands. IV. The Atomic Representation. *Proceedings of the Royal Society A: Mathematical, Physical and Engineering Sciences* **1965**, *285*, 542–560.

[38] Hubbard, J. Electron Correlations in Narrow Energy Bands. V. A Perturbation Expansion About the Atomic Limit. *Proceedings of the Royal Society A: Mathematical, Physical and Engineering Sciences* **1967**, *296*, 82–99.

[39] Hubbard, J. Electron Correlations in Narrow Energy Bands. VI. The Connexion with Many-Body Perturbation Theory. *Proceedings of the Royal Society A: Mathematical, Physical and Engineering Sciences* **1967**, *296*, 100–112.

[40] Imada, M.; Fujimori, A.; Tokura, Y. Metal-insulator transitions. *Reviews of Modern Physics* **1998**, *70*, 1039–1263.

[41] Zaanen, J.; Sawatzky, G. A.; Allen, J. W. Band gaps and electronic structure of transition-metal compounds. *Physical Review Letters* **1985**, *55*, 418–421.

[42] Mott, S. N. Metal-insulator transitions. *Physics Today* **1978**, *31*, 42–47.

[43] Schuler, T. M.; Ederer, D. L.; Itza-Ortiz, S.; Woods, G. T.; Callcott, T. A.; Woicik, J. C. *NiO: A Charge Transfer or Mott-Hubbard Insulator*; 2017.

[44] Scanlon, D. O.; Morgan, B. J.; Watson, G. W.; Walsh, A. Acceptor levels in p-type Cu2O: Rationalizing theory and Experiment. *Physical Review Letters* **2009**, *103*, 096405.

[45] Nolan, M.; Elliott, S. D. The p-type conduction mechanism in Cu2O: a first principles study. *Physical Chemistry Chemical Physics* **2006**, *8*, 5350.

[46] Shockley, W. The Theory of p-n Junctions in Semiconductors and p-n Junction Transistors. *Bell System Technical Journal* **1949**, *28*, 435–489.

[47] Nanova, D.; Scherer, M.; Schell, F.; Zimmermann, J.; Glaser, T.; Kast, A. K.; Krekeler, C.; Pucci, A.; Kowalsky, W.; Schröder, R. R.; Lovrinčić, R. Why Inverted Small Molecule Solar Cells Outperform Their Noninverted Counterparts. *Advanced Functional Materials* **2015**, *25*, 6511–6518.

[48] Pope, M.; Swenberg, C. E. Electronic Processes in Organic Solids. *Annual Reviews of Physical Chemistry* **1984**, *35*, 613–655.

[49] Hill, I.; Kahn, A.; Soos, Z.; Pascal, R. Charge-separation energy in films of π-conjugated organic molecules. *Chemical Physics Letters* **2000**, *327*, 181–188.

[50] Knupfer, M. Exciton binding energies in organic semiconductors. *Applied Physics A: Materials Science and Processing* **2003**, *77*, 623–626.

[51] Peumans, P.; Yakimov, A.; Forrest, S. R. Small molecular weight organic thin-film photodetectors and solar cells. *Journal of Applied Physics* **2003**, *93*, 3693–3723.

[52] Rand, B. P.; Burk, D. P.; Forrest, S. R. Offset energies at organic semiconductor heterojunctions and their influence on the open-circuit voltage of thin-film solar cells. *Physical Review B - Condensed Matter and Materials Physics* **2007**, *75*, 115327.

[53] Popovic, Z. D.; Hor, A.; Loutfy, R. O. A study of carrier generation mechanism in benzimidazole perylene/tetraphenyldiamine thin film structures. *Chemical Physics* **1988**, *127*, 451–457.

[54] Gregg, B. A.; Hanna, M. C. Comparing organic to inorganic photovoltaic cells: Theory, experiment, and simulation. *Journal of Applied Physics* **2003**, *93*, 3605–3614.

[55] Yang, F.; Forrest, S. R. Photocurrent generation in nanostructured organic solar cells. *ACS Nano* **2008**, *2*, 1022–1032.

[56] Barrau, S.; Andersson, V.; Zhang, F.; Masich, S.; Bijleveld, J.; Andersson, M. R.; Inganas, O. Nanomorphology of bulk heterojunction organic solar cells in 2D and 3D correlated to photovoltaic performance. *Macromolecules* **2009**, *42*, 4646–4650.

[57] Tress, W. *Organic Solar Cells Theory, Experiment, and Device Simulation*; Springer Verlag, 2016.

[58] Müller, J. G.; Lupton, J. M.; Feldmann, J.; Lemmer, U.; Scharber, M. C.; Sariciftci, N. S.; Brabec, C. J.; Scherf, U. Ultrafast dynamics of charge carrier photogeneration and geminate recombination in conjugated polymer:fullerene solar cells. *Physical Review B - Condensed Matter and Materials Physics* **2005**, *72*, 195208.

[59] Bakulin, A. A.; Martyanov, D. S.; Paraschuk, D. Y.; Pshenichnikov, M. S.; Van Loosdrecht, P. H. M. Ultrafast charge photogeneration dynamics in ground-state charge-transfer complexes based on conjugated polymers. *Journal of Physical Chemistry B* **2008**, *112*, 13730–13737.

[60] Deibe, C.; Strobe, T.; Dyakonov, V. Role of the charge transfer state in organic donor-acceptor solar cells. *Advanced Materials* **2010**, *22*, 4097–4111.

[61] Credgington, D.; Kim, Y.; Labram, J.; Anthopoulos, T. D.; Durrant, J. R. Analysis of recombination losses in a pentacene/C60 organic bilayer solar cell. *Journal of Physical Chemistry Letters* **2011**, *2*, 2759–2763.

[62] Credgington, D.; Jamieson, F. C.; Walker, B.; Nguyen, T. Q.; Durrant, J. R. Quantification of geminate and non-geminate recombination losses within a solution-processed small-molecule bulk heterojunction solar cell. *Advanced Materials* **2012**, *24*, 2135–2141.

[63] Pal, S. K.; Kesti, T.; Maiti, M.; Zhang, F.; Inganäs, O.; Hellström, S.; Andersson, M. R.; Oswald, F.; Langa, F.; Österman, T.; Pascher, T.; Yartsev, A.; Sundström, V. Geminate charge recombination in polymer/fullerene bulk heterojunction films and implications for solar cell function. *Journal of the American Chemical Society* **2010**, *132*, 12440–12451.

[64] Bakulin, A. A.; Rao, A.; Pavelyev, V. G.; van Loosdrecht, P. H. M.; Pshenichnikov, M. S.; Niedzialek, D.; Cornil, J.; Beljonne, D.;

Friend, R. H. The Role of Driving Energy and Delocalized States for Charge Separation in Organic Semiconductors. *Science* **2012**, *335*, 1340–1344.

[65] Itaka, K.; Yamashiro, M.; Yamaguchi, J.; Haemori, M.; Yaginuma, S.; Matsumoto, Y.; Kondo, M.; Koinuma, H. High-mobility C60 field-effect transistors fabricated on molecular-wetting controlled substrates. *Advanced Materials* **2006**, *18*, 1713–1716.

[66] Opitz, A.; Kraus, M.; Bronner, M.; Wagner, J.; Brütting, W. Bipolar transport in organic field-effect transistors: Organic semiconductor blends versus contact modification. *New Journal of Physics* **2008**, *10*, 065006.

[67] Tress, W.; Inganäs, O. Simple experimental test to distinguish extraction and injection barriers at the electrodes of (organic) solar cells with S-shaped current-voltage characteristics. *Solar Energy Materials and Solar Cells* **2013**, *117*, 599–603.

[68] Brendel, M.; Krause, S.; Steindamm, A.; Topczak, A. K.; Sundarraj, S.; Erk, P.; Höhla, S.; Fruehauf, N.; Koch, N.; Pflaum, J. The effect of gradual fluorination on the properties of FnZnPc thin films and FnZnPc/C60 bilayer photovoltaic cells. *Advanced Functional Materials* **2015**, *25*, 1565–1573.

[69] Vandewal, K.; Gadisa, A.; Oosterbaan, W. D.; Bertho, S.; Banishoeib, F.; Van Severen, I.; Lutsen, L.; Cleij, T. J.; Vanderzande, D.; Manca, J. V. The relation between open-circuit voltage and the onset of photocurrent generation by charge-transfer absorption in polymer: Fullerene bulk heterojunction solar cells. *Advanced Functional Materials* **2008**, *18*, 2064–2070.

[70] Hörmann, U.; Kraus, J.; Gruber, M.; Schuhmair, C.; Linderl, T.; Grob, S.; Kapfinger, S.; Klein, K.; Stutzman, M.; Krenner, H. J.; Brütting, W. Quantification of energy losses in organic solar cells from temperature-dependent device characteristics. *Physical Review B - Condensed Matter and Materials Physics* **2013**, *88*, 235307.

[71] Nayak, P. K.; Bisquert, J.; Cahen, D. Assessing possibilities and limits for solar cells. *Advanced Materials* **2011**, *23*, 2870–2876.

[72] Bigelow, W.; Pickett, D.; Zisman, W. Oleophobic monolayers. *Journal of Colloid Science* **1946**, *1*, 513–538.

[73] Troughton, E. B.; Bain, C. D.; Whitesides, G. M.; Nuzzo, R. G.; Allara, D. L.; Porter, M. D. Monolayer Films Prepared by the Spontaneous Self-Assembly of Symmetrical and Unsymmetrical Dialkyl Sulfides from Solution onto Gold Substrates: Structure, Properties, and Reactivity of Constituent Functional Groups. *Langmuir* **1988**, *4*, 365–385.

[74] Ulman, A. Formation and Structure of Self-Assembled Monolayers. *Chem.rev.* **1996**, *96*, 1533–1554.

[75] Bourgoin, J.-P.; Kergueris, C.; Lefevre, E.; Palacin, S. Langmuir-Blodgett films of thiol-capped gold nanoclusters: fabrication and electrical properties. *Thin Solid Films* **1998**, *327-329*, 515–519.

[76] Love, J. C.; Estroff, L. A.; Kriebel, J. K.; Nuzzo, R. G.; Whitesides, G. M. Self-assembled monolayers of thiolates on metals as a form of nanotechnology. *Chemical Reviews* **2005**, *105*, 1103–1169.

[77] Hanson, E. L.; Schwartz, J.; Nickel, B.; Koch, N.; Danisman, M. F. Bonding Self-Assembled, Compact Organophosphonate Monolayers to the Native Oxide Surface of Silicon. *Journal of the American Chemical Society* **2003**, *125*, 16074–16080.

[78] Pujari, S. P.; Scheres, L.; Marcelis, A. T.; Zuilhof, H. Covalent surface modification of oxide surfaces. *Angewandte Chemie - International Edition* **2014**, *53*, 6322–6356.

[79] Alt, M.; Schinke, J.; Hillebrandt, S.; Hänsel, M.; Hernandez-Sosa, G.; Mechau, N.; Glaser, T.; Mankel, E.; Hamburger, M.; Deing, K.; Jaegermann, W.; Pucci, A.; Kowalsky, W.; Lemmer, U.; Lovrincic, R. Processing follows function: Pushing the formation of self-assembled monolayers to high-throughput compatible time scales. *ACS Applied Materials and Interfaces* **2014**, *6*, 20234–20241.

[80] Abraham, F.; Ford, W. E.; Scholz, F.; Nelles, G.; Sandford, G.; Von Wrochem, F. Surface Energy and Work Function Control of AlOx/Al Surfaces by Fluorinated Benzylphosphonic Acids. *ACS Applied Materials and Interfaces* **2016**, *8*, 11857–11867.

[81] Appleyard, S. F. J.; Day, S. R.; Pickford, R. D.; Willis, M. R. Organic electroluminescent devices: enhanced carrier injection using SAM derivatized ITO electrodes. *Journal of Materials Chemistry* **2000**, *10*, 169–173.

[82] Paniagua, S. A.; Hotchkiss, P. J.; Jones, S. C.; Marder, S. R.; Mudalige, A.; Marrikar, F. S.; Pemberton, J. E.; Armstrong, N. R. Phosphonic acid modification of indium-tin oxide electrodes: Combined XPS/UPS/ contact angle studies. *Journal of Physical Chemistry C* **2008**, *112*, 7809–7817.

[83] Sharma, A.; Kippelen, B.; Hotchkiss, P. J.; Marder, S. R. Stabilization of the work function of indium tin oxide using organic surface modifiers in organic light-emitting diodes. *Applied Physics Letters* **2008**, *93*, 163308.

[84] Hotchkiss, P. J.; Li, H.; Paramonov, P. B.; Paniagua, S. A.; Jones, S. C.; Armstrong, N. R.; Brédas, J. L.; Marder, S. R. Modification of the surface properties of indium tin oxide with benzylphosphonic acids: A joint experimental and theoretical study. *Advanced Materials* **2009**, *21*, 4496–4501.

[85] Hotchkiss, P. J.; Jones, S. C.; Paniagua, S. A.; Sharma, A.; Kippelen, B.; Armstrong, N. R.; Marder, S. R. The modification of indium tin oxide with phosphonic acids: Mechanism of binding, tuning of surface properties, and potential for use in organic electronic applications. *Accounts of Chemical Research* **2012**, *45*, 337–346.

[86] Knesting, K. M.; Hotchkiss, P. J.; MacLeod, B. A.; Marder, S. R.; Ginger, D. S. Spatially modulating interfacial properties of transparent conductive oxides: Patterning work function with phosphonic acid self-assembled monolayers. *Advanced Materials* **2012**, *24*, 642–646.

[87] Ford, W. E.; Abraham, F.; Scholz, F.; Nelles, G.; Sandford, G.; von Wrochem, F. Spectroscopic Characterization of Fluorinated Benzylphosphonic Acid Monolayers on AlOx/Al Surfaces. *The Journal of Physical Chemistry C* **2017**, *121*, 1690–1703.

[88] Schwartz, D. K. Mechanisms and Kinetics of Self-Assembled Monolayer Formation. *Annual Review of Physical Chemistry* **2001**, *52*, 107–137.

[89] Lavrich, D. J.; Wetterer, S. M.; Bernasek, S. L.; Scoles, G. Physisorption and Chemisorption of Alkanethiols and Alkyl Sulfides on Au(111). *The Journal of Physical Chemistry B* **1998**, *102*, 3456–3465.

[90] Bencini, A.; Rajaraman, G.; Totti, F.; Tusa, M. Modeling thiols on Au(111): Structural, thermodynamic and magnetic properties of simple thiols and thiol-radicals. *Superlattices and Microstructures* **2009**, *46*, 4–9.

[91] Lavrich, D. J.; Wetterer, S. M.; Bernasek, S. L.; Scoles, G. Physisorption and Chemisorption of Alkanethiols and Alkyl Sulfides on Au(111). *The Journal of Physical Chemistry B* **1998**, *102*, 3456–3465.

[92] Karpovich, D. S.; Blanchard, G. J. Direct Measurement of the Adsorption Kinetics of Alkanethiolate Self-Assembled Monolayers on a Microcrystalline Gold Surface. *Langmuir* **1994**, *10*, 3315–3322.

[93] Langmuir, I. Surface Chemistry. *Chemical Reviews* **1933**, *13*.

[94] Schinke, J. *Processing and characterization of organic thin films self-assembled monolayers for interface engineering and semiconductors with thermally activated solubility reduction*; Suedwestdeutscher Verlag fuer Hochschulschriften, 2015.

[95] Godin, M.; Williams, P. J.; Tabard-Cossa, V.; Laroche, O.; Beaulieu, L. Y.; Lennox, R. B.; Grütter, P. Surface stress, kinetics, and structure of alkanethiol self-assembled monolayers. *Langmuir* **2004**, *20*, 7090–7096.

[96] Vazquez, H.; Dappe, Y. J.; Ortega, J.; Flores, F. Energy level alignment at metal/organic semiconductor interfaces: "Pillow" effect, induced density of interface states, and charge neutrality level. *Journal of Chemical Physics* **2007**, *126*, 144703.

[97] Alloway, D. M.; Hofmann, M.; Smith, D. L.; Gruhn, N. E.; Graham, A. L.; Colorado, R.; Wysocki, V. H.; Lee, T. R.; Lee, P. a.; Armstrong, N. R. Interface Dipoles Arising from Self-Assembled Monolayers on Gold: UV-Photoemission Studies of Alkanethiols and Partially Fluorinated Alkanethiols. *The Journal of Physical Chemistry B* **2003**, *107*, 11690–11699.

[98] Hotchkiss, P. J. Design, Synthesis, and Use of Phosponic Acids for the Surface Modification of Metal Oxides. Ph.D. thesis, Georgia Institute of Technology, 2008.

[99] Okuyama, H.; Miyajima, T.; Morinaga, Y.; Hiei, F.; Ozawa, M.; Akimoto, K. ZnSe/ZnMgSSe blue laser diode. *Electronics Letters* **1992**, *28*, 1798–1799.

[100] Fan, Y.; Han, J.; He, L.; Saraie, J.; Gunshor, R. L.; Hagerott, M.; Jeon, H.; Nurmikko, A. V.; Hua, G. C.; Otsuka, N. Graded band gap ohmic contact to p-ZnSe. *Applied Physics Letters* **1992**, *61*, 3160–3162.

[101] DePuydt, J. M.; Haase, M. A.; Cheng, H.; Potts, J. E. Electrical characterization of p-type ZnSe. *Applied Physics Letters* **1989**, *55*, 1103–1105.

[102] Morkoç, H.; Strite, S.; Gao, G. B.; Lin, M. E.; Sverdlov, B.; Burns, M. Large-band-gap SiC, III-V nitride, and II-VI ZnSe-based semiconductor device technologies. *Journal of Applied Physics* **1994**, *76*, 1363–1398.

[103] Taniyasu, Y.; Kasu, M.; Makimoto, T. Increased electron mobility in n-type Si-doped AlN by reducing dislocation density. *Applied Physics Letters* **2006**, *89*.

[104] Olivier, J.; Poirier, R. Electronic structure of Al2O3 from electron energy loss spectroscopy. *Surface Science* **1981**, *105*, 347–356.

[105] Wang, F.; Shan, J.; Knoesel, E.; Bonn, M.; Heinz, T. F. Electronic charge transport in sapphire studied by optical-pump/THz-probe spectroscopy. *Ultrafast Phenomena in Semiconductors and Nanostructure Materials VIII* **2004**, *5352*, 216–221.

[106] Hanada, T. *Advances in Materials Research*; Springer Verlag, 2009; pp 1–19.

[107] Lei, T.; Moustakas, T. D.; Graham, R. J.; He, Y.; Berkowitz, S. J. Epitaxial growth and characterization of zinc-blende gallium nitride on (001) silicon. *Journal of Applied Physics* **1992**, *71*, 4933–4943.

[108] Kim, J. H.; Holloway, P. H. Wurtzite to zinc-blende phase transition in gallium nitride thin films. *Applied Physics Letters* **2004**, *84*, 711–713.

[109] Xia, H.; Xia, Q.; Ruoff, A. L. High-pressure structure of gallium nitride: Wurtzite-to-rocksalt phase transition. *Physical Review B* **1993**, *47*, 12925–12928.

[110] Wang, F.-H.; Krüger, P.; Pollmann, J. Electronic structure of (1x1) GaN(0001) and GaN(000-1) surfaces. *Physical Review B* **2001**, *64*, 035305.

[111] Bernardini, F.; Fiorentini, V.; Vanderbilt, D. Spontaneous polarization and piezoelectric constants of III-V nitrides. *Physical Review B* **1997**, *56*, R10024–R10027.

[112] Ambacher, O.; Smart, J.; Shealy, J. R.; Weimann, N. G.; Chu, K.; Murphy, M.; Schaff, W. J.; Eastman, L. F.; Dimitrov, R.; Wittmer, L.;

Stutzmann, M.; Rieger, W.; Hilsenbeck, J. Two-dimensional electron gases induced by spontaneous and piezoelectric polarization charges in N- and Ga-face AlGaN/GaN heterostructures. *Journal of Applied Physics* **1999**, *85*, 3222–3233.

[113] Kim, M.-H.; Schubert, M. F.; Dai, Q.; Kim, J. K.; Schubert, E. F.; Piprek, J.; Park, Y. Origin of efficiency droop in GaN-based light-emitting diodes. *Applied Physics Letters* **2007**, *91*, 183507.

[114] Miller, D. A. B.; Chemla, D. S.; Damen, T. C.; Gossard, A. C.; Wiegmann, W.; Wood, T. H.; Burrus, C. A. Band-edge electroabsorption in quantum well structures: The quantum-confined stark effect. *Physical Review Letters* **1984**, *53*, 2173–2176.

[115] Jasinski, J.; Zakharov, D. N.; Berkeley, L. GaN grown in polar and non-polar directions. *Opto-Electronics Review* **2004**, *12*, 339–346.

[116] Kucharski, R.; Zając, M.; Doradziński, R.; Rudziński, M.; Kudrawiec, R.; Dwiliński, R. Non-polar and semi-polar ammonothermal GaN substrates. *Semiconductor Science and Technology* **2012**, *27*, 024007.

[117] Waltereit, P.; Brandt, O.; Trampert, A.; Grahn, H. T.; Menniger, J.; Ramsteiner, M.; Reiche, M.; Ploog, K. H. Nitride semiconductors free of electrostatic fields for efficient white light-emitting diodes. *Nature* **2000**, *406*, 865–868.

[118] Pearton, S. J.; Abernathy, C. R.; Ren, F. *Gallium Nitride Processing for Electronics, Sensors and Applications*; Springer Verlag, 2006.

[119] Smith, A. R. Reconstructions of GaN(0001) and (000-1) surfaces: Ga-rich metallic structures. *Journal of Vacuum Science & Technology B: Microelectronics and Nanometer Structures* **1998**, *16*, 2242.

[120] Xue, Q.-K.; Xue, Q. Z.; Bakhtizin, R. Z.; Hasegawa, Y.; Tsong, I. S. T.; Sakurai, T.; Ohno, T. Structures of GaN(0001)-(2×2), (4×4), and (5×5) Surface Reconstructions. *Physical Review Letters* **1999**, *82*, 3074–3077.

[121] Segev, D.; de Walle, C. G. V. Origins of Fermi-level pinning on GaN and InN polar and nonpolar surfaces. *Europhysics Letters (EPL)* **2006**, *76*, 305–311.

[122] Segev, D. University of California Postprints Microscopic origins of surface states on nitride surfaces Microscopic origins of surface states on

nitride surfaces. *Journal of Applied Physics Appl. Phys. Lett. J. Appl. Phys. J. Appl. Phys. Appl. Phys. Lett. Appl. Phys. Lett* **2007**, *101*, 81704–152101.

[123] Lin, L. M.; Luo, Y.; Lai, P. T.; Lau, K. M. Influence of oxidation and annealing temperatures on quality of Ga2O3 film grown on GaN. *Thin Solid Films* **2006**, *515*, 2111–2115.

[124] Janzen, O.; Hahn, C.; Mönch, W. Oxidation of GaN{0001}-1×1 surfaces at room temperature. *Eur. Phys. J. B* **1999**, *9*, 315–321.

[125] Wolter, S. D.; Luther, B. P.; Waltemyer, D. L.; Önneby, C.; Mohney, S. E.; Molnar, R. J.; Nneby, C. X-ray photoelectron spectroscopy and x-ray diffraction study of the thermal oxide on gallium nitride. *Applied Physics Letters* **1997**, *701*, 2156–2602.

[126] Du, J.; Zhao, J.; Luo, Q.; Yu, Z.; Xia, J.; Yang, M. Growth and Characteristics Analysis of the Thermal Oxide Grown on Gallium Nitride. Symposium on Photonics and Optoelectronics. 2009.

[127] Nakano, Y.; Jimbo, T. Interface properties of thermally oxidized n-GaN metal-oxide-semiconductor capacitors. *Applied Physics Letters* **2003**, *82*, 218–220.

[128] Schroder, D.; Meier, D. Solar cell contact resistance - A review. *IEEE Transactions on Electron Devices* **1984**, *31*, 637–647.

[129] Long, J. P.; Bermudez, V. M. Band bending and photoemission-induced surface photovoltages on clean n- and p-GaN(0001) surfaces. *Physical Review B* **2002**, *66*, 121308.

[130] Yamada, T.; Ito, J.; Asahara, R.; Watanabe, K.; Nozaki, M.; Nakazawa, S.; Anda, Y.; Ishida, M.; Ueda, T.; Yoshigoe, A.; Hosoi, T.; Shimura, T.; Watanabe, H. Comprehensive study on initial thermal oxidation of GaN(0001) surface and subsequent oxide growth in dry oxygen ambient. *Journal of Applied Physics* **2017**, *121*.

[131] Kronik, L. Surface photovoltage phenomena: theory, experiment, and applications. *Surface Science Reports* **1999**, *37*, 1–206.

[132] Bermudez, V. M. Study of oxygen chemisorption on the GaN(0001)-(1×1) surface. *Journal of Applied Physics* **1996**, *80*, 1190–1200.

[133] Zhang, X.; Ptasinska, S. Electronic and chemical structure of the H2O/GaN(0001) interface under ambient conditions. *Scientific Reports* **2016**, *6*, 24848.

[134] Lagowski, J.; Sproles, E. S.; Gatos, H. C. Quantitative study of the charge transfer in chemisorption; Oxygen chemisorption on ZnO. *Journal of Applied Physics* **1977**, *48*, 3566–3575.

[135] Iqbal, M. Z.; Reshchikov, M. a.; He, L.; Morkoç, H. Effect of ambient on photoluminescence from GaN grown by molecular-beam epitaxy. *Journal of Electronic Materials* **2003**, *32*, 346–349.

[136] Chakrapani, V.; Pendyala, C.; Kash, K.; Anderson, A. B.; Sunkara, M. K.; Angus, J. C. Electrochemical pinning of the fermi level: Mediation of photoluminescence from gallium nitride and zinc oxide. *Journal of the American Chemical Society* **2008**, *130*, 12944–12952.

[137] Shalish, I.; Kronik, L.; Segal, G.; Rosenwaks, Y.; Shapira, Y.; Tisch, U.; Salzman, J. Yellow luminescence and related deep levels in unintentionally doped GaN films. *Physical Review B* **1999**, *59*, 9748–9751.

[138] Shalish, I.; Shapira, Y.; Burstein, L.; Salzman, J. Surface states and surface oxide in GaN layers. *Journal of Applied Physics* **2001**, *89*, 390–395.

[139] Shalish, I.; Kronik, L.; Segal, G.; Shapira, Y.; Eizenberg, M.; Salzman, J. Yellow luminescence and Fermi level pinning in GaN layers. *Applied Physics Letters* **2000**, *77*, 987.

[140] Scherer, M. Correlating structure and function in small molecule organic solar cells by means of scanning probe and electron microscopy. Ph.D. thesis, Technische Universität Braunschweig, 2016.

[141] Binnig, G.; Quate, C. F.; Gerber, C. Atomic force microscope. *Physical Review Letters* **1986**, *56*, 930–933.

[142] Binning, G.; Rohrer, H.; Gerber, C.; Weibel, E. Surface studies by scanning tunneling microscopy. *Physical Review Letters* **1982**, *49*, 57–61.

[143] Ho, H.; West, P. Optimizing AC-mode atomic force microscope imaging. *Scanning* **2006**, *18*, 339–343.

[144] Martin, Y.; Williams, C. C.; Wickramasinghe, H. K. Atomic force microscope-force mapping and profiling on a sub 100-Å scale. *Journal of Applied Physics* **1987**, *61*, 4723–4729.

[145] Erskine-Murray, J. On Contact Electricity of Metals. *Proceedings of the Royal Society of London (1854-1905)* **1898**, *63*, 113–146.

[146] KP Technology, *User Manual v. 7.35*.

[147] Zisman, W. A. A new method of measuring contact potential differences in metals. *Review of Scientific Instruments* **1932**, *3*, 367–370.

[148] Hansen, W. N.; Hansen, G. J. Standard reference surfaces for work function measurements in air. *Surface Science* **2001**, *481*, 172–184.

[149] Roithner LaserTechnik GmbH, *Technical data sheet: XSL-355-5E*.

[150] Roithner LaserTechnik GmbH, *Technical data sheet: RLCU-440*.

[151] Shirley, D. A. High-Resolution X-Ray Photoemission Spectrum of the Valence Bands of Gold. *Physical Review B* **1972**, *5*, 4709–4714.

[152] Haken, H.; Wolf, C. *Molekülphysik und Quantenchemie*, 5th ed.; Springer Verlag, 2006.

[153] Beck, S. Untersuchung des Ladungstransfers in organischen Halbleitern mit in-situ Infrarotspektroskopie. Ph.D. thesis, Universität Heidelberg, 2014.

[154] Sendner, M. Infrarotspektroskopische Untersuchungen von Methylammonium-Blei-Halogenid-Perowskiten. Ph.D. thesis, Universität Heidelberg, 2016.

[155] Pedrós, J.; Takagaki, Y.; Ive, T.; Ramsteiner, M.; Brandt, O.; Jahn, U.; Ploog, K. H.; Calle, F. Exciton impact-ionization dynamics modulated by surface acoustic waves in GaN. *Physical Review B - Condensed Matter and Materials Physics* **2007**, *75*, 115305.

[156] Hauswald, C.; Corfdir, P.; Zettler, J. K.; Kaganer, V. M.; Sabelfeld, K. K.; Fernandez-Garrido, S.; Flissikowski, T.; Consonni, V.; Gotschke, T.; Grahn, H. T.; Geelhaar, L.; Brandt, O. Origin of the nonradiative decay of bound excitons in GaN nanowires. *Physical Review B - Condensed Matter and Materials Physics* **2014**, *90*, 165304.

[157] Laquai, F. Zeitaufgelöste Photolumineszenz. `http://www2.mpip-mainz.mpg.de/groups/laquai/Research/TransientPL`.

[158] Hauswald, C. Dynamics of free and bound excitons in GaN nanowires : Origin of the nonradiative recombination channel. Ph.D. thesis, Humboldt-Universität Berlin, 2015.

[159] Manders, J. R.; Tsang, S. W.; Hartel, M. J.; Lai, T. H.; Chen, S.; Amb, C. M.; Reynolds, J. R.; So, F. Solution-processed nickel oxide hole transport layers in high efficiency polymer photovoltaic cells. *Advanced Functional Materials* **2013**, *23*, 2993–3001.

[160] Koh, S. E.; McDonald, K. D.; Holt, D. H.; Dulcey, C. S.; Chaney, J. A.; Pehrsson, P. E. Phenylphosphonic acid functionalization of indium tin oxide: Surface chemistry and work functions. *Langmuir* **2006**, *22*, 6249–6255.

[161] Schlettwein, D.; Hesse, K.; Gruhn, N. E.; Lee, P. A.; Nebesny, K. W.; Armstrong, N. R. Electronic energy levels in individual molecules, thin films, and organic heterojunctions of substituted phthalocyanines. *Journal of Physical Chemistry B* **2002**, *105*, 4791–4800.

[162] Bruder, I.; Schöneboom, J.; Dinnebier, R.; Ojala, A.; Schäfer, S.; Sens, R.; Erk, P.; Weis, J. What determines the performance of metal phthalocyanines (MPc, M = Zn, Cu, Ni, Fe) in organic heterojunction solar cells? A combined experimental and theoretical investigation. *Organic Electronics: physics, materials, applications* **2010**, *11*, 377–387.

[163] Meiss, J.; Merten, A.; Hein, M.; Schuenemann, C.; Schäfer, S.; Tietze, M.; Uhrich, C.; Pfeiffer, M.; Leo, K.; Riede, M. Fluorinated zinc phthalocyanine as donor for efficient vacuum-deposited organic solar cells. *Advanced Functional Materials* **2012**, *22*, 405–414.

[164] Savoie, B. M.; Rao, A.; Bakulin, A. A.; Gelinas, S.; Movaghar, B.; Friend, R. H.; Marks, T. J.; Ratner, M. A. Unequal partnership: Asymmetric roles of polymeric donor and fullerene acceptor in generating free charge. *Journal of the American Chemical Society* **2014**, *136*, 2876–2884.

[165] Sun, F. Z.; Shi, A. L.; Xu, Z. Q.; Wei, H. X.; Li, Y. Q.; Lee, S. T.; Tang, J. X. Efficient inverted polymer solar cells with thermal-evaporated and solution-processed small molecular electron extraction layer. *Applied Physics Letters* **2013**, *102*, 133303.

[166] Tripathi, V.; Datta, D.; Samal, G. S.; Awasthi, A.; Kumar, S. Role of exciton blocking layers in improving efficiency of copper phthalocyanine based organic solar cells. *Journal of Non-Crystalline Solids* **2008**, *354*, 2901–2904.

[167] Yu, J.; Wang, N.; Zang, Y.; Jiang, Y. Organic photovoltaic cells based on TPBi as a cathode buffer layer. *Solar Energy Materials and Solar Cells* **2011**, *95*, 664–668.

[168] Kyma Technologies, *Technical data sheet: GaN Templates on Sapphire.*

[169] Kyma Technologies, *Technical data sheet: GaN Bulk.*

[170] Kedem, N.; Blumstengel, S.; Henneberger, F.; Cohen, H.; Hodes, G.; Cahen, D. Morphology-, synthesis- and doping-independent tuning of ZnO work function using phenylphosphonates. *Physical chemistry chemical physics* **2014**, *16*, 8310–9.

[171] Chen, S.; Manders, J. R.; Tsang, S.-W.; So, F. Metal oxides for interface engineering in polymer solar cells. *Journal of Materials Chemistry* **2012**, *22*, 24202–24212.

[172] Li, H.; Winget, P.; Brédas, J. L. Transparent conducting oxides of relevance to organic electronics: Electronic structures of their interfaces with organic layers. *Chemistry of Materials* **2014**, *26*, 631–646.

[173] Carp, O.; Huisman, C. L.; Reller, A. Photoinduced reactivity of titanium dioxide. *Progress in Solid State Chemistry* **2004**, *32*, 33–177.

[174] Ramana, C. V.; Julien, C. M. Chemical and electrochemical properties of molybdenum oxide thin films prepared by reactive pulsed-laser assisted deposition. *Chemical Physics Letters* **2006**, *428*, 114–118.

[175] Lu, Y. M.; Hwang, W. S.; Yang, J. S.; Chuang, H. C. Properties of nickel oxide thin films deposited by RF reactive magnetron sputtering. *Thin Solid Films* **2002**, *420-421*, 54–61.

[176] Ding, H.; Gao, Y.; Kim, D. Y.; Subbiah, J.; So, F. Energy level evolution of molybdenum trioxide interlayer between indium tin oxide and organic semiconductor. *Applied Physics Letters* **2010**, *96*, 073304.

[177] Jasieniak, J. J.; Seifter, J.; Jo, J.; Mates, T.; Heeger, A. J. A solution-processed MoOx anode interlayer for use within organic photovoltaic devices. *Advanced Functional Materials* **2012**, *22*, 2594–2605.

[178] Irwin, M. D.; Buchholz, D. B.; Hains, A. W.; Chang, R. P. H.; Marks, T. J. p-Type semiconducting nickel oxide as an efficiency-enhancing anode interfacial layer in polymer bulk-heterojunction solar cells. *Proceedings of the National Academy of Sciences* **2008**, *105*, 2783–2787.

[179] Blom, P. W. M.; Mihailetchi, V. D.; Koster, L. J. A.; Markov, D. E. Device physics of polymer:fullerene bulk heterojunction solar cells. *Advanced Materials* **2007**, *19*, 1551–1566.

[180] de Jong, M. P.; van Ijzendoorn, L. J.; de Voigt, M. J. A. Stability of the interface between indium-tin-oxide and poly(3,4-ethylenedioxythiophene)/poly(styrenesulfonate) in polymer light-emitting diodes. *Applied Physics Letters* **2000**, *77*, 2255–2257.

[181] Kim, Y. H.; Lee, S. H.; Noh, J.; Han, S. H. Performance and stability of electroluminescent device with self-assembled layers of poly(3,4-ethylenedioxythiophene)-poly(styrenesulfonate) and polyelectrolytes. *Thin Solid Films* **2006**, *510*, 305–310.

[182] Kemerink, M.; Timpanaro, S.; De Kok, M. M.; Meulenkamp, E. A.; Touwslager, F. J. Three-dimensional inhomogeneities in PEDOT:PSS films. *Journal of Physical Chemistry B* **2004**, *108*, 18820–18825.

[183] Yan, H.; Lee, P.; Armstrong, N. R.; Graham, A.; Evmenenko, G. A.; Dutta, P.; Marks, T. J. High-performance hole-transport layers for polymer light-emitting diodes. Implementation of organosiloxane cross-linking chemistry in polymeric electroluminescent devices. *Journal of the American Chemical Society* **2005**, *127*, 3172–3183.

[184] Sun, Y.; Takacs, C. J.; Cowan, S. R.; Seo, J. H.; Gong, X.; Roy, A.; Heeger, A. J. Efficient, air-stable bulk heterojunction polymer solar cells using MoOx as the anode interfacial layer. *Advanced Materials* **2011**, *23*, 2226–2230.

[185] Reynolds, K. J.; Barker, J. A.; Greenham, N. C.; Friend, R. H.; Frey, G. L. Inorganic solution-processed hole-injecting and electron-blocking layers in polymer light-emitting diodes. *Journal of Applied Physics* **2002**, *92*, 7556–7563.

[186] Chu, C.-W.; Li, S.-H.; Chen, C.-W.; Shrotriya, V.; Yang, Y. High-performance organic thin-film transistors with metal oxide/metal bilayer electrode. *Applied Physics Letters* **2005**, *87*, 193508.

[187] You, H.; Dai, Y.; Zhang, Z.; Ma, D. Improved performances of organic light-emitting diodes with metal oxide as anode buffer. *Journal of Applied Physics* **2007**, *101*, 026105.

[188] Kröger, M.; Hamwi, S.; Meyer, J.; Riedl, T.; Kowalsky, W.; Kahn, A. P-type doping of organic wide band gap materials by transition metal oxides: A case-study on Molybdenum trioxide. *Organic Electronics* **2009**, *10*, 932–938.

[189] Gwinner, M. C.; Pietro, R. D.; Vaynzof, Y.; Greenberg, K. J.; Ho, P. K. H.; Friend, R. H.; Sirringhaus, H. Doping of organic semiconductors using molybdenum trioxide: A quantitative time-dependent electrical and spectroscopic study. *Advanced Functional Materials* **2011**, *21*, 1432–1441.

[190] Wang, Z.; Waqas Alam, M.; Lou, Y.; Naka, S.; Okada, H. Enhanced carrier injection in pentacene thin-film transistors by inserting a MoO3-doped pentacene layer. *Applied Physics Letters* **2012**, *100*, 043302.

[191] Glaser, T.; Beck, S.; Lunkenheimer, B.; Donhauser, D.; Köhn, A.; Kröger, M.; Pucci, A. Infrared study of the MoO3 doping efficiency in 4,4-bis(N-carbazolyl)-1,1-biphenyl (CBP). *Organic Electronics: physics, materials, applications* **2013**, *14*, 575–583.

[192] Beck, S.; Gerbert, D.; Glaser, T.; Pucci, A. Charge Transfer at Organic/Inorganic Interfaces and the Formation of Space Charge Regions Studied with Infrared Light. *Journal of Physical Chemistry C* **2015**, *119*, 12545–12550.

[193] Wang, J.; Xu, L.; Lee, Y. J.; De Anda Villa, M.; Malko, A. V.; Hsu, J. W. P. Effects of Contact-Induced Doping on the Behaviors of Organic Photovoltaic Devices. *Nano Letters* **2015**, *15*, 7627–7632.

[194] Wang, C.; Liu, X.; Wang, C.; Kauppi, J.; Gao, Y. Electronic structure evolution in doping of fullerene C60 by ultra-thin layer molybdenum trioxide. *Journal of Applied Physics* **2015**, *118*, 085304.

[195] Miyata, N.; Suzuki, T.; Ohyama, R. Physical properties of evaporated molybdenum oxide films. *Thin Solid Films* **1996**, *281-282*, 218–222.

[196] Vasilopoulou, M.; Douvas, A. M.; Georgiadou, D. G.; Palilis, L. C.; Kennou, S.; Sygellou, L.; Soultati, A.; Kostis, I.; Papadimitropoulos, G.; Davazoglou, D.; Argitis, P. The influence of hydrogenation and oxygen

vacancies on molybdenum oxides work function and gap states for application in organic optoelectronics. *Journal of the American Chemical Society* **2012**, *134*, 16178–87.

[197] Papadopoulos, T. A.; Meyer, J.; Li, H.; Guan, Z.; Kahn, A.; Bredas, J.-L. Nature of the interfaces between stoichiometric and under-stoichiometric MoO3 and 4,4'-N,N'-dicarbazole-biphenyl: A combined theoretical and experimental study. *Advanced Functional Materials* **2013**, *23*, 6091–6099.

[198] Guo, Y.; Robertson, J. Origin of the high work function and high conductivity of MoO3. *Applied Physics Letters* **2014**, *105*, 222110.

[199] Bovill, E. S. R.; Griffin, J.; Wang, T.; Kingsley, J. W.; Yi, H.; Iraqi, A.; Buckley, A. R.; Lidzey, D. G. Air processed organic photovoltaic devices incorporating a MoOx anode buffer layer. *Applied Physics Letters* **2013**, *102*, 183303.

[200] Meyer, J.; Shu, A.; Kröger, M.; Kahn, A. Effect of contamination on the electronic structure and hole-injection properties of MoO3/organic semiconductor interfaces. *Applied Physics Letters* **2010**, *96*, 133308.

[201] Zhong, J. Q.; Mao, H. Y.; Wang, R.; Lin, J. D.; Zhao, Y. B.; Zhang, J. L.; Ma, D. G.; Chen, W. Ionization potential dependent air exposure effect on the MoO3/organic interface energy level alignment. *Organic Electronics* **2012**, *13*, 2793–2800.

[202] Irfan, I.; Ding, H.; Gao, Y.; Small, C.; Kim, D. Y.; Subbiah, J.; So, F. Energy level evolution of air and oxygen exposed molybdenum trioxide films. *Applied Physics Letters* **2010**, *96*, 243307.

[203] Butler, K. T.; Crespo-Otero, R.; Buckeridge, J.; Scanlon, D. O.; Bovill, E.; Lidzey, D.; Walsh, A. Band energy control of molybdenum oxide by surface hydration. *Applied Physics Letters* **2015**, *107*, 231605.

[204] Wang, K.-C.; Jeng, J.-Y.; Shen, P.-S.; Chang, Y.-C.; Diau, E. W.-G.; Tsai, C.-H.; Chao, T.-Y.; Hsu, H.-C.; Lin, P.-Y.; Chen, P.; Guo, T.-F.; Wen, T.-C. p-type Mesoscopic Nickel Oxide/Organometallic Perovskite Heterojunction Solar Cells. *Scientific Reports* **2015**, *4*, 4756.

[205] Irfan, I.; James Turinske, A.; Bao, Z.; Gao, Y. Work function recovery of air exposed molybdenum oxide thin films. *Applied Physics Letters* **2012**, *101*, 093305.

[206] Liu, X.; Yi, S.; Wang, C.; Irfan, I.; Gao, Y. Effect of oxygen plasma treatment on air exposed MoOx thin film. *Organic Electronics: physics, materials, applications* **2014**, *15*, 977–983.

[207] Melitz, W.; Shen, J.; Kummel, A. C.; Lee, S. Kelvin probe force microscopy and its application. *Surface Science Reports* **2011**, *66*, 1–27.

[208] Cheung, C. H.; Song, W. J.; So, S. K. Role of air exposure in the improvement of injection efficiency of transition metal oxide/organic contact. *Organic Electronics: physics, materials, applications* **2010**, *11*, 89–94.

[209] Schulz, P.; Cowan, S. R.; Guan, Z. L.; Garcia, A.; Olson, D. C.; Kahn, A. NiOx/MoO3 Bi-layers as efficient hole extraction contacts in organic solar cells. *Advanced Functional Materials* **2014**, *24*, 701–706.

[210] Ratcliff, E. L.; Zacher, B.; Armstrong, N. R. Selective interlayers and contacts in organic photovoltaic cells. *Journal of Physical Chemistry Letters* **2011**, *2*, 1337–1350.

[211] Steirer, K. X.; Chesin, J. P.; Widjonarko, N. E.; Berry, J. J.; Miedaner, A.; Ginley, D. S.; Olson, D. C. Solution deposited NiO thin-films as hole transport layers in organic photovoltaics. *Organic Electronics: physics, materials, applications* **2010**, *11*, 1414–1418.

[212] Ratcliff, E. L.; Meyer, J.; Steirer, K. X.; Armstrong, N. R.; Olson, D.; Kahn, A. Energy level alignment in PCDTBT:PC70BM solar cells: Solution processed NiOx for improved hole collection and efficiency. *Organic Electronics: physics, materials, applications* **2012**, *13*, 744–749.

[213] Newman, R.; Chrenko, R. M. Optical Properties of Nickel Oxide. *Physical Review* **1959**, *114*, 1507–1513.

[214] Kim, K. S.; Winograd, N. X-ray photoelectron spectroscopic studies of nickel-oxygen surfaces using oxygen and argon ion-bombardment. *Surface Science* **1974**, *43*, 625–643.

[215] Hüfner, S.; Osterwalder, J.; Riesterer, T.; Hulliger, F. Photoemission and inverse photoemission spectroscopy of NiO. *Solid State Communications* **1984**, *52*, 793–796.

[216] McKay, J. M.; Henrich, V. E. Surface electronic structure of NiO: Defect states, O2 and H2O interactions. *Physical Review B* **1985**, *32*, 6764–6772.

[217] Hüfner, S.; Steiner, P.; Sander, I.; Reinert, F.; Schmitt, H.; Neumann, M.; Witzel, S. The electronic structure of NiO investigated by photoemission spectroscopy. *Solid State Communications* **1991**, *80*, 869–873.

[218] Hüfner, S.; Steiner, P.; Sander, I.; Reinert, F.; Schmitt, H. The optical gap of NiO. *Zeitschrift für Physik B Condensed Matter* **1992**, *86*, 207–215.

[219] Hüfner, S. Electronic structure of NiO and related 3d-transition-metal compounds. *Advances in Physics* **1994**, *43*, 183–356.

[220] Ratcliff, E. L.; Meyer, J.; Steirer, K. X.; Garcia, A.; Berry, J. J.; Ginley, D. S.; Olson, D. C.; Kahn, A.; Armstrong, N. R. Evidence for near-Surface NiOOH Species in Solution-Processed NiOx Selective Interlayer Materials: Impact on Energetics and the Performance of Polymer Bulk Heterojunction Photovoltaics. *Chemistry of Materials* **2011**, *23*, 4988–5000.

[221] Hall, D. S.; Lockwood, D. J.; Bock, C.; MacDougall, B. R. Nickel hydroxides and related materials: a review of their structures, synthesis and properties. *Proceedings. Mathematical, physical, and engineering sciences / The Royal Society Publishing* **2015**, *471*, 20140792.

[222] Bode, H.; Dehmelt, K.; Witte, J. Zur Kenntnis der Nickelhydroxidelektrode - I. Über das Nickel(II)-hydroxidhydrat. *Electrochimica Acta* **1966**, *11*, 1079–IN1.

[223] Glemser, O.; Einerhand, J. Die chemischen Vorgänge an der Nickelhydroxydanode des Edisonakkumulators. *Berichte der Bunsengesellschaft für physikalische Chemie* **1950**, *54*, 302–304.

[224] Motori, A.; Sandrolini, F.; Davolio, G. Electrical properties of nickel hydroxide for alkaline cell systems. *Journal of Power Sources* **1994**, *48*, 361–370.

[225] De Jesus, J. C.; González, I.; Quevedo, A.; Puerta, T. Thermal decomposition of nickel acetate tetrahydrate: An integrated study by TGA, QMS and XPS techniques. *Journal of Molecular Catalysis A: Chemical* **2005**, *228*, 283–291.

[226] Uhlenbrock, S.; Scharfschwerdt, C.; Neumann, M.; Illing, G.; Freund, H.-J. The influence of defects on the Ni 2p and O1s XPS of NiO. *J. Phys.: Condens. Matter* **1992**, *4*, 7973–7978.

[227] Sasi, B.; Gopchandran, K. G. Nanostructured mesoporous nickel oxide thin films. *Nanotechnology* **2007**, *18*, 115613–115621.

[228] Biesinger, M. C.; Payne, B. P.; Lau, L. W. M.; Gerson, A.; Smart, R. S. C. X-ray photoelectron spectroscopic chemical state quantification of mixed nickel metal, oxide and hydroxide systems. *Surface and Interface Analysis* **2009**, *41*, 324–332.

[229] Kitakatsu, N.; Maurice, V.; Hinnen, C.; Marcus, P. Surface hydroxylation and local structure of NiO thin films formed on Ni(111). *Surface Science* **1998**, *407*, 36–58.

[230] Langell, M. A.; Berrie, C. L.; Nassir, M. H.; Wulser, K. W. Adsorption of acetic acid on hydroxylated NiO(111) thin films. *Surface Science* **1994**, *320*, 25–38.

[231] Langell, M. A.; Nassir, M. H. Stabilization of NiO(111) thin films by surface hydroxyls. *The Journal of Physical Chemistry* **1995**, *99*, 4162–4169.

[232] Payne, B. P.; Biesinger, M. C.; McIntyre, N. S. The study of polycrystalline nickel metal oxidation by water vapour. *Journal of Electron Spectroscopy and Related Phenomena* **2009**, *175*, 55–65.

[233] Cappus, D.; Xu, C.; Ehrlich, D.; Dillmann, B.; Ventrice, C. A.; Al Shamery, K.; Kuhlenbeck, H.; Freund, H. J. Hydroxyl groups on oxide surfaces: NiO(100), NiO(111) and Cr2O3(111). *Chemical Physics* **1993**, *177*, 533–546.

[234] Biesinger, M. C.; Payne, B. P.; Hart, B. R.; Grosvenor, A. P.; McIntryre, N. S.; Lau, L. W.; Smart, R. S. Quantitative chemical state XPS analysis of first row transition metals, oxides and hydroxides. *Journal of Physics: Conference Series* **2008**, *100*, 012025.

[235] Kim, J.; Lee, H. R.; Kim, H. P.; Lin, T.; Kanwat, A.; Mohd Yusoff, A.; Jang, J. Effects of UV-ozone irradiation on copper doped nickel acetate and its applicability to perovskite solar cells. *Nanoscale* **2016**, *8*, 9284–9292.

[236] Milliron, D. J.; Hill, I. G.; Shen, C.; Kahn, A.; Schwartz, J. Surface oxidation activates indium tin oxide for hole injection. *Journal of Applied Physics* **2000**, *87*, 572–576.

[237] Ostapenko, A.; Klöffel, T.; Meyer, B.; Witte, G. Formation and Stability of Phenylphosphonic Acid Monolayers on ZnO: Comparison of in Situ and Ex Situ SAM Preparation. *Langmuir* **2016**, *32*, 5029–5037.

[238] Jesper, M. et al. Dipolar SAMs Reduce Charge Carrier Injection Barriers in n-Channel Organic Field Effect Transistors. *Langmuir* **2015**, *31*, 10303–10309.

[239] Mutin, P.; Guerrero, G.; Vioux, A. Organic–inorganic hybrid materials based on organophosphorus coupling molecules: from metal phosphonates to surface modification of oxides. *Comptes Rendus Chimie* **2003**, *6*, 1153–1164.

[240] Lim, S. C.; Kim, S. H.; Lee, J. H.; Kim, M. K.; Kim, D. J.; Zyung, T. Surface-treatment effects on organic thin-film transistors. *Synthetic Metals* **2005**, *148*, 75–79.

[241] Paramonov, P. B.; Paniagua, S. A.; Hotchkiss, P. J.; Jones, S. C.; Armstrong, N. R.; Marder, S. R.; Bredas, J. L. Theoretical characterization of the indium tin oxide surface and of its binding sites for adsorption of phosphonic acid monolayers. *Chemistry of Materials* **2008**, *20*, 5131–5133.

[242] Hanson, E. L.; Guo, J.; Koch, N.; Schwartz, J.; Bernasek, S. L. Advanced surface modification of indium tin oxide for improved charge injection in organic devices. *Journal of the American Chemical Society* **2005**, *127*, 10058–10062.

[243] Quiñones, R.; Raman, A.; Gawalt, E. S. Functionalization of nickel oxide using alkylphosphonic acid self-assembled monolayers. *Thin Solid Films* **2008**, *516*, 8774–8781.

[244] Ndione, P. F.; Garcia, A.; Widjonarko, N. E.; Sigdel, A. K.; Steirer, K. X.; Olson, D. C.; Parilla, P. A.; Ginley, D. S.; Armstong, N. R.; Richards, R. E.; Ratcliff, E. L.; Berry, J. J. Highly-tunable nickel cobalt oxide as a low-temperature P-type contact in organic photovoltaic devices. *Advanced Energy Materials* **2013**, *3*, 524–531.

[245] Zimmerman, J. D.; Song, B.; Griffith, O.; Forrest, S. R. Exciton-blocking phosphonic acid-treated anode buffer layers for organic photovoltaics. *Applied Physics Letters* **2013**, *103*, 243905.

[246] Bulusu, A.; Paniagua, S. A.; MacLeod, B. A.; Sigdel, A. K.; Berry, J. J.; Olson, D. C.; Marder, S. R.; Graham, S. Efficient Modification of Metal Oxide Surfaces with Phosphonic Acids by Spray Coating. *Langmuir* **2013**, *29*, 3935–3942.

[247] Stolz, S.; Petzoldt, M.; Dück, S.; Sendner, M.; Bunz, U. H. F.; Lemmer, U.; Hamburger, M.; Hernandez-Sosa, G. High-Performance Electron Injection Layers with a Wide Processing Window from an Amidoamine-Functionalized Polyfluorene. *ACS Applied Materials and Interfaces* **2016**, *8*, 12959–12967.

[248] Kamal, H.; Elmaghraby, E. K.; Ali, S. A.; Abdel-Hady, K. Characterization of nickel oxide films deposited at different substrate temperatures using spray pyrolysis. *Journal of Crystal Growth* **2004**, *262*, 424–434.

[249] Mustafa, B.; Griffin, J.; Alsulami, A. S.; Lidzey, D. G.; Buckley, A. R. Solution processed nickel oxide anodes for organic photovoltaic devices. *Applied Physics Letters* **2014**, *104*, 063302.

[250] Barber, M.; Connor, J. A.; Guest, M. F.; Hillier, I. H.; Schwarz, M.; Stacey, M. Bonding in some donor-acceptor complexes involving boron trifluoride. Study by means of ESCA and molecular orbital calculations. *Journal of the Chemical Society, Faraday Transactions 2: Molecular and Chemical Physics* **1973**, *69*, 551–558.

[251] Timpel, M.; Nardi, M. V.; Ligorio, G.; Wegner, B.; Pätzel, M.; Kobin, B.; Hecht, S.; Koch, N. Energy-Level Engineering at ZnO/Oligophenylene Interfaces with Phosphonate-Based Self-Assembled Monolayers. *ACS Applied Materials & Interfaces* **2015**, *7*, 11900–11907.

[252] Tanuma, S.; Powell, C. J.; Penn, D. R. Calculations of electron inelastic mean free paths. V. Data for 14 organic compounds over the 50–2000 eV range. *Surface and Interface Analysis* **1994**, *21*, 165–176.

[253] Wheeler, S.; Deledalle, F.; Tokmoldin, N.; Kirchartz, T.; Nelson, J.; Durrant, J. R. Influence of Surface Recombination on Charge-Carrier Kinetics in Organic Bulk Heterojunction Solar Cells with Nickel Oxide Interlayers. *Physical Review Applied* **2015**, *4*, 024020.

[254] De Los Santos Valladares, L.; Ionescu, A.; Holmes, S.; Barnes, C. H. W.; Bustamante Domínguez, A.; Avalos Quispe, O.; González, J. C.; Milana, S.; Barbone, M.; Ferrari, A. C.; Ramos, H.; Majima, Y. Characterization of Ni thin films following thermal oxidation in air. *Journal of*

Vacuum Science & Technology B, Nanotechnology and Microelectronics: Materials, Processing, Measurement, and Phenomena **2014**, *32*, 051808.

[255] Kim, J. S.; Cacialli, F.; Friend, R. Surface conditioning of indium-tin oxide anodes for organic light-emitting diodes. *Thin Solid Films* **2003**, *445*, 358–366.

[256] Sugiyama, K.; Ishii, H.; Ouchi, Y.; Seki, K. Dependence of indium–tin–oxide work function on surface cleaning method as studied by ultraviolet and x-ray photoemission spectroscopies. *Journal of Applied Physics* **2000**, *87*, 295.

[257] Berry, J. J.; Widjonarko, N. E.; Bailey, B. A.; Sigdel, A. K.; Ginley, D. S.; Olson, D. C. Surface treatment of NiO hole transport layers for organic solar cells. *IEEE Journal on Selected Topics in Quantum Electronics* **2010**, *16*, 1649–1655.

[258] Tress, W.; Leo, K.; Riede, M. Influence of hole-transport layers and donor materials on open-circuit voltage and shape of I-V curves of organic solar cells. *Advanced Functional Materials* **2011**, *21*, 2140–2149.

[259] Steirer, K. X.; Ndione, P. F.; Widjonarko, N. E.; Lloyd, M. T.; Meyer, J.; Ratcliff, E. L.; Kahn, A.; Armstrong, N. R.; Curtis, C. J.; Ginley, D. S.; Berry, J. J.; Olson, D. C. Enhanced efficiency in plastic solar cells via energy matched solution processed NiOx interlayers. *Advanced Energy Materials* **2011**, *1*, 813–820.

[260] Tress, W. Device Physics of Organic Solar Cells. Ph.D. thesis, Technische Universität Dreseden, 2011.

[261] Tress, W.; Corvers, S.; Leo, K.; Riede, M. Investigation of driving forces for charge extraction in organic solar cells: Transient photocurrent measurements on solar cells showing s-shaped current-voltage characteristics. *Advanced Energy Materials* **2013**, *3*, 873–880.

[262] Kim, K. H.; Takahashi, C.; Abe, Y.; Kawamura, M. Effects of Cu doping on nickel oxide thin film prepared by sol–gel solution process. *Optik - International Journal for Light and Electron Optics* **2014**, *125*, 2899–2901.

[263] Kim, J. H.; Liang, P. W.; Williams, S. T.; Cho, N.; Chueh, C. C.; Glaz, M. S.; Ginger, D. S.; Jen, A. K. Y. High-performance and environmentally stable planar heterojunction perovskite solar cells based on

a solution-processed copper-doped nickel oxide hole-transporting layer. *Advanced Materials* **2015**, *27*, 695–701.

[264] Chen, S. C.; Kuo, T. Y.; Lin, Y. C.; Lin, H. C. Preparation and properties of p-type transparent conductive Cu-doped NiO films. *Thin Solid Films* **2011**, *519*, 4944–4947.

[265] Inzani, K.; Nematollahi, M.; Vullum-Bruer, F.; Grande, T.; Reenaas, T. W.; Selbach, S. M. Electronic properties of reduced molybdenum oxides. *Phys. Chem. Chem. Phys.* **2017**, *19*, 9232–9245.

[266] Hall, D. S.; Lockwood, D. J.; Poirier, S.; Bock, C.; MacDougall, B. R. Raman and Infrared Spectroscopy of α and β Phases of Thin Nickel Hydroxide Films Electrochemically Formed on Nickel. *Journal of Physical Chemistry A* **2012**, *116*, 6771–6784.

[267] Nakamura, S.; Chichibu, S. F. *Introduction to nitride semiconductor blue lasers and light emitting diodes*; Taylor & Francis, 2000.

[268] Zhao, S.; Kibria, M. G.; Wang, Q.; Nguyen, H. P. T.; Mi, Z. Growth of large-scale vertically aligned GaN nanowires and their heterostructures with high uniformity on SiOx by catalyst-free molecular beam epitaxy. *Nanoscale* **2013**, *5*, 5283.

[269] Frost, T.; Jahangir, S.; Stark, E.; Deshpande, S.; Hazari, A.; Zhao, C.; Ooi, B. S.; Bhattacharya, P. Monolithic electrically injected nanowire array edge-emitting laser on (001) silicon. *Nano Letters* **2014**, *14*, 4535–4541.

[270] Wölz, M.; Hauswald, C.; Flissikowski, T.; Gotschke, T.; Fernandez-Garrido, S.; Brandt, O.; Grahn, H. T.; Geelhaar, L.; Riechert, H. Epitaxial Growth of GaN Nanowires with High Structural Perfection on a Metallic TiN Film. *Nano Letters* **2015**, *15*, 3743–3747.

[271] Kuykendall, T. R.; Schwartzberg, A. M.; Aloni, S. Gallium Nitride Nanowires and Heterostructures: Toward Color-Tunable and White-Light Sources. *Advanced Materials* **2015**, *27*, 5805–5812.

[272] Hahn, C.; Zhang, Z.; Fu, A.; Wu, C. H.; Hwang, Y. J.; Gargas, D. J.; Yang, P. Epitaxial Growth of InGaN Nanowire Arrays for Light Emitting Diodes. *ACS Nano* **2011**, *5*, 3970–3976.

[273] Ra, Y.-H.; Navamathavan, R.; Park, J.-H.; Lee, C.-R. Coaxial InxGa(1-x)N/GaN Multiple Quantum Well Nanowire Arrays on Si(111) Substrate for High-Performance Light-Emitting Diodes. *Nano Letters* **2013**, *13*, 3506–3516.

[274] Lähnemann, J.; Corfdir, P.; Feix, F.; Kamimura, J.; Flissikowski, T.; Grahn, H. T.; Geelhaar, L.; Brandt, O. Radial Stark Effect in (In,Ga)N Nanowires. *Nano Letters* **2016**, *16*, 917–925.

[275] Armstrong, A.; Li, Q.; Lin, Y.; Talin, A. A.; Wang, G. T. GaN nanowire surface state observed using deep level optical spectroscopy. *Applied Physics Letters* **2010**, *96*, 163106.

[276] Foussekis, M.; Ferguson, J. D.; McNamara, J. D.; Baski, A. A.; Reshchikov, M. A. Effects of polarity and surface treatment on Ga- and N-polar bulk GaN. *Journal of Vacuum Science & Technology B: Microelectronics and Nanometer Structures* **2012**, *30*, 051210.

[277] Guo, W.; Zhang, M.; Banerjee, A.; Bhattacharya, P. Catalyst-Free InGaN/GaN Nanowire Light Emitting Diodes Grown on (001) Silicon by Molecular Beam Epitaxy. *Nano Letters* **2010**, *10*, 3355–3359.

[278] Fernández-Garrido, S.; Kong, X.; Gotschke, T.; Calarco, R.; Geelhaar, L.; Trampert, A.; Brandt, O. Spontaneous Nucleation and Growth of GaN Nanowires: The Fundamental Role of Crystal Polarity. *Nano Letters* **2012**, *12*, 6119–6125.

[279] Reddy, P.; Bryan, I.; Bryan, Z.; Guo, W.; Hussey, L.; Collazo, R.; Sitar, Z. The effect of polarity and surface states on the Fermi level at III-nitride surfaces. *Journal of Applied Physics* **2014**, *116*, 123701–91603.

[280] Himmerlich, M.; Eisenhardt, A.; Shokhovets, S.; Krischok, S.; Räthel, J.; Speiser, E.; Neumann, M. D.; Navarro-Quezada, A.; Esser, N. Confirmation of intrinsic electron gap states at nonpolar GaN(1-100) surfaces combining photoelectron and surface optical spectroscopy. *Applied Physics Letters* **2014**, *104*, 171602.

[281] Seelmann-Eggebert, M.; Weyher, J. L.; Obloh, H.; Zimmermann, H.; Rar, A.; Porowski, S. Polarity of (00.1) GaN epilayers grown on a (00.1) sapphire. *Applied Physics Letters* **1997**, *71*, 2635–2637.

[282] Rouviere, J. L.; Weyher, J. L.; Seelmann-Eggebert, M.; Porowski, S. Polarity determination for GaN films grown on (0001) sapphire and

high-pressure-grown GaN single crystals. *Applied Physics Letters* **1998**, *73*, 668–670.

[283] Bermudez, V. The dependence of the structure and electronic properties of wurtzite GaN surfaces on the method of preparation. *Applied Surface Science* **1998**, *126*, 69–82.

[284] Sloboshanin, S.; Tautz, F. S.; Polyakov, V. M.; Starke, U.; Usikov, A. S.; Ber, B. J.; Schaefer, J. A. Structural, vibrational and electronic properties of faceted GaN (000-1) surfaces. *Surface Science* **1999**, *428*, 250–256.

[285] Schulz, C. H.; Schmidt, T. H.; Flege, J. I.; Berner, N.; Tessarek, C. H.; Hommel, D.; Falta, J. Oxide removal from GaN(0001) surfaces. *Physica Status Solidi (C) Current Topics in Solid State Physics* **2009**, *6*, S305–S308.

[286] Schulz, C.; Kuhr, S.; Geffers, H.; Schmidt, T.; Flege, J. I.; Aschenbrenner, T.; Hommel, D.; Falta, J. Cleaning of GaN(-2110) surfaces. *Journal of Vacuum Science & Technology A: Vacuum, Surfaces, and Films* **2011**, *29*, 011013.

[287] Falta, J.; Schmidt, T. H.; Gangopadhyay, S.; Schulz, C. H. R.; Kuhr, S.; Berner, N.; Flege, J. I.; Pretorius, A.; Rosenauer, A.; Sebald, K.; Lohmeyer, H.; Gutowski, J.; Figge, S.; Yamaguchi, T.; Hommel, D. Cleaning and growth morphology of gan and ingan surfaces. *Physica Status Solidi (B) Basic Research* **2011**, *248*, 1800–1809.

[288] Craft, H. S.; Rice, A. L.; Collazo, R.; Sitar, Z.; Maria, J. P. Spectroscopic measurements of the surface stoichiometry of chemical vapor deposited GaN. *Applied Physics Letters* **2011**, *98*, 082110.

[289] Groh, R.; Gerey, G.; Bartha, L.; Pankove, J. I. On the thermal decomposition of GaN in vacuum. *Physica Status Solidi (A) Applications and Materials Science* **1974**, *26*, 353–357.

[290] Ambacher, O. Thermal stability and desorption of Group III nitrides prepared by metal organic chemical vapor deposition. *Journal of Vacuum Science & Technology B: Microelectronics and Nanometer Structures* **1996**, *14*, 3532.

[291] Fernández-Garrido, S.; Koblmüller, G.; Calleja, E.; Speck, J. S. In situ GaN decomposition analysis by quadrupole mass spectrometry and

reflection high-energy electron diffraction. *Journal of Applied Physics* **2008**, *104*, 033541.

[292] King, S. W.; Barnak, J. P.; Bremser, M. D.; Tracy, K. M.; Ronning, C.; Davis, R. F.; Nemanich, R. J. Cleaning of AlN and GaN surfaces. *Journal of Applied Physics* **1998**, *84*, 5248–5260.

[293] Grandjean, N.; Massies, J.; Semond, F.; Karpov, S. Y.; Talalaev, R. a. GaN evaporation in molecular-beam epitaxy environment. *Applied Physics Letters* **1999**, *74*, 1854.

[294] Widstrand, S. M.; Magnusson, K. O.; Larsson, M. I.; Johansson, L. S.; Gustafsson, J. B.; Moons, E.; Yeom, H. W.; Miki, H.; Oshima, M. Preparation of stoichiometric GaN(0001)-1×1 studied with spectromicroscopy. *Surface Science* **2004**, *572*, 409–417.

[295] King, S. W.; Smith, L. L.; Barnak, J. P.; Ku, J.-H.; Christman, J. A.; Benjamin, M. C.; Bremser, M. D.; Nemanich, R. J.; Davis, R. F. Ex Situ and in Situ Methods for Oxide and Carbon Removal from AlN and GaN Surfaces. *MRS Proceedings* **2011**, *395*, 739.

[296] Smith, L. L.; King, S. W.; Nemanich, R. J.; Davis, R. F. Cleaning of GaN surfaces. *Journal of Electronic Materials* **1996**, *25*, 805–810.

[297] Tsuji, Y.; Watanabe, T.; Nakamura, K.; Makabe, I.; Nakata, K.; Katsuyama, T.; Teramoto, A.; Shirai, Y.; Sugawa, S.; Ohmi, T. XPS analysis of the terminated-bonding states at GaN surface after chemical and plasma treatments. *Physica Status Solidi (C) Current Topics in Solid State Physics* **2013**, *10*, 1557–1560.

[298] Jung, Y.; Ahn, J.; Baik, K. H.; Kim, D.; Pearton, S. J.; Ren, F.; Kim, J. Chemical Etch Characteristics of N-Face and Ga-Face GaN by Phosphoric Acid and Potassium Hydroxide Solutions. *Journal of The Electrochemical Society* **2012**, *159*, H117–H120.

[299] Kim, J. K.; Kim, K. J.; Kim, B.; Kim, J. N.; Kwak, J. S.; Park, Y. J.; Lee, J. L. Effects of surface treatment using aqua regia solution on the change of surface band bending of p-type GaN. *Journal of Electronic Materials* **2001**, *30*, 129–133.

[300] Mishra, M.; Krishna TC, S.; Rastogi, P.; Aggarwal, N.; Chauhan, A. K. S.; Goswami, L.; Gupta, G. New Approach to Clean GaN Surfaces. *Materials Focus* **2014**, *3*, 218–223.

[301] Schultz, T.; Schlesinger, R.; Niederhausen, J.; Henneberger, F.; Sadofev, S.; Blumstengel, S.; Vollmer, A.; Bussolotti, F.; Yang, J. P.; Kera, S.; Parvez, K.; Ueno, N.; Müllen, K.; Koch, N. Tuning the work function of GaN with organic molecular acceptors. *Physical Review B* **2016**, *93*, 125309.

[302] Baker, T. J.; Haskell, B. A.; Wu, F.; Speck, J. S.; Nakamura, S. Characterization of Planar Semipolar Gallium Nitride Films on Sapphire Substrates. *Japanese Journal of Applied Physics* **2006**, *45*, L154–L157.

[303] Koblmüller, G.; Reurings, F.; Tuomisto, F.; Speck, J. S. Influence of Ga/N ratio on morphology, vacancies, and electrical transport in GaN grown by molecular beam epitaxy at high temperature. *Applied Physics Letters* **2010**, *97*, 191915.

[304] Kushvaha, S. S.; Pal, P.; Shukla, A. K.; Joshi, A. G.; Gupta, G.; Kumar, M.; Singh, S.; Gupta, B. K.; Haranath, D. Effect of growth temperature on defects in epitaxial GaN film grown by plasma assisted molecular beam epitaxy. *AIP Advances* **2014**, *4*.

[305] Smith, L. L.; King, S. W.; Nemanich, R. J.; Davis, R. F. Cleaning of GaN surfaces. *Journal of Electronic Materials* **1996**, *25*, 805–810.

[306] Carin, R.; Deville, J. P.; Werckmann, J. An XPS study of GaN thin films on GaAs. *Surface and Interface Analysis* **1990**, *16*, 65–69.

[307] Mishra, M.; Shibin Krishna, T. C.; Aggarwal, N.; Vihari, S.; Kumar Singh Chauhan, A.; Gupta, G. A Comparative Photoelectron Spectroscopic Analysis of MBE and MOCVD Grown Epitaxial GaN Films. *Science of Advanced Materials* **2014**, *6*, 1–6.

[308] Gogova, D.; Hemmingsson, C.; Monemar, B.; Talik, E.; Kruczek, M.; Tuomisto, F.; Saarinen, K. Investigation of the structural and optical properties of free-standing GaN grown by HVPE. *Journal of Physics D: Applied Physics* **2005**, *38*, 2332–2337.

[309] Rickert, K. A.; Ellis, A. B.; Himpsel, F. J.; Sun, J.; Kuech, T. F. N-GaN surface treatments for metal contacts studied via x-ray photoemission spectroscopy. *Applied Physics Letters* **2002**, *80*, 204–206.

[310] Petravic, M.; Deenapanray, P. N. K.; Coleman, V. A.; Kim, K. J.; Kim, B.; Li, G. Core-level photoemission and near-edge x-ray absorption

fine-structure studies of GaN surface under low-energy ion bombardment. *Journal of Applied Physics* **2004**, *95*, 5487–5493.

[311] Wagner, C.; Riggs, W.; Davis, L.; Moulder, J. F.; Muilenberg, G.; Stickle, W. F.; Sobol, P. E.; Bomben, K. D. Handbook of X-Ray Photoelectron Spectroscopy. 1979.

[312] Lai, Y. H.; Yeh, C. T.; Hwang, J. M.; Hwang, H. L.; Chen, C. T.; Hung, W. H. Sputtering and etching of GaN surfaces. *Journal of Physical Chemistry B* **2001**, *105*, 10029–10036.

[313] Ritchie, A.; Eger, S.; Wright, C.; Chelladurai, D.; Borrowman, C.; Olovsson, W.; Magnuson, M.; Verma, J.; Jena, D.; Xing, H. G.; Dubuc, C.; Urquhart, S. Strain sensitivity in the nitrogen 1s NEXAFS spectra of gallium nitride. *Applied Surface Science* **2014**, *316*, 232–236.

[314] Lin, Y.-J.; Tsai, C.-D.; Lyu, Y.-T.; Lee, C.-T. X-ray photoelectron spectroscopy study of (NH4)2Sx-treated Mg-doped GaN layers. *Applied Physics Letters* **2000**, *77*, 687–689.

[315] Morkoç, H. *Nitride semiconductors and devices*; 1999; p 512.

[316] Johnson, J. C.; Choi, H.-J.; Knutsen, K. P.; Schaller, R. D.; Yang, P.; Saykally, R. J. Single gallium nitride nanowire lasers. *Nature Materials* **2002**, *1*, 106–110.

[317] French, R. H. Electronic Band Structure of Al2O3, with Comparison to Alon and AIN. *Journal of the American Ceramic Society* **1990**, *73*, 477–489.

[318] Yim, W. M.; Stofko, E. J.; Zanzucchi, P. J.; Pankove, J. I.; Ettenberg, M.; Gilbert, S. L. Epitaxially grown AlN and its optical band gap. *Journal of Applied Physics* **1973**, *44*, 292–296.

[319] Kibria, M. G.; Zhao, S.; Chowdhury, F. A.; Wang, Q.; Nguyen, H. P. T.; Trudeau, M. L.; Guo, H.; Mi, Z. Tuning the surface Fermi level on p-type gallium nitride nanowires for efficient overall water splitting. *Nature Communications* **2014**, *5*.

[320] Wu, C. I.; Kahn, A.; Taskar, N.; Dorman, D.; Gallagher, D. GaN (0001)-(1×1) surfaces: Composition and electronic properties. *Journal of Applied Physics* **1998**, *83*, 4249–4252.

[321] Schultz, T.; Schlesinger, R.; Niederhausen, J.; Henneberger, F.; Sadofev, S.; Blumstengel, S.; Vollmer, A.; Bussolotti, F.; Yang, J. P.; Kera, S.; Parvez, K.; Ueno, N.; Müllen, K.; Koch, N. Tuning the work function of GaN with organic molecular acceptors. *Physical Review B* **2016**, *93*, 125309.

[322] Reshchikov, M. A.; Foussekis, M.; Baski, A. A. Surface photovoltage in undoped n-type GaN. *Journal of Applied Physics* **2010**, *107*, 113535.

[323] Williams, K. S.; Lenhart, J. L.; Andzelm, J. W.; Bandara, S. V.; Baril, N. F.; Henry, N. C.; Tidrow, M. Z. First principles investigation of water adsorption and charge transfer on III-V(110) semiconductor surfaces. *Surface Science* **2014**, *622*, 71–82.

[324] Reshchikov, M. A.; Sabuktagin, S.; Johnstone, D. K.; Morkoç, H. Transient photovoltage in GaN as measured by atomic force microscope tip. *Journal of Applied Physics* **2004**, *96*, 2556–2560.

[325] Dhesi, S.; Stagarescu, C.; Smith, K.; Doppalapudi, D.; Singh, R.; Moustakas, T. Surface and bulk electronic structure of thin-film wurtzite GaN. *Physical Review B* **1997**, *56*, 10271–10275.

[326] Valla, T.; Johnson, P.; Dhesi, S.; Smith, K.; Doppalapudi, D.; Moustakas, T.; Shirley, E. Unoccupied band structure of wurtzite GaN(0001). *Physical Review B* **1999**, *59*, 5003–5007.

[327] Cho, S. J.; Dogan, S.; Sabuktagin, S.; Reshchikov, M. A.; Johnstone, D. K.; Morkoc, H. Surface band bending in as-grown and plasma-treated n-type GaN films using surface potential electric force microscopy. *Applied Physics Letters* **2004**, *84*, 3070–3072.

[328] Chevtchenko, S.; Ni, X.; Fan, Q.; Baski, a. a.; Morkoc, H. Surface band bending of a-plane GaN studied by scanning Kelvin probe microscopy. *Applied Physics Letters* **2006**, *88*, 122104.

[329] Kempisty, P.; Krukowski, S. On the nature of Surface States Stark Effect at clean GaN(0001) surface. *Journal of Applied Physics* **2012**, *112*, 113704.

[330] McNamara, J. D.; Behrends, A.; Mohajerani, M. S.; Bakin, A.; Waag, A.; Baski, A. A.; Reshchikov, M. A. Surface photovoltage in heavily doped GaN:Si,Zn. *Proceedings of the 27th International Conference on Defects in Semiconductors, ICDS-2013* **2014**, *1583*, 287–291.

[331] Bartoš, I.; Romanyuk, O.; Houdkova, J.; Paskov, P. P.; Paskova, T.; Jiříček, P. Electron band bending of polar, semipolar and non-polar GaN surfaces. *Journal of Applied Physics* **2016**, *119*, 105303–123701.

[332] Foussekis, M.; Baski, A. A.; Reshchikov, M. A. Photoadsorption and photodesorption for GaN. *Applied Physics Letters* **2009**, *94*, 162116.

[333] Hashizume, T.; Ootomo, S.; Inagaki, T.; Hasegawa, H. Surface passivation of GaN and GaN/AlGaN heterostructures by dielectric films and its application to insulated-gate heterostructure transistors. *Journal of Vacuum Science & Technology B: Microelectronics and Nanometer Structures* **2003**, *21*, 1828.

[334] Bermudez, V. Adsorption and photodissociation of 4-haloanilines on GaN(0001). *Surface Science* **2002**, *519*, 173–184.

[335] Bermudez, V. Functionalizing the GaN(0001)-(1×1) surface II. Chemisorption of 3-pyrroline. *Surface Science* **2002**, *499*, 124–134.

[336] Bermudez, V. Functionalizing the GaN(0001)-(1×1) surface I. The chemisorption of aniline. *Surface Science* **2002**, *499*, 109–123.

[337] Bermudez, V.; Long, J. Chemisorption of H2O on GaN(0001). *Surface Science* **2000**, *450*, 98–105.

[338] Bermudez, V. M. Adsorption of 1-octanethiol on the GaN(0001) surface. *Langmuir* **2003**, *19*, 6813–6819.

[339] Demirel, G.; Caglayan, M. O.; Garipcan, B.; Duman, M.; Piskin, E. Formation and organization of amino terminated self-assembled layers on Si(001) surface. *Nanoscale Research Letters* **2007**, *2*, 350–354.

[340] Martinez, G. L.; Curiel, M. R.; Skromme, B. J.; Molnar, R. J. Surface recombination and sulfide passivation of GaN. *Journal of Electronic Materials* **2000**, *29*, 325–331.

[341] Konenkova, E. V. Modification of GaAs(100) and GaN(0001) surfaces by treatment in alcoholic sulfide solutions. *Vacuum* **2002**, *67*, 43–52.

[342] Plucinski, L.; Colakerol, L.; Bernardis, S.; Zhang, Y.; Wang, S.; O'Donnell, C.; Smith, K. E.; Friel, I.; Moustakas, T. D. Photoemission study of sulfur and oxygen adsorption on GaN(0001). *Surface Science* **2006**, *600*, 116–123.

[343] Bain, C. D.; Troughton, E. B.; Tao, Y. T.; Evall, J.; Whitesides, G. M.; Nuzzo, R. G. Formation of Monolayer Films by the Spontaneous Assembly of Organic Thiols from Solution onto Gold. *Journal of the American Chemical Society* **1989**, *111*, 321–335.

[344] Bessolov, V. N.; Lebedev, M. V.; Zahn, D. R. Raman scattering study of surface barriers in GaAs passivated in alcoholic suifide solutions. *Journal of Applied Physics* **1997**, *82*, 0021–8979–1–5.

[345] Tzou, A.-J.; Chu, K.-H.; Lin, I.-F.; Østreng, E.; Fang, Y.-S.; Wu, X.-P.; Wu, B.-W.; Shen, C.-H.; Shieh, J.-M.; Yeh, W.-K.; Chang, C.-Y.; Kuo, H.-C. AlN Surface Passivation of GaN-Based High Electron Mobility Transistors by Plasma-Enhanced Atomic Layer Deposition. *Nanoscale research letters* **2017**, *12*, 315.

Journal publications

1. Hietzschold S., Hillebrandt S., Ullrich F., Bombsch J., Rohnacher V., Ma S., Liu W., Köhn A., Jaegermann W., Pucci A., Kowalsky W., Mankel E., Beck S., and Lovrincic R., Functionalized Nickel Oxide Hole-Contact Layers: Work Function versus Conductivity, *ACS Appl. Mater. Interfaces*, 10.1021/acsami.7b12784, 2017.

2. Ullrich F., Hillebrandt S., Hietzschold S., Rohnacher V., Jaegermann W., Pucci A., Kowalsky, Lovrincic R., Beck S., and Mankel E., Annealing Temperature Dependent Analytical Study on Oxygen Plasma Treated Solution-Processed Nickel Oxide: New Insights into the Correlation of Chemical and Electronic Properties, *In submission*, 2017.

3. Müller L., Rhim S-Y., Sivanesan V., Wang D., Hietzschold S., Reiser P., Mankel E., Beck S., Barlow S., Marder S. R., Pucci A., Kowalsky W., and Lovrincic R., Electric-Field-Controlled Dopant Distribution in Organic Semiconductors, *Adv. Mater.*, 29, 1701466, 2017.

4. Raupp S. M., Merklein L., Hietzschold S., Zürn M., Scharfer P., Schabel W., Slot die-coated blue SMOLED multilayers, *J. Coat. Technol. Res.*, 14, 1029, 2017.

Conference presentations

1. Hietzschold S., Hillebrandt S., Ullrich F., Bombsch J., Rohnacher V., Ma S., Liu W., Köhn A., Jaegermann W., Pucci A., Kowalsky W., Mankel E., Beck S., and Lovrincic R., *Nickel Oxide as Hole-Contact Material in Organic Electronics: The Role of Composition, Microstructure and Surface Functionalization*, Poster, ICOE 2017, St. Petersburg, Russia.

2. Hietzschold S., Bombsch J., Hillebrandt S., Rohnacher V., Ullrich F., Mankel E., Lovrincic R., and Kowalsky W. *Solution-Cast Nickel Oxide Thin Films as Efficient Hole Extraction Layers in Organic Electronics*, Poster, IFSOE 2016, Moscow, Russia.

3. Hietzschold S., Scherer M., Schinke J., Lovrincic R., and Kowalsky W., *Determination of Trap and Band States in Organic Field-Effect Transistors by Scanning Kelvin Probe Microscopy*, Poster, DIPC Interfaces 2014, Donostia-San Sebastian, Spain.

4. Hietzschold S., Scherer M., Schinke J., Lovrincic R., and Kowalsky W., *Determination of Trap and Band States in Organic Field-Effect Transistors by Scanning Kelvin Probe Microscopy*, Poster, Award Nominee, MRS Spring Meeting 2014, San Francisco, USA.
5. Hietzschold S., Scherer M., Schinke J., Lovrincic R., and Kowalsky W., *Determination of Trap and Band States in Organic Field-Effect Transistors by Scanning Kelvin Probe Microscopy*, Poster, DPG Spring Meeting 2014, Dresden, Germany.
6. Hietzschold S., Mathies F., Saive R., Mechau N., and Kowalsky W., *Determination of Trap and Band States in Printable Thin Film Transistors by Scanning Kelvin Probe Microscopy*, Poster, DPG Spring Meeting 2013, Regensburg, Germany.

Supervised theses and research projects

- Jakob Bombsch, M. Sc., Heidelberg University
  Solution-processed nickel oxide as hole-transport layer in organic solar cells
- Stefan Brackmann, M. Sc., Heidelberg University
  Functionalization of n-type wurtzite gallium nitride (0001) surfaces with organic self-assembled monolayers
- Florian Friedrich, B. Sc., Heidelberg University
  Anpassung der Austrittsarbeit von aus Lösung hergestelltem Nickeloxid durch selbstorganisierende Monolagen
- Jakob Bombsch, B. Sc., Heidelberg University
  In-situ Wachstumsstudie von kristallinen Pentacenfilmen auf der SiO_2 *Oberfläche mit Rasterkraftmikroskopie im Ultrahochvakuum*
- Martin Jonak, Research Assistant, Heidelberg University
  Self-assembly of styrene monolayers on the nickel oxide surface

Danksagung

An dieser Stelle möchte ich mich herzlich bei allen bedanken, die mich auf dem Weg zur Promotion begleitet und unterstützt haben. Insbesondere danke ich

Prof. Wolfgang Kowalsky für die Möglichkeit, in seiner Arbeitsgruppe am InnovationLab zu promovieren, sowie für die Unterstützung des Forschungsaufenthaltes und der Teilnahme an zahlreichen internationalen Konferenzen.

Prof. Albrecht Winnacker für die bereitwillige Übernahme des Zweitgutachtens.

Dr. Robert Lovrincic für die wissenschaftliche Betreuung, für das Korrekturlesen der Arbeit und für das Ermöglichen, Auslandserfahrung während der Promotion sammeln zu können.

Prof. Tony Heinz und Dr. Omer Yaffe, die sich als offene und lehrreiche Gastgeber während meiner Zeit an der Columbia University erwiesen haben.

Sabina Hillebrandt und Florian Ullrich für eine motivierende Zusammenarbeit und insbesondere für ihren besonders großen Anteil zum Gelingen der Arbeit durch Messungen mit IR- und Photoelektronenspektroskopie.

meinen Studenten, Jakob Bombsch, Stefan Brackmann, Florian Friedrich sowie auch Valentina Rohnacher und Martin Jonak für ihre wissenschaftlichen Beiträge.

den Kollaborationspartnern am Paul-Drude-Institut in Berlin, Dr. Sergio Fernandez-Garrido, Dr. Thomas Auzelle und Dr. Chiara Sinito.

Dr. Jean-Nicolas Tisserant, Florian Mathies, Lars Müller und Sebastian Raupp,

allen Kollegen und ehemaligen Betreuern am iL,

meiner Familie, Roswitha, Hans-Joachim, Christian und Janina,

einer weiteren Familie, Brigitte, Wolfgang, Julian,

Christina
sowie einigen Freunden in Heidelberg (KBGBS) und Mülheim a.d. Ruhr.

Erklärung:

Ich versichere, dass ich diese Dissertation selbstständig verfasst habe und keine anderen als die angegebenen Quellen und Hilfsmittel benutzt habe.

Heidelberg, den 09.10.2017 ....